

Modeling of Bioheat Transfer Processes at High and Low Temperatures

KENNETH R. DILLER

The University of Texas at Austin, Austin, Texas

I. Introduction

Many important phenomena in living systems are precipitated and/or governed by endogenous or exogeneous heat transfer processes. Organisms ranging in complexity from insects to humans have elaborate mechanisms for responding to thermally challenging environments in order to avoid or minimize injury. In some cases the effective ability to transport heat is either increased or decreased, the internal rate of generation of heat is enhanced or reduced, or the biochemical composition of selected tissues is altered to render the body less sensitive to the effects of extremes in temperature.

Heat transfer has many therapeutic applications involving either a raising or lowering of temperature and often requires precise monitoring of the spatial distribution of thermal histories that are produced during a protocol. Extremes of temperature into the freezing and burning ranges are useful in surgical procedures for selective killing and/or removal of target tissues. Very low temperatures may also be useful for the long term preservation of biologicals with a minimum of chemical deterioration. The potential and practical implications of many of these procedures have been appreciated and understood to varying degrees for hundreds of years, and in some instances, for millennia. In more recent years the ability to perform accurate analysis of heat transfer phenomena has led to a quantitative basis for describing the broad range of bioheat transfer processes that exist, and there has been an increasing interest in modeling the unique features of the flow of heat in living systems.

As an accrual of methods of analysis, relevant property values, and application examples has occurred, there has been a series of review articles and monographs published dealing various aspects of bioheat transfer.

Important among these are the works of The American Institute of Physics [3], Licht [127], Birkebak [15], Chato [35], Stoll [196], Shitzer [192], Bowman *et al.* [24], Shitzer and Eberhart [193], and Chato [37]. During the past decade there has been an increasingly intense interest in bioheat transfer phenomena, with particular emphasis on therapeutic and diagnostic applications. Some of these applications are reviewed in detail in other chapters of the present volume. This chapter has the goals of providing a general background for the previous work done in bioheat transfer, of describing the evolution of modeling techniques to deal with the special problems confronting the analysis of heat transfer processes in biosystems, both *in vivo* and *in vitro*, and of discussing some specific applications that are not covered elsewhere in the present monograph.

A preponderance of the thermal processes of interest in biological systems involves a change of state under either planned or fortuitous conditions. Therefore, a rational general starting point for analysis of the temperature distribution in a system is the standard transient diffusion equation:

$$\frac{\partial T}{\partial t} = \alpha \nabla^2 T + \frac{Q}{\rho c} \quad (1.1)$$

where the Laplacian operator on temperature, $\nabla^2 T$, is manifested in any of the various coordinates as appropriate to the system under consideration.

The internal heat generation, Q , may take on various forms, depending on the system and process of interest. For example, in living tissues there may be convective heat exchange between blood perfused through the local microvascular network and the surrounding tissue under conditions for which the blood and tissue are at different temperatures and the thermally significant elements of the vasculature are distributed either approximately uniformly or in a defined pattern throughout the tissue. In addition, many medical processes involve the application of an external heat source that results in an internal distribution of energy absorption within the tissue, such as occurs during laser, electromagnetic, and ultrasonic irradiation. Endogenous heat generation by metabolism, may also be included as a Q term as appropriate. The variations on this theme for biological applications are nearly endless; we will proceed to address techniques for the modeling of many of the most important and commonly encountered examples of heat transfer processes in living systems.

II. Low Temperature Heat Transfer without Phase Change

It is convenient to consider heat transfer in biological systems at low temperatures in terms of two categories of processes depending on whether

a liquid/solid phase change occurs. The rationale for this approach may be found in differences in both the physical response to the thermal process and the formulation of the modeling equations. In general, the avoidance of solidification and melting issues in both a simpler basis for modeling and a reduced probability for irreversible injury to the subject tissue. Strategies for avoiding freezing during cooling may take one of several forms. Temperatures may be kept at values above the equilibrium phase change state, the nucleation of ice crystals may be blocked by a biochemical modification of the tissue substance, or the cooling process may be rapid enough across the range of states over which nucleation and crystal growth are able to occur to prohibit significant accrual of these kinetic processes. In any case, the temperature distribution within the specimen is described by Eq. (1.1), along with the appropriate boundary and initial conditions.

A. MODELING STRATEGIES

In most applications it is quite reasonable to assume that the initial temperature distribution prior to cooling is isothermal, and, further, the transient thermal process is often precipitated by convective exchange with the environment, with radiation not playing a significant role in the boundary heat transfer. At low temperatures, blood flow is assumed to not exist, and metabolism has no significant effect on the local temperature distribution. For a step change in the environmental temperature and the internal temperature a function of only a single spatial parameter, well known analytical solutions are available in each of the three primary coordinate systems (Carslaw and Jaeger [33]). In each case the transient temperature distribution is described in terms of a series solution.

For Cartesian coordinates the temperature distribution and the initial and boundary conditions are written as follows:

$$\frac{\partial T}{\partial t} = \alpha \frac{\partial^2 T}{\partial x^2} \quad (2.1)$$

subject to the initial condition of a uniform state,

$$T(x, 0) = T_i, \quad -L \leq x \leq L \quad (2.2)$$

symmetry at the center, and convection with the environment at both boundaries:

$$\frac{\partial T}{\partial x} = 0, \quad x = 0 \quad (2.3)$$

$$\pm \frac{\partial T}{\partial x} = -\frac{h}{k}(T - T_e), \quad x = \pm L \quad (2.4)$$

The solution of this problem is a Fourier series, written in terms of the standard set of dimensionless parameters for transient heat transfer analysis (see nomenclature list).

$$\begin{aligned}\Theta(X, Fo_x) &= \frac{T - T_e}{T_i - T_e} \\ &= \sum_{n=1}^{\infty} \Psi_n \exp(-\beta_n^2 at/L^2) \cos(\beta_n x/L) \\ &= \sum_{n=1}^{\infty} \Psi_n \exp(-\beta_n^2 Fo) \cos(\beta_n X)\end{aligned}\quad (2.5)$$

where the constant Ψ_n is defined as

$$\Psi_n = \frac{4 \sin \beta_n}{2\beta_n + \sin(2\beta_n)} \quad (2.6)$$

β_n are the roots of the transcendental equation

$$\beta_n \tan(\beta_n) = \frac{hL}{k} = Bi_x \quad (2.7)$$

In cylindrical coordinates the temperature distribution and the initial and boundary conditions are written as

$$\frac{\partial T}{\partial t} = \frac{\alpha}{r} \frac{\partial}{\partial r} \left(r \frac{\partial T}{\partial r} \right) \quad (2.8)$$

subject to the initial condition

$$T(r, 0) = T_i, \quad 0 \leq r \leq r_o \quad (2.9)$$

plus symmetry at the center and convection with the environment at the boundary.

$$\frac{\partial T}{\partial r} = 0, \quad r = 0 \quad (2.10)$$

$$-\frac{\partial T}{\partial r} = \frac{h}{k}(T - T_e), \quad x = r_o \quad (2.11)$$

The solution of this problem is given by a series.

$$\Theta(R, Fo_r) = \sum_{n=1}^{\infty} \Psi_n \exp(-\beta_n^2 Fo_r) J_0(\beta_n R) \quad (2.12)$$

where the constant Ψ_n is defined for cylindrical coordinates as

$$\Psi_n = \frac{2}{\beta_n} \frac{J_1(\beta_n)}{J_0^2(\beta_n) + J_1^2(\beta_n)} \quad (2.13)$$

J_0 and J_1 are Bessel functions of the first kind and zeroth and first order, respectively, and β_n are the roots of the transcendental equation

$$\beta_n \frac{J_1(\beta_n)}{J_0(\beta_n)} = \frac{hr_o}{k} = Bi_r \tag{2.14}$$

For spherical coordinates the temperature distribution and the initial and boundary conditions are written as follows:

$$\frac{\partial T}{\partial t} = \frac{\alpha}{r^2} \frac{\partial}{\partial r} \left(r^2 \frac{\partial T}{\partial r} \right) \tag{2.15}$$

subject to the initial and boundary conditions defined in Eqs. (2.9-2.11).

The solution of this problem is given by a Fourier series.

$$\Theta(R, Fo_s) = \sum_{n=1}^{\infty} \Psi_n / (\beta_n R) \exp(-\beta_n^2 Fo_s) \sin(\beta_n R) \tag{2.16}$$

where the constant Ψ_n is defined for spherical coordinates as

$$\Psi_n = \frac{4(\sin \beta_n - \beta_n \cos \beta_n)}{2\beta_n - \sin(2\beta_n)} \tag{2.17}$$

β_n are the roots of the transcendental equation

$$1 - \beta_n \cot(\beta_n) = \frac{hr_o}{k} = Bi_s \tag{2.18}$$

For many practical applications only a finite number of terms of the infinite series solutions given in Eqs. (2.5), (2.12), and (2.16) are calculated, depending on the point in time during a transient process to be analyzed. For Fourier numbers, $Fo = \alpha t / L^2$, above a threshold value only the first term is necessary, and as the Fourier number becomes smaller additional terms must be included in the calculation to obtain accurate results. In past analyses to solve for the transient temperature field, computations have usually been limited to just the first four or five terms, and typically, only this number is reported (Schneider [190]; Gröber *et al.* [83]; Gosse [81]). Thus, for each value of the Biot number, $Bi = hL/k$, to be considered, there are four or five roots β_n to be determined.

Heisler [97] has pointed out that in determination of temperature, for $Fo > 0.2$ all but the first term in the previous three equations may be neglected within an accuracy of 1%. Besides the obvious advantage of simplifying the computations by dropping all but the first term, the ratio of temperature at any position in the system to the center line value becomes independent of time. Based on these observations the widely used Heisler charts were generated in which, for $Fo > 0.2$, the temperature at the

geometric center is a function only of time and boundary conditions, and the interior temperatures are a function only of position and the surface thermal resistance. The results of these calculations are presented graphically in a format quite convenient to application by the user, and they are now included in nearly all undergraduate textbooks on heat transfer. For times shorter than $Fo = 0.2$ Heisler solved the equations on an analogue computer, and a set of separate graphs were prepared for which temperature varied as a function of both position and time.

Although the simplifications proposed by Heisler are convenient for many classes of heat transfer engineering problems, they are often totally unacceptable for applications in low temperature bioheat transfer. Events occurring near the initiation of the cooling protocol are usually of governing importance in determining the fate of cooled cells or tissue, and typically they fall within the domain of states for which $Fo < 0.2$. For example, during vitrification of tissues for cryopreservation one of the stages at which the cells may be most susceptible to injury is at high subzero temperatures, corresponding to the conditions just after the start of the cooling process. In addition, although living cells and tissues may be sensitive to exposure at hypothermic temperatures per se, the rate of temperature change generally bears greater influence in dictating whether injury will occur during an excursion to low temperatures. The Heisler charts present data for only the transient temperature profiles, and are therefore not of use for identifying the distribution of cooling and warming rates within a specimen. Thus, for many biological applications it is not appropriate or possible to apply the Heisler charts or the equivalent single term solution to analyse the temperature and cooling rate fields within a specimen shortly after the start of cooling.

Recently, Diller [53, 54] performed a further analysis to extend the existing results described above to include the spatial and temporal variations in the cooling rates and to identify the states near the beginning of a protocol. This effort involved solving the transcendental equations (2.7), (2.14), and (2.18) for the roots β_n and Eqs. (2.6), (2.13), and (2.17) for the associated constants Ψ_n over a range of operating states broader than that available previously. In each of the three basic coordinate systems the first five values of β_n and Ψ_n were computed for incremental values of the Biot number, Bi , between 0 and ∞ . These values are available in tabular format (Diller [53]). In addition, the necessity of obtaining information concerning cooling processes in biological systems immediately after initiation requires that in some instances more than just the first five terms of the series solutions be applied in the calculations. Accordingly, the first 20 values of β_n and Ψ_n were calculated for $Bi = \infty$ in Cartesian, cylindrical, and spherical coordinates. Since the series solution equations in which these

constants are used may include as many as 20 terms for the short time process evaluation of temperature and cooling rate, the values of the constants were computed to seven significant figures in order to ensure the requisite accuracy. These parameter values are presented in Table I.

The expressions for local cooling or warming rates are obtained from the derivatives of Eqs. (2.5), (2.12), and (2.16) (Diller [53]). In Cartesian coordinates the time derivative of Eq. (2.5) is taken as follows:

$$\frac{\partial \Theta}{\partial t} = - \sum_{n=1}^{\infty} \Psi_n \beta_n^2 \alpha / L^2 \exp(-\beta_n^2 Fo_x) \cos(\beta_n X) \tag{2.19}$$

which is written in dimensionless form as $CR = \partial \Theta / \partial Fo$;

$$CR_x = \frac{\partial \Theta(X, Fo_x)}{\partial Fo_x} = - \sum_{n=1}^{\infty} \Psi_n \beta_n^2 \exp(-\beta_n^2 Fo_x) \cos(\beta_n X) \tag{2.20}$$

TABLE I

THE FIRST 20 VALUES OF β_n AND Ψ_n FROM EQS. (2.6), (2.7), (2.13), (2.14), (2.17), AND (2.18) FOR CARTESIAN, CYLINDRICAL, AND SPHERICAL COORDINATES COMPUTED TO SEVEN SIGNIFICANT FIGURES FOR THE BIOT NUMBER $Bi = \infty^a$

n	$Bi_x = \infty$		$Bi_r = \infty$		$Bi_s = \infty$	
	β_n	Ψ_n	β_n	Ψ_n	β_n	Ψ_n
1	$\pi/2$	$1.273\ 240 \times 10^0$	2.404 826	$1.601\ 975 \times 10^0$	π	2.0
2	$3\pi/2$	$-4.244\ 132 \times 10^{-1}$	5.520 078	$-1.064\ 799 \times 10^0$	2π	-2.0
3	$5\pi/2$	$2.546\ 479 \times 10^{-1}$	8.653 728	$8.513\ 992 \times 10^{-1}$	3π	2.0
4	$7\pi/2$	$-1.818\ 914 \times 10^{-1}$	11.791 534	$-7.296\ 453 \times 10^{-1}$	4π	-2.0
5	$9\pi/2$	$1.414\ 711 \times 10^{-1}$	14.930 918	$6.485\ 236 \times 10^{-1}$	5π	2.0
6	$11\pi/2$	$-1.157\ 490 \times 10^{-1}$	18.071 064	$-5.895\ 428 \times 10^{-1}$	6π	-2.0
7	$13\pi/2$	$9.794\ 150 \times 10^{-2}$	21.211 637	$5.441\ 802 \times 10^{-1}$	7π	2.0
8	$15\pi/2$	$-8.488\ 264 \times 10^{-2}$	24.352 473	$-5.078\ 936 \times 10^{-1}$	8π	-2.0
9	$17\pi/2$	$7.489\ 644 \times 10^{-2}$	27.493 479	$4.780\ 125 \times 10^{-1}$	9π	2.0
10	$19\pi/2$	$-6.701\ 261 \times 10^{-2}$	30.634 607	$-4.528\ 506 \times 10^{-1}$	10π	-2.0
11	$21\pi/2$	$6.063\ 045 \times 10^{-2}$	33.775 820	$4.312\ 839 \times 10^{-1}$	11π	2.0
12	$23\pi/2$	$-5.535\ 824 \times 10^{-2}$	36.917 098	$-4.125\ 307 \times 10^{-1}$	12π	-2.0
13	$25\pi/2$	$5.092\ 958 \times 10^{-2}$	40.058 425	$3.960\ 282 \times 10^{-1}$	13π	2.0
14	$27\pi/2$	$-4.715\ 702 \times 10^{-2}$	43.199 791	$-3.813\ 595 \times 10^{-1}$	14π	-2.0
15	$29\pi/2$	$4.390\ 481 \times 10^{-2}$	46.341 188	$3.682\ 084 \times 10^{-1}$	15π	2.0
16	$31\pi/2$	$-4.107\ 224 \times 10^{-2}$	49.482 610	$-3.563\ 301 \times 10^{-1}$	16π	-2.0
17	$33\pi/2$	$3.858\ 302 \times 10^{-2}$	52.624 052	$3.455\ 318 \times 10^{-1}$	17π	2.0
18	$35\pi/2$	$-3.637\ 827 \times 10^{-2}$	55.765 509	$-3.356\ 591 \times 10^{-1}$	18π	-2.0
19	$37\pi/2$	$3.441\ 188 \times 10^{-2}$	58.906 984	$3.265\ 869 \times 10^{-1}$	19π	2.0
20	$39\pi/2$	$-3.264\ 717 \times 10^{-2}$	62.048 468	$-3.182\ 126 \times 10^{-1}$	20π	-2.0

^a From Diller [53, Table 2, p. 186], with permission.

Comparison of Eqs. (2.5) and (2.20) shows that they differ by the factor β_n^2 which multiplies each of the terms in the series expression for the cooling rate. For the values of β obtained as the solution to Eq. (2.7), all but the first term in Eq. (2.20) may be dropped within an accuracy of 1% for $Fo > 0.5$. The higher threshold value of Fo (0.5 for cooling rate as compared to 0.2 for temperature) for approximating the series solution by just the first term is a consequence of $\beta_n^2 > 10 \cdot \beta_1^2$ for $n \geq 2$.

If all but the first term are dropped from Eq. (2.20), then it is easy to see that the ratio of the cooling rates at any position in the system to that at the geometric center is given by the simple expression

$$\frac{\partial \Theta(X, Fo_x)}{\partial Fo_x} = \frac{\partial \Theta(0, Fo_x)}{\partial Fo_x} \cos(\beta_1 X) \quad (2.21)$$

The cooling rate at the center is given at all times by the series solution

$$\frac{\partial \Theta(0, Fo_x)}{\partial Fo_x} = - \sum_{n=1}^{\infty} \Psi_n \beta_n^2 \exp(-\beta_n^2 Fo_x) \quad (2.22)$$

In cylindrical coordinates the corresponding cooling rate is written as

$$CR_r = \frac{\partial \Theta(R, Fo_r)}{\partial Fo_r} = - \sum_{n=1}^{\infty} \Psi_n \beta_n^2 \exp(-\beta_n^2 Fo_r) J_0(\beta_n R) \quad (2.23)$$

The cooling rate at the center is given for all times by

$$\frac{\partial \Theta(0, Fo_r)}{\partial Fo_r} = - \sum_{n=1}^{\infty} \Psi_n \beta_n^2 \exp(-\beta_n^2 Fo_r) \quad (2.24)$$

and the ratio of interior to center cooling rates for $Fo_r > 0.5$ for only the first term of the series is

$$\frac{\partial \Theta(R, Fo_r)}{\partial Fo_r} = \frac{\partial \Theta(0, Fo_r)}{\partial Fo_r} J_0(\beta_1 R) \quad (2.25)$$

In spherical coordinates the corresponding cooling rate is written as

$$CR_s = \frac{\partial \Theta(R, Fo_s)}{\partial Fo_s} = - \sum_{n=1}^{\infty} \Psi_n \beta_n / R \exp(-\beta_n^2 Fo_s) \sin(\beta_n R) \quad (2.26)$$

The cooling rate at the center is given for all times by

$$\frac{\partial \Theta(0, Fo_s)}{\partial Fo_s} = - \sum_{n=1}^{\infty} \Psi_n \beta_n^2 \exp(-\beta_n^2 Fo_s) \quad (2.27)$$

and the ratio of interior to center cooling rates for $Fo_s > 0.5$ for only the first term of the series is

$$\frac{\partial\Theta(R, Fo_s)}{\partial Fo_s} = \frac{\partial\Theta(0, Fo_s)}{\partial Fo_s} \frac{1}{\beta_1 R} \sin(\beta_1 R) \tag{2.28}$$

The use of these expressions to compute cooling rate is illustrated by the data given in Fig. 1. The center plane cooling rate was determined from Eq. (2.20) as a function of the magnitude of the Fourier number using the first 12 values of β_n and Ψ_n as given in Table I. In addition, the magnitudes of each of the 12 individual terms of the series expression are shown. It may be observed clearly that as the Fourier number becomes smaller, denoting times progressively closer to the beginning of the cooling process, it is necessary to add more terms to the series solution, and the primary contribution of these higher order terms is to describe the diminishing value of the cooling rate as the initial conditions of a uniform temperature distribution are approached. As the magnitude of the cooling rate become smaller and as more terms are included in the series solution, it is important to carry more significant figures in the equation constants. Thus, the values of the constants in Table I have a larger number of figures than are encountered normally.

One difference between the standard application of the Heisler charts for determination of the transient temperature distribution in solids and the

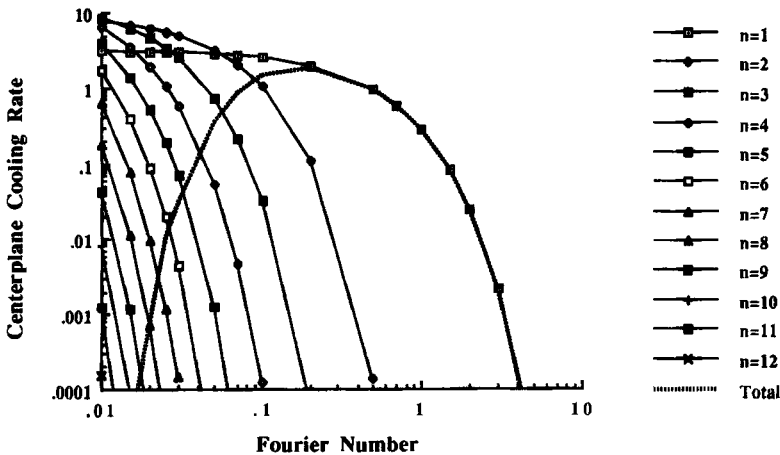


FIG. 1. Variation in magnitude of the first 12 terms of Eq. (2.20) with Fourier number for calculating the cooling rate at the center plane of a slab in Cartesian coordinates. The series summation of the terms is also shown. The Biot number is ∞ . (Reprinted by permission of the Council of the Institution of Mechanical Engineers, Diller, K. R. (1991), *Proc. Institut. Mech. Engrs., J. Engr. Medicine* 204, 179-187.)

present application for determination of cooling rates during cryopreservation is the degree of emphasis on obtaining values for times immediately following initiation of the process (very small Fourier numbers). As is often stated in presentations of the Heisler charts, for most applications of interest it is not necessary to know the temperature in the regime of $Fo < 0.2$, thereby enabling all calculations to be made using the two basic graphs, the center graph to determine transient behavior and the interior graph to determine the spatial distribution. In contrast, the states of greatest interest in cryobiology occur at small values of the Fourier number, so that the simple graphs based on single term solutions become of less utility. As a consequence it has been necessary to put more emphasis on the multiple term solutions of the Fourier series and to develop graphs that show simultaneously both the temporal and spatial variations in cooling rate. Although these graphs are more difficult to read, interpret, and apply than the standard Heisler-type charts, they still represent a considerable savings in effort to obtain estimates of cooling rate under conditions commonly encountered in cryopreservation protocols.

Graphical plots have been made of the series solutions shown previously in this chapter for cooling rate as a function of time and position (Diller [54]) following the approach of Heisler [97]. These plots are valid only for the portion of the cooling process for which the cooling rate at the center of symmetry of the system is decreasing monotonically, i.e., for $Fo \geq 0.5$. Plots of the dimensionless cooling rate at the center of symmetry for a plate, cylinder, and sphere are presented in Figs. 2a, 2b, and 2c, respectively. Three different linear scales for the Fourier number are used to display progressively the broad variation in slopes of the cooling rate function encountered over the spectrum of Biot numbers studied, which covers five orders of magnitude. The plots are used by specification of two of the set of three dimensionless parameters, Bi , Fo , and $\partial\theta/\partial Fo$, with the value of the third being identified by the fixed coordinates on the plot. The range of dimensionless time is limited to $Fo \geq 0.5$, for which only the first terms of Eqs. (2.20), (2.24), and (2.27) are necessary to compute the cooling rate. All of the curves of Fig. 2 show a negative slope associated with the decline in magnitude of cooling rate following the state at which the maximum value was reached. This predicted behavior should be anticipated from the model equations when only the first term is included since they present a single decaying exponential function.

One major difference distinguishing the Heisler charts, which present temperature, from Fig. 2, which presents cooling rate, is that as the Fourier number diminishes the curves of dimensionless temperature for all values of Bi converge to a common limit of 1.0. In contrast, the graphs of Fig. 2 do not display a uniform convergence to 1.0, or even to any single value. This

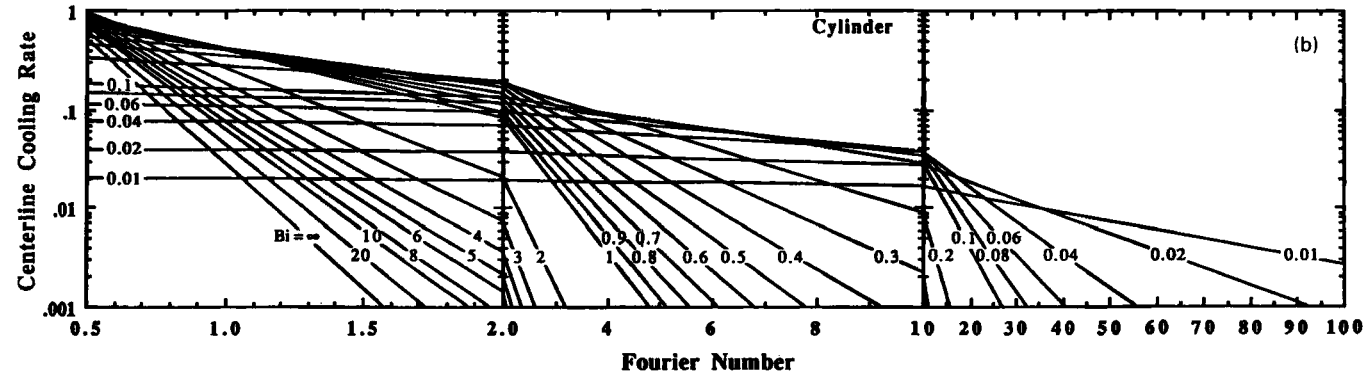
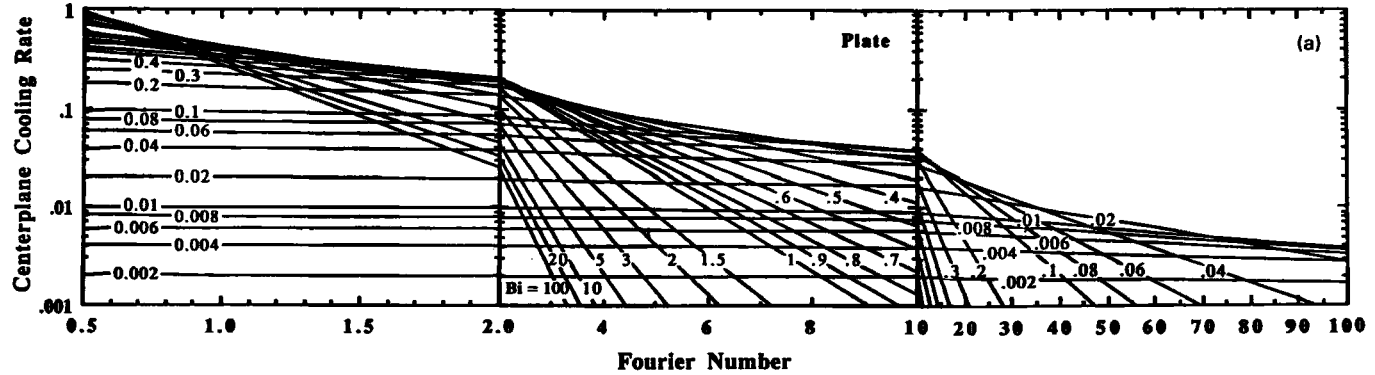
effect is particularly pronounced in the data for Cartesian coordinates. Intuitively, it should be expected that at times close to zero the cooling rate should also be zero until it becomes perturbed from the initial conditions. As will be shown in subsequent graphs, the cooling rates at all positions in the specimen do arise from an initial infinitesimally small value, and the delay period before achieving finite values increases with distance from the surface.

Spatial variations of cooling rate interior to a specimen are described by the curves in Fig. 3. The data in this graph are independent of time; it describes only the local cooling rate as a fraction of the value at the geometric center. Thus, Figs. 2 and 3 are complementary to each other, and they may be used together to calculate both the temporal and the spatial variations in cooling rate within a specimen.

At values of $Fo < 0.5$ more than one term is required to describe the cooling rate solution. In this region the solution is no longer a simple exponential function that yields the straight line plots on semilogarithmic coordinates as shown in Fig. 2. Thus, the solution becomes more complex to calculate and to present in graphical format.

The transient cooling rates at the symmetric centers of a plate, cylinder, and sphere for variations in surface resistance covering four orders of magnitude are shown in Fig. 4 for small values of Fo . Up to five terms were used in the series solutions to calculate the cooling rates for this range of states. These data identify the conditions under which a maximum in the cooling rate is realized, although at positions more proximal to the surface values for Fo of less than even 0.05 are required to show the rise from the initial steady state. Modulation of the cooling rate at the body center by the magnitude of the convective heat transfer (in linear proportion to the Biot number) is clearly apparent. The effect is greatest for small values of Bi , wherein heat transfer between the environment and the specimen center is limited by the magnitude of convection coefficient h . As Bi is increased the cooling rate becomes correspondingly greater and the maximum value is reached at smaller Fo (shorter times). Maximum normalized values in excess of 1.0 are achieved for small thermal resistances, and in general the cooling rates increase progressively from Cartesian to cylindrical to spherical geometries.

Figure 5 presents a special case in which the exact values of the first 20 values of β_n and Ψ_n (see Table I) were applied to calculate the cooling rate for Fourier numbers small enough (0.005) to identify the conditions at which the maximum values of cooling rate are reached for the region bounded by $0 \leq X$ or $R \leq \frac{2}{3}$. These values were calculated for the limiting case of zero surface thermal resistance ($Bi = \infty$), which will result in the largest internal variations in the cooling rate. Surface cooling rates



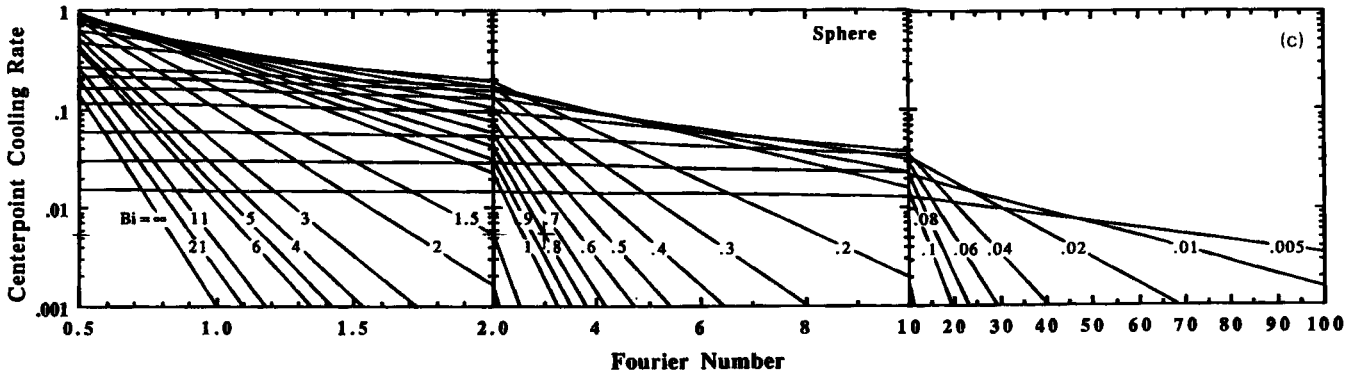
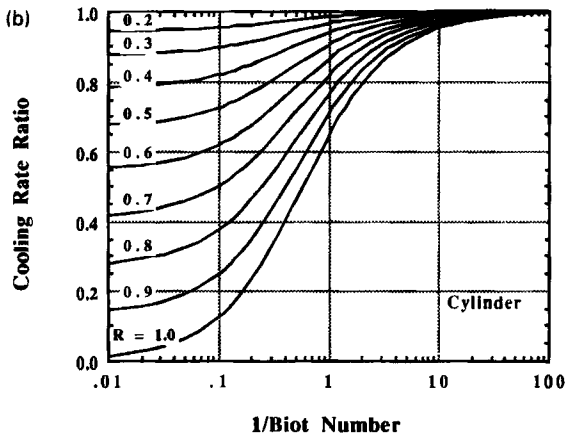
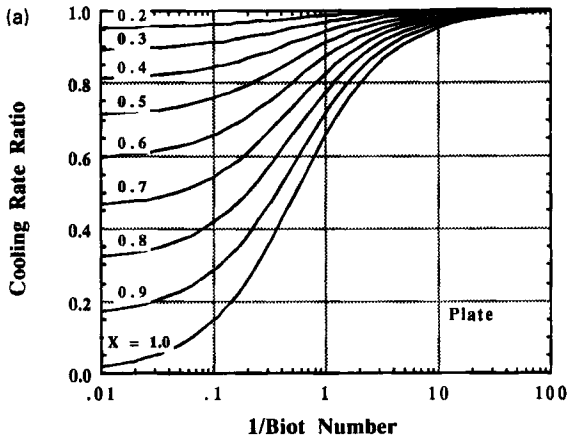


FIG. 2. Dimensionless cooling rate CR at the geometric center of symmetry for a one-dimensional body in the following coordinates: (a) Cartesian, (b) cylindrical, and (c) spherical. The cooling rate is given as a function of the Fourier number Fo for convection at the surface of the body with the environment as characterized by the indicated Biot numbers. The dimensionless parameters in the plots are as follows. (Reprinted by permission of the Council of the Institution of Mechanical Engineers, Diller, K. R. (1991), *Proc. Institut. Mech. Engrs., J. Engr. Medicine* **204**, 188-197.)

$$\begin{aligned}
 CR &= \frac{\partial \theta}{\partial Fo}, & Fo_x &= \frac{\alpha t}{L^2}, & Fo_r &= \frac{\alpha t}{RL^2}, & Fo_s &= \frac{\alpha t}{R^2} \\
 \theta &= \frac{T - T_e}{T_i - T_e}, & Bi_x &= \frac{hL}{k}, & Bi_r &= \frac{hRL}{k}, & Bi_s &= \frac{hRL}{k}
 \end{aligned}$$



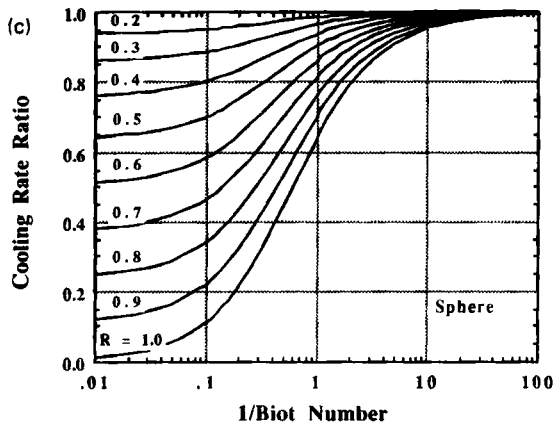
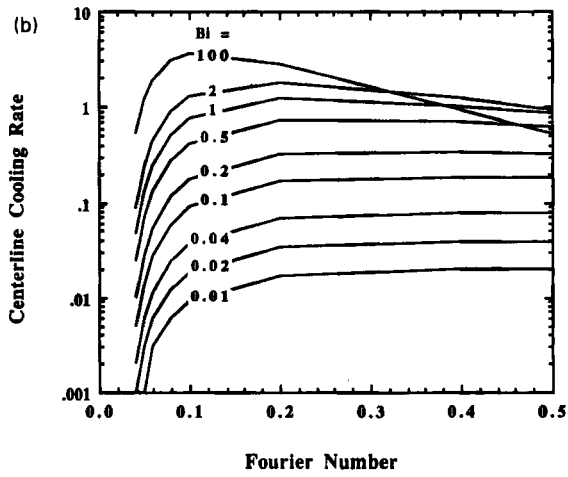
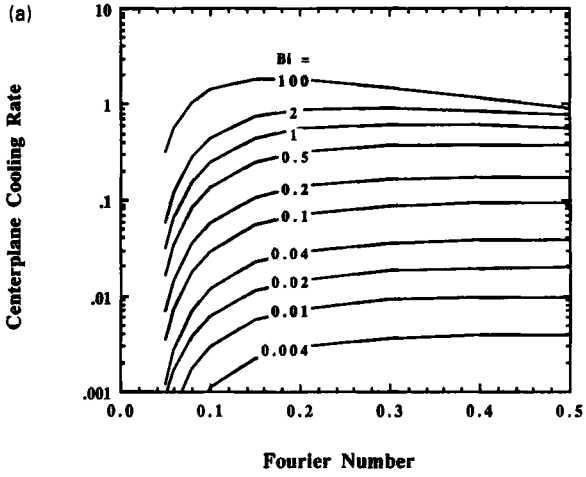


FIG. 3. Ratio of the cooling rates, CRR, in a specimen at the indicated interior points X or R and at the geometric center of symmetry for $Fo \geq 0.5$ in (a) Cartesian, (b) cylindrical, and (c) spherical coordinate systems. The dimensionless parameters in the plots are as follows. (Reprinted by permission of the Council of the Institution of Mechanical Engineers, Diller, K. R. (1991), *Proc. Institut. Mech. Engrs., J. Engr. Medicine* 204, 188-197.)

$$\begin{aligned}
 CRR_x &= \frac{CR(X, Fo_x)}{CR(0, Fo_x)}, & X &= \frac{x}{L}, & \frac{1}{Bi_x} &= \frac{k}{hL} \\
 CRR_r &= \frac{CR(R, Fo_r)}{CR(0, Fo_r)}, & R &= \frac{r}{R}, & \frac{1}{Bi_r} &= \frac{k}{hR} \\
 CRR_s &= \frac{CR(R, Fo_s)}{CR(0, Fo_s)}, & R &= \frac{r}{R}, & \frac{1}{Bi_s} &= \frac{k}{hR}
 \end{aligned}$$



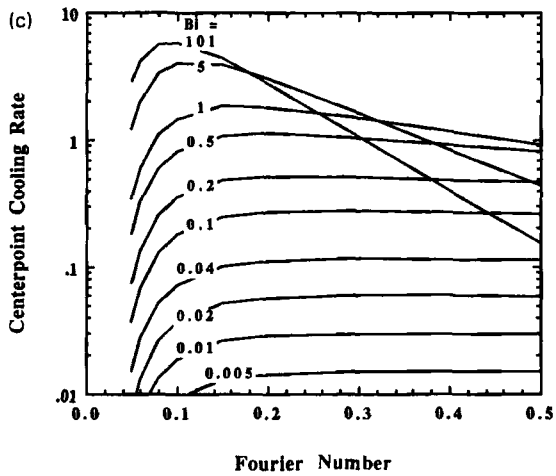
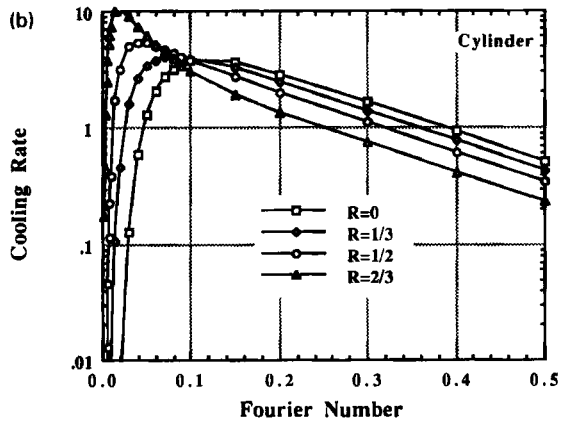
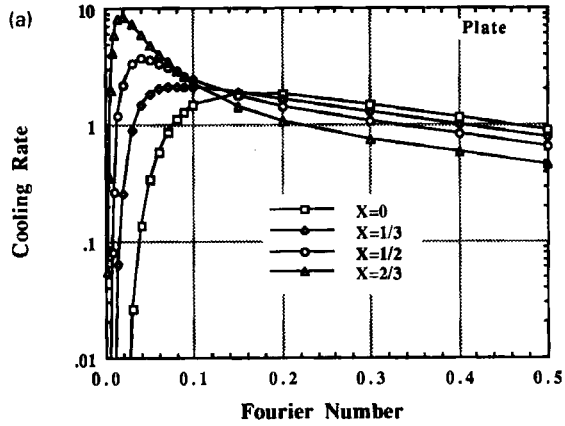


FIG. 4. Calculated cooling rates as a function of Biot number at the center of symmetry for a (a) plate, (b) cylinder, and (c) sphere at small values of the Fourier number, $0.005 \leq Fo \leq 0.5$. (Reprinted by permission of the Council of the Institution of Mechanical Engineers, Diller, K. R. (1991), *Proc. Institut. Mech. Engrs., J. Engr. Medicine* **204**, 188-197.)



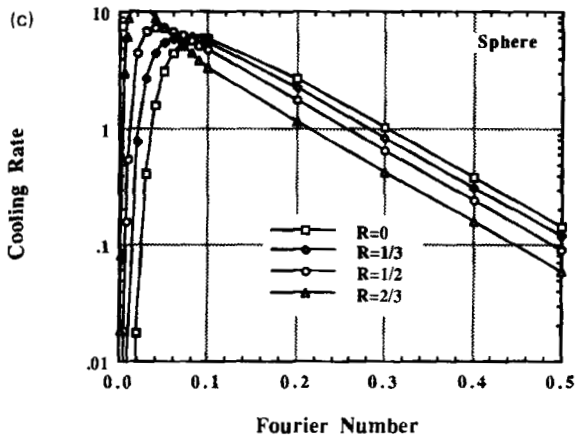


FIG. 5. Cooling rates distributed through a (a) plate, (b) cylinder, and (c) sphere as a function of dimensionless time (Fo) and position for $Bi = \infty$ (no thermal resistance at the surface) at small Fourier numbers. (a) Cartesian, (b) cylindrical, (c) spherical coordinate systems. (Reprinted by permission of the Council of the Institution of Mechanical Engineers, Diller, K. R. (1991), *Proc. Institut. Mech. Engrs., J. Engr. Medicine* **204**, 188-197.)

are not shown, since the change in temperature is essentially instantaneous under these conditions.

In addition, further graphs were presented providing values of the dimensionless cooling rate as a function of position, time, and the boundary conditions as described by the Biot number (Diller [54]). Given the availability of these graphical solutions and a full range of values of the constants in the analytical series solutions, it is now possible that cooling rates may be determined in solids of varying geometry as a function of time and position either by direct computation from the governing transient heat conduction equations or by directly reading from graphs of the solutions. In general the graphical method involves considerably less effort to obtain a numerical value for the cooling rate; this situation is particularly obvious at very small times following initiation of the cooling process for which the computations must contain numerous terms. These are precisely the conditions of most critical importance in applications for cryopreservation. The major disadvantage of the graphical method of solution is that the accuracy is considerably less than that obtained by computation with the series solution terms. The resolution with which the charts can be read is only in the order of 5–10%. However, in many cases it is not necessary or even possible to know the cooling rates more precisely than this tolerance. Also, this accuracy is likely to be no better than that associated with the initial assumptions of single phase heat transfer and homogeneous composition and properties. Thus, this approach to analysis of cooling rates should provide values of first order accuracy that can be used for simple and quick estimates of thermal performance during specific candidate cryopreservation protocols.

B. APPLICATIONS

Vitrification and undercooling are becoming increasingly important mechanisms of achieving the goals of cryopreservation, i.e., to create a state of suspended animation in a living system for which the rates of chemically driven deterioration processes are reduced to near zero and the extent of damage induced by the preservation process is negligible (Fahy *et al.* [69]). The technique of vitrification consists of the solidification of a liquid into an amorphous or glassy state in the absence of an explicit change of phase with the attendant release of latent heat (Fahy [68]). By vitrification the molecular arrangement of the liquid phase is retained to very low temperatures without the formation of a crystalline structure, and there is no alteration in the composition distribution within the solution owing to microsegregation of solvent and solute driven by the freezing process. Both of these phenomena are known to issue in a destructive mechanism that

operates on cells and tissues (Mazur [140]). In contrast, the liquid-to-glass transition is believed to not have adverse biological effects, and it therefore presents a desirable alternative for cryopreservation. Chief impediments to realizing practical vitrification procedures for a wide variety of biological materials are the necessity of modifying the chemical composition of the specimen prior to cooling so as to impede the formation of ice crystals at deep subzero temperatures and the difficulty of effecting sufficiently rapid cooling rates throughout a specimen to limit the progression of the kinetic process of ice nucleation (Fletcher [73]; Hobbs [103]; Boutron [22, 23]; MacFarlane [131]). Coger *et al.* [45] have demonstrated the dependence of ice nucleation on the thermal history (and therefore the position) within a macroscopic system being cooled for the purposes of vitrification.

Undercooling consists of lowering the temperature of a specimen, such as living cells or a labile chemical, to a high subzero temperature which is sufficiently low to retard deterioration for a reasonable period of storage, typically measured in months, but for which no solidification occurs (Franks [75]). A specimen is cooled to a state approaching the conditions for homogeneous nucleation of water without the formation of ice by blocking the local nucleation process. Thus, it is possible to avoid the injurious processes that may result from the formation of an ice phase, the concentration of solutes owing to microsegregation effects and the exposure to high concentration of cryoprotectants necessary to modify the freezing process to achieve a vitrified state. Practical methods are available now for both of these procedures, and these initial successes have stimulated interest in exploiting the techniques to more challenging applications. Control of the heat transfer processes may play a key role in determining the extent to which such applications may be realized.

Some of the heat transfer limited difficulties that confront the vitrification of large scale (10 ml to 1.5 liters) biological systems have been identified and described by Fahy *et al.* [70]). In particular, significant temperature gradients may develop interior to a specimen, and these will give rise to thermal stresses of a magnitude sufficient to cause mechanical failure of the specimen at temperatures below the state at which the liquid solidifies into a glass. Their experimental measurements in 50% (w/w) aqueous solutions of propylene glycol have shown that the magnitude of the local cooling rate (which is typically in the range of 0.2 to 2.5 °C/min) can have a profound influence on the kinetics of the ice nucleation and crystal growth processes; of course, when cooling a system for the purpose of vitrification these are processes to be avoided completely or severely restricted. Further, the incidence of thermal fracturing below the glass transition temperature, T_{gl} , is directly related to the thermal gradients and cooling rate distribution within the specimen.

In a rectangular system, as was used by Fahy *et al.* in their experiments, it is a simple matter to model the temperature distribution as a function of position and time. Either the analytical or graphical approaches described previously in the chapter could be used for this purpose. However, to illustrate an alternate numerical technique which may also be implemented quite easily, a finite difference analysis was set up to simulate the experiments of Fahy *et al.* in which the entire programming and solution procedure was executed with a simple spreadsheet program on a desktop microcomputer (Diller [55]). A symmetric rectangular grid consisting of an array of 8×12 nodes was laid out with $\Delta x = \Delta y$ to obtain a geometric aspect ratio of 1.57, corresponding to the experimental system of Fahy *et al.* Only a single quarter section of the symmetric rectangular shape was considered. Figure 6 shows the six categories of node geometries that occur for this system. The environmental boundary condition consists of convective exchange with surrounding air, and the interior surfaces of symmetry are assumed to be insulated. The node indices used as subscripts indicate position in the x, y coordinate space, and the superscript index indicates the accumulated time increments.

Forward time finite difference equations approximating the energy equation (2.1) and the initial and boundary conditions, Eqs. (2.2)–(2.4), were written for each node. Representative equations for each of the categories of node geometry are given as follows:

nodes (2,2)–(11,7): interior

$$T_{2,2}^{p+1} = \text{Fo}(T_{1,2}^p + T_{3,2}^p + T_{2,1}^p + T_{2,3}^p) + (1 - 4 \text{Fo})T_{2,2}^p \quad (2.29)$$

node (1,1): edge double corner

$$T_{1,1}^{p+1} = 2 \text{Fo}(T_{1,2}^p + T_{2,1}^p + 2 \text{Bi} \cdot T_e) + (1 - 4 \text{Fo} - 4 \text{Bi} \cdot \text{Fo})T_{1,1}^p \quad (2.30)$$

nodes (1,2), etc.: edge surface

$$T_{1,2}^{p+1} = \text{Fo}(2T_{2,2}^p + T_{1,1}^p + T_{1,3}^p + 2 \text{Bi} \cdot T_e) + (1 - 4 \text{Fo} - 2 \text{Bi} \cdot \text{Fo})T_{1,2}^p \quad (2.31)$$

nodes (1,8) and (12,1): insulated edge corner

$$T_{12,1}^{p+1} = 2 \text{Fo}(T_{12,2}^p + T_{11,1}^p + \text{Bi} \cdot T_e) + (1 - 4 \text{Fo} - 2 \text{Bi} \cdot \text{Fo})T_{12,1}^p \quad (2.32)$$

nodes (2,8), etc.: interior insulated surface

$$T_{2,8}^{p+1} = \text{Fo}(2T_{2,7}^p + T_{1,8}^p + T_{3,8}^p) + (1 - 4 \text{Fo})T_{2,8}^p \quad (2.33)$$

node (12,8): interior insulated corner

$$T_{12,8}^{p+1} = 2 \text{Fo}(T_{12,7}^p + T_{11,8}^p) + (1 - 4 \text{Fo})T_{12,8}^p \quad (2.34)$$

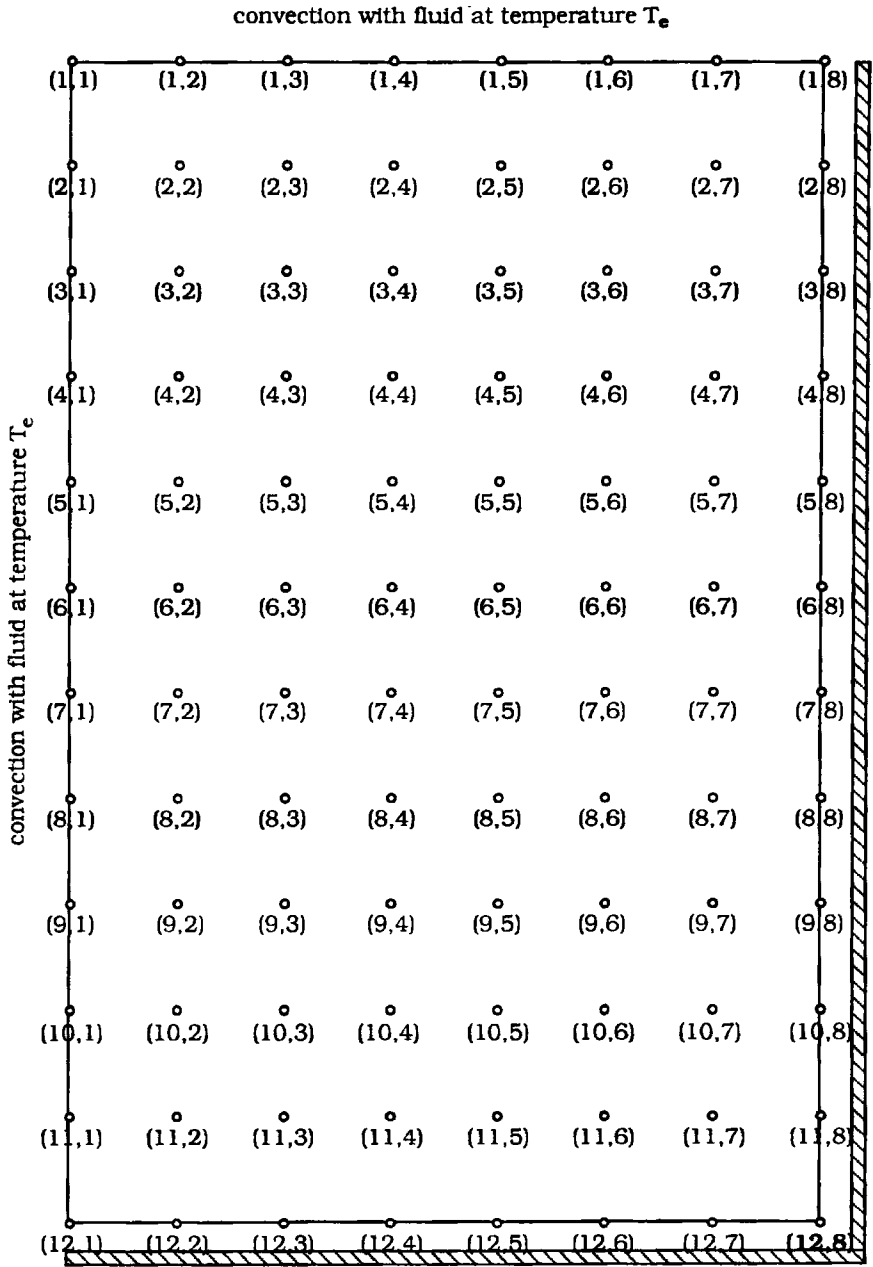


FIG. 6. Finite difference grid for a quarter section of a symmetric rectangular system. (Redrawn from Diller [55, Fig. 1], with permission.)

These equations were solved on a Macintosh computer using a Microsoft Excel spreadsheet program. Implementation of the equations for the grid was particularly convenient in this format in that each of the above six equations only had to be programmed once for a single node. Further nodes that used the same equation were programmed by copying the formula from the original node cell to the new cell, making use of the spreadsheet feature that automatically changes the position indices according to the relative position of the cells in the grid. Values for the initial and boundary condition parameters and system properties were implemented by simple external macro-programs.

Two cooling protocols were of interest for this problem; one addressed the initial cool down from room temperature as effected by a stepwise decrease in the environment to $-150\text{ }^{\circ}\text{C}$. The second considered further cooling from an intermediate equilibration state at $-107\text{ }^{\circ}\text{C}$, which was near the conditions for glass transition, to $-128\text{ }^{\circ}\text{C}$. Figure 7 shows the temperature distribution for the initial cooling process for parameter values of $Bi = 10$ and $Fo = 0.02$ after 28 time steps, corresponding to an elapsed time of approximately 1 min. The temperature field is well behaved for the model and has the shape expected, although it is also obvious that

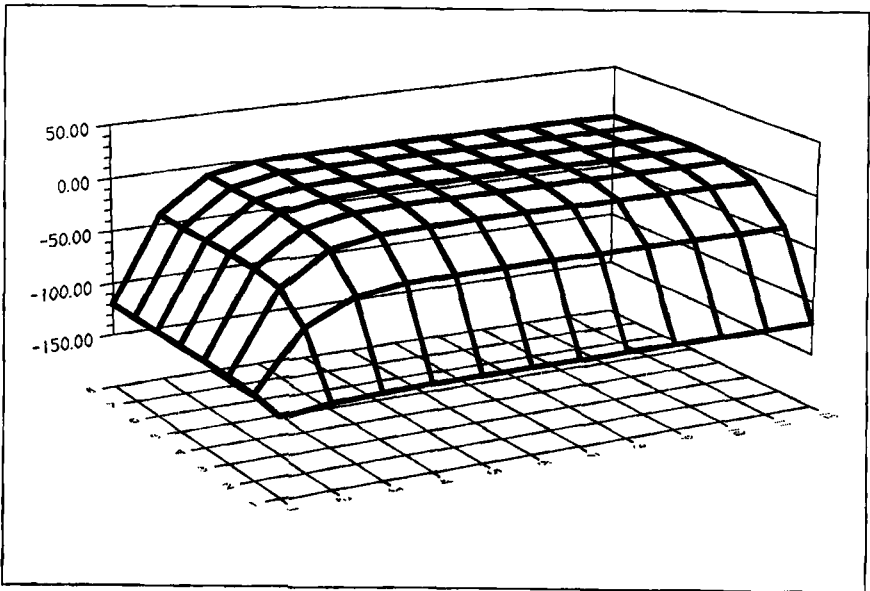


FIG. 7. Two-dimensional temperature distribution after 1 min of cooling from an initial temperature of $4\text{ }^{\circ}\text{C}$ with an environment at $-150\text{ }^{\circ}\text{C}$, $Bi = 10$ and $Fo = 0.02$. (Redrawn from Diller [55, Fig. 2], with permission.)

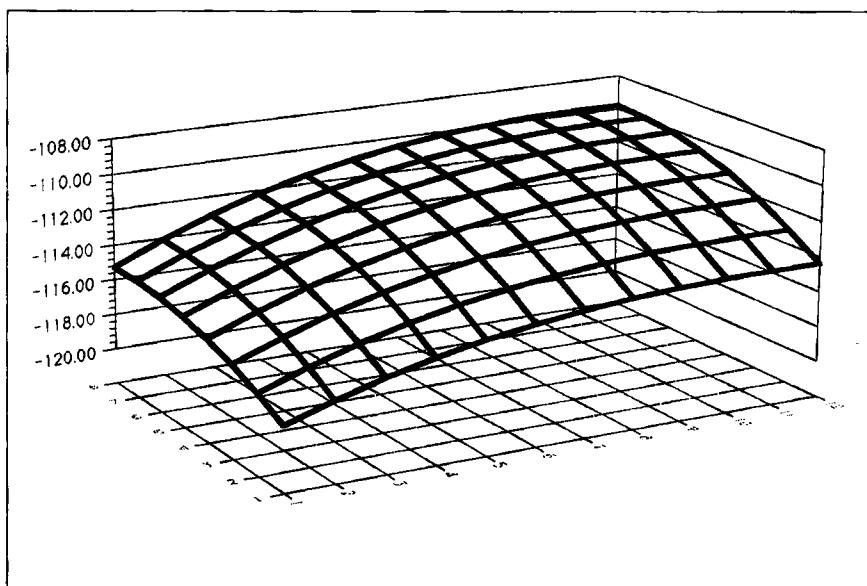


FIG. 8. Two-dimensional temperature distribution at the conditions for which the largest temperature gradients exist for cooling from an annealing temperature of -107°C with an environment at -128°C , $\text{Bi} = 0.1$, and $\text{Fo} = 0.22$. (Redrawn from Diller [55, Fig. 3], with permission.)

very large temperature gradients have developed rapidly. This analysis supports the wisdom of an annealing period as the glass transition state is approached in order for the thermal gradients to relax so that subsequent mechanical stresses can be minimized. The temperature distribution for the subsequent cooling process from -107°C is shown in Fig. 8. It is clear that the thermal gradients are greatly reduced by annealing prior to further cooling through the states for which a glass phase capable of supporting mechanical stress will form. Figure 9 shows a plot of maximum temperature differential that occurs in the system (between the center and edge corner) during the final cooling phase. The differential develops rapidly after the initiation of cooling as the temperature of the corner is reduced quickly. After a maximum differential (equal to approximately 25% of the total excursion in temperature) is reached the magnitude is reduced as the center experiences a significant response to the new boundary conditions.

The temperature computations were easily modified to include determination of the local cooling rate values. The cooling rate was evaluated as a function of time and position simply by dividing the serial temperature

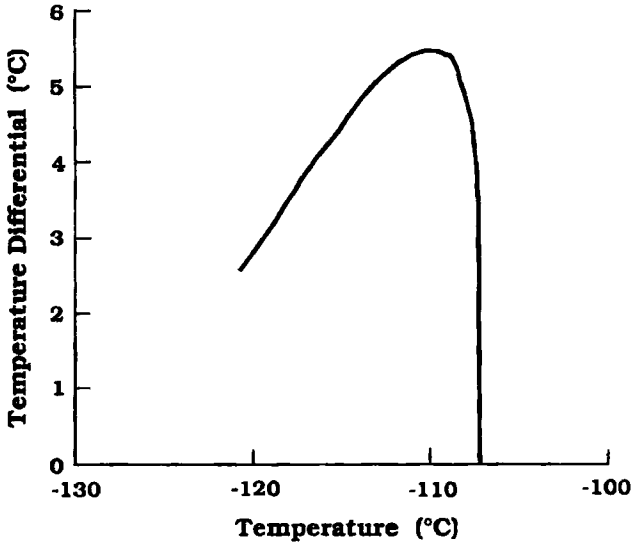


FIG. 9. Temperature differential between the center and an edge corner of a rectangle for cooling from an annealing temperature of -107°C with an environment at -128°C , $Bi = 0.1$ and $Fo = 0.22$. (Redrawn from Diller [55, Fig. 4], with permission.)

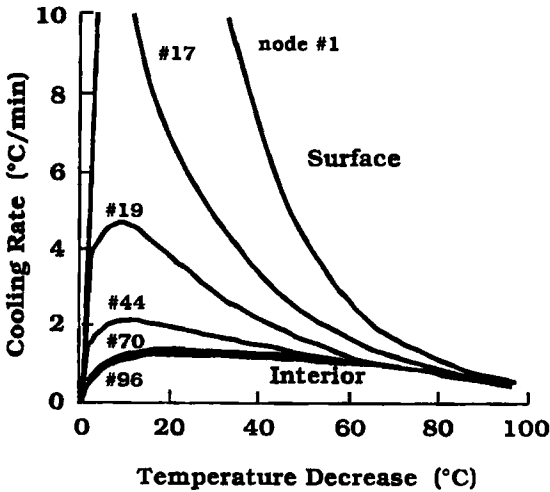


FIG. 10. Cooling rates at selected positions in the rectangular grid for cooling between initial and environmental boundary temperatures of 4 and -107°C , $Bi = 0.14$, and $Fo = 0.2$. (Redrawn from Diller [55, Fig. 5], with permission.)

differential at any given node by the magnitude of the time increment. Cooling rates were determined at several locations in the specimen for both stages of the cooling process. Figure 10 presents plots of the cooling rate as a function of the local temperature reduction from the initial value. In both cases the cooling rates are greater for positions most proximal to the surface and decrease with depth. In addition, the maximum value of the cooling rate is realized at a relatively high temperature from which there is a gradual diminution as the temperature is further lowered. The maximum rate occurs at high temperatures for most superficial locations, owing to the more immediate response to the alteration in boundary conditions. A further use of this analysis can be achieved by using the solution of the transient temperature distribution as the independent forcing function in the thermal stress equations. This analysis will be discussed in a subsequent section of this chapter.

III. Low Temperature Heat Transfer with Phase Change

In most cases, when biological tissues are subjected to subzero temperatures for extended times of exposure, solidification of a portion of the system into an ice phase will occur. The solidification phenomenon greatly increases the complexity of models requisite to describe the governing heat transfer processes. Freezing will commence at the surface of a specimen, issuing in the formation of a discrete zone between the frozen and unfrozen regions that defines a phase interface. With the progression of time the phase interface will move further into the interior of the specimen as the size of the frozen region grows. Latent heat will be liberated at the interface as water molecules change from the liquid to the solid phase. The exchange of latent heat will contribute an additional term thus far not considered in the energy balance represented by Eq. (1.1).

The term on the left of Eq. (1.1) represents changes in the energy stored in the system as manifested by alterations in the temperature (which is defined as sensible heat). In addition, during solidification the stored energy is altered without temperature change by liberation of latent heat, denoted by Λ . Λ is a function of both the amount of energy required to effect a change of phase in a mole of the chemical species of interest and the fraction of the available mass that has undergone a phase alteration. It should be noted that chemically impure systems do not experience phase changes at a singular thermodynamic state or temperature. Accordingly, biological systems, which are aqueous solutions, will solidify progressively over a range of temperatures that may vary from 20 to more than 100 °C.

Equation (1.1) can be modified to account for simultaneous changes in both the sensible and latent heats as follows:

$$\frac{\partial(\rho c T + \Lambda)}{\partial t} = k \nabla^2 T \quad (3.1)$$

Equation (3.1) will apply throughout the specimen, with liquid and solid phase thermal property values invoked locally as appropriate. The difficulty in solving Eq. (3.1) is that the location of the phase boundary at which latent heat is released changes as a function of time, giving rise to the well known moving boundary class of heat transfer problems (see Carslaw and Jaeger [33]). Thus, the magnitude of the heat transfer affects the rate of release of latent heat and thereby the movement and position of the phase interface; however, the locus of the interface must be known *a priori* in order to solve for the temperature distribution to determine the magnitude of the heat flux.

A. ANALYTICAL SOLUTIONS

It is possible to formulate the solidification problem in one dimension for Cartesian coordinates in a homogeneous, isotropic medium that freezes at a single defined temperature, so that an analytical solution can be realized based on the classic work by Neumann (see Carslaw and Jaeger [33]; Crank [48]). The heat diffusion equation is written separately for each phase region, and the latent heat release is applied at the moving boundary between the two phases.

The temperature variations in the liquid, L, and solid, S, domains are described by

$$\frac{\partial \tau_S}{\partial t} = \alpha_S \nabla^2 \tau_S, \quad 0 \leq x \leq x_F \quad (3.2)$$

$$\frac{\partial \tau_L}{\partial t} = \alpha_L \nabla^2 \tau_L, \quad x_F \leq x \quad (3.3)$$

where it is assumed that the solid phase has grown from the surface at $x = 0$ to a position defined by x_F . The uniform initial conditions throughout the specimen are

$$\tau_L = \tau_S = \tau_i, \quad x \geq 0, \quad t = 0 \quad (3.4)$$

and the set of four boundary conditions that hold for the two phase regions

in the systems are stated as

$$\tau_S = 0, \quad x = 0, \quad t > 0 \quad (3.5)$$

$$\tau_L = \tau_S = \tau_m, \quad x = x_F, \quad t > 0 \quad (3.6)$$

$$k_S \frac{\partial \tau_S}{\partial x} - k_L \frac{\partial \tau_L}{\partial x} = \rho \Lambda \frac{dx_F}{dt}, \quad x = x_F, \quad t > 0 \quad (3.7)$$

$$\tau_L = \tau_i, \quad x = \infty, \quad t > 0 \quad (3.8)$$

x_F is the distance from the free surface, and it is assumed that the densities of the two phases are identical.

The classical Neumann solution for the transient temperature in the liquid and solid regions during freezing is given as follows (Carslaw and Jaeger [33]):

$$\begin{aligned} \frac{\tau_S}{\tau_m} &= \frac{\operatorname{erf}\left(\frac{x}{2(\alpha_S t)^{1/2}}\right)}{\operatorname{erf}(\beta)} \\ &= \frac{\operatorname{erf}(\Phi_S)}{\operatorname{erf}(\beta)} \end{aligned} \quad (3.9)$$

$$\begin{aligned} \frac{\tau_L - \tau_i}{\tau_m - \tau_i} &= \frac{\operatorname{erfc}\left(\frac{x}{2(\alpha_L t)^{1/2}}\right)}{\operatorname{erfc}(\beta(\alpha_S/\alpha_L)^{1/2})} \\ &= \frac{\operatorname{erfc}(\Phi_L)}{\operatorname{erfc}(\beta A^{1/2})} \end{aligned} \quad (3.10)$$

for which the dimensionless parameter Φ is defined as the ratio $x/2(\alpha_S t)^{1/2}$ in either the liquid or the solid domain and A is the ratio of the solid to liquid phase thermal diffusivities. Matching the temperatures for the solid and liquid domains at the phase front according to Eq. (3.6) requires that the position and time properties of the phase boundary obey the relationship

$$\beta = \frac{x_F}{2(\alpha_S t)^{1/2}} \quad (3.11)$$

where β is a constant defined as the root of the transcendental equation

$$\beta = \frac{c_S \tau_m}{\Lambda \pi^{1/2}} \frac{\exp(-\beta^2)}{\operatorname{erf}(\beta)} - \frac{c_S(\tau_i - \tau_m)}{\Lambda \pi^{1/2}} \frac{\exp(-\beta^2 A)}{\operatorname{erfc}(\beta A^{1/2})} \frac{k_L}{k_S} A^{1/2} \quad (3.12)$$

The dimensionless ratio $c\tau/\Lambda$ appears in both terms on the right-side of Eq. (3.11). This ratio is commonly referred to as the Stefan number, Ste ;

it is a measure of the relative magnitudes of sensible and latent energy storage during a heat transfer process. In the first term of Eq. (3.12) this ratio is based on the portion of the total sensible energy storage that occurs while the system is in the solid phase, and the second term refers to the portion occurring while the system is in the liquid phase. An additional dimensionless parameter S can be defined based on the ratios of the relative magnitudes of the temperature excursions in the solid and liquid phases and the thermal conductivities and thermal diffusivities of the solid and liquid. The transcendental equation may be written as

$$\beta = \frac{\text{Ste}_s \exp(-\beta^2)}{\pi^{1/2} \text{erf}(\beta)} - \frac{S \text{Ste}_s \exp(-\beta^2 A)}{\pi^{1/2} \text{erfc}(\beta A^{1/2})} \quad (3.13)$$

where

$$S = \frac{\tau_i - \tau_m}{\tau_m} \frac{k_L}{k_S} A^{1/2} \quad (3.14)$$

The solution of Eqs. (3.9) and (3.10) requires specific values for β , which is a function of both the composition and the thermal state of the system, plus the boundary conditions. Values of β were computed by Churchill and Evans [41] for combinations of A , S , and Ste of interest in the solidification of metals. Their data covered the range of $0 \leq A \leq 3$, $0 \leq S \leq 3$, and $0 \leq \text{Ste}^{-1} \leq 3$, which was not at all a match for the states and processes encountered in low temperature biology and therefore of little use for investigating typical cryopreservation protocols. In particular, for metals A is on the order of 1, whereas for aqueous solutions it is approximately an order of magnitude larger. Therefore, the range of states for which values for β have been calculated was extended recently by Diller [52] to enable computation of thermal histories during freezing of biological systems. As a result, cooling rates have been determined for the rapid quenching of biological specimens in the attempt to avoid ice crystal artifacts in cryopreparation for electron microscopy (Diller [51]). The basis for this process has been explained by Robards (Robards and Sleytr [171]) and initial confirming analysis performed by his colleague Bald [7].

B. NUMERICAL SOLUTIONS

In many cases the assumptions of a homogeneous medium that undergoes phase change at a discrete defined temperature and that has a simple one-dimensional geometry are inappropriate for biological systems and processes. It then becomes necessary to apply a numerical approximation technique in lieu of an analytical procedure to obtain a solution for the transient temperature field and the associated cooling and warming rate

distribution throughout the system (Hayes and Diller [91]). In addition, simultaneous coupled heat and mass transfer will govern the response of the tissue to the phase change process, leading to further complications in formulating and solving models of freezing protocols (Rubinsky [178]).

An important consideration when evaluating freezing processes in biological tissues arises from the fact that the system composition consists of one or more solutes in an aqueous solution. In some applications the concentration may be isotonic, but the cryopreservation of tissues requires the addition of a cryoprotective agent (CPA), which is often present at a concentration of 2 M or higher. The addition of a CPA alters the freezing characteristics of the system substantially by modifying both the equilibrium phase diagram and the kinetics of the ice nucleation process. Considerations of the latter phenomenon are outside the scope of the present review, although it should be noted that recently there has been increasing interest in this process, and the understanding has improved substantially as a result of both experimental and analytical investigations (Franks [74]; Vigier and Vassoille [211]).

The biological effects of modifications to the phase diagram can be considerable. Although it is thought that the primary action of CPAs in protecting cells against freeze/thaw damage is based on their colligative properties (Mazur [139]; Taylor [204]), they also cause several changes in the heat transfer behavior of the system. The thermal transport properties k and α will be modified in proportion to the CPA concentration. Further, the initiation of the solidification processes will be shunted to a lower temperature due in part to the freezing point depression of the solute. Finally, the phase change process will be distributed over a range of temperatures equal to or exceeding that defined by the equilibrium phase change and the eutectic states, depending on the kinetics of ice and eutectic nucleation phenomena.

Each of these three effects can be included in thermal models of the governing heat transfer processes. The first effect requires relatively straightforward changes in the thermal properties of the system, although values for tissues and CPA solutions over the temperature range experienced during cryopreservation are scarce. There have recently been several studies to measure these properties, and some values are now available in the literature (Valvano *et al.* [208]; Valvano [207]; Bai and Pegg [6]). Second, depression of the freezing point is compensated for in modeling by a simple adjustment of the value of τ_m in the equations. Third, the distribution of the latent heat evolution over a range of temperatures has a strong influence on the thermal history within that range. The Neumann solution discussed previously in this chapter assumes that the entire latent heat is released at a single temperature, and changes in stored energy during the

remainder of a cooling process are governed exclusively by the sensible heat properties of the medium. For a chemical solution this assumption is not valid, and since there is an ongoing exchange between the sensible and latent effects, the cooling rate can be effected significantly. This phenomenon can be important for cryopreservation procedures since the temperature range over which most of the latent heat is released corresponds to the critical range of states in which osmotic transport of water and CPA will occur across cell membranes; this is the crucial process in controlling the injury mechanisms that may act on cells during cryopreservation. Hayes and Diller have made an extensive study of the effect of CPA concentration on the cooling rates within a specimen that will result from the application of defined boundary conditions (Diller *et al.* [62]; Hayes *et al.* [93]). These studies are dependent on the recent work of several investigators in measuring and/or computing the portion of equilibrium phase diagrams relevant to cryobiological processes for a number of commonly encountered CPA solutions (Cocks *et al.* [44]; Hildebrandt *et al.* [102]; Fahy [66]; Jochem and Körber [111]; Pegg and Arnaud [161]).

Accounting for the release of latent heat across a finite range of temperatures introduces nonlinearities into a heat transfer model that prohibit an analytical solution. Although both finite difference and finite element methods can be employed to obtain a numerical solution to this problem, the latter has seen more widespread application, in part due to the inherent ability to incorporate relatively easily the complex morphologies often encountered with biological examples.

When evaluating the rate of evolution of latent heat in Eq. (3.1) it is convenient to break the expression into the product of two terms, each of which can be determined from independent sources. Thus, we can write (Hayes *et al.* [93])

$$\frac{\partial \Lambda}{\partial t} = \frac{\partial \Lambda}{\partial T} \cdot \frac{\partial T}{\partial t} \quad (3.15)$$

The first term on the right of Eq. (3.15) can be obtained in a straightforward manner by applying the lever rule to a phase diagram of the solution under analysis. Figure 11 shows (a) an example phase diagram for a binary aqueous solution for sodium chloride along with (b) a plot of the latent heat release as a function of temperature for the illustrated phase diagram. Curves are shown for three different initial solute concentrations. The slope of the curve in Fig. 11b provides a measure of the first term addressed in Eq. (3.15). Note that the slope is greatest at the state of initial formation of solid phase, and it decreases monotonically to the eutectic point. It is assumed that the solution remaining when the eutectic point is reached is frozen over a 1 °C temperature interval. In general, the shape

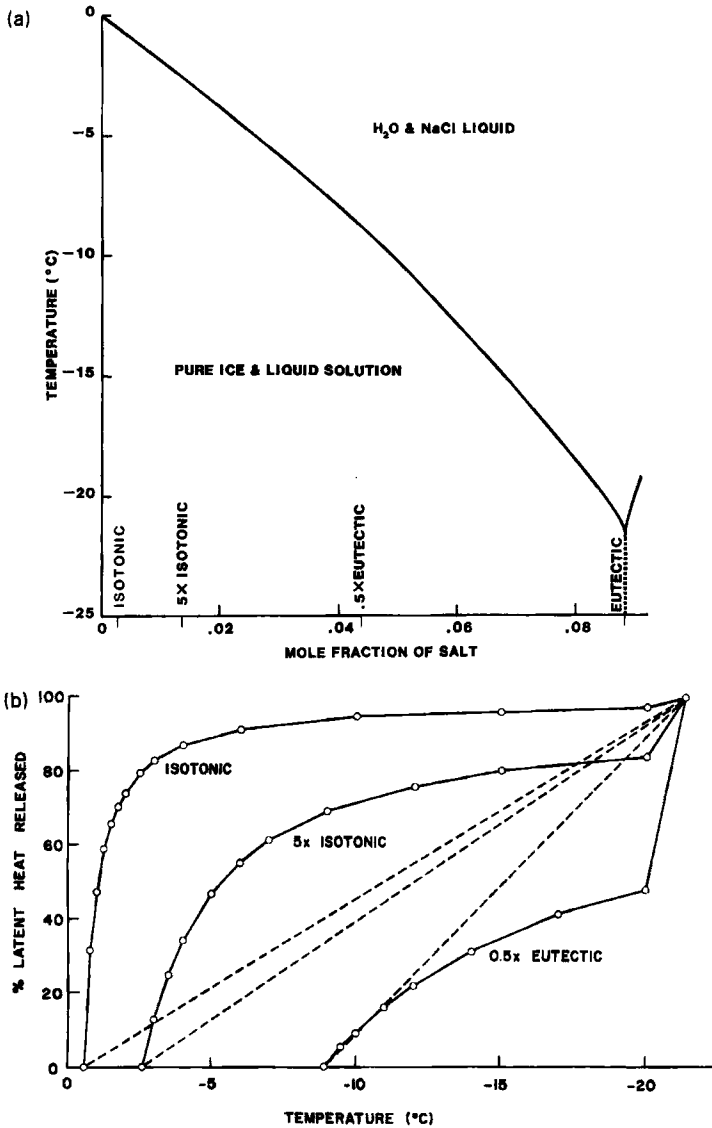


FIG. 11. (a) A binary equilibrium phase diagram for an aqueous solution illustrating the melting point at the initial concentration, the liquidus line, and the application of the lever rule to determine the fraction of the solvent (water) solidified at any subfreezing temperature. (b) Plot of the release of latent heat as a function of temperature during equilibrium solidification of a solution as determined by application of the lever rule to the phase diagram shown in (a). For comparison linear patterns of latent heat release with temperature over the range of solidification states are shown. (Redrawn from Hayes *et al.* [93, Figs. 1 and 2, p. 67], with permission.)

of this curve is strongly dependent on the composition and initial concentration of the solute(s) in the solution, and the presence of a CPA may alter it extensively. As the concentration is raised, the slope of the curve in Fig. 11b decreases for any defined temperature, and an increasing fraction of the latent heat is released at the eutectic point.

The second term on the right of Eq. (3.15) is the value of the local cooling rate, which is calculated from the solution of the transient temperature field. Thus, it is possible to rewrite Eq. (3.1) as

$$\frac{\partial \left[T \left(\rho c + \rho \frac{\partial \Lambda}{\partial T} \right) \right]}{\partial t} = k \nabla^2 T \quad (3.16)$$

A uniform initial temperature distribution is given as

$$T(x, 0) = T_i(x) \quad (3.17)$$

and at the surface the temperature may be prescribed as

$$T(0, t) = T_0 \quad (3.18)$$

Alternatively, it may be more appropriate to define a convective heat flux at the surface.

$$k \frac{\partial T(0, t)}{\partial t} = h[T_0 - T(0)] \quad (3.19)$$

The phase interface is not defined at a discrete location, but it consists of a mushy zone that contains both liquid and solid components. Within the mushy zone the relative rates at which latent and sensible energies are evolving are a function of the fraction of the local solution that is solidified. It is possible to rewrite the left side of Eq. (3.16) in terms of an apparent specific heat, c , which is defined as (Hayes *et al.* [95])

$$c(T) = \left[c + \frac{\partial \Lambda}{\partial T} \right] (T) \quad (3.20)$$

A revised format for Eq. (3.16) may now be written as

$$\rho c(T) \frac{\partial T}{\partial t} = k \nabla^2 T \quad (3.21)$$

which holds throughout the entire system. In many analyses for which the influence of latent heat release over a finite range of temperatures was to be considered, the function $\partial \Lambda / \partial T$ in Eq. (3.15) was assumed to obey a simple

linear relationship, as indicated by the broken lines in Fig. 11b. The solid line curve represent a more rigorous thermodynamic evaluation of the latent heat release as determined from the phase diagram by application of the lever rule. As will be shown, these two approximations produce greatly different thermal histories within the domain of states over which the phase change occurs, and this is approximately the range of states that defines the conditions that govern the mechanism and severity of freezing injury to living cells. Thus, for biological applications it is particularly critical that the thermal history be predicted as accurately as possible at high subzero temperatures.

The finite element method was applied to obtain a numerical solution to the above problem (Hayes and Diller [90]; Hayes *et al.* [93]). The specific problem addressed consisted of a long cylindrical container filled with a sodium chloride solution at one of various initial concentrations. Temperature variations along the length were ignored, and a cylindrically symmetric grid consisting of 28 quadratic elements (57 nodes) was fitted to the system geometry, as illustrated in Fig. 12. A specific set of dimensions and physical properties were prescribed for the system so that it could be solved to obtain thermal histories at any of the nodal loci. These values are presented in Table II. The influence of a number of the parameters of the numerical scheme on the predicted thermal behavior was investigated, including the assumed pattern of evolution of latent heat with decreasing temperature and the initial concentration of solute in the solution. It was demonstrated that both of these parameters can have a large effect on the predicted cooling rate through the range of temperatures over which the solidification process occurs and thereby significantly bias the predicted response of cells subjected to a given cooling protocol imposed in the specimen environment.

Figure 13 presents thermal histories at selected nodes during the freezing of an isotonic solution under the conditions described in Table II with the release of latent heat either distributed linearly between the equilibrium

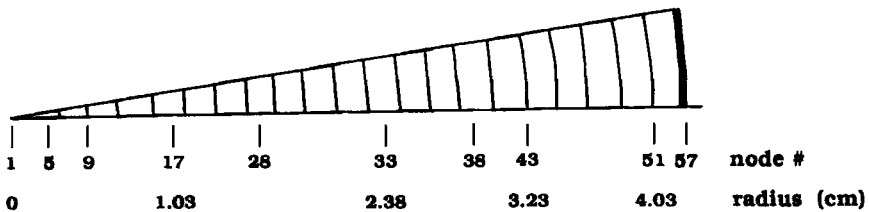


FIG. 12. Finite element grid for a solution held in a symmetric cylindrical container. The grid consists of 28 quadratic elements, all of which have uniform nodal spacing. (Redrawn from Hayes *et al* [93, Fig. 3, p. 67], with permission.)

TABLE II
SYSTEM AND PROPERTY VALUES USED IN A FINITE ELEMENT MODEL FOR THE FREEZING
OF A SALT SOLUTION IN A CYLINDRICAL CONTAINER^a

Property		Value	Units	
Container outer radius		4.33	cm	
Container wall thickness		0.1	cm	
Finite element node radial spacing—Solution		7.6	mm	
Finite element node radial spacing—Container wall		5	mm	
Uniform initial temperature, T_i		10.5	°C	
Cooling rate in environment		-5	°C/min	
Minimum temperature in environment, T_0		-80	°C	
Convective film coefficient at container surface, h		167	W/m ² ·°C	
		Solution	Container	
Heat capacity, ρc	Liquid	4.08	2.08	J/cm ³ ·°C
	Solid	1.88		
Thermal conductivity, k	Liquid	0.59	3.28	W/m·°C
	Solid	2.22		
Heat capacity, Λ		326		J/cm ³

^aFrom Hayes *et al.* [95, Table 1, p. 237], with permission.

phase change and eutectic temperatures or as determined by application of the lever rule to the phase diagram (see the two uppermost curves in Fig. 11b). The value of the convective film coefficient was set rather high to simulate the forced convection environment created in most commercial controlled rate biological freezers. Simple qualitative comparison of the two sets of curves shows a considerable difference in the morphology of the thermal histories at all locations within the specimen. Assumption of a linear evolution of latent heat over the range of phase change states produces both a smoothing of the transient temperature curves and about a 15% increase in the period of time requisite to complete the solidification process, with a proportional diminution in the calculated cooling rates. Since the cooling rate is of critical importance in governing the response of tissues during freezing, the common simplifying assumption of a linear process for release of latent heat is unacceptable for many applications in cryobiology. Thermal histories calculated based on the nonlinear pattern of latent heat release shown in Fig. 11b are characterized by a protracted plateau at states near the equilibrium phase change temperature where alterations in the stored energy are dominated by the initial rapid evolution

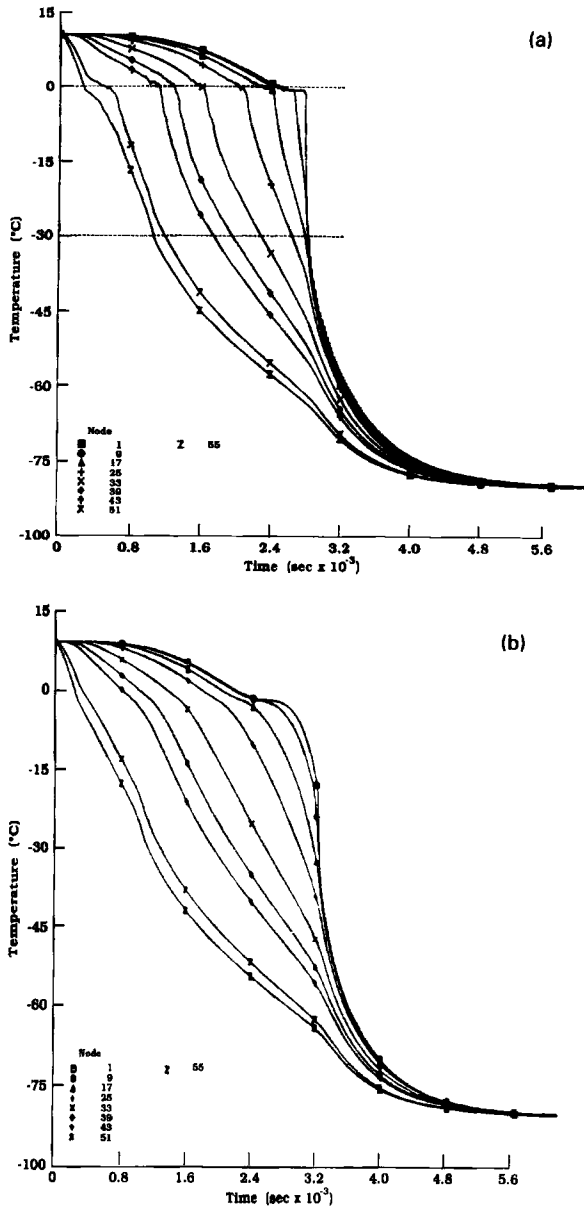


FIG. 13. Simulated temperature histories at incrementally spaced radial positions for freezing of aqueous solutions having an initial isotonic concentration. (a) Latent heat release pattern with temperature as determined from the phase diagram in Fig. 11a. (b) Linear pattern of latent heat release with temperature as shown in Fig. 11b. (Redrawn from Diller *et al.* [62, Figs. 4 and 5, p. 238], with permission.)

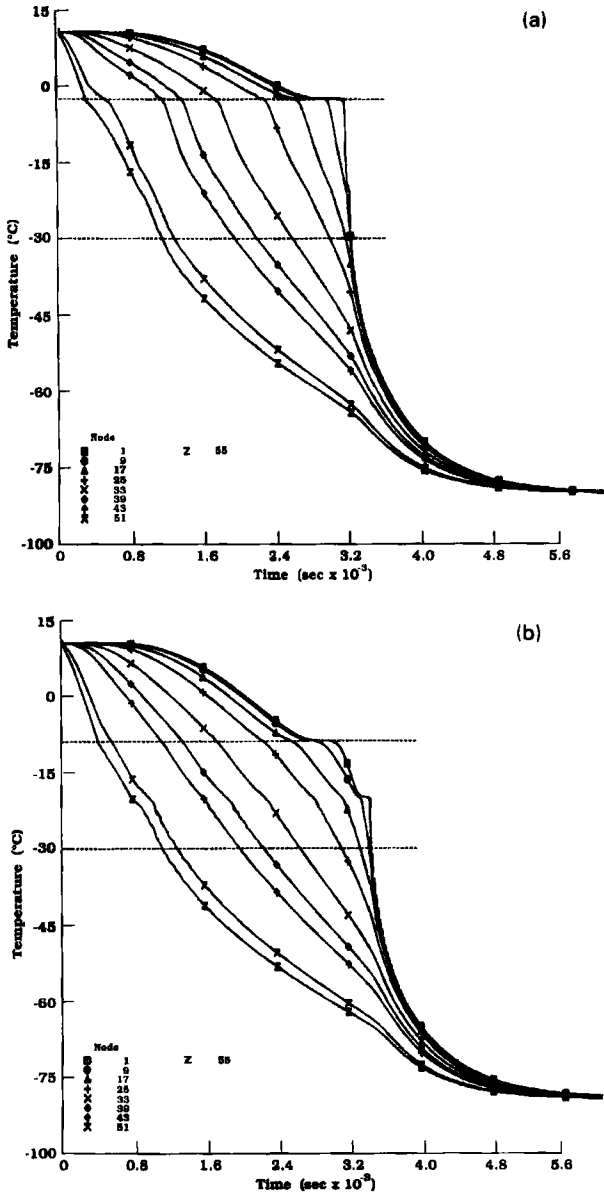


FIG. 14. Simulated temperature histories at incrementally spaced radial positions for freezing of aqueous solutions having a nonlinear latent heat release pattern with temperature as determined from the phase diagram in Fig. 11a. (a) Initial solute concentration of five times isotonic. (b) Initial solute concentration of one-half eutectic. (Redrawn from Diller *et al.* [62, Figs. 6 and 7, p. 239], with permission.)

of latent heat. Consequently, there will be a protracted period of exposure to large solute concentrations at high subzero temperatures, which will combine to enhance the extent of cellular dehydration with the attendant effects on survival. Subsequently, the cooling rates experienced at lower temperatures will be larger because more of the heat removed from the system will be realized as changes in the stored sensible energy (i.e., as temperature changes). In general, these effects are more pronounced at interior positions.

The effects of increased initial solute concentration on the thermal histories are illustrated in Fig. 14. Due to the elevated solute concentration the onset of solidification is prolonged to a lower temperature, resulting in greater sensible energy removal from the system by heat diffusion in the liquid phase. Consequently, due to the delayed phase change, the temperature does not drop as rapidly since the heat must be removed via a medium (water) having lower thermal diffusivity than ice. Further, a higher proportion of the latent heat release is focused at the eutectic state, associated with solidification of the residual eutectic solution, issuing in a second plateau in the thermal history due to the temporarily increased ratio of latent to sensible energy evolution. These effects are exacerbated with higher initial solute concentrations. Clearly, accurate modeling of process kinetics in conjunction with a phase change process requires that the distribution of latent heat release be treated with due regard to thermodynamic property integrity.

C. APPLICATIONS

A primary application for the above calculations of the spatial distribution of thermal histories during freezing is to invoke an appropriate definition of the cooling rate to map the cooling history throughout a specimen. Since the temperature change is continuous in both position and time during the cooling process, it is not immediately apparent *a priori* how to arrive at the most relevant definition of the cooling rate (Luyet [129, 130]; Meryman [145]; Rinfret [170]). Indeed, it has proved to be a challenging task to identify a rational basis by which a freezing process can be characterized in terms of a single value of the cooling rate. Oftentimes in experimental and clinical applications it is desirable to be able to use the output from a single thermal probe to describe the temperature history, providing a data base that can be related to an analytical model of the process.

In principle, the magnitude of the cooling rate is most critical over the range of states for which the dehydration of cells occurs. Since the cell membrane permeability decreases exponentially with temperature, at deep

subzero temperatures there will be no appreciable transport of water or CPA for quite long periods of exposure. Of secondary consideration are phase relaxation and recrystallization processes (Gittus [78]; Gorelik [80]; Knight *et al.* [114]; MacFarlane and Forsyth [132]), which may occur over a broader range of states extending from high subzero temperatures to below -100°C , and these processes may also exert a profound influence on the survival of frozen/thawed cells (Knight and Duman [115]; Fahy [67]). However, in general the time constants for recrystallization phenomena are much longer than those for membrane transport processes. Therefore, membrane transport tends to be a function exclusively of the high subzero portions of the cooling and warming processes, whereas recrystallization is also governed by the choice of storage temperature, although in some cases the warming rate is also a critical parameter, especially if intracellular ice has formed during the cooling process (Mazur [136, 137]).

Given that it is possible to describe the temperature in a system during a freeze/thaw protocol as a continuous function of both position and time, there still remain multiple issues to resolve in arriving at a complete and relevant characterization of the thermal history. Since the cooling rate is not of a uniform magnitude for all positions and times, it is necessary to average the thermal history over either time or temperature to obtain a representative value for the cooling rate at any given location in a freezing system. Further, it is necessary to evaluate which position in a specimen is the most suitable to represent the cooling rate for the entire sample mass. Often the thermal history at the geometric center of the mass is selected intuitively for this purpose; however, this is one of the worst choices of position from the perspective of providing information that can be considered representative of the entire sample mass. Fortunately, it will be shown that analytical techniques can be applied effectively to address all of the above concerns and obtain a quantitative basis of understanding for interpretation of thermal histories during freezing and thawing.

Hayes *et al.* [96] have investigated various approaches that may be appropriate for defining an average cooling rate during the freezing of biological specimens. Two specific techniques were presented for determining a single value for the average cooling rate corresponding to a general transient thermal process involving a phase change distributed over a range of temperatures. In both techniques the cooling rate was averaged over the thermal history identified for a particular set of states; the set of states was defined in terms of an increment in either time or temperature during the process. Based on considerations outlined above, the cooling rate was determined for the portion of a freezing process for which the local temperature exists within the bounds of 0 and -30°C . Time and temperature averages of the cooling rate were then calculated from the local thermal

histories $T(x, t)$ according to the following relations:

$$B_t(x) = \frac{\int_{t_0}^{t_{-30}} B(x) dt}{\int_{t_0}^{t_{-30}} dt} \quad (3.22)$$

$$B_T(x) = \frac{\int_0^{-30} B(x) dT}{\int_0^{-30} dT} \quad (3.23)$$

t_0 and t_{-30} represent the times at which the temperature at a position x first reaches 0 and -30°C , respectively. The local values of the cooling rate, $B(x)$, were determined from an analysis of the transient temperature field in a specimen as obtained using the finite element method to solve Eq. (3.21). The finite element grid shown in Fig. 12 and the dimensions and property values given in Table II were assumed. The instantaneous cooling rate was approximated by dividing the difference between the prior and present values of the local temperature by the magnitude of the time step. This value was then identified with either the local temperature or the elapsed time since reaching 0°C to be applied in the cooling rate calculations.

In addition, a series of simple temperature histories were assumed for which the evaluation of the averaged cooling rates using Eqs. (3.22) and (3.23) was intuitive and straightforward. Seven example cooling protocols are shown in Fig. 15. The seven cases depicted represent various generic scenarios representative of the types of temperature excursions that might typically be encountered during a biological freezing protocol. Only the first case shows a continuous linear cooling process between the initial and final temperatures; the other cases illustrate the thermal rebound, plateauing, and holding phenomena that are common to biological freezing processes and that may have a significant effect on the magnitude of an averaged cooling rate calculated from the thermal history.

Table III presents the time and temperature averaged values of the cooling rate for the protocols defined in Fig. 15 and calculated with Eqs. (3.22) and (3.23). Several relative features of the time and temperature averaging methods are apparent from these data. It is most obvious that the two methods of averaging can give widely disparate results for identical protocols. In many of the cases the difference was by a factor of 2 or greater, and for the group of protocols evaluated there were instances for which the largest magnitude was predicted by each of the methods; i.e., there was no consistent bias with either method. In some of the protocols

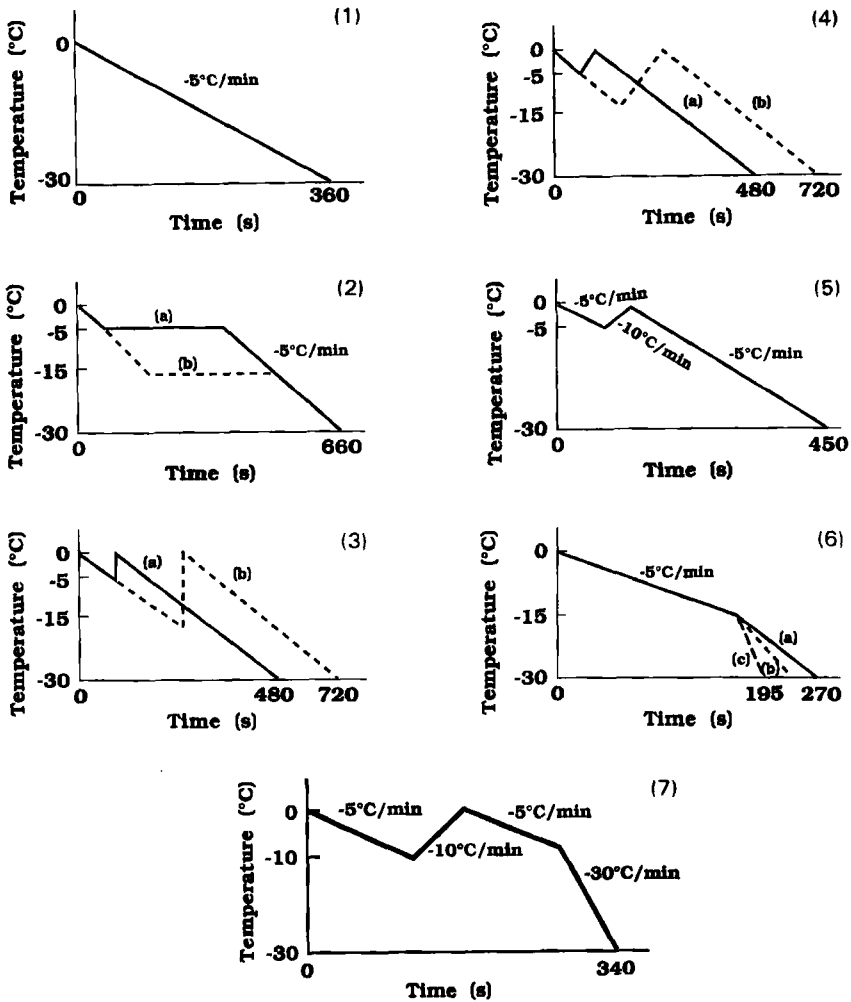


FIG. 15. Seven simulated thermal histories used in comparing cooling rates from 0 to -30°C based on averaging over either time or temperature between the initial and final states. (1) Constant cooling rate of $5^{\circ}\text{C}/\text{min}$ for the entire process. (2) Constant cooling rate of $5^{\circ}\text{C}/\text{min}$ with an intermediate holding period of 5 min at -5 or -15°C . (3) Constant cooling rate of $5^{\circ}\text{C}/\text{min}$ with a stepwise increase to 0°C at -5 or -15°C . (4) Constant cooling rate of $5^{\circ}\text{C}/\text{min}$ with an intermediate rewarming process at $5^{\circ}\text{C}/\text{min}$ to 0°C initiated at -5 or -15°C . (5) Constant cooling rate of $5^{\circ}\text{C}/\text{min}$ with an intermediate rewarming process at $10^{\circ}\text{C}/\text{min}$ to 0°C initiated at -5°C . (6) Constant cooling rate of $5^{\circ}\text{C}/\text{min}$ incremented at -15°C to 10, 30, or $60^{\circ}\text{C}/\text{min}$. (7) Multiple step protocol starting with a cooling rate of $5^{\circ}\text{C}/\text{min}$ to -10°C , rewarming at $10^{\circ}\text{C}/\text{min}$ to 0°C , cooling at $5^{\circ}\text{C}/\text{min}$ back to -10°C , and then further cooling at a rate of $-30^{\circ}\text{C}/\text{min}$. (Redrawn from Hayes *et al.* [96, Figs. 2-8, pp. 106, 107], with permission.)

TABLE III
TIME AND TEMPERATURE AVERAGED COOLING RATES CALCULATED
FOR THE THERMAL PROTOCOLS DEFINED IN FIG. 15.^a

Protocol No.	CR _t (x) (°C/min)	CR _T (x) (°C/min)
1	5.00	5.00
2 (a)	2.73	5.00
(b)	2.73	5.00
3 (a)	5.00	5.00
(b)	5.00	5.00
4 (a)	3.75	5.00
(b)	2.50	5.00
5	4.00	3.13
6 (a)	6.70	7.50
(b)	8.60	17.50
(c)	9.20	32.50
7	5.30	12.50

^aFrom Hayes *et al.* [96, Table 1, p. 105], with permission.

there were alternating cooling and warming steps, which the temperature averaging procedure will tend to cancel out of the calculations, but which will affect directly the time averaging calculations since the clock is running continuously during an experiment. Constant temperature holding processes are transparent to temperature averaging. Further, the temperature averaging method gives equal weight to all cooling rates, whereas time averaging biases the calculations toward slower cooling processes since a longer period of time is required to traverse a given temperature range. From the perspective of applications in cryobiology it is probably more justifiable to adopt time averaging measures for calculating a representative cooling rate from the thermal history at a given location. Most of the phenomena that govern the cellular response to freezing and thawing are kinetic, being highly dependent on the time of exposure at a given temperature. Thus, the physiological systems of interest have a built-in time averaging mechanism during the response to a transient spectrum of temperatures. Thermal protocols generated from finite element modeling studies also showed similar distinctions between the time- and temperature-based averaging procedures for calculating single cooling rates to represent nonlinear thermal processes (Hayes *et al.* [96]).

Rubinsky and Cravalho [180] also addressed the complementary problem of obtaining a quantitative method of evaluating the thermal histories distributed throughout a macroscopic dimensionless specimen during a cryopreservation process in terms of the cooling rate. In many applications the cooling rate is the only parameter that is measured and, possibly, controlled,

and it is usually monitored at only a single location. Thus, there is a justified concern over the magnitude of variation in cooling rate with position and time in the specimen. Their objective was to define the cooling rate at a given location and temperature in terms of dimensionless parameters that could be plotted to provide a graphical solution for the cooling rate as a function of a limited set of initial and boundary conditions and CPA compositions and concentrations. A front tracking finite element method (Rubinsky and Cravalho [181]; Yoo and Rubinsky [230]) was applied to study the solidification process for a one-dimensional system in Cartesian coordinates.

The governing energy equations were formulated for determination of the transient temperature distribution during solidification of a solution in terms of a set of equivalent thermodynamic properties that include the effects of the gradient in thermal properties that occur across the phase change zone. The temperatures in the liquid and solid regions obey respectively

$$\rho c_L(\tau) \frac{\partial \tau_L}{\partial t} = \frac{\partial}{\partial x} \left(k_L(\tau) \frac{\partial \tau_L}{\partial x} \right) \quad (3.24)$$

$$\rho c_S(\tau) \frac{\partial \tau_S}{\partial t} = \frac{\partial}{\partial x} \left(k_S(\tau) \frac{\partial \tau_S}{\partial x} \right) \quad (3.25)$$

where τ is the temperature referenced to the phase change state $\tau = T - T_m$.

The only boundary conditions addressed in this analysis were for a constant imposed environmental cooling rate B . For a symmetric planar system of thickness $2L$, the initial and boundary conditions are given as

$$\tau(x, 0) = \tau_i \quad (3.26)$$

$$\tau(\pm L, t) = -Bt \quad (3.27)$$

$$\frac{\partial \tau}{\partial x}(0, t) = 0 \quad (3.28)$$

$$\tau(x_F(t), t) = 0 \quad (3.29)$$

$$k_L \frac{\partial \tau_L}{\partial x} - k_S \frac{\partial \tau_S}{\partial x} = \rho \Lambda \frac{dx_F(t)}{dt} \quad (3.30)$$

where the moving front position at time t is indicated by $x_F(t)$. The finite element formulation of this problem was stated in the form

$$\mathbf{C} \frac{\partial \tau}{\partial t} - \mathbf{K} \tau = \mathbf{Q} \quad (3.31)$$

where \mathbf{K} and \mathbf{C} are the conductivity and heat capacity matrices and \mathbf{Q} is

the point heat flow input matrix at the phase interface:

$$\mathbf{Q} = \rho \Lambda \frac{dx_F(t)}{dt} \tag{3.32}$$

This model assumes an explicit discontinuity in the material properties at the interface. This condition is met strictly only for the solidification of a pure liquid which occurs at a single defined state. However, in biological applications the solidifying liquid is always a solution for which the phase change process is distributed in both temperature and space. This process results in a mushy zone along the growth direction consisting of a mixture of solid and liquid phases. Within the mushy zone Rubinsky and Cravalho assumed that the solid and liquid phases are in local equilibrium, the relationship between the solute concentration and the temperature being defined by the constitutive phase diagram, such as that shown in Fig. 11a, appropriate to the chemical components present. Further, it was assumed that microsegregation effects occurred on a scale smaller than the resolution of the model, and that the primary segregation pattern was in planes orthogonal to the growth direction so that the gradients described in the model were not affected.

Data were adapted from the ternary phase diagram of Shepard *et al.* [191] for water, sodium chloride, and glycerol to determine the constitutive properties for use in the model calculations. Thus, for any given temperature in the mushy zone it was possible to compute explicitly the fractions of the mass in the solid (ice) and liquid phases. Equivalent thermal properties were then determined from the known properties of the pure components of the solution in proportion to their mass fractions. An equivalent thermal conductivity was defined by

$$k(\tau) = \frac{k_{ice}(\tau)w_{ice}(\tau) + k_{wtr}(\tau) + k_{gly}(\tau)w_{gly}(\tau)}{w_{wtr-i} + w_{gly}} \tag{3.33}$$

and an equivalent heat capacity by

$$\rho c(\tau) = \frac{\frac{dw_{ice}}{d\tau} \rho_{ice} \Lambda(\tau) + \rho c_{ice}(\tau)w_{ice}(\tau) + \rho c_{wtr}(\tau)w_{wtr}(\tau) + \rho c_{gly}(\tau)w_{gly}(\tau)}{w_{wtr-i} + w_{gly}} \tag{3.34}$$

The differential term in Eq. (3.34) is evaluated from the empirical data available from the phase diagram which describes the fraction of a solution which is solidified as a function of temperature. A plot of this type of information is given in Fig. 11b. Plots of the equivalent heat capacity as a function of temperature for two initial solution compositions are shown in Fig. 16.

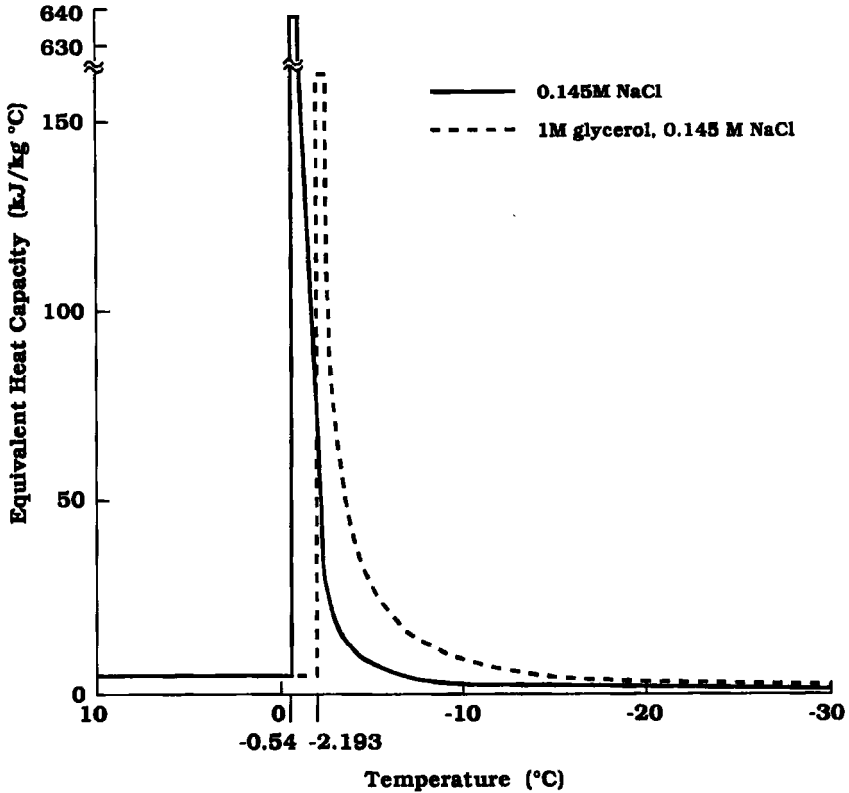


FIG. 16. Equivalent heat capacity calculated for aqueous solutions of initial composition having 0.145 M NaCl and 1 M glycerol plus 0.145 M NaCl. (Redrawn from Rubinsky and Cravalho [182, Fig. 4, p. 308], with permission.)

The statement of the freezing problem given by Rubinsky and Cravalho [182] requires that the solidification phenomenon occur at a specific and unique state and location in the system; however, the definition of the equivalent heat capacity in Eq. (3.34) incorporates the effects of latent heat release distributed over a range of states. To avoid this dichotomy in application of the front tracking finite element formulation to the solidification of impure solutions, an additional property called the localized latent heat, Λ_F , was defined at an equivalent phase front F . This equivalent localized latent heat was taken to represent the total latent heat released over a range of states identified with the advancing edge of the mushy zone, considered to be the forward tip of the growing dendrites, and a position, $F(t)$, within the zone. These states were designated by two isotherms lying normal to the growth direction, τ_f and τ_s , respectively.

The cumulative latent heat released across this section of the mushy zone was assumed to be concentrated at the singular position F with isotherm τ_F . The localized latent heat was then calculated as follows:

$$\Lambda_F = \int_{\tau_i}^{\tau_F} \frac{d}{d\tau} \frac{w_{wtr}(\tau)}{w_{wtr-i}} \Lambda(\tau) d\tau \quad (3.35)$$

Rubinsky and Cravalho made the assumption that if the localized latent heat was calculated over a small range of temperatures in comparison with the total temperature differential across the mushy zone, the results of the analysis would be accurate with respect to a model that accounted for the actual distributed pattern of latent heat release. This approach to analysis of the solidification problem was based on the prior work of Bonacina *et al.* [20].

The following procedure was adopted to apply the equivalent property concept to the forward tracking finite element method for solidification analysis. It was assumed that an initial composition of the system to be frozen had been determined. To start, a value for the localized latent heat was calculated for an arbitrarily selected temperature, τ_F , with the constraint that $\tau_i - \tau_F$ be small relative to the total temperature differential realized across the mushy zone for the chemical system of interest. Next, the equivalent thermal conductivity and heat capacity were calculated at the state for τ_F . A linear interpolation scheme was adopted to compute values of the thermal properties at arbitrary temperatures from a set of known values at discrete temperature increments. Finally, the equivalent property values were applied to the solution technique for a pure system to find the temperature distributions in regions considered as equivalent to completely liquid and completely solid that adjoin the location of τ_F at $F(\tau)$.

Several solidification scenarios were investigated with this analysis technique. The most simple analysis addressed the freezing of pure water initially held at its equilibrium phase change temperature, 0°C . Figure 17 presents the relationship between the cooling rate at the advancing phase interface and the Stefan number, which was defined for this application in terms of the temperature difference between the interface and the external boundary:

$$\text{Ste} = \frac{c_s(\tau_F - \tau_o)}{\Lambda} \quad (3.36)$$

Since the cooling rate imposed at the boundary was constant, the boundary temperature τ_o decreased with time as a linear function. Thus, in Fig. 17 the Stefan number is a direct measure of the elapsed time measured from the departure of the phase interface from the boundary. τ_F has a constant value of 0°C .

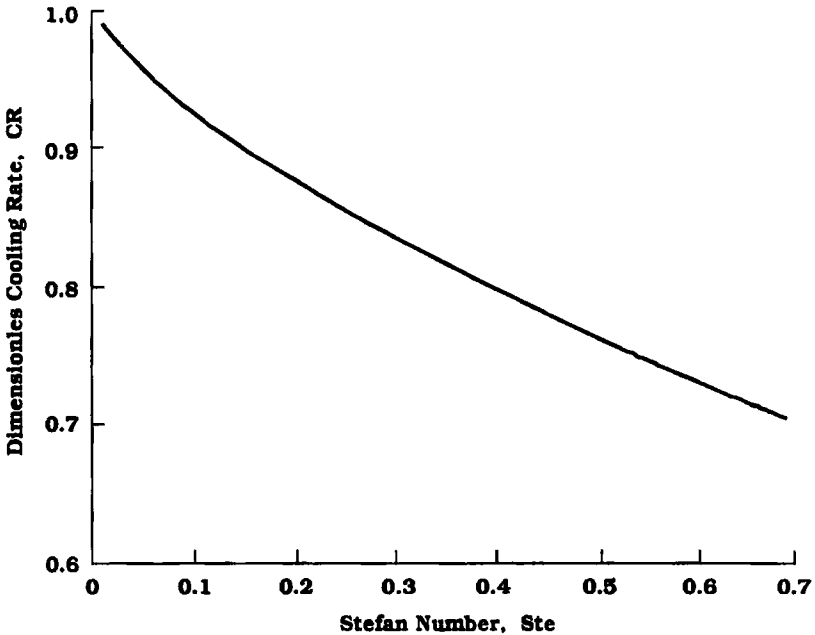


FIG. 17. Cooling rate at the advancing phase interface relative to the boundary cooling rate as a function of the local Stefan number for the solidification of pure water in a one-dimensional slab. (Redrawn from Rubinsky and Cravalho [182, Fig. 5, p. 309], with permission.)

The results of the analysis were also used to illustrate a second dimensionless relationship among the system parameters. In Fig. 18 a dimensionless heat flux, HF, is plotted as a function of the Stefan number. The dimensionless HF function is defined as the ratio of the heat flux at the exterior boundary of the system, q_0 , to the rate of energy extraction from the frozen region. It is described as

$$HF = \frac{q_0 x_0^2}{\alpha_S (\tau_F - \tau_0)} \quad (3.37)$$

where x_0 is the position of the phase front at the instant the outer surface temperature is τ_0 . As seen in Fig. 18, the magnitudes of HF and Ste remain nearly equal throughout the process, indicating that the rate of heat removal from the surface is approximately equivalent to rate of evolution of latent heat at the moving phase boundary.

Next, Rubinsky and Cravalho combined Figs. 17 and 18 to obtain a method of estimating the rate of cooling on the moving boundary of a pure system during freezing. Figure 19 shows simultaneous plots of the Stefan number and the dimensionless heat flux as a function of the instantaneous

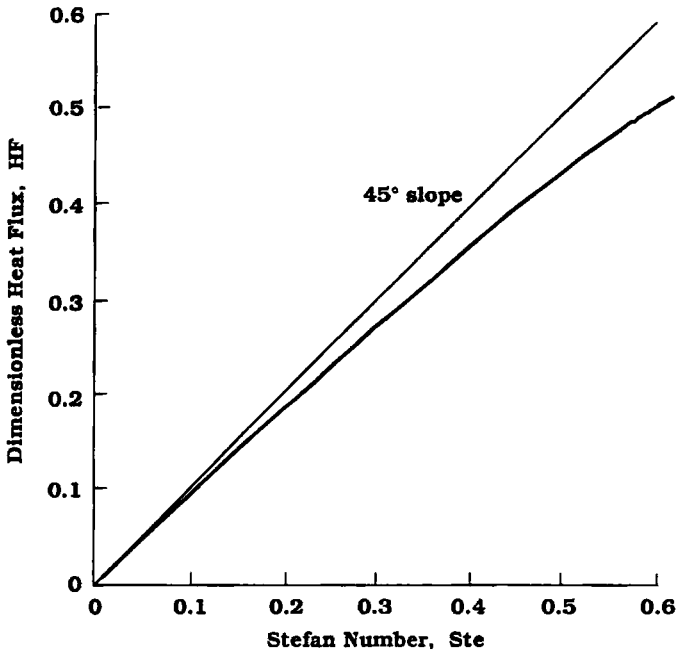


FIG. 18. Dimensionless heat flux as a function of the local Stefan number for the solidification of pure water in a one-dimensional slab. See Eq. (3.37) for definition of the heat flux. (Redrawn from Rubinsky and Cravalho [182, Fig. 6, p. 310], with permission.)

temperature differential between the surface and the moving phase interface. The point of intersection of the Ste and HF curves on Fig. 19 identifies the conditions for which these two parameters are equal. Since τ_F is fixed for the freezing process, the intersection locus identifies the value of the surface temperature, τ_o , corresponding to the state at which the interface reaches the location x_o in the system. The value of the Stefan number at the intersection is then applied to Fig. 17 to identify the corresponding magnitude of the cooling at the interface when it has reached the location x_o .

When the pure liquid is initially superheated prior to the initiation of cooling, the thermal history may be altered significantly due to the greater importance of sensible energy changes compared with latent changes. Rubinsky and Cravalho confirmed the results of others that a higher initial temperature will result in an increased cooling rate at the phase interface and at the center of symmetry of the system. They demonstrated these results numerically by comparison of the thermal histories at selected locations for identical boundary cooling protocols with initial temperatures of 20 and 0 °C. This centerline effect of higher biasing of the cooling rates indicates that the geometric center of a specimen is an unwise choice of

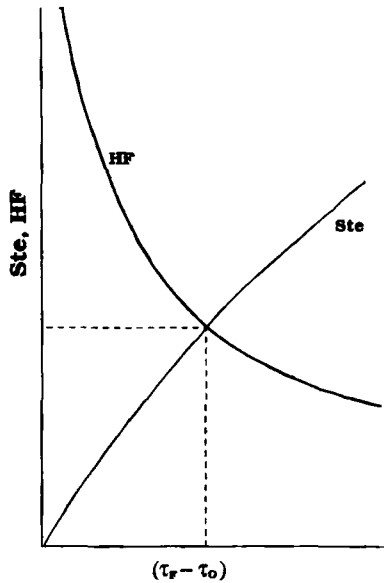


FIG. 19. Simultaneous plots of the Stefan number, Ste , and the dimensionless heat flux, HF , as a function of the instantaneous temperature differential between the surface and the moving phase interface. (Redrawn from Rubinsky and Cravalho [182, Fig. 7, p. 310], with permission.)

location from which to monitor a thermal history representating a cooling protocol. Unfortunately, the point of symmetry is often used to measure temperature during clinical and experimental freezing protocols. More will be said concerning this issue subsequently.

The Stefan number was modified to address the evaluation of the balance between sensible and latent heat effects when cooling was initiated from a superheated state. The modified Stefan number was defined as

$$Ste = \frac{c_S(\tau_F - \tau_o)}{\Lambda + c_L(\tau_i - \tau_F)} \quad (3.38)$$

which reverts to Eq. (3.36) when the initial and freezing temperatures are equal. The cooling rates were measured at the temperature τ_F and the location x_o .

The modified Stefan number of Eq. (3.38) was used to plot the cooling rates achieved at the phase interface as a function of the initial uniform temperature in the specimen. Data for initial temperatures of 0 and 40 °C are shown in Fig. 20. For these two cases the cooling rates are identical at the boundary, by definition from the problem formulation, and as the solidification process progresses, the cooling rate predicted for the superheated

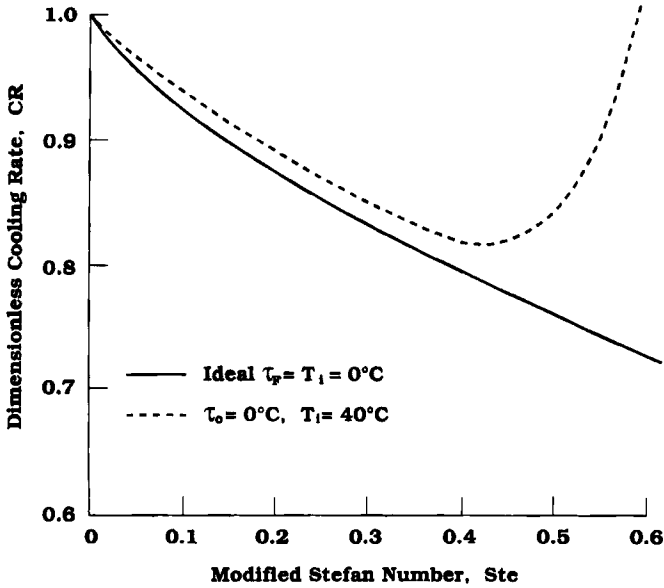


FIG. 20. Variation in the dimensionless cooling rate, B/B_0 , at the advancing phase interface as a function of modified Stefan number (Eq. (3.38)) for different initial uniform temperatures in the specimen. A constant cooling rate B_0 is imposed at the boundary. (Redrawn from Rubinsky and Cravalho [182, Fig. 10, p. 313], with permission.)

case becomes increasingly greater than that for the system initially at the phase change temperature. The exacerbation of this effect as the centerline is approached is very apparent. Thus, the method for determining the cooling rates at interior locations using the combined values from universal curves, derived for pure systems with no initial superheating, in Figs. 17 and 18 for cooling rate and the dimensionless heat flow can only provide a lower bound of the actual cooling rate which may be anticipated.

Finally, Rubinsky and Cravalho made further modifications to their analysis to include the effects of solute in the solidifying liquid. The chemical systems considered included aqueous solutions with 0.145 M NaCl and various concentrations of glycerol. To address these impure systems it was necessary to make further modifications to the Stefan number, based on the localized latent heat for solutions, Eq. (3.35):

$$Ste = \frac{\int_{\tau_F}^{\tau_0} \rho c d\tau}{\Lambda_F + \int_{\tau_1}^{\tau_F} \rho c d\tau} \tag{3.39}$$

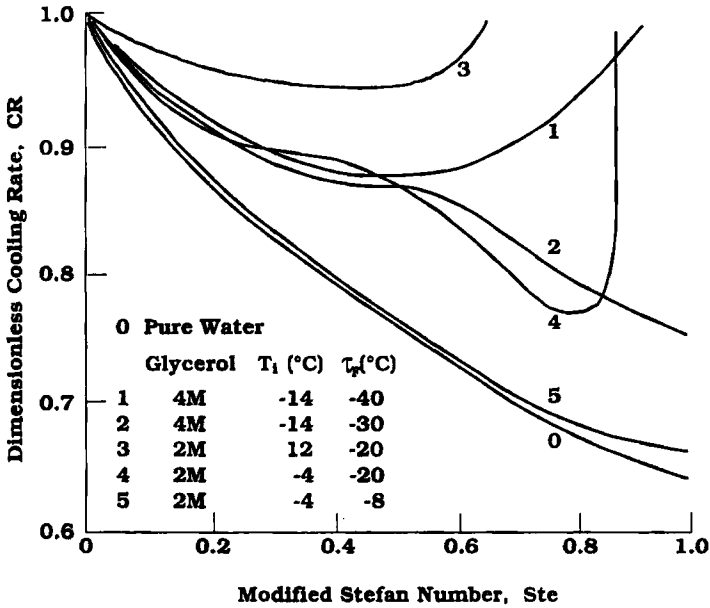


FIG. 21. Variation in the dimensionless cooling rate, B/B_0 , at the advancing phase interface as a function of modified Stefan number (Eq. (3.39)) for impure solutions having different initial uniform temperatures. A constant cooling rate B_0 is imposed at the boundary. (Redrawn from Rubinsky and Cravalho [182, Fig. 13, p. 315], with permission.)

The dimensionless cooling rate, evaluated at the advancing phase front of a solidifying solution relative to the constant value at the surface, was determined as a function of the modified Stefan number for six combinations of glycerol concentration, initial temperature, and temperature in the mushy zone for which the cooling rate was evaluated, as indicated in the plots of the data given in Fig. 21. The results are similar to those shown in Fig. 20 for solidification of pure water from a superheated state. For all cases the cooling rate for a solution is higher than for pure water with no superheating. The extent of the differential and the centerline enhancement of cooling rate is dependent on the combination of solution and thermal protocol parameters. In contrast to the great demonstrated sensitivity of the dimensionless cooling rate to the superheating and composition parameters, there was very little change in the value of the dimensionless heat flux with these parameters. Thus, as may be anticipated, there was little change in the magnitude of heat flux through the solidified portion of the system with changes in composition and in the extent of sensible energy released in the liquid phase.

Recently Hartmann *et al.* [89] have explored further aspects of this problem by considering the most appropriate position in a system of finite dimensions which should be used to define a singular thermal history representative of the temporally and spatially variable cooling process throughout the specimen. They developed a model for a single dimensioned container filled with an aqueous isotonic solution undergoing a freezing process. The one-dimensional, symmetric model was designed to account for the influences of external cooling conditions, heat transport through a supporting container wall and constraining freezing bag, and the nonplanar solidification of the aqueous solution. Changes in energy storage during the freezing process were characterized in terms of an equivalent heat capacity combining both latent and sensible terms according to the weight fraction of the solution solidified locally, Eqs. (3.33)–(3.35) (Rubinsky and Cravalho [182], and were solved via the finite difference method. Within the moving mushy zone associated with the advancing solidification front it was assumed that the upper and lower limits of the phase change temperature range were given by the equilibrium freezing state and the eutectic state for an isotonic solution. Supersaturation and mass diffusion processes were neglected.

A specific physical system was assumed for performing the calculations consisting of a plate-shaped freezing container that was submerged vertically into a bath of boiling liquid nitrogen. The container was fabricated of a copper outer shell with wall thickness of 2.0 mm, having an inner Teflon/capton bag of 0.07 mm thickness, filled with a 0.9% NaCl and water solution with a half-thickness of 2.5 mm. Five finite difference nodes were located in both the container and the bag and fifty nodes in the solution. The convective heat transfer coefficient was based on experimental data for the film boiling curve for liquid nitrogen and expressed in terms of an empirical correlation equation:

$$\text{Nu} = 0.309 \text{ Ra}^{0.309} \quad (3.40)$$

where the Rayleigh number is fit to the data by the expression

$$\text{Ra} = \frac{\beta g \rho_v^3 (\rho_l - \rho_v) \mu_v c_v}{\mu_v^2} \left(\frac{\Lambda_v}{c_v \Delta T_{\text{sat}}} + 0.5 \right) \quad (3.41)$$

In addition, since the solution was assumed to be in continuous thermodynamic equilibrium it was possible to predict the concentration gradients that would develop during solidification directly from the temperature fields via the coupling described by the phase diagram. For a given temperature the corresponding solute concentration could be determined explicitly from the liquidus curve.

This model was used to solve for the transient temperature fields in the physical system for specific freezing protocols. Figures 22 and 23 present plots of temperature and concentration as functions of position at incremental times and as functions of time at incremental positions, respectively, resulting from immersion of a container of isotonic saline directly from room temperature into a bath of boiling liquid nitrogen at

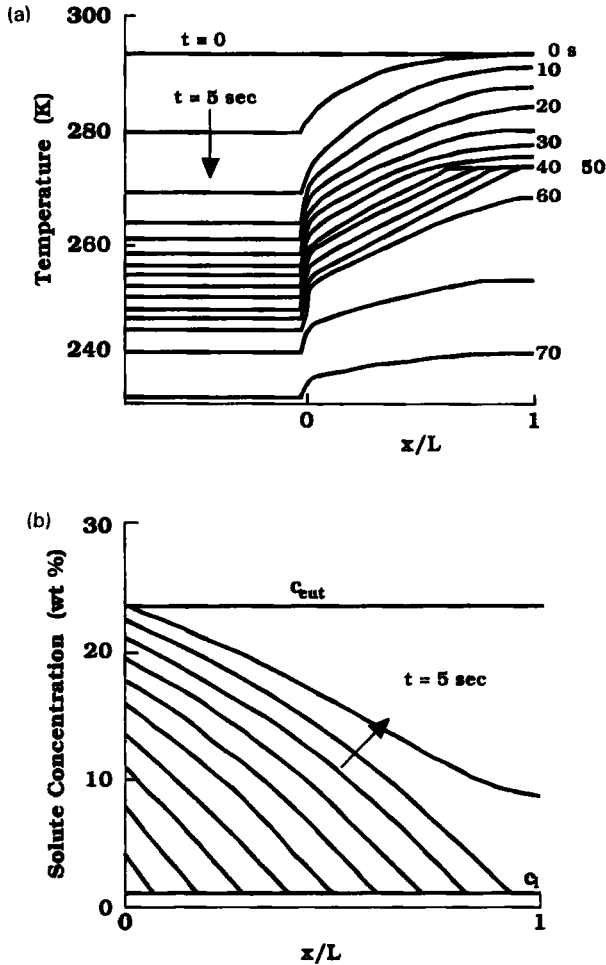


FIG. 22. Calculated temperature (a) and concentration (b) profiles through a one-dimensional container and specimen at incremental times (5 s) following immersion of an isotonic solution into a liquid nitrogen bath from an initial temperature of 20 °C. (Redrawn from Hartmann *et al.* [00, Fig. 2, p. 118], with permission.)

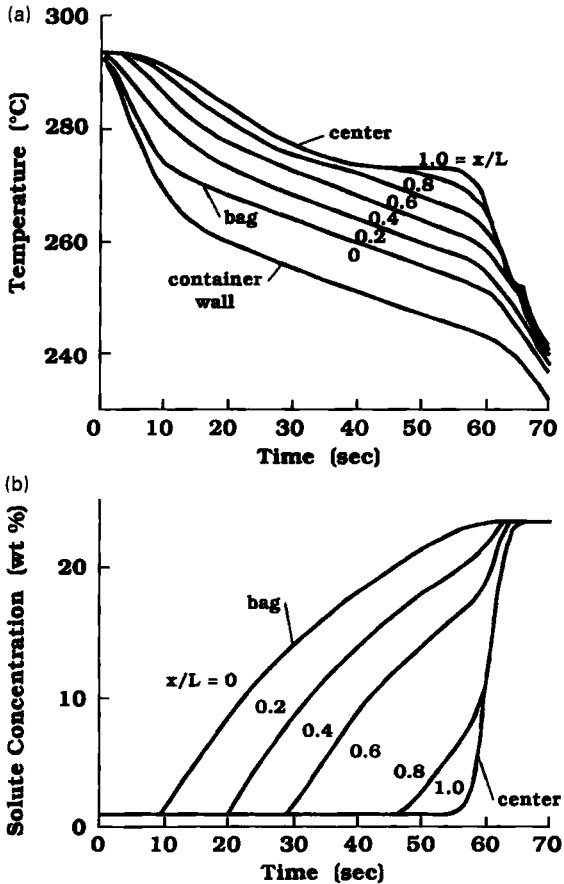


FIG. 23. Calculated temperature (a) and concentration (b) histories through a one-dimensional container and specimen at incremental equidistant locations ($2\Delta x/L = 0.2$) for conditions identical to those of Fig. 22. (Redrawn from Hartmann *et al.* [89, Fig. 3, p. 119], with permission.)

-196 °C. The thermal gradients in Fig. 22a are inversely proportional to the thermal conductivities of the component materials, and the characteristic sharp transition to a plateau occurs in the aqueous solution at the temperature associated with the onset of solidification. This presentation format provides a different basis for realizing the centerline acceleration of the cooling rate as the opposing phase fronts grow together. Subsequent to the initial plateau during solidification, the separation between the thermal profiles becomes remarkably larger as the centerline along the right axis of the plot is approached.

The same data are plotted in the format of thermal histories in Fig. 23a, providing a complementary perspective on the freezing process. The boundary conditions imposed on the system are described by the temperature profile for the container wall. A large differential occurs across the inner bag, which has a low thermal conductivity. Plateaus occur with the initial liberation of latent heat, corresponding to the state defined by the intersection of the liquidus curve and the isoconcentration line for the initial liquid composition on the phase diagram for the system, and at the eutectic point, where a further release of latent heat is assumed for the remaining liquid solution. The plateauing effects are increased as the centerline is approached.

Figures 22b and 23b present the corresponding concentration profiles and histories. The bounds on solution concentration between the initial and eutectic values are denoted by the parallel horizontal lines in Fig. 22b. Since the freezing process occurs over a range of states, a mushy zone develops between the regions that are fully liquid and fully solid. Within this zone the phase interface will have a microscopic morphology consisting of cellular or dendritic projections of ice growing along the direction of the temperature gradient surrounded by concentrated liquid solution. The mass distribution of ice and concentrated liquid solution along any plane normal to the growth direction is assumed to follow the function defined by applying the lever rule to the system phase diagram (see Figs. 11a and 11b). Thus, the curves shown in Fig. 22b depict the concentration gradients that should develop during solidification in the intercellular and interdendritic liquid channels. These profiles have a nearly linear character, which has been demonstrated experimentally with special cryomicroscopic stages for freezing aqueous salt solutions by Körber and Scheiwe [117] and Kouroush *et al.* [118].

The concentration histories shown in Fig. 23b show a very large variation with position in the solution. This phenomenon may have quite important consequences for cryobiological applications. A biological specimen presents a spatial distribution of cells during a cryopreservation protocol, whether it is a homogenous suspension of individual cells or an organized tissue or organ. As was described earlier, cells are subjected to osmotic stress during cryopreservation owing to the freeze-concentration of solutes. The response to this osmotic stress plays a major role in determining the mechanism and magnitude of any injury phenomena that may be active and therefore on the survival from a freezing and thawing protocol. The local variation in solute concentration with time defines the osmotic boundary conditions to which cells will be submitted as a function of spatial distribution within the specimen. Figure 23b demonstrates that there may be extremely large gradients in the concentration history with location in a specimen during freezing. By direct implication, this means that there may

be correspondingly large differences in the osmotic history and in the degree of injury to cells, which could well lead to unacceptable survival statistics for a cryopreserved population of cells. For example, as the center of the system is approached the concentration increment from the initial to the eutectic value may approximate a step function, which would be followed closely by solidification. These conditions are most conducive to the formation of intracellular ice, which nearly always issues in cellular injury.

These data present a graphic illustration of the need for planned control of the thermal histories within a specimen during a cryopreservation protocol. In many applications the importance of this phenomenon can be controlled and reduced by pretreatment of the specimen with a CPA to limit both the extent of solute concentration shown in Fig. 23b, for which no CPA was present, and the magnitude of the osmotic stress to which the cells are subjected. Thus, the broad spectrum of concentration histories depicted in Fig. 23b can be considered as representative of a worst case scenario, which could be modified significantly by the addition of a CPA. Further, addition of a CPA prior to cooling increases the probability that solute concentration and temperature will not follow the equilibrium relationship described by the liquidus curve on the phase diagram. Indeed, many CPAs are known to be very effective in promoting vitrification, including delay or avoidance of nucleation of both the solid water and eutectic phases (Fahy [68]). From the above perspective, the analysis of Hartman *et al.* [89] should therefore be taken to describe a limiting case of the solute concentration phenomenon during freezing.

The data for the temperature distribution within the system can be used to describe the movement of the anterior and posterior boundaries of the mushy zone, which are identified as the ice dendritic tips and the basal plane eutectic troughs. Figure 24 presents a plot of the positions of these boundaries with time for the protocol described in the previous two figures. The growth rate of the dendrite tips is nearly constant initially, and as the center of the specimen is approached the centerline effect is observed as the velocity increases noticeably owing to a progressive diminution of the mass and superheating in the liquid phase lying ahead at the interface which must be cooled before freezing may commence. It may be observed that for the protocol being modeled the dendrite tips arrive at the system center before the eutectic state is reached at the outer boundary. Eventually the basal plane moves through the system at a much more rapid rate than the dendrite tips. This effect may be attributed to the smaller latent heat of the eutectic solution as compared to water, which for the present case has a ratio of 0.63, and the thermal conductivity of the mass between the basal plane and the boundary higher than that between the dendrite tips and the boundary, owing to the intervening solidification of the mushy zone.

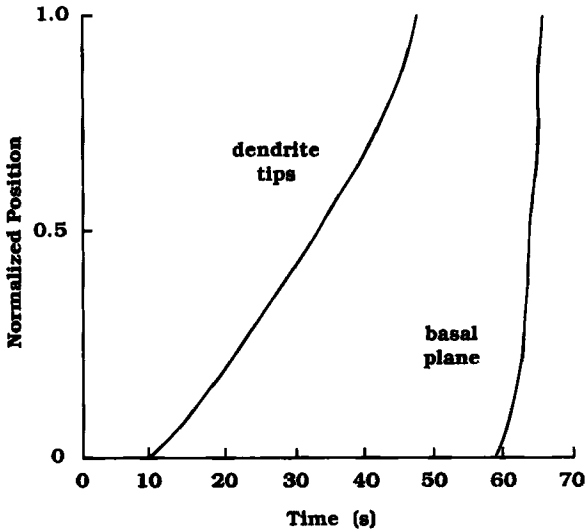


FIG. 24. Location of the tips of the growing ice dendrites and of the basal plane of the solute channels between the dendrites for the freezing protocol of Fig. 22. (Redrawn from Hartmann *et al.* [89, Fig. 4, p. 120], with permission.)

These simulations were compared with temperature data from experiments to which the boundary and initial conditions and the thermal properties for the model had been matched. The two sets of results demonstrate a good match, except near the centerline, where the temperature drop off the solidification plateau occurs sooner than predicted by the model. A conjectured explanation for this difference was that natural convection in the liquid phase through the vertical plane in the container enhanced the heat transfer away from the superheated liquid, and this effect was not included in the unidimensional model. In addition, the small plateau in the thermal history associated with nucleation of the eutectic solution was observed at about 10 °C below the value from the equilibrium phase diagram. As often happens during the freezing of biological systems, the eutectic solution does not behave in accordance with the equilibrium phase diagram, but experiences an extended degree of supercooling prior to nucleation.

A primary objective of the analysis of Hartmann *et al.* was to identify the single location in a freezing specimen that would provide the data to describe the thermal history most representative of the entire system. Since the cooling rate varies as a function of both position and thermodynamic state, i.e., temperature, it was necessary to define an appropriate averaging technique to characterize the transient temperature profile at any location

in terms of a single parameter. For this purpose, the cooling rate was defined by the time average method for the temperature range between the freezing temperature and -30°C , as discussed previously (Hayes *et al.* [96]).

The time averaging definition of the cooling rate was applied to the thermal histories calculated for the standard metal container/Teflon bag/isotonic saline system used for this series of simulations quenched into liquid nitrogen to evaluate the magnitude of the variation in cooling rate within the specimen. The reference cooling rate, B_0 , as defined at the outer extremity of the specimen (inner surface of the container bag) was determined to be 33 K/min for the quenching protocol. The results of these calculations are plotted in Fig. 25, along with determination of the velocity of the phase interface as it moves through the system. These data quantify the observations from Figs 22 and 23 that the cooling rate increases as the center is approached. It is clear that the increase is monotonic, and that at the centerline the magnitude is fourfold greater than at the surface.

In order to quantify how well the cooling rate at a specific point represents the distribution of cooling rates over the entire system, a new variable, $\Xi(x)$, called the "representation parameter" was defined. $\Xi(x)$ is calculated for a given location (x) as the fraction Ξ of the entire volume for which the cooling rates do not vary more than 50% from the local value of $B(x)$. The 50% criterion was chosen somewhat arbitrarily, but with justification

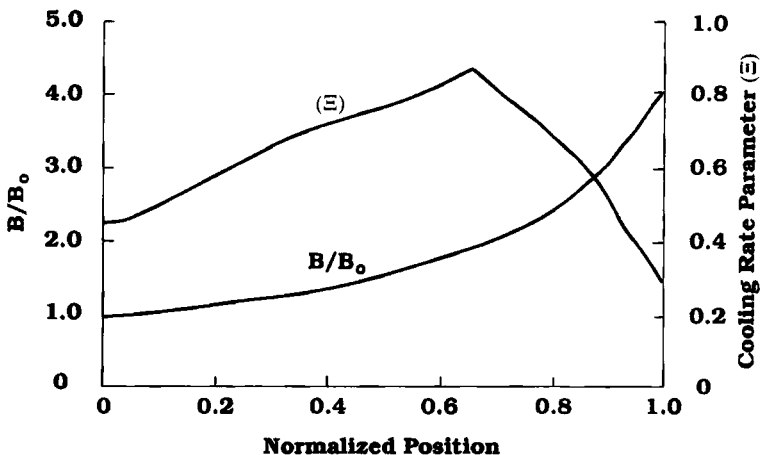


FIG. 25. Spatial variation of the averaged dimensionless cooling rate, B/B_0 , and the representation parameter, $\Xi(x)$, (defined in the text) within the specimen volume for the quenching protocol defined for Fig. 22. The reference cooling rate is defined at the inner surface of the Teflon bag in which the specimen is contained. (Redrawn from Hartmann *et al.* [89, Fig. 6, p. 122], with permission.)

based on the spectrum of values often encountered on diagrams of survival as a function of cooling rate. The value of $\Xi(x)$ can be computed as a continuous function of position from the cooling rate data, and it is presented on Fig. 25 for the quenching protocol. It is immediately obvious that the centerline presents the least representative location for monitoring the cooling rate and that there is an intermediate location where the $\Xi(x)$ function reaches a clear maximum value.

Although analysis of the previously described protocol based on a specific experimental trial provides information of relevance for a subset of cryobiological procedures, Hartmann *et al.* were interested in assessing whether it was possible to address the issue of spatial distribution of cooling rates in a more global context that could be applied to a wide variety of geometries and thermal boundary conditions. To this end they performed systematic perturbations in the surface cooling rate and in the thickness of the specimen to evaluate different combinations of the rapidity of change of the thermal forcing function and effective time constant for the transient response of the system. The Fourier number was used as a basis to identify an appropriate group of parameters by which this analysis could be characterized.

The Fourier number is defined by

$$Fo = \frac{\alpha t}{L^2} \quad (3.42)$$

The surface cooling rate B_0 was assumed to be held constant, and a cooling parameter was defined as a modification of the Fourier number as

$$Fo^* = B \cdot L^2 \quad (3.42a)$$

Note that this parameter has dimensions of ($K \cdot mm^2/s$). Fo^* was used to characterize systems that were similar with respect to geometry and spatial distribution of cooling rates. Systems of biological relevance were evaluated for values of Fo^* that spanned six orders of magnitude. Values for the individual cases considered are presented in Table IV.

Figure 26 presents the variation in local cooling rate for freezing processes characterized by three different values of Fo^* . In one case $Fo^* = 0.45$, which is typical of procedures for which the container is thin and/or the cooling rate is small. In the second and third cases $Fo^* = 12.5$ and 400, corresponding to intermediate and large values for these parameters. For $Fo^* = 0.45$ the dendrite tips reach the container center with no perceptible change in the temperature profile and the cooling rate constant (at a very small value) throughout the specimen. In the second case the dendrite tips reach the center before any of the specimen has been cooled to below the eutectic state. For the most rapidly cooled system a

TABLE IV
 VALUES OF THE PARAMETER Fo^* IN $(K \cdot mm^2/s)$ FOR COMMONLY ENCOUNTERED RANGES OF SURFACE COOLING RATES, B_o , AND CONTAINER THICKNESS, L , IN THE CRYOPRESERVATION OF BIOLOGICAL SPECIMENS^a

L (mm)	B_o (K/min)				
	0.1	1	10	100	1000
1	0.0017	0.017	0.17	1.7	17
2	0.0067	0.067	0.67	6.7	67
5	0.042	0.42	4.2	42	420
10	0.17	1.7	17	170	1700

^a From Hartmann *et al.* [89, Table 1, p. 123], with permission.

large portion of the specimen is reduced to temperatures below $-30^\circ C$, which is the lower limiting state for which cooling rates were defined, by the time the forward edge of the phase front reaches the center. Only the central portion of the specimen experiences a significant alteration in the cooling rate from the surface value. In all three cases the maximum cooling rate occurred at the center of the specimen, confirming that it is one of the least desirable positions to obtain a representative thermal history. Indeed, the $\Xi(x)$ shows a minimum value there, indicating that the center is the worst location for monitoring the temperature.

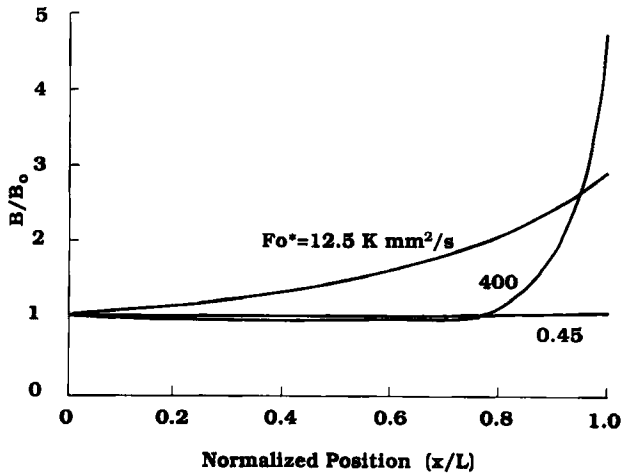


FIG. 26. Local variation in the normalized cooling rate for protocols characterized by the indicated values of Fo^* . (Redrawn from Hartmann *et al.* [89, Fig. 7, p. 123], with permission.)

The suitability of a given position in a specimen for representing the thermal history of the entire specimen is a function of the magnitude of the boundary cooling rate applied. Figure 27 presents a plot of the range of positions for which the locally measured cooling rate represents at least 80% of the total system volume, as a function of the constant cooling rate at the boundary and the system dimensions, represented by Fo^* . The accuracy in representing the thermal history is relatively insensitive to position for small Fo^* , and at large Fo^* it is only necessary that the probe not be close to the geometric center. However, for intermediate values of Fo^* , which characterize many cryopreservation protocols, the range of acceptable probe positions becomes very narrow. The optimum choice is restricted to a narrow interval at $2x/L \approx \frac{2}{3}$.

The cooling rate representation function is plotted as a function of Fo^* for three different probe positions in Fig. 28. For small cooling rates and/or thin specimens the thermal gradients in the specimen are minimal, and virtually any probe position will provide an acceptable measure of the transient temperature of the system. As the dimensions and/or cooling rate increase the probe position becomes much more important. The surface provides a much more meaningful measure of the thermal history than does the center, and the cooling rate representation at the dimensionless position of $2x/L = \frac{2}{3}$ is near to the optimum that can be achieved.

The conclusion and recommendation of Hartmann *et al.* [89] is that a standard criterion be adopted for measuring the thermal history during freezing protocols based on placing the probe $\frac{2}{3}$ of the distance from the surface toward the centerplane of a rectangular container. This standard

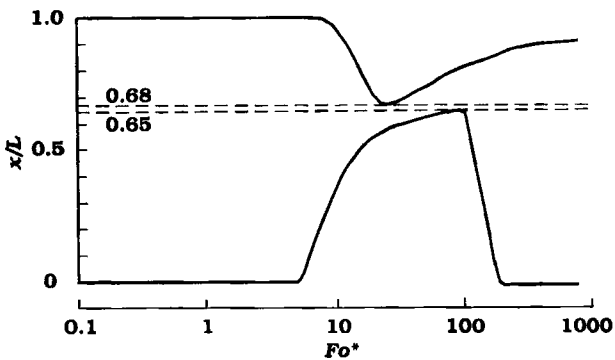


FIG. 27. Identification of the area in a specimen (indicated by crosshatching) for which a locally measured cooling rate represents the cooling rate in at least 80% of the total volume, assuming the rate of surface cooling is constant. (Redrawn from Hartmann *et al.* [89, Fig. 10, p. 125], with permission.)

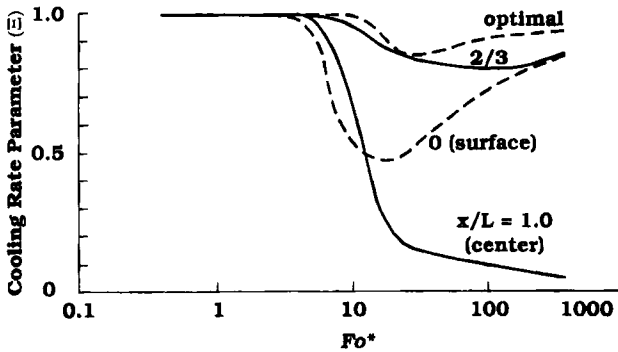


FIG. 28. Comparison of the cooling rate representation function $\Xi(x)$ for specific dimensionless probe locations, with constant surface cooling rates. (Redrawn from Hartman *et al.* [89, Fig. 11, p. 125], with permission.)

would have the benefits of enabling the most meaningful comparison of data acquired by investigators in different laboratories, of providing the most representative data for the thermal history of the specimen, and of minimizing the criticality of probe placement position. This work is a good example of the practical advantage to be gained for clinical applications of a straightforward heat transfer analysis of a process critical to cryopreservation. It remains to extend this analysis to cylindrical geometries, which comprise a significant portion of the container shapes used in cryopreservation procedures.

Recently a physical process established many years previously by metallurgists for the study of solidification has been adapted to the freezing of biological systems (Rubinsky and Ikeda [184]). Directional solidification consists of moving a liquid specimen to be frozen through a stationary temperature gradient to establish a phase front that is fixed in an absolute frame of reference but is moving in the specimen at a rate identical with the velocity with which it is being moved. Typically this process is adapted to systems of rather small dimensions, and it has been applied frequently in the design of microscope stages for the observation of solidification processes (Hunt *et al.* [104]; Jones [112]). The operation of a directional solidification system is illustrated in Fig. 29. A liquid specimen is distributed in a thin plane that is advanced by external mechanical means past a pair of heated and cooled blocks that are fixed in position. The system is designed to ensure good thermal contact between the specimen and the temperature source and sink. As a consequence, a temperature gradient is established through the specimen that does not change in time. If the specimen is advanced at a constant velocity the solidification will occur as a steady state process, producing a homogeneous solid phase. In addition, it becomes

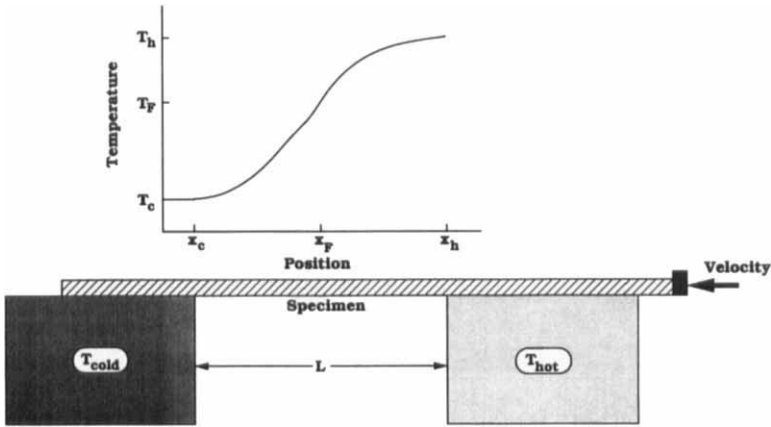


FIG. 29. Geometry and thermal boundary conditions for a directional solidification system. The temperature source and sink are fixed, and the specimen is forced through the stationary temperature gradient at a constant velocity to produce a steady state moving phase boundary.

possible to isolate the component physical parameters that define the cooling rate, namely the temperature spatial gradient, K , and the rate of movement of the temperature field through the specimen, V , so that their effects can be evaluated in an uncoupled experimental environment (Beckmann *et al.* [10]).

$$B = \frac{\partial x}{\partial t} \cdot \frac{\partial T}{\partial x} = V \cdot K \quad (3.43)$$

In addition to the study of physical aspects of the cooling process, directional solidification has been a useful experimental technique for analysis of the response of living tissues to freezing. Both suspensions of individual cells (Beckmann *et al.* [10]; Rubinsky *et al.* [179]) and thin tissue slices (Rubinsky *et al.* [185]; Rubinsky and Pegg [186]) may be frozen on this type of system, enabling the effects of the magnitudes of temperature gradient and the velocity of the phase interface to be evaluated independently. In addition, it is possible to produce a specimen frozen with a uniform thermal history.

The temperature field that is produced in a directional solidification apparatus has been analyzed by Rubinsky *et al.* [179]. For a specimen moving at a uniform velocity V the temperature distribution is governed by the movement past the high and low temperature blocks and the diffusion of heat in the specimen according to

$$\frac{\partial^2 T}{\partial x^2} - \frac{V}{\alpha} \frac{\partial T}{\partial x} = 0, \quad 0 \leq x \leq L \quad (3.44)$$

where L is the separation of the temperature controlled blocks and the thermal diffusivity α is that of the substrate on which the specimen is mounted. The substrate dominates the mass of the moving portion of the system between the temperature blocks and therefore the thermal field. It is assumed that thermal transients associated with the initial movement of the specimen from rest are of minimal effect at the time of analysis so that steady state conditions prevail. The boundary conditions are set by the controlled temperature blocks:

$$T(0) = T_h, \quad x = 0 \tag{3.45}$$

$$T(L) = T_c, \quad x = L \tag{3.46}$$

The solution to this problem yields a temperature distribution described as

$$T(x) = T_h + [T_c - T_h] \frac{\left[\exp\left(\frac{V}{\alpha} \cdot x\right) - 1 \right]}{\left[\exp\left(\frac{V}{\alpha} \cdot L\right) - 1 \right]}, \quad 0 \leq x \leq L \tag{3.47}$$

The cooling rate may be written in terms of Eq. (3.43)

$$B(x) = \frac{\partial T(x)}{\partial t} = V \cdot \frac{\partial T}{\partial x} = \frac{[T_c - T_h]V^2}{\alpha} \frac{\left[\exp\left(\frac{V}{\alpha} \cdot x\right) \right]}{\left[\exp\left(\frac{V}{\alpha} \cdot L\right) - 1 \right]} \tag{3.48}$$

The upper and lower bounds on the cooling rate occur at the cold and hot ends of the specimen, respectively, so that

$$\frac{[T_c - T_h]V^2}{\alpha \left[\exp\left(\frac{V}{\alpha} \cdot L\right) - 1 \right]} \leq \frac{\partial T(x)}{\partial t} \leq \frac{[T_c - T_h]V^2}{\alpha} \frac{\left[\exp\left(\frac{V}{\alpha} \cdot L\right) \right]}{\left[\exp\left(\frac{V}{\alpha} \cdot L\right) - 1 \right]} \tag{3.49}$$

The average cooling rate for the specimen is obtained simply as a linear function of the system geometry and boundary conditions, which has been assumed in most applications:

$$\frac{\partial T(\text{avg})}{\partial t} = \frac{[T_c - T_h]V}{L}, \quad 0 \leq x \leq L \tag{3.50}$$

Bald [7] has pointed out that in many applications the critical state at which the cooling rate should be evaluated is defined by the phase change

temperature. Assuming that the phase change process can be described in terms of a single temperature, T_F , Eq. (3.47) could be solved for the x_F corresponding to T_F which could then be substituted into Eq. (3.48) to obtain the cooling rate at that location. It is likely that further analysis will be forthcoming for this process since it holds considerable promise as both an experimental and a clinical tool.

IV. High Temperature Heat Transfer

There are three primary categories of events in which bioheat transfer at high temperatures may be encountered: therapeutic and surgical protocols and accidents (burns). Historically, interest and concern have probably been more intense and long-standing in the latter than in the former, although within the past decade there have been important advances in the use of hyperthermic regimens in a wide variety of therapeutic procedures, especially for applications in cancer. The necessity of developing a reliable and accurate predictive ability for planning hyperthermic protocols is obvious and has led to an intense level of activity in the modelling of bioheat transfer at moderate temperatures. In addition, surgical procedures have been developed which make use of electrical or optical sources to create an intense, short duration heating of tissue to achieve controlled destruction within a defined target volume. The present analysis will be directed to situations in which elevated tissue temperatures are encountered in each of the above contexts.

A. PHYSIOLOGICAL BACKGROUND

A vast majority of thermal burns occur as a result of high temperature environmental insult to the skin. Burns are one of the most widely encountered forms of trauma, ranging from a mild but painful level to life-threatening intensity. It is estimated that more than two million burns occur annually in the United States, with about half severe enough to require medical treatment, 10% requiring hospitalization, and 10,000 to 12,000 resulting in deaths (Salisbury and Pruitt [189]; Jay *et al.* [108]). They are the third leading cause of accidental death, and first for persons aged under 40. In many instances burns occur in the routine familiarity of the home or work environment under conditions which are not viewed as being overtly hazardous (Dussan and Weiner [63]). Very often burns are produced as a consequence of a heat flux applied at the skin surface, but other sources include the inhalation of heated gases and the flow of electrical current through the body from a high voltage source to ground. Less severe insults

can result from exposure to electromagnetic generating devices. Surface burns may result from heat loads applied by radiation, convection and/or conduction associated with exposure to flames, a scalding fluid, or a high temperature substrate, respectively.

A rigorous description of the genesis of a thermal burn process requires a basic understanding of the physiology of the tissue involved. The skin is a unique tissue in the body in many ways, being by both size and weight the largest organ, constituting about 15% of the total body mass. Skin has a number of vital functions which include protection of the underlying tissues from chemical, physical, and thermal insult; thermal regulatory actions including sweating, thermal insulation, and modulation of blood flow to a profuse microcirculatory plexus; permeation barrier to both environmental and body fluids and chemicals and disease organisms; sensory perceptions of pain, temperature, and touch; and presentation of our personal appearance to the world, be it one of beauty or, in the case of a severe burn, one that is scarred and deformed and can represent a serious physical and emotional handicap.

The structure of the skin is represented by a simple sketch of the cross section in Fig. 30. Anatomically the skin consists of a layered structure of three parallel strata: a thin outer epidermis; a dense noncellular connective

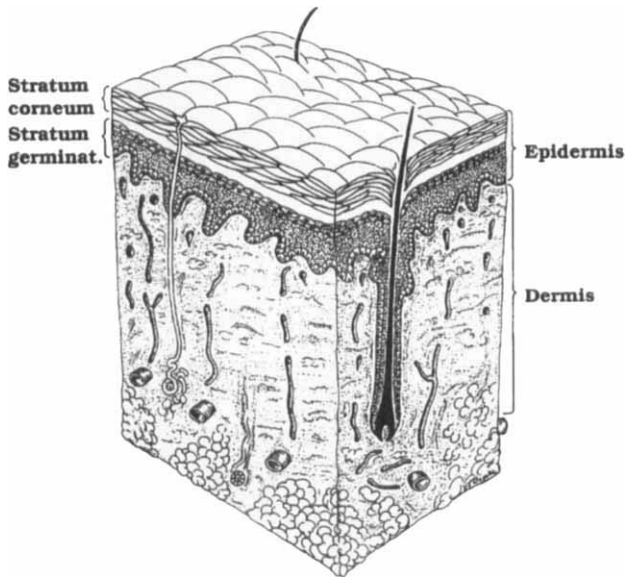


FIG. 30. Sketch of the layered structure of human skin. (Redrawn from Johnson, C. L., O'Shaughnessy, E. J. and Ostergren, G., *Burn Management*, Fig. 2.1, p.6, Raven Press, Ltd., 1981.)

tissue, the dermis, perfused with microvessels in a particular morphology; and a thick subcutaneous fatty tissue, the hypodermis (Ham and Cormack [84]). The epidermis and dermis are joined firmly together to form an integral covering for the body that varies in thickness from less than 0.5 mm to more than 4 mm, depending on the location. Accordingly, there is a large variation over the body of the sensitivity to thermal insult and susceptibility to severe burn injury.

The epidermis has a stratified structure consisting of many layers of cells (Fig. 31). The interface between the epidermis and dermis is characterized by a three-dimensional network of interdigitated convolutions forming ridges, or papillae, that enable the skin to resist tangential stress. The innermost stratum is the basal layer from which cells are generated and which contacts the deeper neurological and vascular supplies. Anterior is a granulosum with a large transferable water content that is involved in water retention and heat regulation. The cells of this layer eventually die and form the outermost stratum corneum, a layer of waterproof fibrous keratin protein. The keratin normally contains only about 15% water, but immersion in a hydrous environment increases this percentage causing a wrinkling and softening of the skin, whereas necrosis issues in chapping and calluses.

The underlying dermis is many times thicker than the epidermis, and it contains the vascular, nervous, and lymphatic supplies for the skin, as well

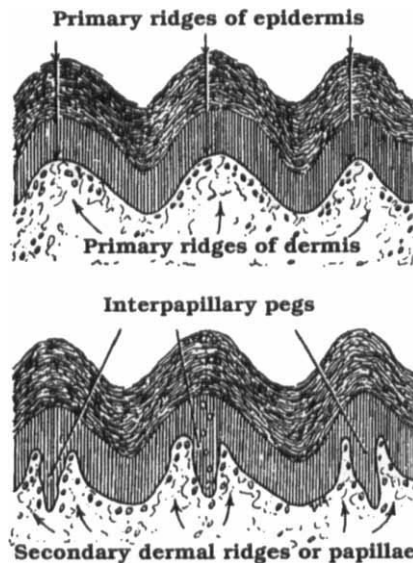


FIG. 31. Stratified structure of the epidermis, including the papillary interface with the dermis. (Redrawn from Ham and Cormack [84, Fig. 20-2, p. 617], with permission.)

as providing the supporting structure of the skin. The papillary layer is the most superficial structure, lying adjacent to the epidermis. It consists of numerous small, vascularized, and highly sensitive protuberances called papillae, which rise perpendicularly. These papillae are minute conical eminences with rounded or blunted extremities that are received into matched ridges on the underside of the epidermis. Each papilla has many very small and closely interlaced bundles of finely fibrillated tissue, with a few elastic fibers and a single blood capillary loop running vertically toward the surface of the skin (Bollinger *et al.* [19]; Fagrell [65]). The blood flow in the dermis accounts for the nutritional supply, cellular and humoral defences, and a major portion of the thermal regulatory function. As illustrated in Fig. 32, the vascular morphology consists of a rich network of branching arterial and venous arcades that are interconnected in a regular pattern (Zweifach [231]). Small arteries enter the subcutaneous tissue to form a system of long arterioles of about $50\text{-}\mu\text{m}$ diameter into the subdermal plexus (Fagrell [65]). These vessels branch regularly into a finer network, becoming the dermal plexus and finally the subpapillary plexus. The arteriolar network is matched morphologically by a venular plexus.

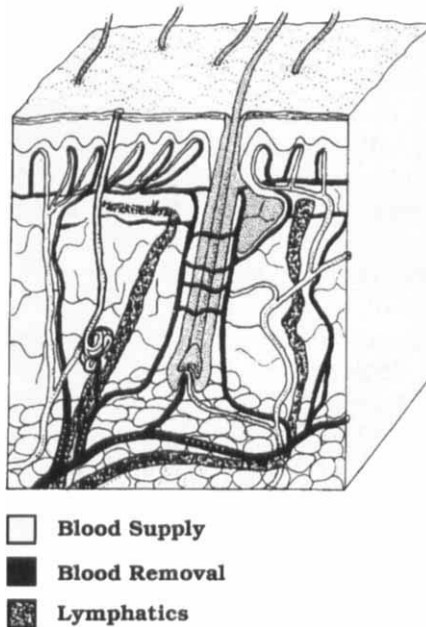


FIG. 32. Papillary interface between the epidermis and dermis. (Redrawn from Ryan [188, Fig. 1, p. 528], with permission.)

An important and unique aspect of the skin circulation is the presence of a large number of direct shunts from arteries to veins, called arteriovenous (AV) anastomoses. When opened, the AV anastomoses enable nearly all of the blood supply to be diverted from the subpapillary plexus, thereby increasing the effective thermal insulation of the skin between the subcutaneous tissue and the environment. Alternatively, the vast vascular bed of the skin can open up to accept as much as 20% of the total cardiac output when the subpapillary plexus becomes engorged with blood. In this state there is a minimal thermal resistance between the blood supply to the skin and the environment. The small blood vessels of the skin have extensive sympathetic innervation and are highly responsive to neurogenic and humoral constrictor and dilator influences arising from various forms of local and systematic stress. This function obviously plays a large role in the overall thermoregulatory function of the body; it may also have a strong influence on the transient temperature field that develops during mild thermal insult.

Beneath the dermis, the subcutaneous layer forms a stratum of connective tissue. It is dominated by the presence of fat cells. The thickness of this layer may vary considerably with location on the body surface, and also among persons. The blood supply to the skin arises through parallel arteriole venule pairs rising vertically through the subcutaneous layer. Heat transfer between the skin and the environment can be affected greatly by the thickness of the subcutaneous fat layer.

The magnitude of a burn wound is usually classified clinically in terms of a degree of severity, with a first-degree being the least severe and third-degree and higher resulting in permanent destruction of the affected tissue. A key factor in determining whether necrosis will occur is the degree to which microcirculatory blood flow is maintained to the burned area. In general, the extent to which the circulation is impaired is directly proportional to the severity of the burn insult. The burn may cause a direct impairment of the microcirculatory perfusion, and the long term survival of the affected tissue is dependent on preserving the patency of the vascular network (Cope and Moore [46]; Branemark *et al.* [25]; Moncrief [147]).

The most common basis for describing a burn wound is from the perspective of a clinician who is faced with diagnosing and treating the injury. Thus, a macroscopic characterization of the burn wound has been developed with a very specific set of principles for evaluation (see, for example, Krizek *et al.* [119]). A first-degree burn involves only temporary discomfort due to irritation of the nerve endings in layers below the stratum corneum, along with a slight edema. The surface appearance is of a general erythema caused by vasodilation of subpapillary vessels in the affected area, and the response is localized to the heated tissue. Although

denaturation of the outermost layer of dead keratin cells occurs at the elevated temperature, which may lead to a slight peeling, the normal healing process proceeds uninhibited with migration of cells to the epithelial surface.

A second-degree, i.e., partial thickness, burn may be classified clinically into two subcategories of superficial and deep, based on the penetration depth of the injury into the skin. Simply considered, a partial thickness injury is one in which the loss is less than the full thickness of skin. In a superficial burn wound, a significant fraction of the basal cells of the corium are not destroyed, enabling the healing process to proceed in a normal pattern. However, the permeability of the vascular endothelium in the subpapillary plexus is increased greatly, issuing in the extravascular accumulation of edema fluid with blistering. The plasma leakage occurs mainly from the papillary and subpapillary capillary beds of the dermis. Because these superficial vessels become dilated the skin appears red; in contrast, for more severe burns these vessels become coagulated, losing all perfusion of blood, giving the skin a more pale appearance. The stratum corneum usually forms a waterproof covering over the wound, preventing bacterial influx and containing the blister fluid. Rupture of this covering will result in an open weeping wound and an increased susceptibility to infection. Large scale weeping leads to a greatly increased metabolic load to compensate for the latent heat expended during surface evaporation of fluid, having the same effect as profuse sweating (Fallon and Moyer [71]). Because a majority of the basal cells are not injured during a superficial burn, epithelial regeneration is normally prompt and complete without scarring.

Contrastingly, in a deep second-degree burn much of the basal cell layer is destroyed, rendering the healing process much more problematic. Vascular injury is characterized by widespread stasis and destruction of endothelial cells in the subpapillary plexus. Blistering is not widespread, but a water-permeable eschar of plasma and cells forms over the wound, through which evaporative fluid loss may be very high and bacterial invasion may be relatively unhindered. If infection can be limited, this type of wound has the potential for spontaneously regenerating the epithelium. The wound becomes resurfaced with damaged epithelial cells from the hair follicles and the margins of the injured area. A new epidermis is regenerated primarily from the living epithelium originating deep in the hair follicles by growing out from the external root sheaths. However, the healed skin is not fully normal in that it will be thinner than prior to the injury, have diminished sensory capacity, and be lighter than surrounding tissue due to the permanent loss of melanocytes. A failure to develop interpapillary ridges may result in a susceptibility to tearing under tangential stress loading.

A third-degree injury is termed a full thickness burn because all epidermal elements and the supporting dermal structure are destroyed. All perfusion to local blood vessels is lost so that there is no vascular response within the immediate injury area. Only in the peripheral regions are the vascular and cellular response typical of inflammation observed. There is no sensation of pain in this tissue due to the destruction of nervous function, and the superficial eschar that is formed is highly permeable to both water and bacteria. Tissue death may result directly from thermal injury or subsequently from ischemia and bacterial invasion. From this state there is no possibility of a spontaneous healing of the wound, and skin grafting is necessary. Hypertrophic scar formation is a common occurrence in this type of wound, issuing a heavy raised mass of angry red appearance and a propensity for contraction and distortion of the surrounding skin.

A fourth-degree wound can occur as a result of the incineration of tissue. The injury may extend through the subcutaneous layer to involve the fascia, muscle, periosteum, and bone. The epithelial healing process is not greatly different from a third-degree wound, except for complications due to the added injury to underlying tissues.

In addition to the events at the site of thermal insult as described in the preceding paragraphs, in major burns systemic effects derived from local physiological phenomena play an important role in total response to the injury. The function of all major organ systems of the body will be altered due to the effects of a major burn. Some of these changes are related directly to the stress of the injury and the release of endogeneous inflammatory mediators into the circulatory system, while other alterations are associated with the altered functional capacity of the skin. Thus, although the actual duration of the thermal insult is usually quite short, the biochemical and physiological response and subsequent rehabilitation is of an extended duration that may last for months and years (Johnson *et al.* [110]).

The preceding discussion has described burns in the context of clinical, macroscopic evaluation. However, an alternate and no less valid basis for viewing burn injury is from a microscopic perspective on a scale at which significant gradients in temperature field occur. This approach is complementary to observations of the burn response that can be made with a light microscope.

Vasodilation is the only major change that occurs in a first-degree burn, resulting in the familiar reddening appearance of the skin. Microvascular flow is also maintained in a second-degree burn, but the vascular permeability is increased (Green and Diller [82]) resulting in the accumulation of fluid in the interstitium with the formation of blisters with concomitant weeping if the integrity of the skin surface is compromised. The increment

in vascular permeability is a result of the opening of gaps in the endothelial lining of the vessels, primarily the venules (Aggarwal *et al.* [1]), or by direct damage to the endothelial cells (Cotran and Manjo [47]). The increase in permeability is nearly immediate, and it appears to be a result of both direct thermal injury and the release of chemical mediators (Arturson [5]). The alteration of the vascular endothelium allows an overall fluid loss and drop in plasma volume, which is a prime factor causing shock in untreated large burns. If the vascular barrier is severely damaged there may also be extravasation of red cells locally.

A third-degree burn results in a loss of blood flow in the microcirculation, leading to eventual necrosis of the tissue. There is nearly always extensive plasma loss associated with third-degree burns because the spatial gradients in a temperature field requisite to produce severe focal injury will cause more moderate effects in the surrounding tissue. In deep burns there may be a considerable collection of interstitial fluid under the wound before any surface swelling is manifested. During the postburn period there are changes in the blood rheology such as higher viscosity (McMantus *et al.* [144]), and a marked increase in the aggregation of platelets in the injured area (Eurenius and Rotherberg [64]).

Other physiological and physical factors may also influence the response to a defined thermal insult. Variables include pigmentation and water content of skin, regional variations in skin thickness, the presence of hair and oils, and the local state of microvascular perfusion. These factors may all affect the diffusion of heat through the tissue, and thereby the local temperature/time history that issues in the burn injury. In principle it should be possible to account for all of the above parameters as they appear in the constitutive properties of the skin.

B. THERMAL BURNS TO THE SKIN

Thermal burns occur as a consequence of tissue exposure to elevated temperatures for an extended period of time. However, definition of the combinations of temperature and time requisite to produce graded thermal injury has proven difficult to identify quantitatively. One fact is clear, the relationship is not linear, as was supposed in early analyses. This theory is embraced in the concept of the critical thermal load (CTL), in which the severity of injury was predicted as being proportional to the total energy delivered to the tissue during the course of an insult. The CTL is calculated as the integral of the transient heat flux delivered over the time of exposure. This theory is based on the assumption that the injury is a function of only the total energy dosage accrued; thus, equal energy delivered should issue in equal injury. Stoll was one of the first investigators to demonstrate

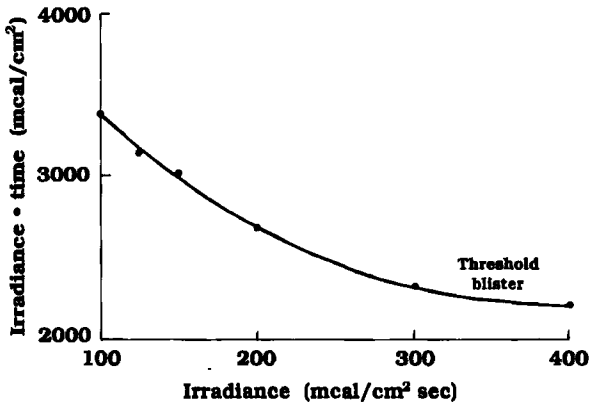


FIG. 33. Product of irradiance flux and time of exposure to produce a threshold injury characterized by blister formation. (Redrawn from Stoll [196, Fig. 4, p. 124], with permission.)

unequivocally the fallacy of this argument (Stoll [196]). She demonstrated to the contrary that a large dose of energy delivered over a very long time may produce no injury whatsoever, but the same energy delivered in a very short time could cause severe injury. Figure 33, plotted from her data, shows that the product of energy flux and time of exposure to produce a given threshold level of injury is nonlinearly dependent on the magnitude of the flux. In the series of experiments, human skin (her own) was irradiated from a heated source at varying intensities (energy flux) to produce a threshold injury characterized as the formation of a blister. At high levels of energy flux the slope of the curve for product of flux and time decreased dramatically. The obvious implication is that as the flux was increased to high levels the required time of exposure decreased disproportionately rapidly. Since the higher fluxes would have produced correspondingly higher temperatures, the time-temperature relationship should also be presumed to be nonlinear. Both experiments and mathematical models of the thermal burn process have corroborated this assumption.

The first report of the quantitative relationship of time and temperature to produce a threshold thermal injury was by Moritz and Henriques [148]. They conducted experiments on pig and human skin to determine the combinations of temperature and time of exposure to create various graded threshold levels of injury. In general, they found that a burn of specified degree of severity is produced by progressively decreasing temperatures as the time of exposure is increased logarithmically. Their data for two levels of injury are plotted in Fig. 34; these levels can be considered to correspond to first- and second-degree burns as evaluated according to the macroscopic criterion described previously. The fact that the data as

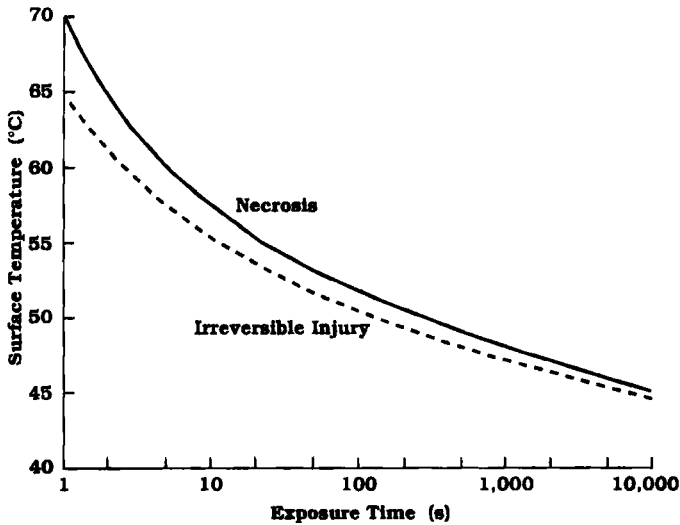


FIG. 34. Measured values of time and temperature to produce graded levels of burn injury. (Redrawn from Moritz and Henriques [148, Fig. 4, p. 711], with permission.)

plotted on semilogarithmic coordinates are approximated reasonably well by a straight line has implications for identification of the mechanism of injury, as will be discussed in Section VI of this review.

Subsequently other experimental data have been obtained that support the pioneering work of Moritz and Henriques. Stoll and her co-workers conducted an extensive series of investigations on the thermal/temporal conditions to produce graded burn injury and different pain intensities (Stoll and Green [200]; Stoll and Chianta [199]). Much of these data are for human subjects and were obtained from her own forearm. Ross and Diller [175] performed a complementary series of measurements in which the physiological response to thermal insult was evaluated at the micro-circulatory level in an animal model. All of these investigators noted the exponential relationship between the effective insult temperature and the time of exposure in determining the burn severity. Thus, it is possible to express this phenomenon in terms of a simple relationship between time, t , and temperature rise (Ross and Diller, [175]):

$$t = t_b \exp(T_b - T) \tag{4.1}$$

or, in terms of equivalent dimensionless parameters for time, φ , and temperature, ϑ ,

$$\varphi = \xi \exp(-\vartheta) \tag{4.2}$$

Experimental data such as the above that have been well documented in many different experimental environments point to a clear rationale for modeling of the thermal history during the burn process in order to obtain a better understanding of the genesis of a high temperature thermal injury and a basis for predicting the potential hazard of exposure to environments at elevated temperatures. Further, the availability of a reliable model for high temperature injury would provide a desirable technique for evaluating burn scenarios as an alternative to experiments that are inherently difficult to conduct and expensive in both physical and subject resources.

Analysis of the thermal history during a burn injury should provide a description of the variation of temperature in both space and time. Evaluation of the local history would then provide an indication of the temporal and spatial distributions of the accrual of injury on a microscopic scale; integration of this function over the entire affected volume would provide a figure that could be related to the macroscopic observable injury as represented in Eqs. (4.1) and (4.2). Thus, the modeling of burn injury processes begins with a standard heat transfer analysis of the transient temperature in the tissue as a function of the initial and boundary conditions, the geometry and constitutive properties of the tissue, and other physiological and/or clinical parameters such as the perfusion rate of blood, metabolism, and irradiation by an external energy source.

In general, the transient temperature in the skin during a burn obeys Eq. (1.1) with the inclusion of additional energy terms as appropriate. During a severe burn incident the thermal effects of metabolism and microvascular blood perfusion are negligible. Further, in a major burn the dimensions of the affected area are large compared with the tissue thickness, so that if edge effects are not included the system geometry in which the temperature field is of interest can be represented in single dimensional Cartesian coordinates:

$$\frac{\partial T(x, t)}{\partial t} = \alpha \frac{\partial^2 T(x, t)}{\partial x^2} \quad (4.3)$$

This equation has been solved for a wide range of boundary conditions to simulate various burn sequences. In addition to their pioneering experimental studies, Henriques and Moritz [100] were also the first to propose a successful thermal model of a burn injury. To complement analysis of the thermal field Henriques also postulated a function to quantify the damage owing to high temperature exposure based on an Arrhenius type of reaction. The instantaneous rate of production of injury, Ω , was described as

$$\frac{\partial \Omega(x, t)}{\partial t} = \xi \exp \left[-\frac{\Delta E}{\Re T(x, t)} \right] \quad (4.4)$$

where ξ is a scaling constant and ΔE is the activation energy for the biochemical processes that are assumed to govern the development of injury in tissues. The expression for $T(x, t)$ is obtained from the solution of Eq. (4.3) with the appropriate initial and boundary conditions. Equation (4.4) may be integrated over the period of the burn to identify a measure of total accrual of thermal injury as a function of position within the tissue:

$$\Omega(x) = \xi \int_0^t \exp\left[-\frac{\Delta E}{\Re T(x, t)}\right] dt \quad (4.5)$$

Further discussion of the Ω function will be presented in Section VI. Suffice it to note for the present that calculation of injury to tissue requires as a requisite a solution for the transient temperature field throughout the region of involvement.

The initial problem solved by Henriques and Moritz dealt with burns caused by convective interaction with a heated fluid. Thus, the surface boundary condition was defined by the standard convective transport equation:

$$q_0(t) = h[T_e - T(0, t)] \quad (4.6)$$

The skin was treated as a homogeneous, semi-infinite medium with constant thermal properties and a uniform initial temperature of T_i in order to obtain an analytical solution to the problem (Carslaw, [32]):

$$\Theta(l, t) = \operatorname{erf}\left(\frac{\gamma}{\sqrt{t}}\right) \left\{ \exp\left[\frac{hl}{k} \left(1 + \frac{hlt}{4\gamma^2 k}\right)\right] \right\} \left\{ 1 - \operatorname{erf}\left[\frac{\gamma}{\sqrt{t}} \left(1 + \frac{hlt}{2\gamma^2 k}\right)\right] \right\} \quad (4.7)$$

where $\Theta(l, t)$ is the dimensionless temperature relative to the initial and environmental values at a depth l into the skin at time t .

If there is direct contact with a heated substrate the effective heat transfer coefficient h becomes very large so that the film resistance is negligible, and the skin surface assumes the environmental temperature. Under these conditions the solution simplifies to the error function:

$$\Theta(l, t) = \operatorname{erf}\left(\frac{\gamma}{\sqrt{t}}\right) \quad (4.8)$$

Subsequent to the above work, Büttner [28] continued his earlier studies initiated in Germany after coming to the U.S. Air Force School of Aerospace Medicine in San Antonio. His work was of particular interest to the military at a time when a major war was only recently concluded in which burn injuries to both military personnel and civilians occurred in great proportions, and new weapons were being developed with unprecedented capability for delivering thermal injuries to people on a large scale heretofore unknown (Büttner [27]).

Büttner solved a number of cases of burn scenarios requiring mathematical sophistication greater than had been addressed previously. For example, he considered the effect of a nonuniform initial temperature distribution in the skin. In most instances the surface will be cooler than the interior, which is perfused with blood at varying rates. Thus, the initial temperature in the skin was taken to be

$$T(x, 0) = T_{o,i} + \zeta x \quad (4.9)$$

A constant heat flux was assumed to be impingent onto the surface:

$$\frac{\partial T(0, t)}{\partial x} = -\frac{q_o}{k} \quad (4.10)$$

The solution to this problem is given by

$$T(x, t) - T_{o,i} = \zeta x + \left\{ \frac{q_o}{k} + \zeta \right\} \left\{ \frac{2\sqrt{\alpha t}}{\sqrt{\pi}} \exp\left(\frac{-x^2}{4\alpha t}\right) - x \left[1 - \operatorname{erf}\left(\frac{x}{2\sqrt{\alpha t}}\right) \right] \right\} \quad (4.11)$$

Büttner [28] also presented an alternative solution to the convection heating problem addressed by Henriques and Moritz in Eq. (4.7) as

$$\Theta(x, t) = \operatorname{erf}\left(\frac{x}{2\sqrt{\alpha t}}\right) + \exp\left[\frac{h^2\alpha t}{k^2} + \frac{hx}{k}\right] \left[1 - \operatorname{erf}\left(\frac{x}{2\sqrt{\alpha t}} + \frac{h}{k}\sqrt{\alpha t}\right) \right] \quad (4.12)$$

where the temperature at the surface is given by

$$\Theta(0, t) = \exp\left[\frac{h^2\alpha t}{k^2}\right] \left[1 - \operatorname{erf}\left(\frac{h}{k}\sqrt{\alpha t}\right) \right] \quad (4.13)$$

The protective effect of an outer layer of clothing against an environment at high temperature was also considered by Büttner. To address this problem a coordinate system was established in which the surface of the skin was located at the origin, and the temperature at the outer layer of the garment where $x = -d$ was assumed to increase in a step-wise manner to the environmental value. Thus,

$$T(x, 0) = T_i \quad \text{and} \quad T(-d, t) = T_e \quad (4.14)$$

Büttner treated the problem as if the temperature fields in the garment and skin could be solved as uncoupled problems. The heat flux to the skin surface from the garment was written as

$$\frac{\partial T(0, t)}{\partial t} = \frac{T_e - T_o}{d} G(\zeta^2) \quad (4.15)$$

where the term $G(\zeta^2)$ was defined as

$$G(\zeta^2) = 1 - 2 \sum_{n=1}^{\infty} (-1)^{n-1} \exp(-n^2 \zeta^2) \tag{4.16}$$

and

$$\zeta^2 = \frac{\alpha_c \pi t}{d} \tag{4.17}$$

There are two time domains for which values of G are identified. At very short times, defined by $\zeta^2 < 0.2$, for which the effects of the change in boundary conditions have not reached the skin surface, G is equal to zero. At intermediate times for which the heat flux is increasing at the skin surface, for $0.2 < \zeta^2 < 1.0$, G is given by

$$G(\zeta^2) = 1.2 \frac{k_c}{k} \sin[M(\zeta^2 - 0.2)] \tag{4.18}$$

where $M = 0.872 \text{ s}^{-1}$. Finally, for large times at $1.0 < \zeta^2$ G approaches a steady state so that

$$G(\zeta^2) = 1.2 \frac{k_c}{k} \tag{4.19}$$

The temperature history at the surface of the skin in the intermediate time domain is given by

$$\tau(0, t) = 1.2 k_c \frac{T_e - T_o}{d} (k_c \rho_c c_c M)^{1/2} \left\{ \sin \left[M(\zeta^2 - 0.2) - \frac{\pi}{4} \right] + \frac{1}{\sqrt{2}} \right\} \tag{4.20}$$

Büttner also investigated the postburn cooling portion of the thermal insult process to determine if the period of time following removal of the heat source might play an important role in the development of the wound. His hypothesis was that even though the environment was returned to noninjurious conditions, the temperatures within the skin would remain for a further period of time at a state exceeding the threshold for damage. Thus, there would be a limit to the extent to which the burn process could be halted by removal of the offending heat source. This analysis was based on the assumption that heat would be dissipated from the skin only by diffusion to the underlying subcutaneous tissue, with convection through the garment to the environment being negligible. Further, it was assumed that at a penetration depth d the skin behaved as a semi-infinite medium, with the initial temperature T_i persisting. During cooling the thermal gradient was assumed to be linear so that the initial conditions for the cooling process became

$$\tau(x, 0) = T_o \left(1 - \frac{x}{d} \right), \quad 0 \leq x \leq d \tag{4.21}$$

The solution of this problem describes a uniform exponential decay in temperature at all positions within the skin:

$$\tau(x, t) = T_0 \sum_{n=1}^{\infty} \frac{\exp - [u(2n + 1)^2]}{(2n + 1)^2} \quad (4.22)$$

where

$$u = \frac{\alpha \pi^2 t}{4d^2} \quad (4.23)$$

An alternative cooling scenario was assumed for burns such as might be caused by flash explosions for which there would be a very short exposure to a very high intensity source. In this case the temperature distribution at the termination of the exposure period was taken to be increased to a uniform value within a very thin stratum, g , near the surface and to be unperturbed at all deeper locations. The initial conditions for cooling then became

$$\tau(x, 0) = T_0, \quad 0 \leq x \leq g \quad (4.24)$$

$$\tau(x, 0) = 0, \quad g < x \quad (4.25)$$

After the explosion the effects initially confined to the surface region were propagated into the deeper regions of the skin according to the relation

$$\tau(x, t) = T_0 \left[\operatorname{erf} \left(\frac{x + g}{2\sqrt{\alpha t}} \right) - \operatorname{erf} \left(\frac{x - g}{2\sqrt{\alpha t}} \right) \right] \quad (4.26)$$

For this type of surface heating the injury process would appear to persist at interior locations for a significant time following completion of the insult.

Burns caused by high temperature radiation sources were another problem of interest to Büttner [29]. He assumed that a radiant flux impinging onto the skin could be resolved into two components; one which penetrated into the skin, I , and one which did not, ϑ . The distinction between I and ϑ is primarily attributable to the absorption characteristics of the skin and is strongly dependent on wavelength. A radiant flux component that is absorbed strongly resulting in a deposition of energy within a layer of tissue immediately adjacent to the surface issues in a simple boundary condition

$$\frac{\partial T(0, t)}{\partial x} = -\frac{\vartheta}{k} \quad (4.27)$$

A radiant flux that is weakly absorbed issues is an internally distributed heating source. Therefore, Eq. (1.1) must be modified to reflect the added energy term as follows:

$$\frac{\partial T(x, t)}{\partial t} = \alpha \frac{\partial^2 T(x, t)}{\partial x^2} + \frac{I \eta \exp(-\eta x)}{\rho c} \quad (4.28)$$

η is the absorption coefficient for the wavelength of the incident radiation. A uniform initial temperature is assumed, and the radiant fluxes both undergo a step change from zero to constant values at time $t = 0$. The solution for this problem is

$$\begin{aligned} \tau = & -\frac{\vartheta}{2k\eta} \left\{ \left[\exp(\alpha^2\eta^2t - \eta x) + \exp(\alpha^2\eta^2t + \eta x) \right] \right. \\ & \cdot \left[1 - \operatorname{erf}\left(\eta\sqrt{\alpha t} - \frac{x}{2\sqrt{\alpha t}}\right) \right] \left. - \frac{\vartheta}{2k\eta} \exp[-\eta x] + \exp\left[\frac{-x^2}{4\alpha t}\right] \right. \\ & \cdot \left. \frac{2(\vartheta + 1)\sqrt{\alpha t}}{k\sqrt{\pi}} - \frac{x(\vartheta + 1)}{k} \left[1 - \operatorname{erf}\left(\frac{x}{2\sqrt{\alpha t}}\right) \right] \right\} \end{aligned} \quad (4.29)$$

At the surface the temperature history reduces to

$$\tau = -\frac{\vartheta}{k\eta} \{ \exp(\alpha^2\eta^2t) [1 - \operatorname{erf}(\eta\sqrt{\alpha t})] \} + \frac{2(\vartheta + 1)t}{k\rho c\sqrt{\pi}} - \frac{\vartheta}{2k\eta} \quad (4.29)$$

In a third and later publication Büttner focused on the more specific problem of burns caused by deeply penetrating heat sources (Büttner [30]). Of particular interest were scenarios involving high radiation intensities combined with short exposure times in order to simulate the effects that might be caused by an atomic bomb explosion. The goal of this study was to develop a facility by which, under the above conditions, the degree of tissue necrosis could be predicted as a function of depth in the skin and the energy density of the incident radiation. In developing an appropriate model it was necessary for Büttner to address complicating factors due to the nonlinear distributed absorption of radiant energy with depth in the skin and the strong variation in the effective conductivity of the skin as a function of local temperature. To address these two issues, the heat generation due to absorption of radiant energy incident with a fluence rate of ϕ and the effective thermal conductivity were both stated in terms of depth into the skin, x . The generation of heat was expressed as

$$Q(x) = \phi(1 - K)\eta(x) = I\eta(x) \quad (4.30)$$

where the fraction of radiation reflected from the surface is given by K , and the fraction absorbed at a depth x is given by η . The thermal conductivity was determined by

$$k(x) = 7(1 + 3x) \quad (10^{-4} \text{ cal/cm}\cdot\text{s}\cdot^\circ\text{C}) \quad (x \text{ in cm}) \quad (4.31)$$

based on data available at the time from prior studies by both himself (Büttner [26]) and several others. Owing to the temperature dependence of the conductivity, it was necessary to account for its variation with position

in writing the heat diffusion equation. Thus,

$$\rho c \frac{\partial T(x)}{\partial t} = k(x) \frac{\partial^2 T(x)}{\partial x^2} + \frac{\partial k(x)}{\partial x} \frac{\partial T(x)}{\partial x} + Q(x) \quad (4.32)$$

Equations (4.30) and (4.31) were substituted into Eq. (4.32), and the second term on the right was dropped based on order of magnitude considerations. The value of the product ρc was set equal to zero, and the following initial and boundary conditions were applied:

$$t = 0, \quad T(x, 0) = 37^\circ\text{C} \quad (4.33)$$

$$x = 0, \quad \frac{\partial T(x)}{\partial x} = 0; \quad x \gg 0, \quad T(x, 0) = 37^\circ\text{C} \quad (4.34)$$

Note that these boundary conditions assume that the surface of the skin is insulated. Thus, the only avenue of dissipation for absorbed energy is conduction to underlying tissues.

The nonlinear nature of Eq. (4.32) precluded direct solution by analytical techniques; therefore, Büttner applied a difference equation approximation to the differential equation, which was then solved by manual calculations. By assuming uniform time and spatial increments throughout the system, Eq. (4.32) becomes

$$T(x_i t_{k+1}) = T(x_i t_k) + \frac{7 \Delta t (1 + 3x_i) 10^{-4}}{\Delta x^2} [T(x_{i+1} t_k) - 2T(x_i t_k) + T(x_{i-1} t_k)] + Q(x) \Delta t \quad (4.35)$$

The duration of intense irradiation was assumed to last for 2 s, which at the time was considered to be a very brief exposure, but now is orders of magnitude longer than the exposure periods for many laser irradiation protocols. At the conclusion of the irradiation the model was continued by setting the source term to zero and fixing the thermal conductivity at a constant value of 1 (cal/cm·s·°C) to determine the thermal history as the absorbed energy was dissipated from the locally heated area. Two scenarios were evaluated; in one case perfect insulation of the surface was maintained, and in the second the affected area was covered immediately with a hand, providing a sink of matching thermal properties for removal of heat.

Figure 35 presents the evolution of temperature profiles at selected incremental positions in the skin during irradiation with an intensity of 1 cal/s·cm². It is noteworthy that the temperature rise at each location plotted is nearly a linear function over the duration of the exposure. Büttner was also quite interested in the thermal history following completion of

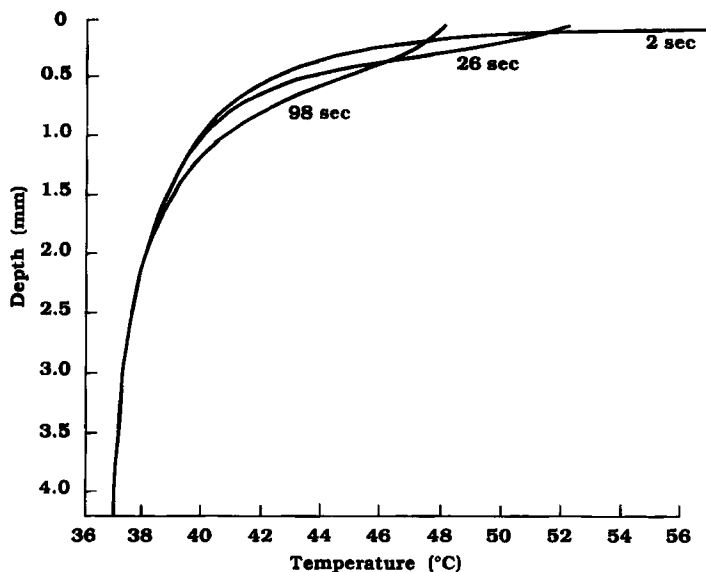


FIG. 35. Temperature distributions in the human skin at various times following exposure to a radiant flux of $1 \text{ cal/cm}^2 \cdot \text{s}$ for 2 s. (a) 0 s; (b) 24 s; (c) 96 s. (Redrawn from Büttner [30, Fig. 3, p. 214], with permission.)

the insult phase of an irradiation protocol to determine whether a significant component of the injury process may occur after the heating source is no longer active. Figures 36 and 37 depict the two extreme scenarios described previously. In the case of a perfectly insulated skin surface, the absorbed heat must diffuse to the interior region, which is indicated by the progressive slow decrease in the temperature at the boundary accompanied by a rise at proximal interior positions. Contrastingly, when a second skin surface is brought into intimate contact with the surface there is an immediate drop in the boundary temperature and a reversal in the slope of the temperature near the point of contact. The loss of heat to the surface is continual, and diffusion to the interior is minimal as indicated by the absence of any significant temperature rise.

Based on these results, Büttner offered a number of suggestions for response to exposure to a high intensity radiation. For example, immediate surface cooling of irradiated tissue is recommended, as well as hiding from the direct line of irradiation and spinning the body around to minimize the cumulative effects at any one location. Subsequent experiments and analysis by the present reviewer (Ross and Diller [176]; Thompson and Diller [205]; Diller *et al.* [61]) and others (Jakobsson and Arturson [107])

have indicated that there is thermally no benefit to postburn cooling therapy, although the biochemical processes governing the inflammatory response may be altered to advantage. Spinning and hiding maneuvers may be of value for thermal protection, although they have not been included during the intervening four decades into the standard repertoire of responses to be executed during an atomic blast.

Büttner presented plots of many other predicted temperature responses to burn scenarios in his set of three papers. A number of the numerical results obtained for specific burn insults using his models have been summarized previously and are readily available (Diller [49]).

Stoll conducted a very extensive and innovative combined experimental and modeling investigation into the physical and physiological parameters that govern the burn injury process and worked on the development of clothing to afford protection against fire hazards (Stoll and Chianta [197-199]; Stoll and Green, [200]; Weaver and Stoll [213, 214]. Her work led directly to the development of materials now in wide use for garments by military personnel, firemen, motor racing drivers, and others. The

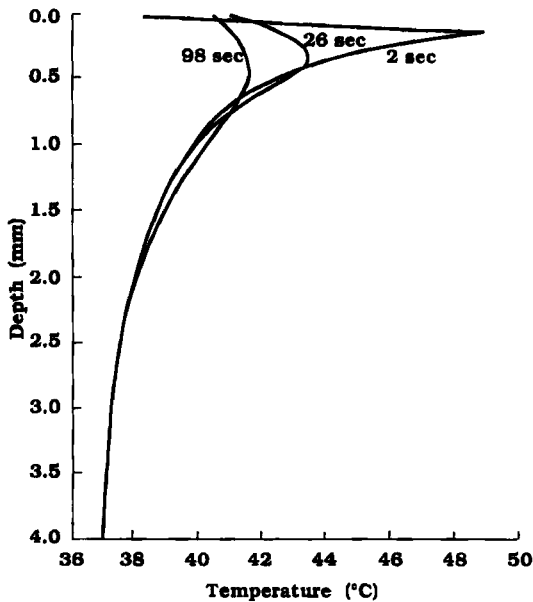


FIG. 36. Temperature distributions in the human skin for the identical heating protocol as Fig. 35, except that immediately upon completion of the irradiation an identical tissue surface at the initial temperature was brought into perfect thermal contact at the surface to provide accelerated cooling of the burned skin. (a) 0 s; (b) 24 s; (c) 96 s. (Redrawn from Büttner [30, Fig. 4, p. 215], with permission.)

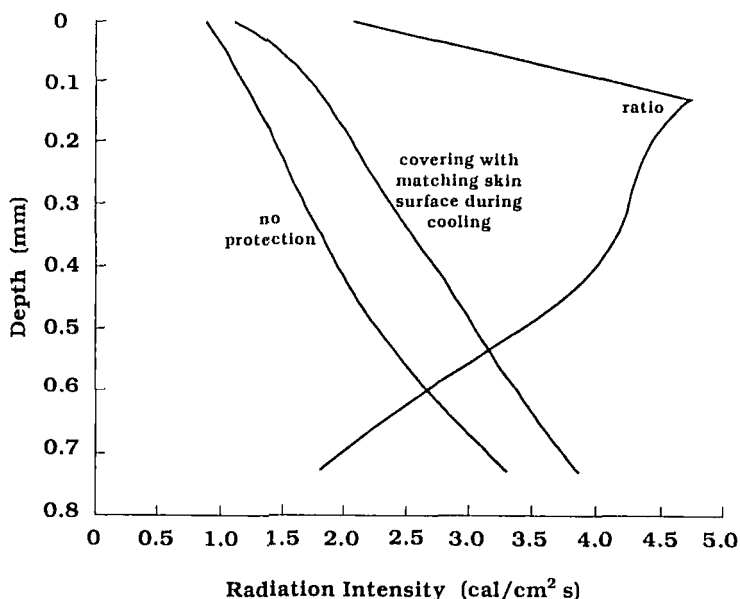


FIG. 37. Threshold irradiation fluxes necessary to produce permanent necrosis of tissue at the indicated depths for the same protocol as defined in Fig. 35. Curve (I) is for the surface insulated following the radiation; curve (II) is for surface contact with a matched tissue, as in Fig. 36; curve (III) is the ratio of the threshold fluxes for the two cases. (Redrawn from Büttner [30, Fig. 5, p. 218], with permission.)

models for burn processes showed clearly that the spatial temperature distribution within the skin would lead to a microscopic scale gradient in the burn severity. Therefore, experiments were made to measure the temperatures at the skin surface and the interface between the epidermis and dermis (at a depth of $80\ \mu\text{m}$) during radiation burns (from a flame source) (Weaver and Stoll [214]). Under the experimental conditions the incident radiation would have been absorbed essentially at the surface of the skin. Examples of the temperature rise and fall during the heating and cooling phases of representative burn scenarios are shown in Fig. 38. The data demonstrate clearly the time lag in thermal response between the surface and even a shallow surface location. During heating the interior is cooler than the surface, and during cooling it is warmer.

Weaver and Stoll [214] developed a model to simulate the experimental conditions under which these data were obtained. They assumed that a constant radiant heat flux q was absorbed at the skin surface, lasting for a duration of t_b , following which the skin was exposed to a cooling environment. The expression for transient temperature during the entire protocol

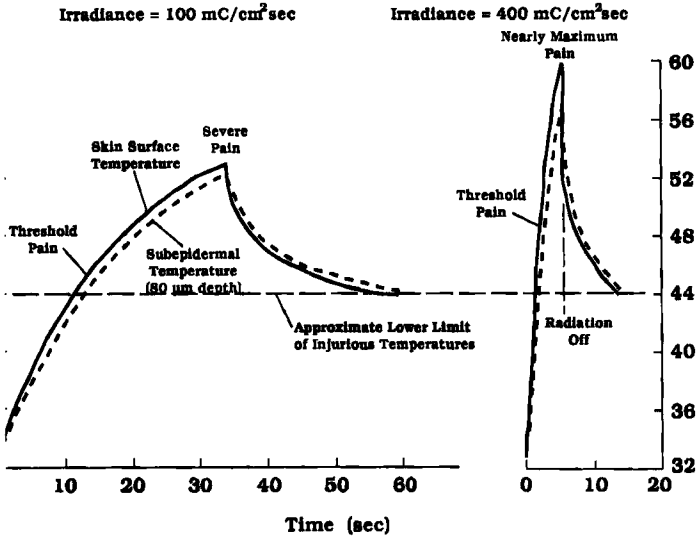


FIG. 38. Measured temperature/time histories at the skin surface and interface between the epidermis and dermis for thermal radiation burns. (Redrawn from Stoll [196, Fig. 25, p. 126], with permission.)

including the heating and cooling phases

$$\begin{aligned}
 \tau = & \frac{q}{k} \left\{ \frac{2\sqrt{\alpha t} \exp[-x^2/4\alpha t]}{\sqrt{\pi}} - x \left[1 - \operatorname{erf}\left(\frac{x}{2\sqrt{\alpha t}}\right) \right] \right\} \\
 & - \frac{q}{k} \left\{ \frac{[2\sqrt{\alpha[t-t_b]} \exp(-x^2/4\alpha[t-t_b])]}{\sqrt{\pi}} - x \left[1 - \operatorname{erf}\left(\frac{x}{2\sqrt{\alpha[t-t_b]}}\right) \right] \right\}
 \end{aligned}
 \tag{4.36}$$

In addition, Stoll was the first investigator to employ the digital computer as a tool to calculate the thermal history during a burn and to use the resulting nonlinear function to estimate the consequent extent of tissue damage (Stoll [214]). Both the experimental and the modeling data of Stoll indicated that there was a considerable period of time following removal of the heat source during which the tissue temperature remained above the threshold for injury (which she identified as being in the range of 44 °C and higher). Although this observation is true, subsequent modeling by Diller *et al.* [61] and subsequent experimental corroboration by Jakobsson and Arturson [107] have demonstrated that injury accrual during the cooling period does not make a significant contribution to the overall wound severity. Further work with the finite element computer model of Diller

and Hayes [60] has demonstrated its accuracy and efficacy for modeling the burn process to skin for a variety of tissue geometries and environmental conditions.

C. ELECTRICAL BURNS

An important subset of thermal burns is injury that occurs as a consequence of resistance heating owing to the flow of electrical current through tissue (Pruitt and Mason [169]; Bingham [14]). The obvious major distinguishing factor of electrical burns is that the source of energy is generated from an internal source as opposed to being delivered by external means of application. In addition to the thermal effects, electrical trauma may also produce other neurological and/or electrophysiological dysfunction in the victim.

The basis of an electrical burn is the joule heating that occurs under the application of a field of sufficient strength. Owing to the good electrical conductivity of aqueous solutions, relatively large currents can be supported via the mobility of ions. The result is the generation of heat associated with frictional losses along the current path. The rate of heating is predicted simply by Ohm's law:

$$i(t) = \sigma E(t) \quad (4.37)$$

Although the conductivity is generally a mathematically complex quantity, for the commercial power frequency of 60 Hz, σ is predominantly real, and its value is governed by the properties of the interstitial fluid (Lee and Kolodney [122]). For the commonly encountered sinusoidal alternating current systems operating at a frequency f , the current density and electric field can be written as

$$i(t) = i \sin(2\pi ft) \quad (4.38)$$

$$E(t) = E \sin(2\pi ft) \quad (4.39)$$

The local rate of heating is a function of the current density and electric field:

$$Q(t) = \frac{E(t) \cdot i(t)}{2} = \frac{i^2(t)}{2\sigma} \quad (4.40)$$

The expression for heat generation may be applied directly in the energy balance equation to determine the transient temperature distribution during electrical heating.

A further complicating factor in modeling the temperature field resulting from the application of an electrical field to a body arises from the network topology relative to the field. In multiple aspects, biological tissues and

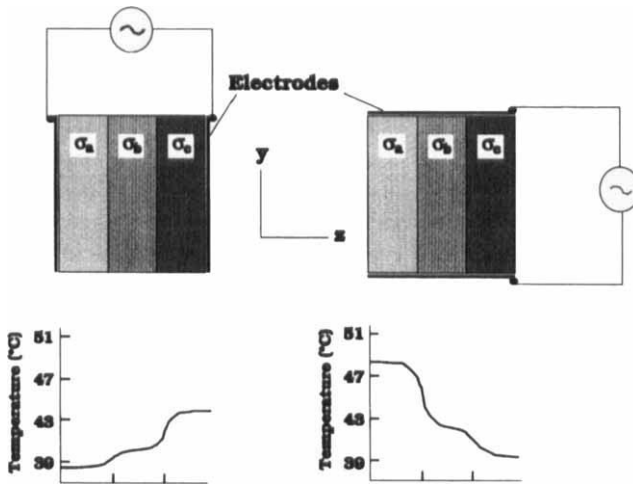


FIG. 39. A three-layered composite system across which an electric field was applied in either a (A) series or (B) parallel configuration. The thermal properties of all materials were identical to an isotonic saline solution, but the electrical conductivities were set at 10 , 5 , and $2 \Omega^{-1}/\text{m}$ for the materials a, b, and c, respectively. Forty volts were applied across the composite, and the temperature after 5 s was calculated and plotted as indicated. (Redrawn from Lee and Kolodney [122, Fig. 1, p. 664], with permission.)

organisms must be considered as composite systems having locally unique property values. Due to biological structure, it is often not appropriate to assume isotropy. This principle is illustrated by Lee and Kolodney [122] as follows. Assume a trilayered composite tissue system consisting of three homogeneous materials in perfect thermal and electrical contact, as shown in Fig. 39. The thermal properties of each layer were assigned the same values, equal to normal saline solution, but the electrical conductivities were different as indicated. A voltage was applied across opposing electrodes that were assumed to be thermally insulating. When the layers were in a series configuration with the electrodes, all layers experienced a common current density, and the electrical field strength differed in inverse proportion to the electrical conductivity. When the layers were in a parallel configuration, all layers experienced a common electrical field, and the current was proportional to the conductivity. Greatly different temperature profiles are produced in the composite system depending on whether a voltage is applied in parallel or in series with the layered geometry. For the parallel arrangement, the material with the greatest conductivity (a) was subjected to the largest temperature rise, whereas for a series arrangement it had the smallest temperature rise.

Of particular interest to Lee and Kolodney was the rate of heating produced in an adult male in a typical high voltage accident in which a 20,000-V ac powerline is contacted. It was assumed that the electric field was applied longitudinally through the arms and thorax from a high voltage source to ground, and the heating was modeled in a cross section of the upper arm nearest the source, based on the axisymmetric tissue geometry shown in Fig. 40. Note that for this geometry the tissues of the arm are arranged in a parallel configuration with the field source. The bioheat equation was applied with the electrical heating term included as an energy source:

$$\frac{\partial T(r, t)}{\partial t} = \frac{\alpha}{r} \frac{\partial^2 r T(r, t)}{\partial r^2} - \frac{\rho_b c_b \omega_b}{\rho c} [T(r, t) - T_b] + \frac{i^2(r)}{2\sigma(r)\rho c} \quad (4.41)$$

Convective cooling to the surrounding air was assumed at the surface of the skin, with a film coefficient of $h = 1 \text{ W/m}^2 \cdot \text{°C}$. The temperature of perfused blood entering the tissue was $T_b = 37 \text{ °C}$, with the local perfusion rates for the individual tissues adopted from the values given by Chen [38]. An initial temperature distribution matching that of Pennes for the arm at rest was assumed (Pennes [165]). Characteristic electrical and thermal

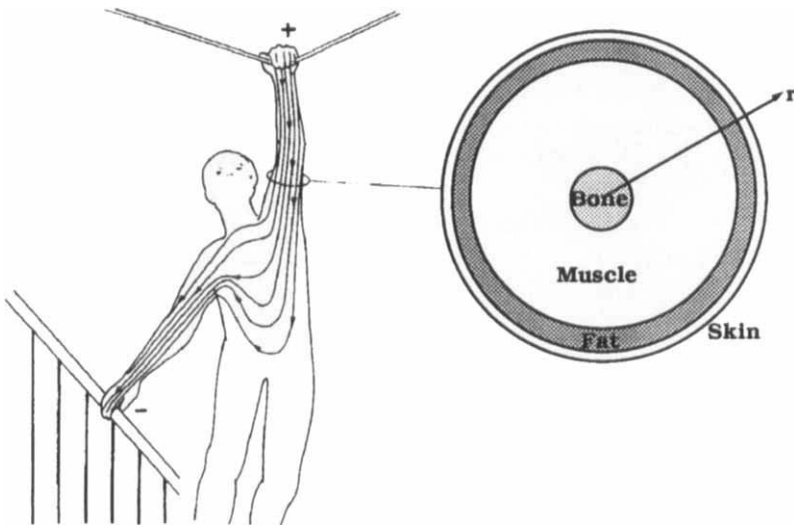


FIG. 40. Model for the cross section of the forearm during application of a high electrical voltage from hand to hand. Current flux lines are indicated through the body, including the upper extremities and torso. The arm is assumed to consist of symmetric layers of bone, skeletal muscle, fat, and skin in a cylindrical geometry with an outer radius of 5 cm. (Redrawn from Lee and Kolodney [122, Fig. 2, p. 665], with permission.)

properties were applied for the component tissues of the arm as obtained from the literature (Geddes and Baker [77]; Bowman *et al.* [24]). Equation (4.41) was solved for applied currents between 0 and 20 A using the finite element method to obtain maps of the temperature as a function of position and time.

The radial temperature distribution across the arm after 10 s of heating at various electrical currents is shown in Fig. 41. Blood flow effects were omitted from these calculations. The temporal responses to heating at a specific location in each of the four tissues of the arm are plotted in Fig. 42. A current of 10 A was applied for 10 s, and the temperature history was followed for approximately a half hour subsequent to heating. Profiles were determined both with and without perfusion of blood. It is apparent for the conditions assumed that perfusion has a large effect on the dissipation of heat following the termination of heating. In part this behavior can be attributed to the quite small value of the convective heat transfer coefficient assumed for the skin/air interface. When the perfusion is set to zero the route available for dissipation of the energy deposited by electrical heating is via the path of surface convection, which presents a relatively large thermal resistance. Therefore, the large temperature gradients created by the differential heating among the tissues, as seen in Fig. 41, are slowly diminished by internal diffusion within the arm. Contrastingly, the internal convection provided by the circulation of blood effectively and uniformly reduced the elevated temperature throughout the arm.

In addition to the obvious thermal consequences of high energy electrocution, there is the possibility of further mechanisms of injury, such as by damage to the cell membranes. Anecdotal evidence supports this hypothesis,

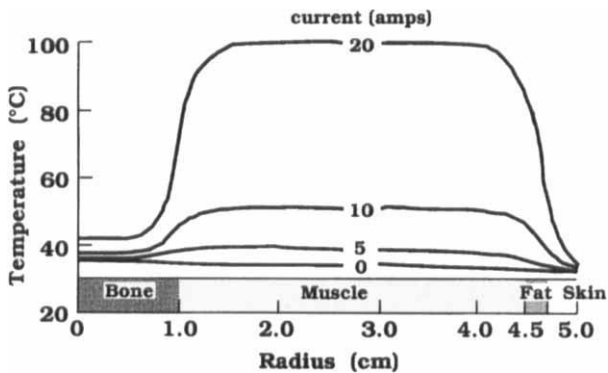


FIG. 41. Temperature profiles through the forearm after 10 s of heating with a voltage of 20,000 V and the indicated currents. (Redrawn from Lee and Kolodney [122, Fig. 3, p. 666], with permission.)

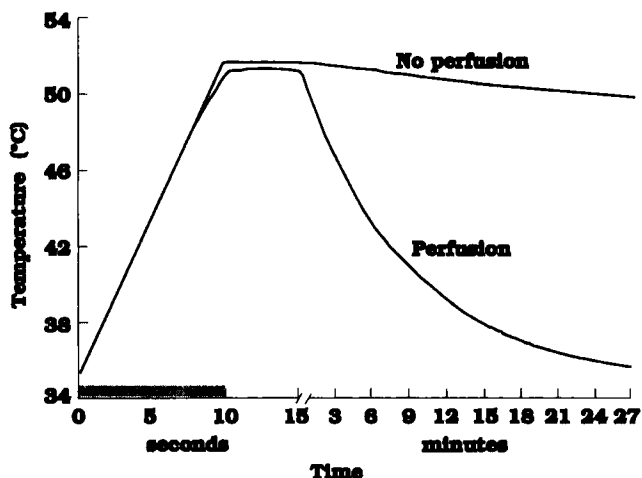


FIG. 42. Calculated transient temperature at the radial midpoint of the muscle of the forearm for heating with a current of 10 A for 10 s. Subsequently the tissue is cooled by convection to the environment either with or without local blood perfusion, as indicated. Note that the time scale is discontinuous during the cooling period. (Redrawn from Lee and Kolodney [122, Fig. 4, p. 667], with permission.)

which was also quantified in conjunction with the above analysis (Lee and Kolodney [123]). In general, the results of this modeling analysis are at least in qualitative agreement with clinical observations. For example, the presence of deep necrosis is usually accompanied by the absence of uninjured skin. Further, as pointed out by Robson [172], damage to cell membranes could have an effect on the local release of inflammatory mediators, which would in turn modify the microcirculatory blood flow. Spatial variations in this phenomenon could account for the patchy pattern of injury observed with electrical burns, given the importance of the magnitude of perfusion on governing the transient temperature response to electrocution. Baxter has hypothesized an alternate distribution of temperature elevation among the various tissues owing to electrical heating (Baxter [8]). However, as noted in Fig. 39, establishing a series rather than a parallel topology of the tissue structure with the applied electric field can produce an inverted pattern of heating in a defined composite system. There is undoubtedly a distribution of this topology factor that occurs among electrocution accidents.

Another situation in which the electrical heating of tissue is of great importance occurs in electrosurgery. The practice of electrosurgery is closely related to the phenomenon of electrical burns, but the boundary conditions

are controlled aggressively to limit the electrical fields produced and thereby use the localized heating of tissue to advantage. Nonetheless, when improperly executed, electrosurgery has the inherent risk of producing undesired burns to the patient. Analysis of the coupled thermal-electrical processes that govern electrosurgery has been described recently in a very clear and complete exposition (Pearce [158]), and readers are referred to this source for further information.

D. LASER IRRADIATION

The development and wide spread adoption of lasers during the past several decades has given rise to a new area of burn studies, i.e., temperature rise associated with the absorption of high intensity irradiation of light. Lasers are now in quite broad use as a surgical instrument. Not only is the heat generated by absorption of laser light efficacious in the destruction of targeted tissue, but other nonthermal effects are valuable aids for diagnosis and treatment of a wide range of pathologies (Berns [13]).

Following the introduction of lasers in the early 1960s there was particular concern over the potential for incurring injury to the eye owing to the absorption of energy causing elevated temperatures. In fact, ocular injury due to observation of intense light has been an everpresent problem; common sources are encountered in the environment during solar eclipses and bright sun on snow, in specific occupations such as arc welding, and in the military with the bright flash when large guns and rockets are fired (Allen and Polhamus [2]). However, the widespread adoption of lasers has exacerbated this potential hazard (Welch and Polhamus [218]).

When tissue is irradiated with laser light an internally distributed energy source is created owing to the absorption properties of the tissue (Welch *et al.* [220]). Laser burns are usually distinguished from standard thermal burns due to several characteristics. The energy flux may be very high, exceeding 10^{10} W/cm², and of extremely short duration in the range of nanoseconds or less; the cross-sectional dimensions of the beam are often comparable with the penetration depth of the thermal field created, making the use of Cartesian coordinates unacceptable; local tissue temperatures achieved may exceed those that occur in common burns by a large factor issuing in carbonizing, vaporization, and ablation. These special physical characteristics produce some equally novel physiological responses which have been exploited in the development of new surgical and therapeutic modalities. As would be expected, there are some unique modeling problems associated with analysis of laser irradiation that are not encountered in the consideration of standard burns.

Among the first investigators to analyze the thermal response of tissue to light irradiation was Wray [226]. His objective was to develop a model which would allow prediction of retinal burns in persons or animals owing to exposure to the thermal fireball resulting from a nuclear detonation. He modeled the eye in which a two-dimensional transient temperature distribution was created by an irradiation field. Equation (1.1) was solved in cylindrically symmetric coordinates with an internal energy source due to the absorption of light to obtain a description of the radial and axial variations in the transient temperature:

$$\frac{\partial T}{\partial t} = \alpha \left[\left(\frac{1}{r} \frac{\partial T}{\partial r} + \frac{\partial^2 T}{\partial r^2} \right) + \frac{\partial^2 T}{\partial z^2} \right] + \frac{Q(r, z, t)}{\rho c} \tag{4.42}$$

Often the temperature scale in Eq. (4.42) is shifted so that the rise τ above the initial value is determined. The energy source due to the absorption of light is given by

$$\frac{Q(r, z, t)}{\rho c} = \int_{\lambda_{\min}}^{\lambda_{\max}} v(r)H(\lambda, t) \left[-\frac{dW}{dz}(\lambda, z) \right] d\lambda \tag{4.43}$$

The values for λ_{\min} and λ_{\max} define the range of wavelengths over which the irradiation occurs. The gradient in transmission of irradiation through the tissue can be quantified easily if it is acceptable to assume a Lambert-Beers absorption pattern. In many tissues there is a large differential in the absorption properties among various morphological strata. Therefore, for a simple two layer tissue in which the outer stratum is designated by a thickness d , the axial irradiation absorption gradient can be determined as follows:

$$-\frac{dW}{dz}(\lambda, z) = \eta_1(\lambda) \exp[\eta_1(\lambda)z] \tag{4.44}$$

for the surface layer, and

$$-\frac{dW}{dz}(\lambda, z) = \eta_2(\lambda) \exp\{[\eta_2(\lambda) - \eta_1(\lambda)]d - \eta_2(\lambda)z\} \tag{4.45}$$

for the interior layer.

Wray [226] applied this model to determine the variations in temperature along the radial, axial, and temporal coordinates for a 20-ms irradiation of the eye with a 500- μm image diameter with differential absorptions in the choroid and pigment epithelium. The structure of the eye illustrating the morphology of the absorbing layers of the retina is shown in Fig. 43, and the data for the differential coefficients of absorption of light in the pigment epithelium and choroid are presented in Fig. 44. Selected results

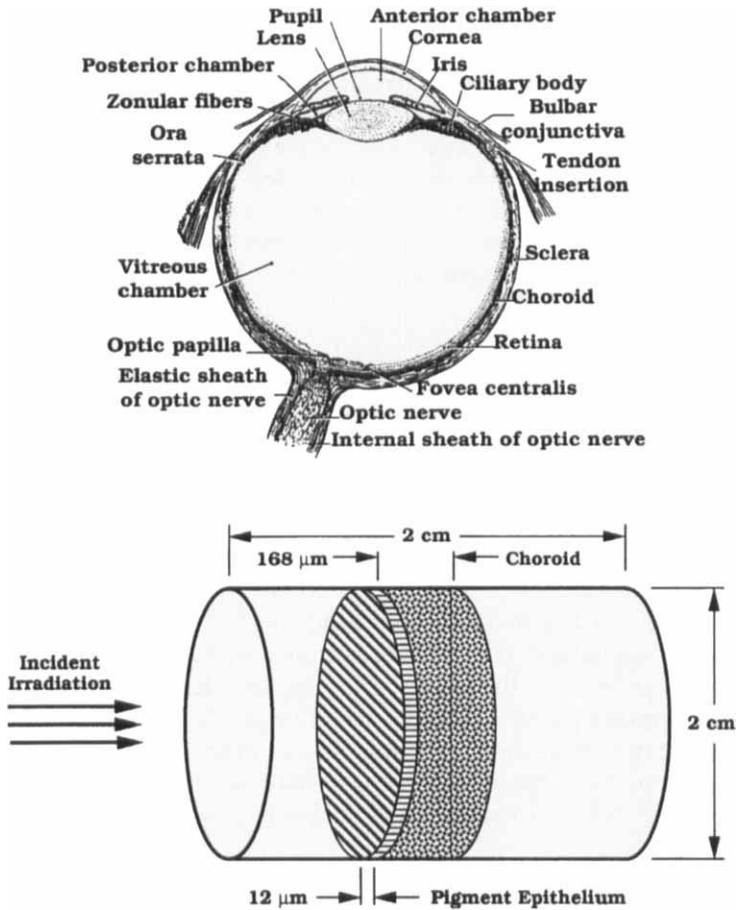


FIG. 43. Schematic drawing of the structure of the eye. (a) Overall view. (From Woodburne and Burkel [225, Fig. III-85, p. 290], with permission.) (b) Morphology through the retina. (Redrawn from Allen and Polhamus [2, Fig. 8, p. 256], with permission.)

from the simulations of Wray are presented in Fig. 45. The axial profile shows a rapid temperature rise in the pigment epithelium where the highest absorption occurs, followed by a rapid drop with depth from the front surface. The radial profile is nearly uniform over the diameter of the image disc, and then decreases in the periphery. In both cases the profiles are smeared due to diffusion of heat from the central region of absorption in the tissue. The thermal history demonstrates a typical temperature rise with elapsed time during irradiation, followed by a gradual drop subsequent to the cessation of irradiation as heat diffuses into the surrounding tissue.

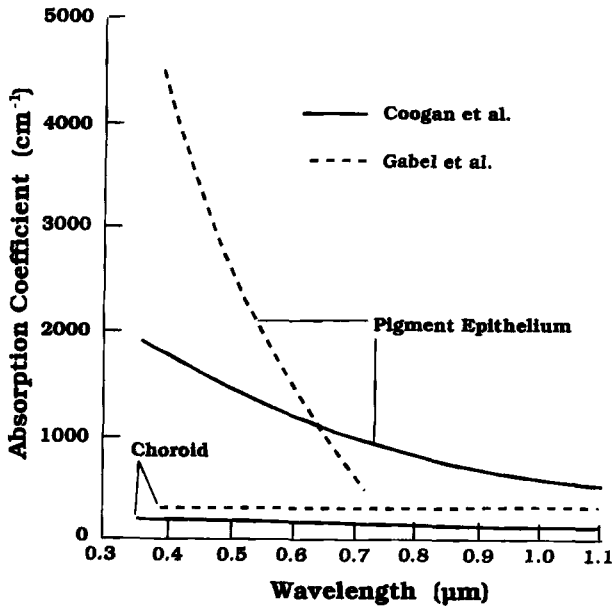


FIG. 44. Data for absorption coefficients of the pigment epithelium and choroid of the eye as a function of wavelength. (Tabular data of Wray [226] was plotted by Allen and Polhamus [2, Fig. 10, p. 257], from which it is redrawn with permission.)

At the same time Vos [212] published a thermal model for intense illumination of the retina in order to evaluate the prior experimental data of Ham *et al.* [85] for flash binding. He considered a simple rectangular geometry for the retina consisting of a square slab of dimensions $2L \times 2L$, and a thickness $2d$. The illumination was characterized as a constant flux I that was absorbed uniformly within the tissue, and the effects of convective heat transfer between the tissue and perfused blood were neglected. The temperature rise in the irradiated tissue was written according to Carslaw and Jaeger [33], with the origin of the coordinate system positioned at the center of the tissue:

$$\tau(x, y, z, t) = \frac{I}{16d} \int_0^t \left[\operatorname{erf} \frac{d+z}{\sqrt{4\alpha t}} + \operatorname{erf} \frac{d-z}{\sqrt{4\alpha t}} \right] \left[\operatorname{erf} \frac{L+x}{\sqrt{4\alpha t}} + \operatorname{erf} \frac{L-x}{\sqrt{4\alpha t}} \right] \cdot \left[\operatorname{erf} \frac{L+y}{\sqrt{4\alpha t}} + \operatorname{erf} \frac{L-y}{\sqrt{4\alpha t}} \right] dt \tag{4.46}$$

Application of this solution for the transient temperature field with the experimental data from Ham *et al.* [85] for lesions produced by flash exposures to a carbon arc lamp produced rather striking results.

Temperature rises above the physiological state in the central region of the image that were requisite to obtain a fit with the data indicated a state well in excess of conditions for which boiling would occur. It was hypothesized that the formation of steam should play a central role in the creation of a lesion in the retina under intense illumination, and the thermal analysis was

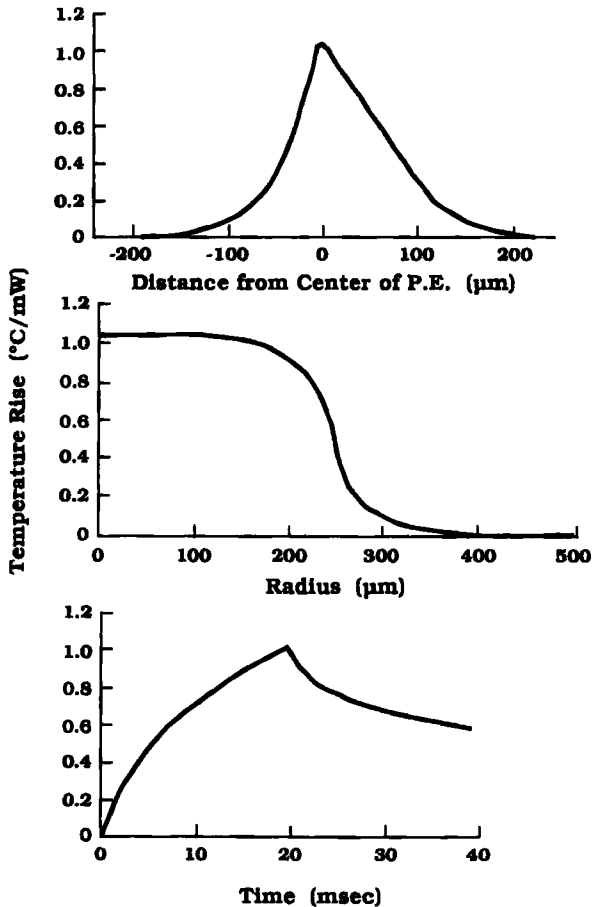


FIG. 45. Temperature rise values calculated for 20-ms unit power irradiation with a 500- μm diameter image size to the eye, with different absorption coefficients in the choroid and pigment epithelium. (a) Axial temperature distribution along the axis of irradiation at the time for which the maximum temperature is achieved. (b) Radial temperature distribution normal to the center of the pigment epithelium at the time for which the maximum temperature is achieved. (c) Transient temperature history along the irradiation axis at the center of the pigment epithelium. (Tabular data of Wray [226] was plotted by Allen and Polhamus [2, Fig. 6, p. 253], from which it is redrawn with permission.)

modified to provide an indication of the possibility of the production of a vapor phase. It should be noted that subsequent experimental and modeling analyses have confirmed that under certain conditions of irradiation, phase change processes have a large influence on the transient temperature field and on the resulting lesions that are realized.

Vos assumed that the propensity for boiling could be estimated by computing the transient temperature field under the assumption of no phase change, and retroactively determining the excess specific energy above the equilibrium phase change state that would be available for altering the latent energy of the tissue. To this end, the difference in the local temperature and $100\text{ }^{\circ}\text{C}$ was calculated at the completion of an irradiation protocol, divided by the specific heat of water, and compared with the latent heat of evaporation for water to obtain an indication of the extent of boiling that might have occurred. Although this procedure is a crude approximation to the solution of the difficult moving boundary problem, Vos obtained estimates of the mass of steam formed as a function of irradiation image size that provided a reasonable correlation with the data of Ham *et al.* for the conditions of lesion formation. Figure 46 presents the calculations for mass of steam produced as a function of the size of the illumination image on the retina. Although it is not stated in Vos's paper,

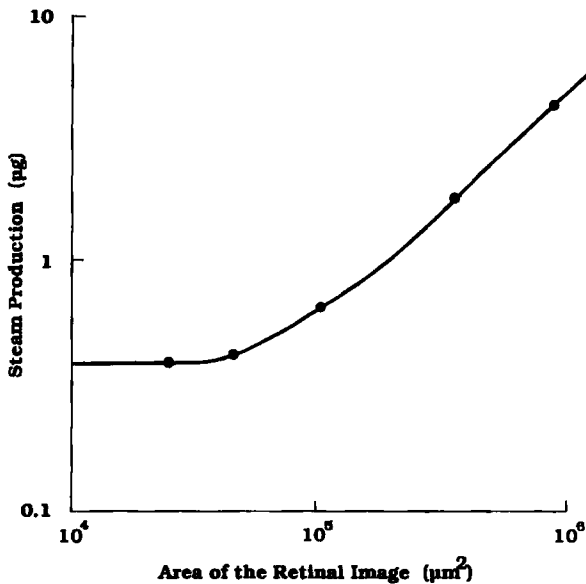


FIG. 46. Estimated steam production owing to intense illumination of the retina with various image sizes. (Adapted with permission from *Bull. Math. Biol.* 24, J. J. Vos, "A Theory of Retinal Burns," 1962, Pergamon Press plc.)

it is presumed that these calculations were performed for a uniform period of illumination, which would appear from some of his other discussions to be on the order of 0.2 s. Although this analysis can be faulted in many aspects, it did provide a starting point for subsequent investigations into the thermal injury process owing to irradiation with high intensity light sources.

Subsequent workers refined the early work of Wray and Vos. For example, Clarke *et al.* [43] derived an analytical solution for the steady state temperature distribution reached in a medium with uniform absorption of the incident radiation, as opposed to a more rational assumption of axial decay in the intensity of energy deposition as predicted by a Beer's law type of function. The differential absorption properties of the ocular elements, pigment epithelium, and choroidal tissues were accounted for in their model, with coefficients of absorption respectively of 0.045, 314, and 45 cm^{-1} at approximately the wavelength of 632.8 nm for a helium-neon laser. The resulting pattern of power deposition along the axis of irradiation is shown in Fig. 47.

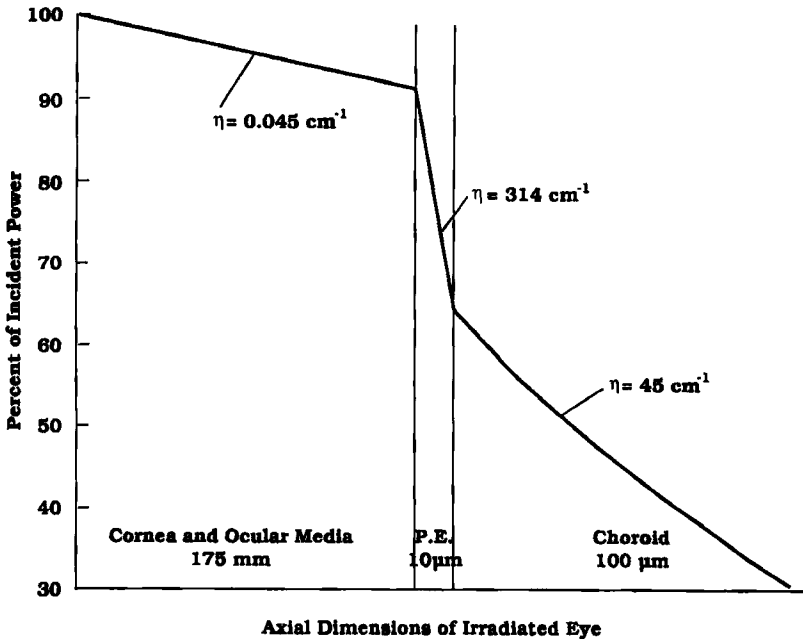


FIG. 47. Intensity profile for a uniformly absorbed beam of laser irradiation as it penetrates the eye. The cross section of the absorbing region is assumed to be a right circular cylinder, outside of which there is no interaction with the light. (Redrawn from Clarke *et al.* [43, Fig. 2, p. 1052], with permission.)

The steady state temperature field was determined as a function of the generation of energy by the absorption of incident irradiation

$$k \nabla^2 T = -\eta I(r, 0) \exp[-\eta z], \quad 0 \leq z \leq z_0, \quad 0 \leq r \leq r_0 \quad (4.47)$$

where $I(r, 0)$ is the power density radial profile of the incident radiation at the surface, and absorption is assumed to be uniform within the cylindrical region bounded radially by r_0 and axially by z_0 , and to be zero beyond these boundaries. The solution for the temperature distribution along the axis of irradiation is given as

$$T(0, z) = \frac{\eta I(r, 0)}{2k} \exp[-\eta z_0] \int_0^{z_0} \exp[-\eta z'] [r_0^2 + (z - z')^2]^{1/2} - [z - z'] dz' \quad (4.48)$$

This expression was expanded in a series and integrated term by term to obtain a working solution.

Simulations of irradiation protocols were performed for image radii between 5 and 1000 μm , and the temperature rise was determined along the axis, where the maximum values were achieved, for a power density of 1 W/cm^2 averaged across the image impinging onto the retina. Additional parameters computed included the axial position at which the highest temperature occurred, and the power density at the retina and the total incident power requisite to produce a 10 $^\circ\text{C}$ rise at the hot spot. Values of these parameters computed for 14 different beam radii are presented in Table V, and the power density to effect a 10 $^\circ\text{C}$ temperature rise is plotted as a function of beam radius in Fig. 48. These simulations demonstrate clearly several thermal phenomena that characterize this type of laser irradiation. As the radius decreases by two and a half orders of magnitude, at a constant power density the net rate of energy delivery to the eye will drop by about five orders of magnitude. Thus, the data in columns two and three show that associated with this drop in total power delivered there will be a corresponding diminution by several orders of magnitude in the temperature at the hottest point along the axis, and the location of the hot spot will move forward toward the anterior surface of the pigment epithelium. Alternatively, if the conditions are evaluated requisite to produce a fixed magnitude of 10 $^\circ\text{C}$ in the temperature rise at the hottest point along the axis for all beam sizes, the data in columns 4 and 5 show that the power density increases nearly linearly with the decreasing radius of the laser beam, but the total power integrated over the net beam cross-sectional area displays only a moderate decrease in magnitude.

The direct correspondence between the combination of power density and beam radius to produce a specified maximum temperature rise is shown in Fig. 49 along with a limited amount of experimental data obtained by

TABLE V
 MAXIMUM COMPUTED STEADY STATE TEMPERATURE RISE DUE TO ILLUMINATION OF THE
 RETINA FOR THE INDICATED RANGE OF BEAM DIAMETERS WITH A COMMON POWER DENSITY
 OF 1 W/cm^2 ^a

Radius (μm)	τ ($^{\circ}\text{C}/\{\text{W}/\text{cm}^2\}$)	$z(\tau_{\text{max}})$	$I(r, 0) @ \tau = 10^{\circ}\text{C}$	$I_{\text{net}} @ \tau = 10^{\circ}\text{C}$
1000	4.15	10-	2.41	82.3
800	3.30	10-	3.03	66.2
500	2.03	9+	4.93	42.1
400	1.60	9+	6.25	34.1
250	0.968	9	10.3	20.0
200	0.758	9-	13.2	18.0
150	0.550	8+	18.2	14.0
100	0.345	8-	29.0	9.90
75	0.247	7+	40.5	7.78
50	0.152	7-	65.8	5.62
25	0.0648	6	154	3.29
12.5	0.0269	5+	372	1.98
10.0	0.0201	5	498	1.70
5.0	0.0078	5-	1282	1.09

^aFrom Clarke *et al.* [43], with permission.

the authors for irradiation of rabbit eyes. The animal data and model show a very good match, although the authors commented that there was a considerable range of disagreement with the data for similar experiments conducted in other laboratories. It should also be pointed out that although this model identifies several consistent trends in the steady state thermal behavior of tissue under laser irradiation, they are easily anticipated on an intuitive basis, and much of the interest in modeling the thermal aspects of laser-tissue interactions has been focused on the transient effects. Especially at very short irradiation periods with high intensity sources some very nonlinear effects are encountered, and new phenomena continue to be identified to the present time. As will be shown in subsequent discussion, modeling of the transient thermal aspects of these processes has been quite useful in the interpretation and understanding of the governing mechanisms.

Lin [128] demonstrated an analytical solution for the transient temperature field during laser irradiation of a homogeneous, nonperfused tissue, based on the application of Hankel and Fourier transform methods to solve the governing boundary value problem. For a cylindrically symmetric system the temperature rise $\tau(r, z, t)$ owing to a source $Q(r, z, t)$ is described

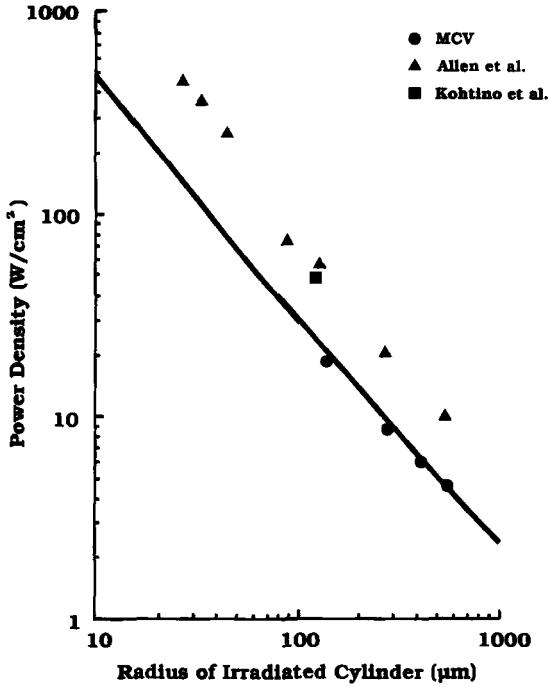


FIG. 48. Calculated power density requisite to cause a maximum temperature rise of 10 °C in the eye as a function of the incident beam. Experimental data points are shown for comparison. (Redrawn from Clarke *et al.* [43, Fig. 3, p. 1052], with permission.)

by the standard equation

$$\frac{\partial \tau}{\partial t} = \frac{1}{r} \frac{\partial}{\partial r} \left[\alpha_r r \frac{\partial \tau}{\partial r} \right] + \frac{\partial}{\partial z} \left[\alpha_z \frac{\partial \tau}{\partial z} \right] + \frac{Q(r, z, t)}{\rho c} \tag{4.49}$$

where two different cases of boundary conditions were considered, and the thermal conductivities are allowed to vary in the radial and axial directions as denoted by the subscripts. For a temperature specified initially and at the outer limits of the r and z coordinates,

$$\begin{aligned} \tau(r, z, 0) &= f_0(r, z) \\ \frac{\partial \tau(0, z, t)}{\partial r} &= 0, & \tau(r_o, z, 0) &= f_3(z, t) \\ \tau(r, 0, t) &= f_1(r, t), & \tau(r, L, t) &= f_2(r, t) \end{aligned} \tag{4.50}$$

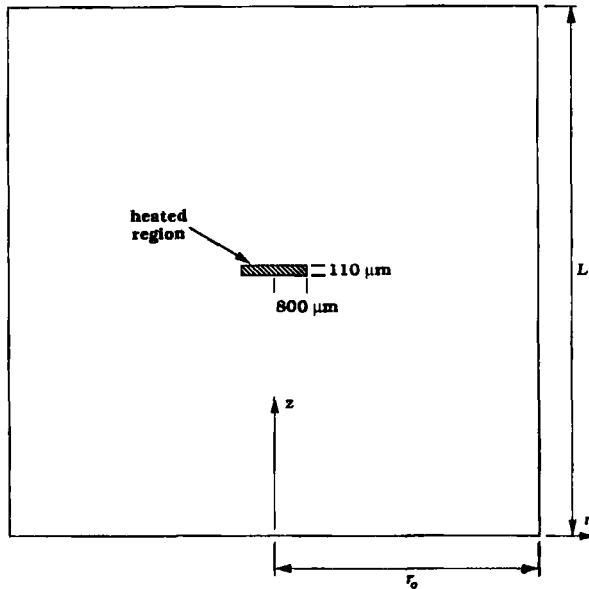


FIG. 49. Geometric system for analysis of laser irradiation onto the retina. The irradiation is symmetric with the z axis. (Redrawn from Wissler [223, Fig. 1, p. 208], © 1976 IEEE.)

Alternatively, for a heat flux at the outer radial surface of the system,

$$\begin{aligned} \tau(r, z, 0) &= f_0(r, z) \\ \frac{\partial \tau(0, z, t)}{\partial r} &= 0, \quad k_r \frac{\partial \tau(r_o, z, t)}{\partial r} + h\tau(r_o, z, t) = 0 \quad (4.51) \\ \tau(r, 0, t) &= f_1(r, t), \quad \tau(r, L, t) = f_2(r, t) \end{aligned}$$

Lin used the Hankel transform (Snedon [194]) to eliminate the r coordinate in the above formulation. This transform is defined as

$$\mathbf{H}_i[\tau(r, z, t)] \equiv \tau_i(z, t) \equiv \int_0^{r_o} r J_0(\lambda_i r) \tau(r, z, t) dr \quad (4.52)$$

in which the eigenvalues λ_i are the positive roots of $J_0(\lambda_i r_o) = 0$.

The transformed equations for the first case given above become

$$\frac{\partial \tau_i}{\partial t} = \alpha_r [\lambda_i r_o J_1(\lambda_i r_o) f_3 - \lambda_i^2 \tau_i] + \frac{\partial}{\partial z} \left[\alpha_z \frac{\partial \tau_i}{\partial z} \right] + \frac{\mathbf{Q}_i}{\rho c} \quad (4.53)$$

$$\tau_i(z, 0) = \mathbf{f}_0(\lambda_i, z), \quad \tau_i(0, t) = \mathbf{f}_1(\lambda_i, t), \quad \tau_i(L, t) = \mathbf{f}_2(\lambda_i, t) \quad (4.54)$$

where \mathbf{Q}_i is the Hankel transform of the source term, and the functions \mathbf{f} are defined as the transformed initial and boundary conditions.

Next, a finite Fourier transform was applied, as defined by

$$F_n[\tau_i(z, t)] \equiv \tau_{in}(t) \equiv \int_0^L \sin\left(\frac{n\pi z}{L}\right) \tau_i(z, t) dz \tag{4.55}$$

Application to the Hankel transformed equations yields

$$\begin{aligned} \frac{\partial \tau_{in}}{\partial t} = & \alpha_r [\lambda_i r_o J_1(\lambda_i r_o) \mathbf{f}_3 - \lambda_i^2 \tau_{in}] + \frac{\alpha_z n\pi}{L} [(-1)^{n+1} \mathbf{f}_2 + \mathbf{f}_1] \\ & - \frac{\alpha_z n^2 \pi^2}{L^2} \tau_{in} + \frac{Q_{in}}{\rho c} \end{aligned} \tag{4.56}$$

$$\tau_{in}(0) = \mathbf{f}'_0(0) \tag{4.57}$$

and \mathbf{f}'_0 is the double transformed initial condition.

The solution to this problem was obtained by the Laplace transform method and a series of subsequent inverse transforms to obtain the following expressions for the two cases evaluated. For a specified temperature at the outer radial boundary

$$\begin{aligned} \tau(r, z, t) = & \frac{4}{Lr_o^2} \sum_{n=1}^{\infty} \sum_{i=1}^{\infty} \frac{J_0(\lambda_i r_o) \sin(n\pi z/L) \exp[-(\alpha_r \lambda_i + \alpha_z n^2 \pi^2/L^2)t]}{J_1^2(\lambda_i r_o)} \\ & \cdot \int_0^L \int_0^{r_o} r f_0(r, z) J_0(\lambda_i r_o) \sin \frac{n\pi z}{L} dr dz \\ & + \frac{4}{\rho c L r_o^2} \sum_{n=1}^{\infty} \sum_{i=1}^{\infty} \frac{J_0(\lambda_i r_o) \sin(n\pi z/L)}{J_1^2(\lambda_i r_o)} \int_0^t \int_0^{r_o} \int_0^L r Q(r, z, t) J_0(\lambda_i r_o) \\ & \cdot \sin \frac{n\pi z}{L} \exp \left[-\left(\alpha_r \lambda_i + \frac{\alpha_z n^2 \pi^2}{L^2} \right) (t - \lambda) \right] dr dz d\lambda \\ & + \frac{4\alpha_z n\pi}{L^2 r_o^2} \sum_{n=1}^{\infty} \sum_{i=1}^{\infty} \frac{J_0(\lambda_i r_o) \sin(n\pi z/L)}{J_1^2(\lambda_i r_o)} \\ & \cdot \int_0^t \int_0^{r_o} [(-1)^{n+1} f_2(r, \lambda) + f_1(r, \lambda)] J_0(\lambda_i r_o) \\ & \cdot \exp \left[-\left(\alpha_r \lambda_i + \frac{\alpha_z n^2 \pi^2}{L^2} \right) (t - \lambda) \right] dr d\lambda \\ & + \frac{4\alpha_r}{L r_o} \sum_{n=1}^{\infty} \sum_{i=1}^{\infty} \lambda_i \frac{J_0(\lambda_i r_o) \sin(n\pi z/L)}{J_1(\lambda_i r_o)} \int_0^t \int_0^L f_3(z, \lambda) \sin \frac{n\pi z}{L} \\ & \cdot \exp \left[-\left(\alpha_r \lambda_i + \frac{\alpha_z n^2 \pi^2}{L^2} \right) (t - \lambda) \right] dz d\lambda \end{aligned} \tag{4.58}$$

In the case of a heat flux specified at the outer radial boundary, the eigenvalues satisfy the transcendental equation

$$\lambda_i J_1(\lambda_i r_o) - h J_0(\lambda_i r_o) = 0 \quad (4.59)$$

which leads to the following solution:

$$\begin{aligned} \tau(r, z, t) = & \frac{4}{L r_o^2} \sum_{n=1}^{\infty} \sum_{i=1}^{\infty} \frac{\lambda_i^2 J_0(\lambda_i r_o) \sin(n\pi z/L) \exp[-(\alpha_r \lambda_i + \alpha_z n^2 \pi^2/L^2)t]}{(h^2 + \lambda_i^2) J_0^2(\lambda_i r_o)} \\ & \cdot \int_0^L \int_0^{r_o} r f_0(r, z) J_0(\lambda_i r_o) \sin \frac{n\pi z}{L} dr dz \\ & + \frac{4}{\rho c L r_o^2} \sum_{n=1}^{\infty} \sum_{i=1}^{\infty} \frac{\lambda_i^2 J_0(\lambda_i r_o) \sin(n\pi z/L)}{(h^2 + \lambda_i^2) J_0^2(\lambda_i r_o)} \int_0^t \int_0^{r_o} \int_0^L r Q(r, z, t) J_0(\lambda_i r_o) \\ & \cdot \sin \frac{n\pi z}{L} \exp \left[- \left(\alpha_r \lambda_i + \frac{\alpha_z n^2 \pi^2}{L^2} \right) (t - \lambda) \right] dr dz d\lambda \\ & + \frac{4\alpha_z n\pi}{L^2 r_o^2} \sum_{n=1}^{\infty} \sum_{i=1}^{\infty} \frac{\lambda_i^2 J_0(\lambda_i r_o) \sin(n\pi z/L)}{(h^2 + \lambda_i^2) J_0^2(\lambda_i r_o)} \\ & \cdot \int_0^t \int_0^{r_o} [(-1)^{n+1} f_2(r, \lambda) + f_1(r, \lambda)] J_0(\lambda_i r_o) \\ & \cdot \exp \left[- \left(\alpha_r \lambda_i + \frac{\alpha_z n^2 \pi^2}{L^2} \right) (t - \lambda) \right] dr d\lambda \\ & + \frac{4\alpha_r}{L r_o} \sum_{n=1}^{\infty} \sum_{i=1}^{\infty} \lambda_i \frac{\lambda_i^2 J_0(\lambda_i r_o) J_1(\lambda_i r_o) \sin(n\pi z/L)}{(h^2 + \lambda_i^2) J_0^2(\lambda_i r_o)} \int_0^t \int_0^L f_3(z, \lambda) \sin \frac{n\pi z}{L} \\ & \cdot \exp \left[- \left(\alpha_r \lambda_i + \frac{\alpha_z n^2 \pi^2}{L^2} \right) (t - \lambda) \right] dz d\lambda \quad (4.60) \end{aligned}$$

Although Lin provided no computation examples to demonstrate the utility of his analytical solutions, the basic method of analysis he developed was subsequently refined, expanded upon, and used to demonstrate for the first time a number of important characteristics of the thermal interaction of laser irradiation with living tissues.

Wissler also used analytical methods to obtain an expression for the transient temperature field in the retina during laser irradiation (Wissler [223]). His analysis treated the effects of several parameters including multiple absorbing layers, each having distinct thermal and optical properties, thermal interaction between the irradiated tissue and blood perfusion,

and time variation in the intensity of the irradiation source. Thus, Wissler was able to demonstrate that the advantages of an analytical solution can be made to incorporate many of the practical characteristics encountered in laser-tissue interactions.

The problem addressed by Wissler assumed a symmetrical light source directed onto the eye for which absorption was concentrated serially in the pigment epithelium and choroid. Variations of the beam radius at the anterior surface of the pigment epithelium were considered over the range $5 \mu\text{m}$ to 3mm . The dimensions of the heated and surrounding regions are shown in Fig. 49 in a cylindrical coordinated system. The problem statement is presented as

$$\rho c \frac{\partial \tau}{\partial t} = \frac{1}{r} \frac{\partial}{\partial r} \left[kr \frac{\partial \tau}{\partial r} \right] + \frac{\partial}{\partial z} \left[k \frac{\partial \tau}{\partial z} \right] + Q(r, z, t) - \omega(z) \rho c \tau \quad (4.61)$$

$$\tau(r, z, 0) = 0$$

$$\frac{\partial \tau(0, z, t)}{\partial r} = 0, \quad \tau(r_o, z, t) = 0 \quad (4.62)$$

$$\tau(r, 0, t) = 0, \quad \tau(r, L, t) = 0$$

The equations are written in terms of the temperature rise τ owing to heating by the source Q , and the region under consideration is large enough so that for the period of analysis the thermal effects of the irradiation are not propagated to the boundary. Blood perfusion in the tissue is represented by the term ω such that there is a convective effect within the tissue that is uniform at the macroscopic scale of analysis that is proportional to the rise in temperature above the initial value.

This problem was solved by Wissler via the application of finite transforms, including in order the Hankel transform \mathbf{H} and one defined by himself \mathbf{W} . The Hankel transform was defined previously in Eq. (4.52), and the inverse function is given as

$$\tau(r, z, t) = \frac{2}{r_o^2} \sum_{i=1}^{\infty} \tau_i(z, t) \frac{J_0(\lambda_i r)}{J_1(\lambda_i r_o)^2} \quad (4.63)$$

The Hankel transform of Eqs. (4.61) and (4.62) issues in the following results:

$$\rho c \frac{\partial \tau_i}{\partial t} = -k \lambda_i^2 \tau_i + \frac{\partial}{\partial z} \left[k \frac{\partial \tau_i}{\partial z} \right] + \mathbf{Q}_i - \omega \rho c \tau_i \quad (4.64)$$

$$\tau_i(z, 0) = 0, \quad \tau_i(0, t) = 0, \quad \tau_i(L, t) = 0 \quad (4.65)$$

The Wissler transform is defined as

$$\mathbf{W}_i[\tau_i(z, t)] \equiv \theta_{ij}(t) \equiv \int_0^L \rho c p(\xi_{ij}, z) \tau_i(z, t) dz \quad (4.66)$$

in which $p(\xi_{ij}, z)$ satisfies the equations

$$\frac{d}{dz} \left[k \frac{dp}{dz} \right] - [k\lambda_i^2 + \omega \rho c - \rho c \xi_{ij}] p = 0$$

$$p(\xi_{ij}, 0) = 0, \quad p(\xi_{ij}, L) = 0 \quad (4.67)$$

with the inverse transform

$$\tau_i(z, t) = \sum_{j=1}^{\infty} \frac{\theta_{ij}(t) p(\xi_{ij}, z)}{N_{ij}} \quad (4.68)$$

with the function N_{ij} defined by

$$N_{ij} = \int_0^L \rho c p(\xi_{ij}, z)^2 dz \quad (4.69)$$

Application of the Wissler transform serially to the Hankel transform equations issues in the following formulation of the boundary value problem:

$$\frac{d\theta_{ij}}{dt} = -\xi_{ij} \theta_{ij} + \mathbf{Q}_{ij} \quad (4.70)$$

in which

$$\mathbf{Q}_{ij} = \int_0^L \mathbf{Q}_i(z, t) p(\xi_{ij}, z) dz \quad (4.71)$$

and the initial condition is given by

$$\mathbf{Q}_{ij}(0) = 0 \quad (4.72)$$

Wissler obtained the solutions for several different cases pertaining to specific definitions of the source function. Two will be discussed here: a constant source of illumination persisting for a defined duration of time, following which it is reduced to zero in a step-wise manner; and a short pulse of illumination. Of particular interest to practical laser applications is an extension of the latter case in which the pulse is repeated with constant time intervals between serial pulses. These source functions will be considered in order.

First, the irradiation will be modeled as constant for a period of time, t_p , after which the intensity goes to zero. It is desirable to know the continuous thermal history in the tissue starting with the commencement of irradiation.

The source is described as a function of position in radial and coordinates:

$$\begin{aligned} \mathbf{Q}(r, z) &= R(r)Z(z), & 0 < t < t_p \\ \mathbf{Q}(r, z) &= 0, & t_p < t \end{aligned} \tag{4.73}$$

The transformed expressions for the source function are

$$\mathbf{Q}_i = Z(z) \int_0^{r_0} r J_0(\lambda_i r) R(r) dr, \quad 0 < t < t_p \tag{4.74}$$

$$\mathbf{Q}_i = 0, \quad t_p < t$$

$$\mathbf{Q}_{ij} = \int_0^L Z(z) p(\xi_{ij} z) dz \int_0^{r_0} r J_0(\lambda_i r) R(r) dr \equiv \mathbf{Q}_{ij}^*, \quad 0 < t < t_p \tag{4.75}$$

$$\mathbf{Q}_{ij} = 0, \quad t_p > t$$

As a consequence,

$$\theta_{ij} = \frac{\mathbf{Q}_{ij}^*}{\xi_{ij}} [1 - \exp(-\xi_{ij} t)], \quad 0 < t < t_p$$

$$\theta_{ij} = \frac{\mathbf{Q}_{ij}^*}{\xi_{ij}} [1 - \exp(-\xi_{ij} t_p)] [\exp\{-\xi_{ij}(t - t_p)\}], \quad t_p < t \tag{4.76}$$

When t_p is large enough, $(\xi_{ij} t_p) > 4$ and a steady state will be approached.

$$\tau(r, z, t) \rightarrow \frac{2}{r_0^2} \sum_{i=1}^{\infty} \frac{J_0(\lambda_i r)}{J_1(\lambda_i r_0)^2} \sum_{j=1}^{\infty} p(\xi_{ij} t) \frac{\mathbf{Q}_{ij}^*}{\xi_{ij} N_{ij}} \tag{4.77}$$

For the initial stage of the heating process,

$$1 - \exp(-\xi_{ij} t) \approx \xi_{ij} t \tag{4.78}$$

and

$$\theta_{ij} \approx \mathbf{Q}_{ij}^* t \tag{4.79}$$

which results in

$$\tau(r, z, t) \approx \frac{2t}{r_0^2} \sum_{i=1}^{\infty} \frac{J_0(\lambda_i r)}{J_1(\lambda_i r_0)^2} \sum_{j=1}^{\infty} p(\xi_{ij} t) \frac{\mathbf{Q}_{ij}^*}{N_{ij}} \tag{4.80}$$

Note that this expression is simply t times the series expansion for $Q/\rho c$, and therefore the initial increase in temperature is linear and proportional to the local rate of heat deposition divided by the local heat capacity.

If the irradiation occurs as a short pulse of duration t_p ,

$$1 - \exp(-\xi_{ij} t_p) \approx \xi_{ij} t_p \tag{4.81}$$

and

$$\theta_{ij} \approx \mathbf{Q}_{ij}^* t_p \exp[-\xi_{ij}(t - t_p)], \quad t_p < t \tag{4.82}$$

Thus,

$$\tau(r, z, t) \approx \frac{2t_p}{r_0^2} \sum_{i=1}^{\infty} \frac{J_0(\lambda_i r)}{J_1(\lambda_i r_0)^2} \sum_{j=1}^{\infty} p(\xi_{ij} t) \frac{Q_{ij}^* \exp[-\xi_{ij}(t - t_p)]}{N_{ij}} \quad (4.83)$$

This result can be used to describe a series of $n + 1$ short laser pulses by representing the pulses as a series of Dirac delta functions, such that if Δt is the time increment between pulses

$$Q_{ij}^*(t) = Q_{ij}^* t_p \sum_{k=0}^n \delta(t - k \Delta t) \quad (4.84)$$

If $n \Delta t < t < (n + 1) \Delta t$,

$$\begin{aligned} \theta_{ij}(t) &= Q_{ij}^* t_p \int_0^t \sum_{k=0}^n \delta(t - k \Delta t) \exp[-\xi_{ij}(t - t')] dt' \\ &= Q_{ij}^* t_p \sum_{k=0}^n \exp[-\xi_{ij}(t - k \Delta t)] \\ &= Q_{ij}^* t_p \exp[-\xi_{ij}(t - n \Delta t)] \sum_{k=0}^n \exp[-\xi_{ij} k \Delta t] \end{aligned} \quad (4.85)$$

For a very long series of pulses, $n \rightarrow \infty$, and

$$\sum_{k=0}^n \exp[-\xi_{ij} k \Delta t] \rightarrow [1 - \exp(-\xi_{ij} \Delta t)]^{-1} \quad (4.86)$$

so that

$$\theta_{ij}(t_n^+) \rightarrow Q_{ij}^* t_p [1 - \exp(-\xi_{ij} \Delta t)]^{-1} \quad (4.87)$$

in which t_n^+ denotes the limit as t approaches $n \Delta t$ from the right. The preceding equation shows that θ_{ij} decays exponentially during the period between pulses. Therefore, immediately prior to the subsequent pulse

$$\begin{aligned} \theta_{ij}(t_{n+1}) &\rightarrow \theta_{ij}(t_n^+) \exp(-\xi_{ij} \Delta t) \\ &= Q_{ij}^* t_p [\exp(-\xi_{ij} \Delta t) - 1]^{-1} \end{aligned} \quad (4.88)$$

From these results it is apparent that if Δt is small enough to allow the approximation of $\exp(\xi_{ij} \Delta t) - 1$ by $\xi_{ij} \Delta t$, the temperature field immediately prior to a subsequent pulse becomes the steady state field produced by steady exposure at a mean power level of $Q_p t_p / \Delta t$, where Q_p is the peak power level. For these conditions, the temperature rise is linear in time and proportional to the local value of $Q/\rho c$.

Wissler computed the transient temperature fields for a number of different temporal laser irradiation functions. It was assumed that the source strength within the absorbing region was uniform in planes perpendicular to the axis of the beam for a circle of radius 800 μm . An exponential decrease in

the source strength along the axis of irradiation was assumed according to

$$\begin{aligned}
 Q &= Q_0 \eta_1 \exp[-\eta_1(z - L_1)] & L_1 \leq z \leq L_2 \\
 &= Q_0 \eta_2 \exp[-\eta_1(L_2 - L_1) - \eta_2(z - L_2)], & L_2 \leq z \leq L_3 \\
 &= Q_0 \eta_3 \exp[-\eta_1(L_2 - L_1) - \eta_2(L_3 - L_2) - \eta_3(z - L_3)], & L_3 \leq z
 \end{aligned}
 \tag{4.89}$$

where η_1 , η_2 , and η_3 are the absorption coefficients in the pigment epithelium, choroid, and sclera, respectively, and L_1 , L_2 , and L_3 are the coordinates at the front of each of these regions. The values of these parameters used by Wissler for his calculations were $\eta_1 = 637.6 \text{ cm}^{-1}$, $\eta_2 = 76.3 \text{ cm}^{-1}$, $\eta_3 = 0, 76.3, \text{ or } 637.6 \text{ cm}^{-1}$, $L_2 - L_1 = 10 \mu\text{m}$, and $L_3 - L_2 = 100 \mu\text{m}$.

Many analyses of laser tissue interaction in the eye have assumed that only the pigment epithelium and choroid interact optically, and therefore thermally, with the incident beam. As indicated by the above coefficients, Wissler also evaluated the effect of the posterior sclera layer on the temperature rise in the retina owing to laser irradiation. Figure 50 presents a comparison of the temperature gradients produced along the axis of the beam both with and without energy absorption in the sclera. These results show clearly that the temperature rise in the eye may be underestimated significantly if absorption in the sclera is neglected. This prediction was in

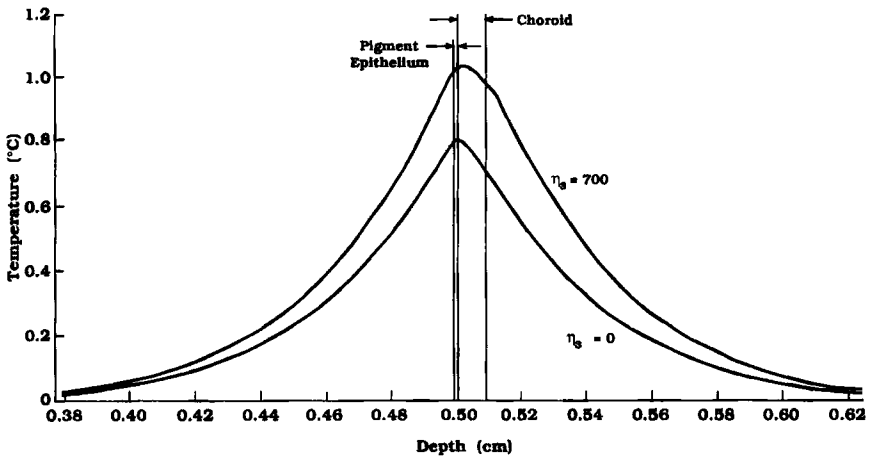


FIG. 50. Axial temperature profiles through the eye for constant irradiation lasting 1.6 s. The two curves represent no interaction between the laser beam and the sclera, $\eta_3 = 0$, and absorption in the sclera, $\eta_3 = 700 \text{ cm}^{-1}$. (Redrawn from Wissler [223, Fig. 3, p. 211], © 1976 IEEE.)

agreement with the results of prior studies (Cain and Welch [31]) in which the measured temperature rise in the retina was about 30% higher than expected based on simulations using a model in which absorption in the sclera was neglected (Mainster *et al.* [133–135]; White *et al.* [222]).

Radial temperature profiles were also computed for constant irradiation, as illustrated in Fig. 51. Three values of thermal conductivity were used for the computations to test the sensitivity of the temperature distribution to the conductivity. As anticipated, the diffusion of heat away from the absorbing region is reduced for small conductivities. A 6% change in the thermal conductivity issues in a 10% change in the centerline temperature.

The effect of blood perfusion on the temperature gradients in the eye was addressed previously by Roulier [177], suggesting that for extended periods (>0.1 s) of irradiation perfusion may have a significant effect.

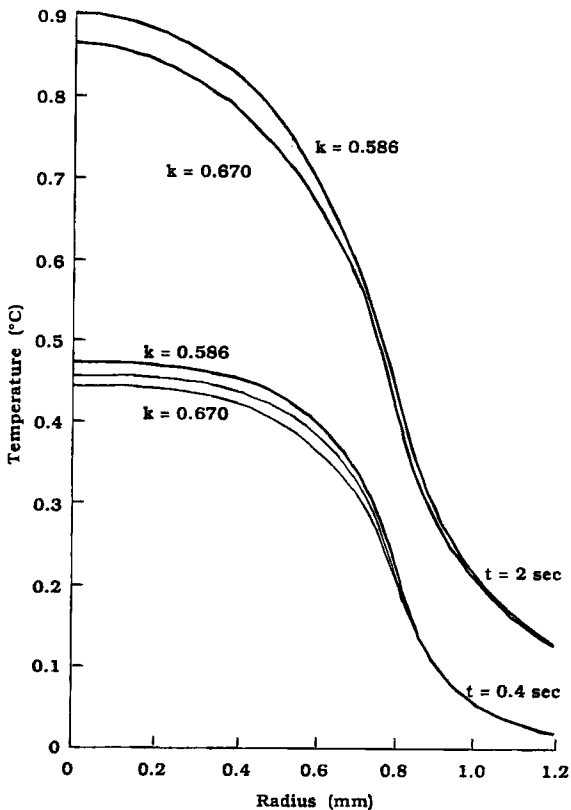


FIG. 51. Radial temperature profiles through the eye for constant irradiation. The sensitivity of the temperature distribution to the thermal conductivity is shown for $k = 0.586, 0.628,$ and 0.670 W/m·°C. (Redrawn from Wissler [223, Fig. 4, p. 212], © 1976 IEEE.)

The convective cooling effect of blood perfusion was simulated for irradiation periods between 0.1 and 1.0 s, as shown in Fig. 52. Examination of these curves indicates that the extent of the alteration to the temperature distribution by blood perfusion is dependent primarily on two parameters: the magnitude of the perfusion rate and the duration of irradiation. Blood perfusion is assumed to cool the local tissue via convective heat exchange. Wissler explained the biasing of this convective effect to the latter stages of an irradiation protocol in terms of an evaluation of the eigenvalues for a uniform system with null boundary conditions:

$$\xi_{ij}^* = \frac{k}{\rho c} [\lambda_i^2 + (j\pi/L)^2] + \omega \tag{4.90}$$

for which $\lambda_1 = 2.4048/r_o$, $\lambda_2 = 5.5201/r_o$, and $\lambda_3 = 8.6537/r_o$. The relative contributions of the various terms in Eq. (4.90) may be evaluated for typical states encountered. For example, values of $r_o = 2.5$ mm and $L = 5.0$ mm are reasonable, and the smallest value of $\lambda_i^2 + (j\pi/L)^2$ is 392.3. If the middle value for thermal conductivity of $k = 0.628$ (W/m·°C) is applied, the lower limit for the conduction terms is 0.59, and the convection term must be of a similar order of magnitude to be of importance. This

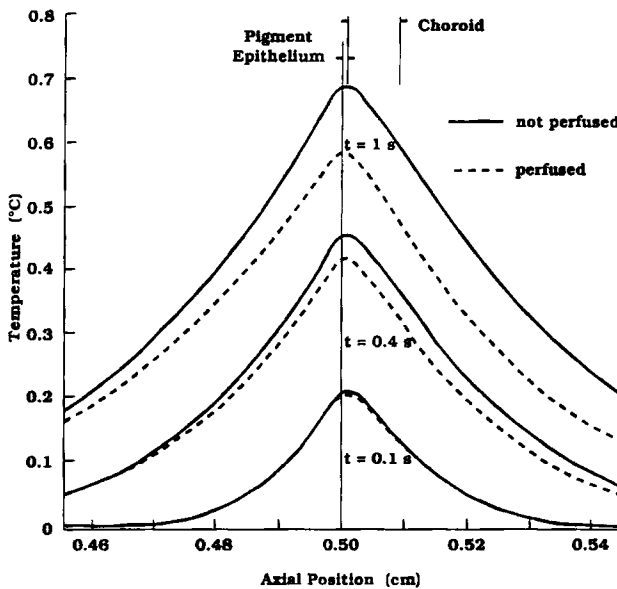


FIG. 52. Axial temperature distributions computed both with and without blood perfusion of the choroid. (Redrawn from Wissler [223, Fig. 6, p. 213], © 1976 IEEE.)

condition occurs only for the later portion of an irradiation protocol, since during the initial stages of heating the response is determined by the higher order terms, which are dominated by conduction.

The effects of a repeatedly pulsed laser source are shown in Fig. 53 for variations in the interval between serial pulses. The radial temperature profile is presented for each pulse interval, each of which is computed for the same mean power level averaged over the entire duration of the protocol. Thus, for a given mean power level, the energy delivered for each pulse is inversely proportional to the pulse rate. The curves demonstrate that for pulse rates of 1000 s^{-1} the background temperature approaches that obtained for continuous irradiation at the same mean power level. As the rate decreases, the background temperature level within the illuminated region decreases. However, the temperature distribution in the surrounding tissue is virtually identical for all protocols.

Mainster *et al.* [133–135] formulated a numerical model for the transient temperature field created by optical irradiation in a composite layered

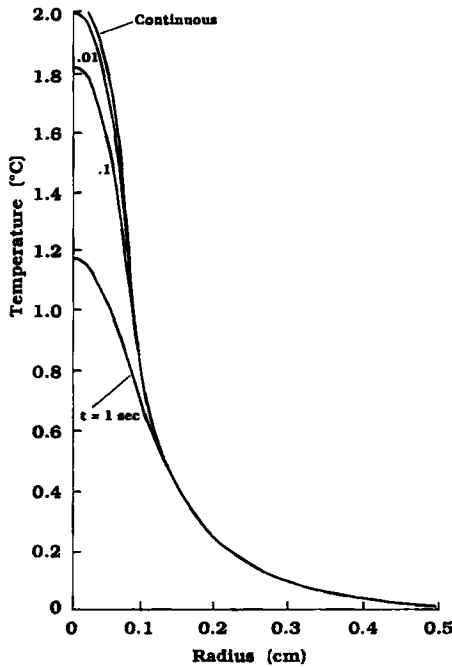


FIG. 53. Radial temperature distributions in the retina for pulsed laser illumination. Δt indicates the power-off pause between successive pulses. The mean power averaged over the total duration for each protocol is identical. (Redrawn from Wissler [223, Fig. 7, p. 214], © 1976 IEEE.)

tissue having differential thermal and optical properties, some of which may vary as a function of state, and complex morphology. The differential equation describing the temperature field was written for symmetric cylindrical coordinates:

$$\rho(z)c(z) \frac{\partial T}{\partial t} = \frac{k}{r} \frac{\partial T}{\partial r} + \frac{\partial}{\partial r} \left[k \frac{\partial T}{\partial r} \right] + \frac{\partial}{\partial z} \left[k \frac{\partial T}{\partial z} \right] + Q(r, z, t) \quad (4.91)$$

Equation (4.91) was formulated into a set of finite difference equations which could be solved for a grid appropriate to the problem of interest. To analyze the laser heating of the retina a nonlinear grid was designed in which the highest node density was centered on the region where internal light absorption would be greatest, with a progressive coarsening toward the periphery to minimize the required expenditure of computational effort. An example of the type of grid they designed is shown in Fig. 54. A Peaceman-Rachford procedure was used for the finite difference method as follows:

$$\rho(z)c(z) \frac{\partial T}{\partial t} \Big|_{i,j,k+1/2} = \frac{2\rho_i c_i}{\Delta t_k} [T_{i,j,k+1/2} - T_{i,j,k}], \quad j = 0, 1, 2, \dots, n \quad (4.92)$$

$$\Delta t_k = t_{k+1} - t_k \quad (4.93)$$

$$\frac{k}{r} \frac{\partial T}{\partial r} \Big|_{i,j,k} = \frac{k_j}{r_j} \left[\frac{T_{i,j+1,k} - T_{i,j-1,k}}{r_{j+1} - r_{j-1}} \right], \quad j = 1, 2, \dots, n - 1 \quad (4.94)$$

$$\frac{k}{r} \frac{\partial T}{\partial r} \Big|_{i,0,k} = \frac{\partial}{\partial r} \left[k \frac{\partial T}{\partial r} \right] \Big|_{i,0,k}, \quad j = 0 \quad (4.95)$$

$$\frac{\partial}{\partial r} \left[k \frac{\partial T}{\partial r} \right] \Big|_{i,j,k} = \frac{2k_j}{r_{j+1} - r_{j-1}} \left[\frac{T_{i,j+1,k} - T_{i,j,k}}{r_{j+1} - r_j} - \frac{T_{i,j,k} - T_{i,j-1,k}}{r_j - r_{j-1}} \right], \quad j = 1, 2, \dots, n - 1 \quad (4.96)$$

$$\frac{\partial}{\partial r} \left[k \frac{\partial T}{\partial r} \right] \Big|_{i,0,k} = \frac{k_j}{r_1^2} [T_{i,1,k} - T_{i,0,k}], \quad j = 0 \quad (4.97)$$

$$\begin{aligned} \frac{\partial}{\partial z} \left[k \frac{\partial T}{\partial z} \right] \Big|_{i,j,k} &= \frac{2k_j}{z_{j+1} - z_{j-1}} \left[\frac{T_{i,j+1,k} - T_{i,j,k}}{z_{j+1} - z_j} - \frac{T_{i,j,k} - T_{i,j-1,k}}{z_j - z_{j-1}} \right] \\ &+ \left[\frac{k_{j+1} - k_{j-1}}{z_{i+1} - z_{i-1}} \right] \left[\frac{T_{i+1,j,k} - T_{i-1,j,k}}{z_{i+1} - z_{i-1}} \right], \\ &j = 0, 1, 2, \dots, n \end{aligned} \quad (4.98)$$

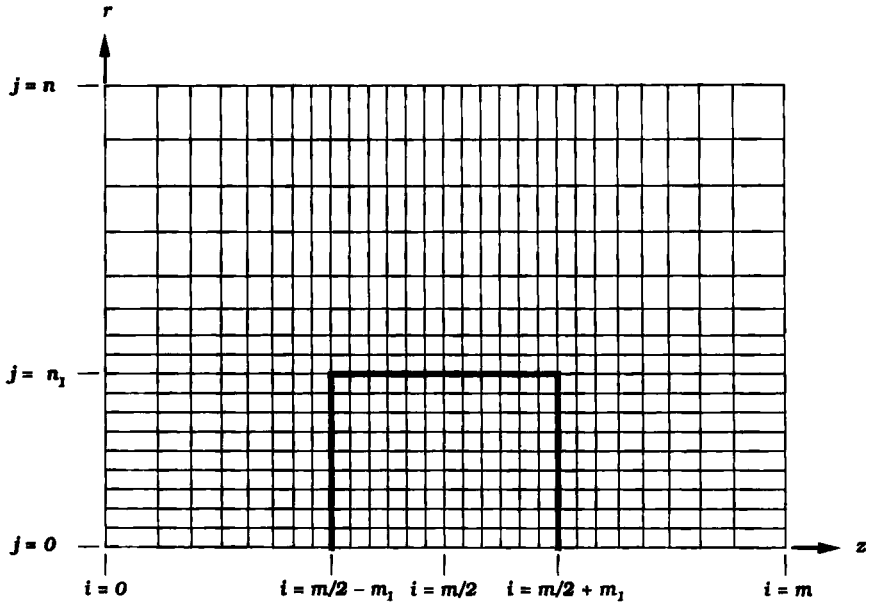


FIG. 54. Nonlinear finite difference grid for modeling transient temperature field in the retina due to a distributed internal heat source created by laser irradiation. (Redrawn from Mainster *et. al.* [135, Fig. 1, p. 305], with permission.)

The spacing of adjacent nodes on the grid shown in Fig. 54 is defined by the following relations. The central area of high resolution in which the laser irradiation occurs is defined by the area of dimensions $0 \leq z \leq n_1$ and $(m/2) - m_1 \leq r \leq (m/2) + m_1$:

$$z_{i+1} - z_i = \Delta z (\Pi_1) \left[\frac{m}{2} - m_1 - i \right], \quad 0 \leq i \leq \frac{m}{2} - m_1 - 1 \quad (4.99a)$$

$$z_{i+1} - z_i = \Delta z, \quad \frac{m}{2} - m_1 \leq i \leq \frac{m}{2} + m_1 + 1 \quad (4.99b)$$

$$z_{i+1} - z_i = \Delta z (\Pi_1) \left[i - \frac{m}{2} - m_1 + i \right], \quad \frac{m}{2} + m_1 \leq i \leq m - 1 \quad (4.99c)$$

$$r_{i+1} - r_i = \Delta r, \quad j \leq n_1 - 1 \quad (4.100a)$$

$$r_{i+1} - r_i = \Delta r (\Pi_2) [j + 1 - m_1], \quad n_1 \leq j \leq n - 1 \quad (4.100b)$$

where Π_1 and Π_2 are constant axial and radial stretching ratio constants for calculating the node spacing in the finite difference grid.

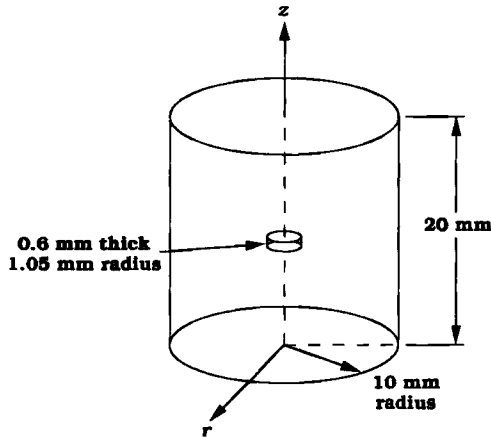


FIG. 55. Model for a uniform cylindrical heat source embedded in a homogeneous system. (Redrawn from Mainster *et al.* [135, Fig. 2, p. 308], with permission.)

This model was tested by evaluating a problem for which an analytical solution was available for comparison. The problem addressed is shown in Fig. 55, consisting of a small cylindrical heat source of uniform intensity embedded in a large homogeneous environment. The power density of the source was 41.9 W/cm^3 , and the initial temperature distribution was uniform at 0°C . The boundary was maintained constant at this same temperature during the heating process, and the thermal properties of the source volume and the surrounding medium were identical and constant at $k = 0.0586 \text{ W/m }^\circ\text{C}$, $c = 4.19 \text{ J/gm }^\circ\text{C}$, and $\rho = 10^{-6} \text{ gm/m}^3$. The analytical solution for this problem is taken from Carslaw and Jaeger [33]:

$$\begin{aligned}
 T(r, z, t) = & \frac{T_0}{4} \sqrt{\frac{\rho c}{\pi k^3}} \int_0^t \frac{dt'}{\sqrt{t-t'}} \int_{-0.03}^{+0.03} \exp\left[\frac{-(z')^2 \rho c}{4(t-t')k} dx'\right] \\
 & \cdot \int_0^{0.105} \exp\left[\frac{-(r')^2 \rho c}{4(t-t')k} r' dr'\right] \quad (4.101)
 \end{aligned}$$

The finite difference model and analytical equation were used to evaluate this problem for a number of cases designed to determine the sensitivity of several parameters of the numerical method. Table VI presents the parameter values tested for the numerical model for each case, and the resulting values calculated are presented along with the analytical solution in Table VII. These results verified the utility of a nonuniform grid to model problems for which the spatial variations in temperature gradient were large, and it defined upper limits on the relative size time steps that could

TABLE VI
PARAMETER VALUES TESTED FOR THE FINITE DIFFERENCE SOLUTION OF THE
UNIFORM CYLINDRICAL SOURCE PROBLEM^a

Case	Π_1	Π_2	m	n	Δr (mm)	Δz (mm)	Time step sequence (s)
I	1	1	100	100	0.20	0.10	0.001, 0.01, 0.1, 1, 10, 100, ...
II	1	1	100	100	0.20	0.10	0.005, 0.01, 0.02, 0.05, 0.1, 0.2, ...
III	1	1	100	100	0.20	0.10	0.05, 0.1, 0.2, 0.5, 1, 2, 5, 10, ...
IV	1	1	100	100	0.20	0.10	0.5, 1, 2, 5, 10, 20, 50, ...
V	1	1	32	32	0.60	0.30	0.005, 0.01, 0.02, 0.05, 0.1, 0.2, ...
VI	1.1	1.06	100	50	0.05	0.10	0.005, 0.01, 0.02, 0.05, 0.1, 0.2, ...

^a From Mainster *et al.* [135], with permission.

TABLE VII
COMPARISON OF ANALYTICAL AND NUMERICAL VALUES FOR TEMPERATURE RISE FOR THE
UNIFORM CYLINDRICAL SOURCE PROBLEM FOR VARIOUS COMBINATIONS OF
MODEL PARAMETERS AS DEFINED IN TABLE VI^a

Time steps (s)	Case (°C)						Analytical solution
	I	II	III	IV	V	VI	
1×10^{-3}	0.0096						0.0100
2×10^{-3}							0.0200
5×10^{-3}		0.0498			0.0499	0.0498	0.0500
1×10^{-2}	0.100	0.100			0.0966	0.100	0.100
2×10^{-2}		0.200			0.198	0.200	0.200
5×10^{-2}		0.495	0.494		0.490	0.498	0.498
1×10^{-1}	0.970	0.972	0.971		0.963	0.978	0.979
2×10^{-1}		1.85	1.85		1.85	1.84	1.83
5×10^{-1}		3.94	3.94	4.00	4.16	3.86	3.84
1×10^0	6.47	6.29	6.29	6.32	6.99	6.15	6.12
2×10^0		9.04	9.04	9.03	10.3	8.87	8.90
5×10^0		12.5	12.5	12.5	14.1	12.3	12.1
1×10^1	15.1	14.4	14.4	14.4	16.1	14.2	14.1
2×10^1		16.0	16.0	16.0	17.7	15.7	15.7
5×10^1		17.4	17.4	17.1	19.1	17.2	17.1
1×10^2	18.3	18.1	18.1	18.1	19.8	17.9	17.8
2×10^2		18.5	18.5	18.5	20.3	18.4	18.3
5×10^2		18.7	18.7	18.7	20.4	18.7	18.8
1×10^3	18.7	18.7	18.7	18.7	20.4	18.7	19.0

^a From Mainster *et al.* [135], with permission.

be applied to maintain accuracy in the solution. This approach was adopted directly for further analysis of laser irradiation of tissues (White *et al.* [222]; Preibe and Welch [166, 167]), plus the effects of blood flow on the temperature distribution were added (Welch *et al.* [221]).

Mainster *et al.* [134] also used their model to investigate the effects of differing internal source strength and distribution functions on the temperature field created in the retina. Figures 56 and 57 illustrate the irradiance and heat source strength profiles for uniform and Gaussian laser beam profiles projected onto the retina. The beams are assumed to be circularly symmetric, and the source strength patterns are discontinuous due to the differential absorption properties of the tissue layers in the retina. The absorption patterns issued in axial heat source strength distributions in the pigment epithelium and choroid as described by the following relations, where 1 and 2 denote the pigment epithelium and choroid, respectively:

$$Q_1(r, z) = b(r)I_o\eta_1 \exp[-\eta_1 z] \tag{4.102}$$

and

$$Q_2(r, z) = b(r)I_o\eta_2 \exp[d_1(\eta_2 - \eta_1) - \eta_1 z] \tag{4.103}$$

The radial irradiation patterns for the uniform and Gaussian distributions are given respectively by

$$b(r) = 1, \quad (r \leq r_L); \quad b(r) = 0, \quad (r > r_L) \tag{4.104}$$

and

$$b(r) = \exp\left[-\frac{r^2}{2\sigma^2}\right] \tag{4.105}$$

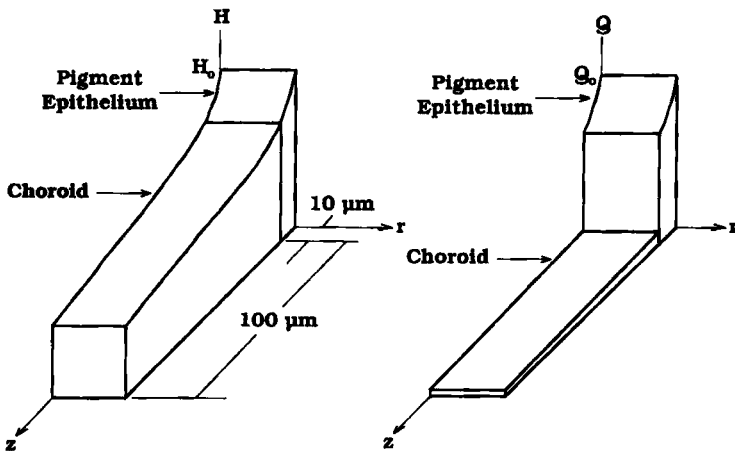


Fig. 56. Irradiance and heat source strength axial and radial distribution in the retina for a uniform image. (Redrawn from Mainster *et al.* [134, Fig. 1, p. 265], with permission.)

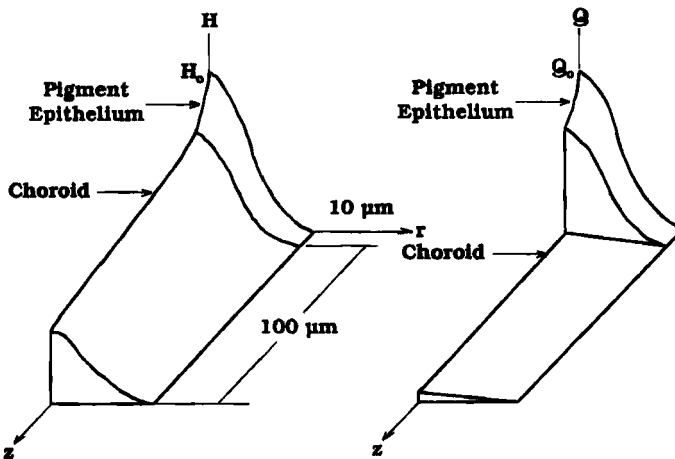


FIG. 57. Irradiance and heat source strength axial and radial distribution in the retina for an image having a Gaussian radial function. (Redrawn from Mainster *et al.* [134, Fig. 2, p. 265], with permission.)

Mainster *et al.* [134] calculated the temperature distributions in the retina for a step pulse of irradiation of duration 1.5×10^{-4} s at a wavelength of 700 nm, for which the absorption coefficients in the pigment epithelium and choroid are $\eta_1 = 310 \text{ cm}^{-1}$ and $\eta_2 = 53 \text{ cm}^{-1}$. The image dimensions for the two beam profiles were set at $r_L = 100 \mu\text{m}$ and $\sigma = 100 \mu\text{m}$. The axial temperature distribution in the retina at various times during and subsequent to the termination of irradiation is shown in Fig. 58. The temperature rise is normalized to the source strength of the incident irradiation. The curves for only a uniform beam are shown since there is very little difference with the temperature field produced by a Gaussian beam along the axis of irradiation. The nonhomogeneous deposition of power as depicted in Fig. 56 is clearly reflected in the temperature distribution during the irradiation. Subsequently, with the evolution of time, heat diffuses from the hot spot by conduction. Increments in the temperature rise in the absorbing media become proportionally smaller at increasing times as conduction to surrounding tissues is more significant. Interestingly, after termination of the irradiation the temperature continues to rise at some locations in the choroid, which has a relatively low coefficient of absorption, due to the diffusion of heat from the adjacent pigment epithelium where the temperature is higher. Radial temperature distributions for the two beam patterns are shown in Fig. 59 both during and following irradiation. The temperature profiles closely follow the patterns of energy deposition depicted in Fig. 57 for short irradiation

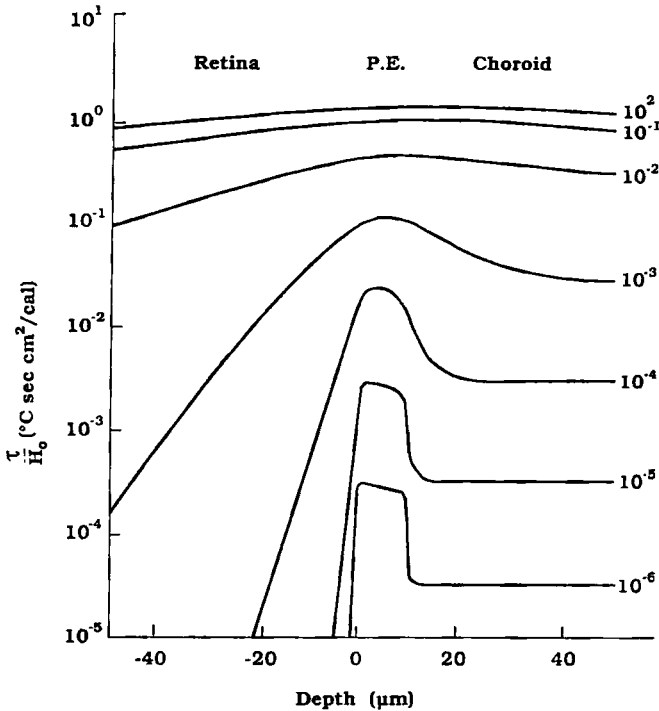


FIG. 58. Temperature rise along the axis of illumination in the retina at various times (s) (a) during and (b) following a 10^{-4} s pulse with a uniform intensity laser. (Redrawn from Mainster *et al.* [134, Fig. 5, p. 266], with permission.)

periods, subsequent to which extensive diffusion is observed. Diffusion of heat into the surrounding tissue occurs more slowly for the Gaussian than for the uniform deposition profile, for which the gradients created are larger.

Takata also developed a model for the temperature distribution during the laser irradiation of tissue; the subject of interest in his model was blood perfused skin (Takata *et al.* [203]). In addition, he considered the effect of phase change of water from liquid to vapor. The laser image was assumed to be cylindrically symmetric. Thus, Eq. (4.91) was applicable to describe the temperature function, with the addition of specific energy terms to account for the effects of blood flow and evaporation:

$$\rho(z)c(z)\frac{\partial T}{\partial t} = \frac{k}{r}\frac{\partial T}{\partial r} + \frac{\partial}{\partial r}\left[k\frac{\partial T}{\partial r}\right] + \frac{\partial}{\partial z}\left[k\frac{\partial T}{\partial z}\right] + Q(r, z, t) - \Lambda - \omega(z)(T - T_a) \tag{4.106}$$

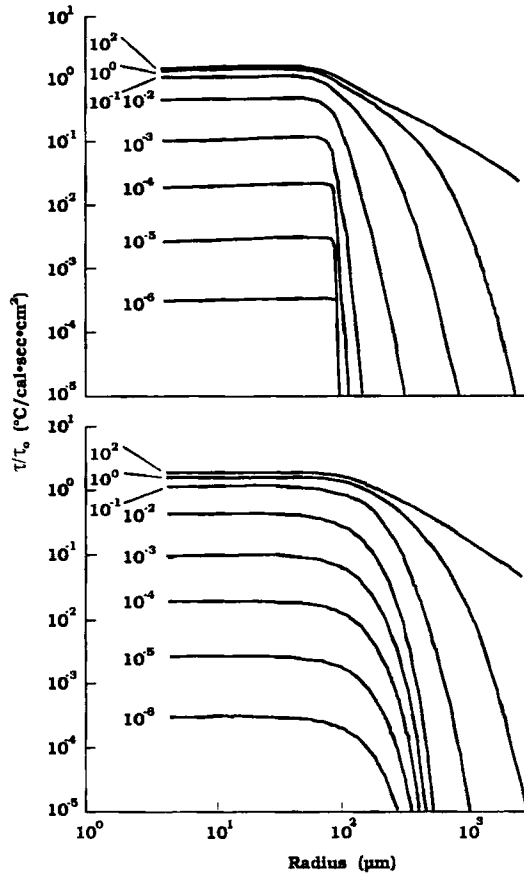


FIG. 59. Radial temperature distributions, normalized to the source strength, at $1 \mu\text{m}$ behind the front of the pigment epithelium (a) during and (b) following a 10^{-4} s pulse via laser beams having uniform and Gaussian radial distributions. (Redrawn from Mainster *et al.* [134, Fig. 6, p. 266], with permission.)

The convective heat exchange between tissue and blood perfused through the microvascular bed is accounted for by the term $\omega(z)(T - T_a)$. In this expression the distribution of microvascular perfusion is assumed to be locally homogeneous, but to vary with macroscopic position z within the skin. The magnitude of heat transfer is proportion to the difference between the temperatures of blood entering the microvascular bed from feeder arterioles, T_a , and the local tissue, T , in that the blood and tissue are assumed to come to thermal equilibrium within the bed. This assumption has been verified subsequently by others (Chato [36]).

The deposition of energy in the tissue owing to the laser irradiation is assumed to follow a pattern defined by Beer's law, resulting in an attenuation with depth into the absorbing layers of the retina as described by

$$a(r, z, t) = a(r, 0, t) \exp\left[-\int_0^z \eta(r) dz\right] \quad (4.107)$$

Simultaneously with the laser irradiation the tissue is cooled by a convective exchange with the environment, which is represented by the standard expression:

$$\frac{\partial T(r, 0, t)}{\partial z} = -\frac{h}{k} [T(r, 0, t) - T_e] \quad (4.108)$$

The magnitude of the effective convective heat transfer coefficient is dependent on whether a layer of sweat is present. Further, the formation of a blister layer on the surface of the skin will have a significant influence on heat transfer between underlying tissue and the environment. The blister will contribute both a thermal resistance to the diffusion of heat and a latent heat due to the evaporation of fluid, although Takata ignored the latter phenomenon.

In recent years as the applications of lasers to medicine and biology have become more widespread and refined and as lasers with higher power intensity, shorter pulse durations, and a broader spectrum of wavelengths have become available commercially, there has become a greater concern for implementing models to accurately understand the thermal response of living tissues to laser irradiation (e.g., Welch *et al.* [219, 220]; Choeng and Welch [40]). The parallel development of new and more accurate experimental methods for acquiring and analyzing data for the optical and thermal phenomena that govern the processes of laser tissue interaction has led to the realization that models must incorporate a higher degree of sophistication and specificity than has been available previously in order to answer critical questions in this rapidly growing field. Reviews by Welch [215, 216] have addressed the thermal aspects of many of these issues, and the remainder of the present review will be used to summarize these results and to discuss further subsequent developments.

A significant advantage of the laser as a means of depositing energy into biological tissue derives from the fact that different tissues have quite distinct absorption properties that are highly wavelength dependent. Thus, by selecting a specific laser source it is possible to tune an irradiation protocol to cause heating to be biased toward certain targeted structures in a tissue. For example, as a consequence, it is possible to coagulate vessels lying deep within the skin, while causing minimal damage to overlying

epidermal and dermal elements (Anderson and Parrish [4]). However, developing methods of analysis able to address these processes accurately presents a correspondingly greater challenge to the modeler.

A further consideration arises from the fact that the optical interaction between laser irradiation and tissues does not follow the simple Beer's law absorption relationship that has traditionally been assumed for the energy deposition term in thermal models (Motamedi *et al.* [149]). Light that enters a tissue may be absorbed, transmitted, and/or scattered, depending on the properties of the tissue and the wavelength of the light. The proportions of scattered light that are eventually transmitted backward or forward or are absorbed depend on internal reflectances and the absorption characteristics of the medium. The analysis of illumination processes involving multiple reflections has been addressed in terms of the theory presented by Kubelka [120, 121].

When laser irradiation occurs in the visible and near-infrared wavelengths scattering interactions become dominant since incident light may penetrate several millimeters into a tissue. Under this mode of action, the decrease in light intensity with depth may still follow an exponential function in accordance with Beers' law, but the distribution results from a combination of direct absorption and random scattering. This phenomenon can be represented as (Welch [215])

$$I(z) = I_0 \exp(-\chi z) \quad (4.109)$$

where I_0 is the intensity of light incident at the surface, and the absorption, η , scattering, χ , and attenuation, κ , coefficients of the tissue are related by

$$\kappa = \eta + \chi \quad (4.110)$$

The heat deposition term in the energy equation can then be written as

$$Q(r, z) = \frac{\partial[\eta I(r, z)]}{\partial z} \quad (4.111)$$

The component of the radiation entering the tissue, given by $[\chi I(r, z)]$, does not contribute to the heating effect since it is not absorbed. The function $I(r, z)$ can be estimated from an analysis of the scattering and propagation of light as a function of the optical properties of the tissue. For example, the Kubelka-Munk two-flux theory for light distribution in tissue (Kubelka [120]) predicts that the absorption and scattering of a diffuse flux in a turbid medium issues in an intensity distribution of a Gaussian beam defined at the surface by

$$I_0(r, z = 0) = I_0 \exp[-r^2/2\sigma^2] \quad (4.112)$$

that at a depth z in the medium is reduced to

$$I(r, z) = I_0 \exp[-r^2/2\sigma^2] \exp[-z\sqrt{2\eta(2\eta + 4\chi)}] \quad (4.113)$$

This expression would then be used in Eq. (4.111) to specify the heat source term in a transient diffusion equation for determining the temperature distribution.

As an example of the use of this approach, van Gemert *et al.* [209] obtained values for the absorption and scattering parameters *in vitro* human arterial wall and plaque at a series of laser wavelengths, as shown in Table VIII. This small amount of data illustrates clearly the large variations that can occur in the optical properties of tissue as a function of specimen and wavelength. An important application of this type of data is the analysis of laser angioplasty processes (Welch *et al.* [220]). Figure 60 shows the collimated, diffuse, and total contributions to the irradiance computed along the laser beam center for the indicated absorption and scattering coefficients. For this case, about half of the heat generated in the tissue would be due to scattered, not collimated, light.

Van Gemert and Welch [210] have made a further approximation to the transient temperature rise in laser irradiated tissue by introducing time constants for radial and axial conduction of heat issuing from distributed energy absorption. This approach was introduced initially for single dimensional analysis of laser thermal effects by Anderson and Parrish [4] and Boulnois [21]. For conditions under which the laser beam diameter was is much greater than the penetration depth, i.e., $\eta\sigma \gg 1$, the heat conduction issues primarily in axial gradients; conversely, for $\eta\sigma \ll 1$, the axial gradient is small, and the radial gradient dominates (Preibe and Welch [167]). Welch and van Gemert addressed the more challenging problem for which the axial and radial gradients are of a similar order of magnitude.

Justification for invoking an approximation to the more rigorous analytical solution for the temperature rise is based on the realization that

TABLE VIII
MEASURED COEFFICIENTS OF ABSORPTION AND SCATTERING FOR THE HUMAN
VESSEL WALL AND PLAQUE AT THE INDICATED WAVELENGTHS OF ILLUMINATION^a

Tissue type	514.5 nm		633 nm		1060 nm	
	η (cm^{-1})	χ	η (cm^{-1})	χ	η (cm^{-1})	χ
Vessel wall	5.6	5.5	0.9	3.2	0.5	1.4
Plaque	9.0	9.5	1.0	6.0	0.7	1.2

^a From van Gemert *et al.* [209], with permission.

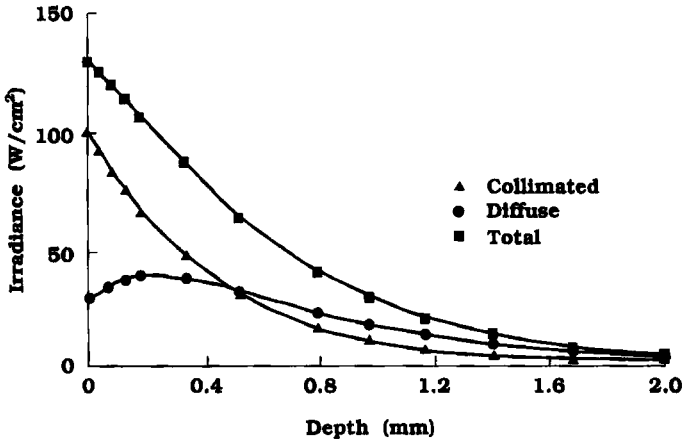


FIG. 60. Light distribution along the axis of illumination at 514.5 nm in a homogeneous tissue with both absorption and scattering. $\eta = 6.3 \text{ cm}^{-1}$ and $\chi = 16.1 \text{ cm}^{-1}$. The irradiation power was 2 W, and the beam size was 2 mm. (Redrawn from Welch *et al.* [220, Fig. 10B, p. 105], with permission.)

many processes involving laser-tissue thermal interaction may issue in dehydration, vaporization, ablation, carbonization, and/or denaturation of the medium. As a consequence, there will be gross nonlinearities in both the thermal and the optical properties upon which an analytical solution is based. Absolute confidence in the results of a model based on the assumption of constant constitutive properties must therefore be compromised. Analysis of the response of tissue to laser irradiation, especially for a combination of high intensity and short duration, in terms of the effective conduction time constants offers a simplification to the more complex analytical solution by which the physical principles governing the process may be simulated with a greater degree of relevancy to the actual tissue behavior.

The analysis was applied for only short irradiation protocols so that internal heat transport was dominated by diffusion; it was shown previously by Welch *et al.* [221] that exposure periods of greater than about 5 s are necessary in order to provide adequate time for convective exchange with blood perfused through the local microcirculation to have significant influence on the temperature distribution. Thus, the transient temperature rise is described by the basic diffusion equation (4.49):

$$\frac{\partial \tau}{\partial t} = \frac{1}{r} \frac{\partial}{\partial r} \left[\alpha_r r \frac{\partial \tau}{\partial r} \right] + \frac{\partial}{\partial z} \left[\alpha_z \frac{\partial \tau}{\partial z} \right] + \frac{Q(r, z, t)}{\rho c} \quad (4.49)$$

with the heat source written in terms of the product of the local radiation fluence rate and the absorption coefficient:

$$Q(r, z) = \eta\phi(r, z) \tag{4.114}$$

It is assumed that the temperature rise is proportional to the fluence rate for the complete process, although the dependence may be nonlinear as designated by $f(t)$:

$$\tau(r, z, t) = f(t)\phi(r, z) \quad \text{for } t \geq 0 \tag{4.115}$$

In addition, the local fluence is written as the product of two independent terms whose values are functions only of either the radial, $\mathbf{R}(r)$, or the axial, $\mathbf{Z}(z)$, coordinate:

$$\phi(r, z) = I_o\mathbf{R}(r)\mathbf{Z}(z) = I_o\Phi(r, z) \tag{4.116}$$

I_o is the incident irradiation flux onto the tissue and $\Phi(r, z)$ is a normalized fluence rate. $\tau(r, z, t)$ is assumed to have a spatial behavior such that Eq. (4.49) can be written in terms of separated variables with $\mathbf{R}(r)$ and $\mathbf{Z}(z)$ the eigenfunctions of their respective differential operators:

$$-\frac{1}{t_r}\mathbf{R}(r) = \alpha \left[\frac{d^2\mathbf{R}(r)}{dr^2} + \frac{1}{r} \frac{d\mathbf{R}(r)}{dr} \right] \tag{4.117}$$

$$-\frac{1}{t_z}\mathbf{Z}(z) = \alpha \frac{d^2\mathbf{Z}(z)}{dz^2} \tag{4.118}$$

Here $1/t_r$ and $1/t_z$ are eigenvalues. The boundary conditions are fixed by assuming a radially symmetric laser beam and negligible convective transport at the air-tissue interface. Thus,

$$\frac{d\mathbf{R}(r)}{dr} = 0 \quad \text{at } r = 0 \tag{4.119}$$

$$\frac{d\mathbf{Z}(z)}{dz} = 0 \quad \text{at } z = 0 \tag{4.120}$$

Equations (4.117) and (4.118) are solved independently to obtain

$$\mathbf{R}(r) = J_o \left(2.40 \frac{r}{r_o} \right) \tag{4.121}$$

$$\mathbf{Z}(z) = \cos \left(\frac{\pi}{2} \frac{z}{z_o} \right) \tag{4.122}$$

where r_o and z_o are the imposed limits of temperature rise and light distribution in the radial and axial directions, and the factor 2.40 in Eq. (4.121) is the first zero of the zeroth order Bessel function. These expressions for the $\mathbf{R}(r)$ and $\mathbf{Z}(z)$ functions may be substituted into Eqs. (4.117) and (4.118),

from which the radial and axial time constants are written as

$$\frac{1}{t_r} = \alpha \frac{5.76}{r_o^2} \quad (4.123)$$

$$\frac{1}{t_z} = \alpha \frac{\pi^2}{4z_o^2} \quad (4.124)$$

These relationships indicate that the time constants in both coordinates should be proportional to the ratio of the penetration depth squared over the thermal diffusivity.

If an overall time constant for the process is defined by assuming that the time constants for the radial and axial diffusion processes interact with a parallel topology as indicated by

$$\frac{1}{t} = \frac{1}{t_r} + \frac{1}{t_z} \quad (4.125)$$

then the governing partial differential equation for the heat transport process (4.49) can be written from Eqs. (4.117) and (4.118) as an ordinary differential equation:

$$\frac{d\tau(r, z, t)}{dt} = \frac{\eta\phi(r, z)}{\rho c} - \frac{\tau(r, z, t)}{t} \quad (4.126)$$

for which the solution is

$$\tau(r, z, t) = \frac{t\eta\phi(r, z)}{\rho c} \left[1 - \exp\left(-\frac{t}{t}\right) \right] \quad (4.127)$$

At large times, the solution goes to a steady state value, and the exponential term in Eq. (4.127) becomes insignificant:

$$\tau(r, z, t) = \frac{t\eta\phi(r, z)}{\rho c} \quad (4.128)$$

Van Gemert and Welch point out that if the medium is assumed to have the thermal transport properties of water, i.e., $\alpha \approx 0.18 \text{ mm}^2/\text{s}$, specific values can be calculated for the time constants associated with irradiation protocols. Thus, if the units of r_o and z_o are millimeters and of t are seconds,

$$t_r \approx 5.55 \frac{r_o^2}{5.76} \approx r_o^2 \quad (4.129)$$

$$t_z \approx 5.55 \frac{4z_o^2}{\pi^2} \approx (1.5z_o)^2 \quad (4.130)$$

$$t \approx \frac{r_o^2}{1 + r_o^2/(1.5z_o)^2} \quad (4.131)$$

A laser beam is assumed to be incident at an air-tissue interface with a defined power level and a $1/e^2$ radius of σ . The interaction dimensions of the tissue are established as

$$r_o = \sigma \tag{4.132}$$

$$z_o = 2/\kappa \tag{4.133}$$

where the attenuation coefficient along the axis of irradiation is defined for this analysis as

$$\kappa = \eta + (1 - \epsilon)\chi \tag{4.134}$$

with ϵ defined as an anisotropy coefficient for light scattering in the tissue of interest. Based on these assumptions, the time constants for an irradiation process become

$$t_r = \frac{1}{\alpha} \frac{\sigma^2}{5.76} \approx \sigma^2 \tag{4.135}$$

$$t_z = \frac{1}{\alpha} \frac{16}{\pi^2 \kappa^2} \approx (3.0/\kappa)^2 \tag{4.136}$$

$$t = \frac{1}{\alpha(2.40)^2} \left[\frac{\sigma^2}{1 + [\sigma\kappa/3.0]^2} \right] \approx \frac{\sigma^2}{1 + [\sigma\kappa/3.0]^2} \tag{4.137}$$

where the following units are used: t (s); σ (mm); κ (mm^{-1}). Finally, the spatial and temporal distributions in the temperature rise can be written as a function of the optical and thermal properties of the tissue and parameters of the laser beam upon substitution of the time constant expressions into Eq. (4.127):

$$\tau(r, z, t) = \frac{I_o \eta \Phi(r, z)}{k(2.40)^2} \left[\frac{\sigma^2}{1 + [\sigma\kappa/3.0]^2} \right] \left[1 - \exp\left(-\frac{t}{t}\right) \right] \tag{4.138}$$

Figure 61 presents a plot of the behavior described in this relationship, for which the transient temperature rise is normalized against the maximum rise that could be realized at long term steady state and is plotted as a function of time normalized to the system thermal time constant. (It should be pointed out that this reference is only a pseudo-steady state temperature rise since, as was noted above, the analysis is based on assumptions that are valid only for short periods of irradiation.) The governing equation for this figure is

$$\frac{\tau(r, z, t)}{\tau_{ss}(r, z, t)} = \left[1 - \exp\left(-\frac{t}{t}\right) \right] \exp\left(\frac{t_p - t}{t}\right) \tag{4.139}$$

for an irradiation pulse period denoted by t_p . This prediction indicates that the maximum temperature at any location within the active confines of the system will be reached in about three thermal time constants.

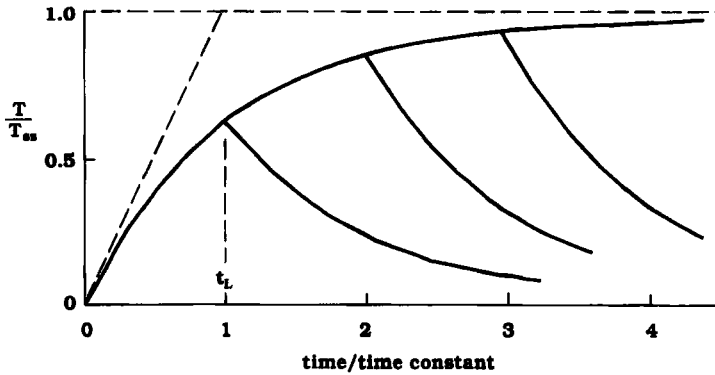


FIG. 61. Transient temperature rise at any radial and axial position within the boundaries defined by r_o and z_o . Irradiation pulse periods, t_p , of one, two, or three time constants are followed by cooling after laser power is switched off. (Redrawn from van Gemert and Welch [210, Fig. 3, p. 410], with permission.)

The time constant model was compared for three test cases with a finite difference solution to Eq. (4.49) (Welch [216]) and with a further simplified model in which thermal diffusion effects were omitted:

$$\frac{\partial \tau}{\partial t} = \frac{\eta \phi(r, z, t)}{\rho c} \quad (4.140)$$

from which

$$\tau(r, z, t) = \frac{\eta \phi(r, z, t)}{\rho c} t \quad (4.141)$$

The test cases were defined according to the following limiting conditions:

penetration depth $>$ beam radius; $z_o > r_o$

penetration depth = beam radius; $z_o = r_o$

penetration depth $<$ beam radius; $z_o < r_o$

These cases will be considered in order by specifying values for the beam parameters and tissue properties to force the required conditions.

(i) $z_o \approx 20r_o$ is achieved by setting $\sigma = 0.1$ mm, $\eta = 1$ mm $^{-1}$, and $\chi = \varepsilon = 0$, issuing in $\kappa = \eta$ and $z_o = 2/\kappa = 2$ mm. $r_o = \sigma = 0.1$ mm. The radial and axial time constants are $t_r = 10^{-2}$ s and $t_z = 9$ s, so that $t = 1.08 \times 10^{-2}$ s $\approx t_r$. The results of the three models are plotted in Fig. 62. Comparison of the three curves shows that for times smaller than 10^{-3} s the temperature rise is dominated by direct absorption from the laser, following which heat diffusion plays a progressively important role.

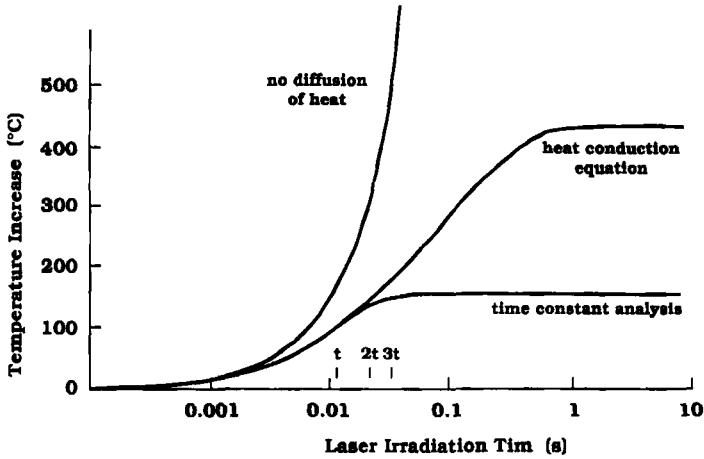


FIG. 62. Temperature rise at $r = z = 0$ during laser irradiation of a homogeneous tissue for which the time constant for radial diffusion is much more rapid than that for axial diffusion. (Redrawn from van Gemert and Welch [210, Fig. 4.a, p. 412], with permission.)

The two models that account for diffusion effects predict considerably lower temperatures, owing to the fact that absorbed energy is applied both to direct increase of temperature and to diffusion to cooler areas. Subsequently, the time constant model agrees well with the numerical solution for $t \leq 3t$, and thereafter the departure between the two curves grows rapidly. At longer irradiation times the temperature goes to a steady state value for the full thermal analysis (Eq. 4.49) that is considerably higher than the time constant analysis. This behavior issues from the fact that the actual physical dimensions of the tissue that is thermally involved in the irradiation process grows with time to become much larger than the r_o and z_o limits assumed for the time constant analysis. As the energy absorbed from the laser irradiation diffuses to a progressively larger volume of tissue, the temperature will continue to rise in the central region until a balance is achieved between the rate of deposition and diffusion to the periphery. Thus, the domain of validity for applying the simplified time constant analysis to this class of problems is defined clearly at irradiation times less than two or three time constants.

(ii) $z_o \approx r_o$ is achieved by setting $\sigma = 0.5 \text{ mm}$, $\eta = 0.6 \text{ mm}^{-1}$, $\chi = 41.4 \text{ mm}^{-1}$, and $\epsilon = 0.91$, issuing in $\kappa = 4.326 \text{ mm}^{-1}$ and $z_o = 2/\kappa = 0.46 \text{ mm}$. $r_o = \sigma = 0.5 \text{ mm}$. The thermal time constant for this system is $t = 0.179 \text{ s}$, which is more than 10 times longer than for the previous example. Figure 63 presents plots of the predicted transient temperatures for the three models. The match among the models is less close for this

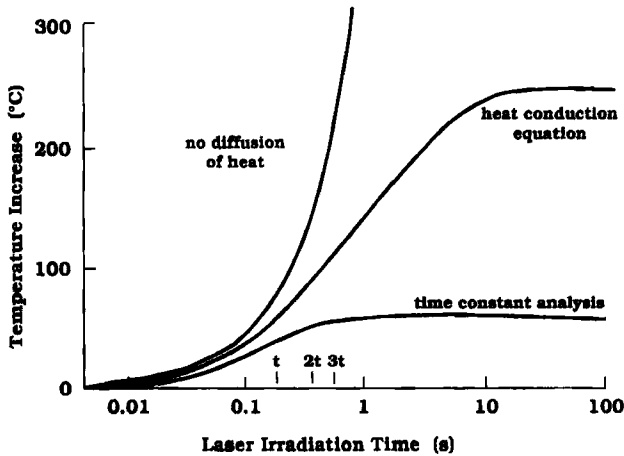


FIG. 63. Temperature rise at $r = z = 0$ during laser irradiation of a homogeneous tissue for which the time constants for radial and axial diffusion are approximately equal. (Redrawn from van Gemert and Welch [210, Fig. 4.b, p. 412], with permission.)

case, which is likely attributable to the larger volume of tissue assigned to the time constant model which will result in a broader distribution of the governing temperature gradients. Departure of the time constant approximation to the full thermal analysis becomes unacceptably large for times exceeding one or two time constants.

(iii) $5z_0 \approx r_0$ is achieved by setting $\sigma = 1$ mm, $\eta = 10$ mm⁻¹, and $\chi = \varepsilon = 0$, issuing in $\kappa = 10$ mm⁻¹ and $z_0 = 2/\kappa = 0.2$ mm. $r_0 = \sigma = 1.0$ mm. The thermal time constant for this system is $t = 0.0896$ s, and Fig. 64 presents plots of the predicted transient temperatures for the three models under these conditions. The agreement between the time constant and the full thermal analysis is acceptable to larger times for this case, that being to about three time constants.

In summary, the two-dimensional time constant approximation to the solution of the transient temperature field owing to laser irradiation of a homogeneous tissue provides a computationally simple alternative to the more rigorous analysis with the diffusion equation, which for this application requires numerical solution. The primary limitation of the technique is that it is valid only for relatively short periods of irradiation as defined by the time constants of the system for radial and axial thermal diffusion. For many applications this may not be a severe constraint since energy is delivered to the subject tissue via short pulses at high power levels in order to minimize the effects of diffusion and achieve a confined zone of response.

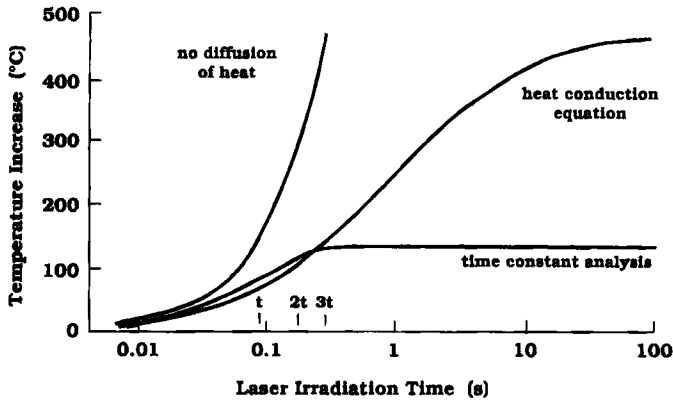


FIG. 64. Temperature rise at $r = z = 0$ during laser irradiation of a homogeneous tissue for which the time constant for axial diffusion is much more rapid than that for radial diffusion. (Redrawn from van Gemert and Welch [210, Fig. 4.c, p. 412], with permission.)

In addition, the accuracy of the time constant model is diminished for the portion of a protocol subsequent to the laser being turned off. The model has been extended recently (Çilesiz and Diller [42]) by the method of network thermodynamics (Oster *et al.* [154]; Mikulecky [146]) to more rigorously address the complete protocol. A simple four node grid was established by which the radial and axial temperature distributions resulting from irradiation with a Gaussian shaped beam could be described (Fig. 65). The fluence rate was averaged over the tissue volume associated with each node to provide for the energy source driving the transient thermal response. The network thermodynamics model was expressed in terms of the bond graph technique (Paynter [157]; Karnopp *et al.* [113]; Beaman and Paynter [9]) as shown in Fig. 66. It is beyond the scope of the present review to discuss this modeling methodology; however, the above references may be consulted for details and examples. The icon based model shown in Fig. 66 was translated directly by computer algorithm into the governing state equations which were solved numerically to determine the temperature history at each of the nodes for an irradiation protocol and system properties and dimensions identical to those used by van Gemert and Welch [210]. The temperature histories for each of the four nodes are shown in Fig. 67. The pattern of response corresponds with experimental data for similar protocols, showing the anticipated spatial distribution of magnitudes and time delay in temperature rise and fall. Initial results obtained by this simple network thermodynamic model indicate that further effort is warranted in developing the technique to a more sophisticated level.

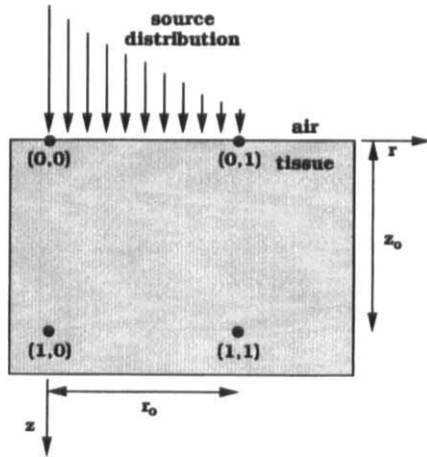


FIG. 65. Four node geometry for modeling the radial and axial temperature distribution in tissue during laser irradiation. The energy deposition and diffusion processes are assumed to be confined to the immediate region bounded in the radial and axial directions by r_0 and z_0 , respectively. (From Çilesiz and Diller [42, Fig. 1], with permission.)

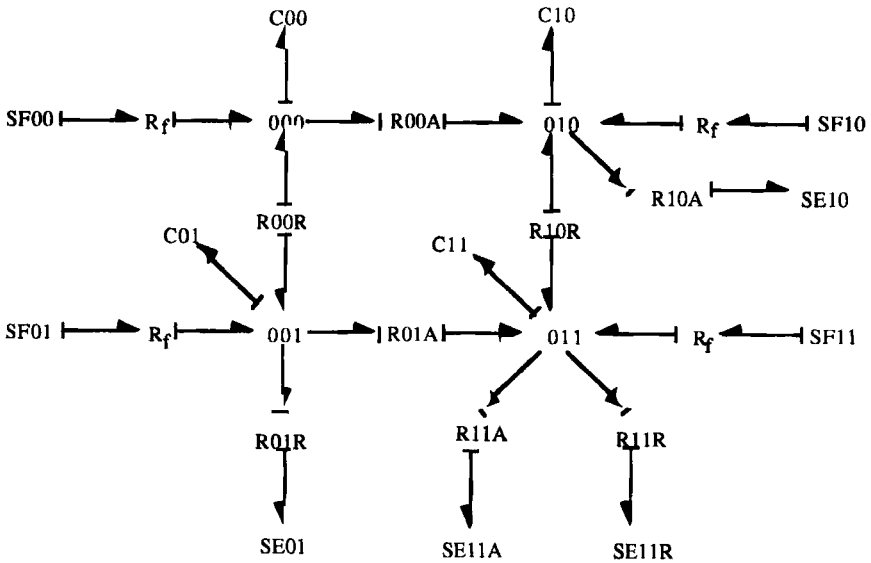


FIG. 66. Bond graph model for laser irradiation in the physical system shown in Fig. 65. See Paynter [157], Karnopp *et al.* [113], or Beaman and Paynter [9] for explanation of bond graphs. (From Çilesiz and Diller [42, Fig. 2], with permission.)

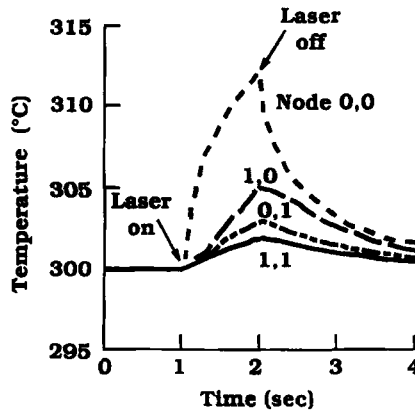


FIG. 67. Transient temperatures for the four nodes identified in Fig. 65 during and following a 1-s irradiation protocol. (From Çilesiz and Diller [42, Fig. 3], with permission.)

E. HYPERTHERMIA THERAPY

One of the most rapidly developing application areas of bioheat transfer deals with the use of hyperthermia in the treatment of cancer, either as a singular therapy or as an adjuvant to other modalities. Although there is a long history of the application of heat as a method of controlling or reducing tumors, strong clinical activity directed toward the adoption of this technique, with an accompanying acceleration in research activity, has occurred only during the past two decades.

Hyperthermia therapy presents a plethora of challenging heat transfer problems for solution. Accordingly, engineers have played a central role in the development of practical devices for effecting hyperthermic protocols, as well as providing a rigorous basis for understanding the mechanisms that govern the processes of energy deposition and diffusion within a tumor and its embedding tissue. Bioheat transfer modeling has been a focal tool in this activity, and an extensive literature has developed quickly in the field. In the context of the present review the topic of hyperthermia could easily be expounded to the point of becoming the dominant discussion of the chapter. However, a number of excellent reviews have been prepared that cover hyperthermia in a format quite complementary to the present work. Thus, the reader is referred to selected other reviews as follows, with the realization that even the list of reviews is not comprehensive. Also, there are several journals in which much of the literature is reported on modeling of the creation, measurement, and control of the transient thermal fields to effect hyperthermic protocols.

An edited monograph which has proved to contain a wealth and breadth of references and enlightening commentary is that of [201]. Topics covered range from basic heat transfer modeling through biological and clinical considerations. More recently, a series of monographs on clinical thermology has been published. Extensive review articles are presented on models for calculation of the patterns of power deposition in hyperthermia, by Paulsen [156], and of the prediction of thermal dosimetry for treatment planning, by Roemer [173]; other articles provide a rigorous formulation of the equations for electromagnetic (Hand [88]) and ultrasonic (Hynynen [105]) means of selective energy deposition for hyperthermia. An extensive review article on heat transfer processes in hyperthermia that includes a bibliography current through 1990 with more than 400 references has been prepared by Roemer [174]. Many more directed articles are also available in the *International Journal of Hyperthermia*, which has been published since 1985. The results of research concerning techniques for controlled energy deposition into tumors and the prediction and measurement of the resulting transient temperature fields are reported frequently in the *IEEE Transactions on Biomedical Engineering* and the *Transactions of the ASME, Journal of Biomechanical Engineering*.

V. Thermally Controlled Kinetics at Low Temperatures

The rates of nearly all processes in biological systems are reduced at hypothermic and cryogenic temperatures. The phenomenon may be used to benefit many applications such as the long term preservation of tissues and organs by banking for subsequent transplantation (Pegg and Karrow [163]) or the induction of temporary hypothermia for selected surgical procedures under reduced metabolic requirements (Olsen *et al.* [152]). Even so, nearly all low temperature biological procedures involve rate processes on which the desired objective is directly dependent. Thus, temperature control, if possible, becomes an important process design parameter. In addition, for many biological systems the temperature is one of the few parameters that can be manipulated externally to exercise control over internal processes. In a complementary manner, thermal regulation has long been used in the control of an extremely broad spectrum of industrial processes.

Two important examples of low temperature processing procedures in biological systems will be discussed for which regulation of the temperature history and its spatial distribution are of critical importance in determining the success or failure. The first case to be considered is the cryopreservation of living cells, in which the medium experiences a phase change as an integral part of the process. The phase change is anticipated, and the

process must be designed to account for the effects of coupled heat and mass transfer. The second case is the freezing of macroscopic dimensioned tissues and organs. This process involves a more complex set of phenomena for which not only are heat and mass transfer of critical importance, but they may lead to the formation of thermal stresses in a tissue that can cause catastrophic injury if the thermal protocol is not controlled properly.

A. CELLULAR CRYOINJURY DURING FREEZING AND THAWING

The cryopreservation of living cells and tissues is a thermally driven process that is governed by internal mass transfer resulting from concentration gradients established owing to the progressive transition between the liquid and solid phases. The thermodynamic coupling between the temperature and solute concentration fields is illustrated in Fig. 11a. In practical cryopreservation protocols the heat transfer process is established most often on a macroscopic scale as compared to the microscopic dimensions of the individual cells of the specimen. In contrast, the mass transfer processes occur on a microscopic scale more closely approximating the size of cells. The relative scales of these simultaneous transport processes during cryopreservation are depicted in Fig. 68. Further detailed discussion of these phenomena are available in the texts of Chalmers [34] and Flemmings [72].

Together the heat and mass transfer processes shown constitute the thermal and osmotic environment for the individual cells of a biological system. Both the local temperature and solute concentration may vary strongly as a function of the thermal history during a preservation protocol as well as of the initial conditions. In addition, there will be a large hysteresis in the local thermal and osmotic histories experienced during a sequential freezing and thawing process that starts and ends at an identical state. Therefore, in general, the kinetics experienced during freezing and thawing are quite different. The following discussion will focus on freezing processes, with differences associated with thawing considered subsequently.

A further concurrent transport process of great importance in the cellular response to freezing and in the manifestation of different modes of injury occurs at an even smaller scale than those described previously in this chapter. In order for a living cell to survive freezing it is necessary that it be able to exchange water with its environment as the concentration and temperature of the local solution change (Levin [126]). Cell plasma membranes offer a finite resistance to the movement of water (and also to many CPAs), thereby enabling a progressive dehydration in response to the elevated solute concentrations that occur during freezing. This transport

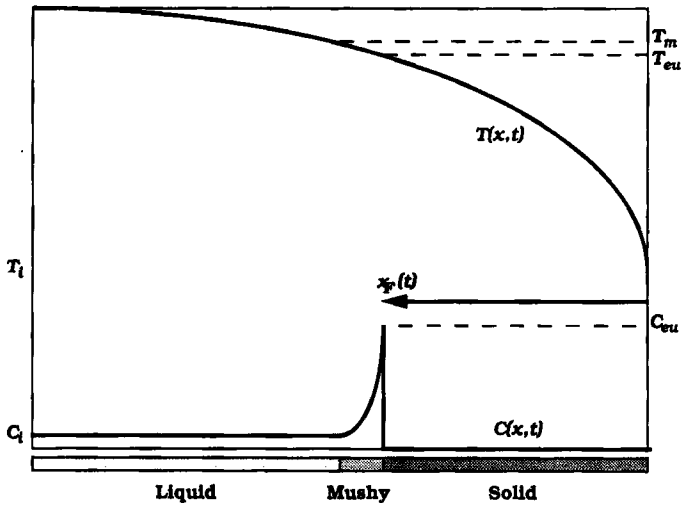


FIG. 68. Example of the spatial scales of the temperature and solute concentration gradients during the freezing of an aqueous solution. $x_f(t)$ represents the position of the growing solid-liquid phase interface relative to the exterior boundary of the system. Since the phase transition occurs over a range of temperatures between the equilibrium melting and eutectic values, the interface consists of a mushy region across which the solute gradient occurs. The buildup of solute rejected from the solid phase will also extend via diffusion into the liquid region ahead of the advancing interface producing a region of constitutional supercooling.

process occurs on a length scale smaller than $1 \mu\text{m}$. In addition, it is strongly dependent on the magnitude of the absolute temperature, in that there is an exponential decrease in permeability with falling temperature (McGrath [142]). As a consequence, for almost all cell types at temperatures below about -20°C there is very little possibility for significant transmembrane transport.

In summary, the following scenario emerges to describe simultaneous transport processes during the freezing of cells. A temperature field is imposed externally on a biological system as a function of the thermal boundary conditions in conjunction with the system dimensions and constitutive properties. Following the nucleation of ice in the extracellular region of the system there will be change in local solution concentration at the advancing ice front, via thermodynamic coupling as evidenced by the phase diagram, as it moves through the specimen issuing in a large buildup of solute in front of and diffusing ahead of the interface. The interface will grow from the surface region to the specimen interior as a function of the rate of heat transfer from the system and the internal temperature field.

As the interface encounters individual cells they will be subjected to an osmotic stress determined by the degree to which the solute concentration has risen above the initial uniform value within the tissue. Cells will dehydrate at a rate balanced by the concentration differential across the membrane and the resistance of the membrane to transport of the molecular species of interest, be it water and/or a CPA.

The movement of a chemical species across a cell membrane under the action of an applied concentration differential can be expressed in terms of a simple flux equation for a transported species, q :

$$J_q = P_q(T) \cdot \Delta C_q \quad (5.1)$$

The temperature dependence of the permeability P is usually described in terms of an Arrhenius-type relationship (Levin [125]):

$$P_q(T) = P_{qg} \cdot \exp\left(-\frac{\Delta E}{\mathfrak{R}} \left(\frac{1}{T} - \frac{1}{T_g}\right)\right) \quad (5.2)$$

The permeability is related to a reference state, g , that is usually identified at 0 °C and 1 atmosphere of pressure.

Körber has performed an extensive and elegant analysis of the combined thermal, chemical, and mechanical interactions that occur between a growing phase interface and living cells suspended in the medium (Körber [116]). During the solidification of a biological solution there is not only a redistribution of electrolytic solutes rejected from the ice phase (Wollhöver *et al.* [224]), as described previously, but also the dissolution of gaseous solutes with bubble formation and the rejection and entrapment of second phase inclusions, such as cells. It was observed that gas bubbles are nucleated from solution when a predictable degree of supersaturation was reached owing to exclusion from the growing ice phase, followed by a rapid rate of growth in size. Bubbles entrapped in the liquid ahead of the advancing ice front alternately were repulsed from the solid, and then entrapped when threshold conditions were satisfied, as characterized by a critical value for the interface velocity. The critical velocity was a function of the local thermal gradient and the size of the bubble. Similar rejection/entrapment behavior was observed for cells in suspension. These phenomena act in concert to define the environment to which cells are subjected during cryopreservation. Although rigorous predictive models are not yet available for development of this complex, multiple domain environment for freezing protocols, it is clear that most of the governing processes are driven by thermally controlled kinetics. The window opened by this kind of research illustrates the need for further analysis of the kinetics of low temperature biological processes.

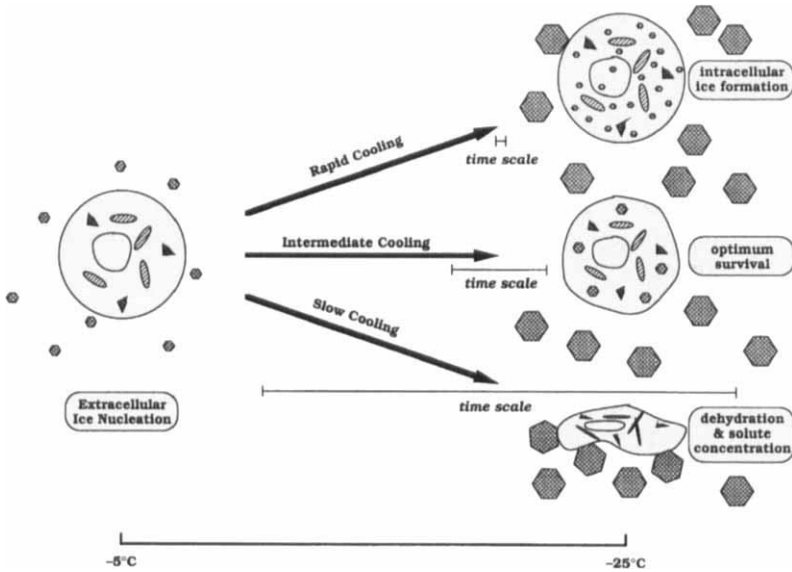


FIG. 69. Variations in the osmotic response of a cell suspended in a freezing solution as a function of the local rate of cooling. (Modified from figures and discussion by Mazur [138, Fig. 3, p. 21], with permission.)

Depending on the extent of dehydration experienced by a cell following the nucleation of extracellular ice, there are several possible scenarios to which it may be subjected, as illustrated in Fig. 69. Ice will form initially exclusively in the extracellular space, and the cell plasma membranes will act as barriers to the growth of ice into the intracellular solution. However, the membranes do allow exchange of water between the intracellular and extracellular spaces at a finite limited rate. If the local cooling rate is slow, there will be adequate time at high subzero temperatures for water to leave the cell under action of the osmotic pressure gradient and to be added by solidification to the extracellular ice phase. In the extreme case, it is possible for a cell to lose more than 95% of the available intracellular water by this process, resulting in extensive dehydration. Alternatively, if the cooling rate is rapid the range of high subzero temperatures at which the membrane permeability is large enough to permit the passage of water in response to an osmotic gradient will be traversed in a very short period compared to the time necessary for any significant exosmosis of water to accrue, and nearly all water will be retained within the cell at deep subzero temperatures. Since the intracellular water can remain in the liquid state to only a limited degree of supercooling, intracellular ice will be nucleated eventually. Both of the scenarios described above will issue in cellular injury, although by differing

mechanisms. In the former case, injury occurs associated with exposure to concentrated solutes and extensive dehydration; in the latter case the presence of intracellular ice leads directly to injury (for a more complete discussion see Mazur [139] and Taylor [204]).

An intermediate state can be achieved by moderating the kinetics of the two processes described above via control of the thermal history, and also by modifying the initial chemical state of the system prior to the initiation of freezing. Figure 69 shows that at cooling rates intermediate between slow and rapid the extent of both dehydration and intracellular ice formation will be reduced, with a result that the net injury to the cell will be a minimum. This effect is often described via a survival signature in which the survival of frozen/thawed cells is plotted as a function of the cooling rate. Extensive experimental data are available to corroborate this effect (for summaries see Mazur [136, 139] and Taylor [204]). The typical shape of a survival signature is shown in Fig. 70. The survival drops off at both low and high cooling rates as the two separate injury mechanisms become progressively dominant. Further, the exact dimensions of the survival signature are cell species dependent. The survival behavior of a particular cell to a given thermal protocol is a function of multiple parameters, including the membrane permeability and its temperature coefficient, the prefreezing presence of a CPA, as well as any unique physiological sensitivity to injury.

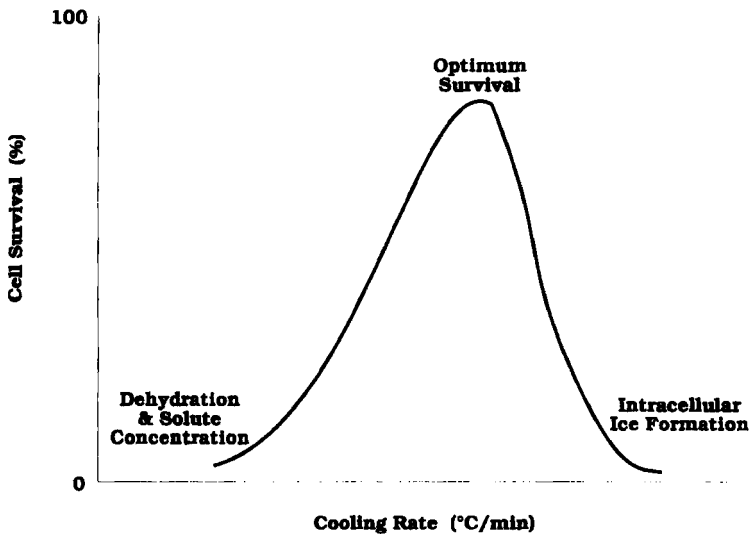


Fig. 70. Characteristic shape of a survival signature for frozen and thawed cells, indicating the two domains of injury associated with slow and rapid cooling which combine to create an intermediate range of cooling rates over which survival is optimal.

Survival signature data are applicable to living systems on a cellular basis. Thus, if there are gradients of thermal history within a tissue during freezing, it is expected that similar gradients should occur for cell survival. Gradients in the thermal protocol will issue not only in direct variations in the cellular response, but also in a spatial distribution in the pattern of change in the osmotic stress developed. In organized tissues it is typical to encounter many different cell types, each of which will have unique survival characteristics to freezing and thawing, resulting in an additional factor convolved onto the physicochemical parameters that govern the injury processes during cryopreservation. Given this background, it is clear that it is important to be able to predict and control the cooling rate over some critical range of temperatures and freezing states in order to regulate the spatial extent of injury during any given freeze/thaw protocol (Chmiel *et al.* [39]; Hayes *et al.* [95]). In many applications, such as cryopreservation, the objective of manipulation of the protocol parameters is to maximize the survival of tissue, whereas in cryosurgery the objective is to maximize tissue injury within a defined spatial domain.

If it is possible to predict the local thermal history during freezing and/or thawing using the methods discussed in Section III, then the cooling rate map for the specimen can be combined with a survival signature of the type given in Fig. 70 for the appropriate cell species to produce a survival atlas for the specimen (Hayes *et al.* [94]). In this manner it should be possible to manipulate the thermal parameters, and in some cases also the chemical parameters, of the freezing and thawing procedure to advantage in achieving a defined objective. When freezing tissue *in situ* there is little that can be done to change the chemical basis for the cellular response to freezing, such as adding a CPA; however, for *in vitro* tissues alteration of the chemical composition of the specimen before and after freezing has been a primary key to success in realizing clinical applications of cryobiology. The following discussion will illustrate how modeling techniques may be applied to analyze the spatial variations in survival during the freezing of a tissue with a large enough geometry to support significant gradients in thermal history.

Hayes *et al.* [94] have applied the apparent heat capacity method (Eq. (3.20)) in conjunction with finite element analysis to predict the distribution of thermal histories in a cylindrical container filled with an aqueous solution in response to various temperature protocols imposed at the boundary. Local values of the cooling rate were calculated by time averaging of the thermal history over the temperature range between -2.8 and -30 °C as per Eq. (3.22). These cooling rates were then matched to an appropriate survival signature such as that illustrated in Fig. 70, from which it was possible to predict the distribution of injury (or survival) within a specimen that would result from the protocol of interest. Several different

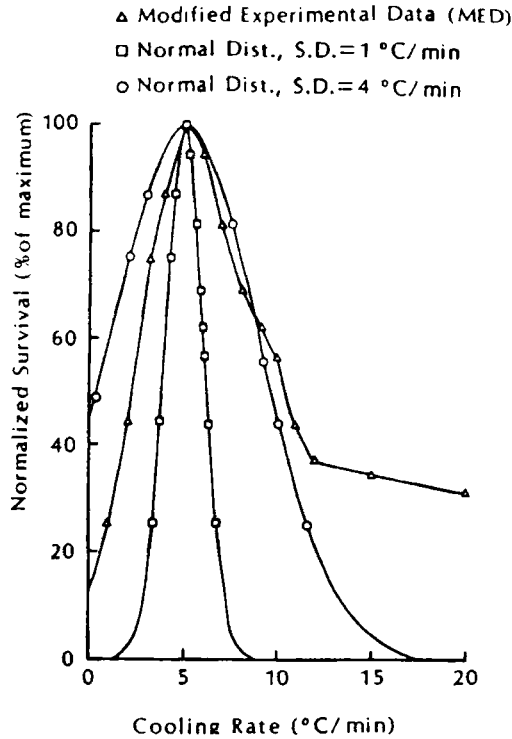
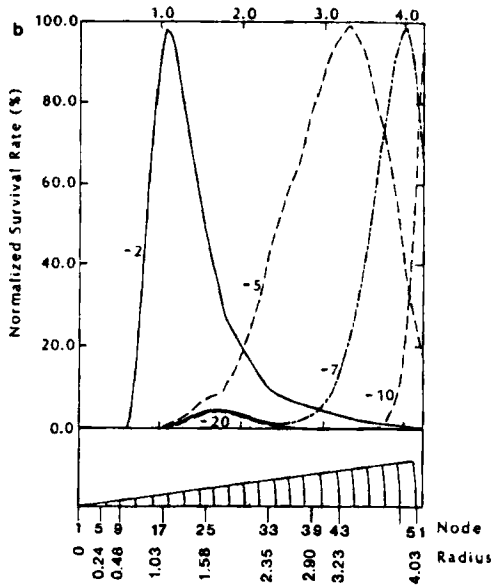
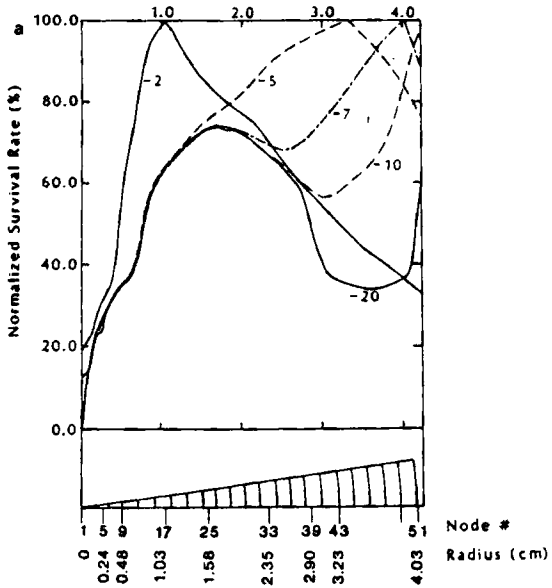


FIG. 71. Simulated survival signatures adapted by Hayes *et al.* for determination of the spatial distribution of injury in frozen tissues as a function of the local thermal histories. All signatures have been normalized to reflect optimum survival at a cooling rate of 5 °C/min and to set the optimum at 100%. The experimental data were taken from Mazur *et al.* [141]. (Redrawn from Hayes *et al.* [94, Fig. 1, p. 68], with permission.)

simulated survival signatures were applied for the analysis by Hayes *et al.*, and these are shown in Fig. 71. The shapes of the signature are all similar, and they were normalized along the cooling rate axis to provide a large portion of overlap with the rates predicted for the thermal protocols that were evaluated.

Constant cooling rates of -2 , -5 , -7 , -10 , and -20 °C/min to a minimum temperature of -120 °C were assumed at the surface of a cylindrical container of 4-cm radius. The thermal histories and cooling rates calculated throughout the specimen were similar in character with those discussed previously in Section III. The computed cooling rates were matched with each of the survival signatures shown in Fig. 71 to obtain plots of the cell survival within the specimen as a function of position. These survival maps are presented in Fig. 72. They illustrate graphically



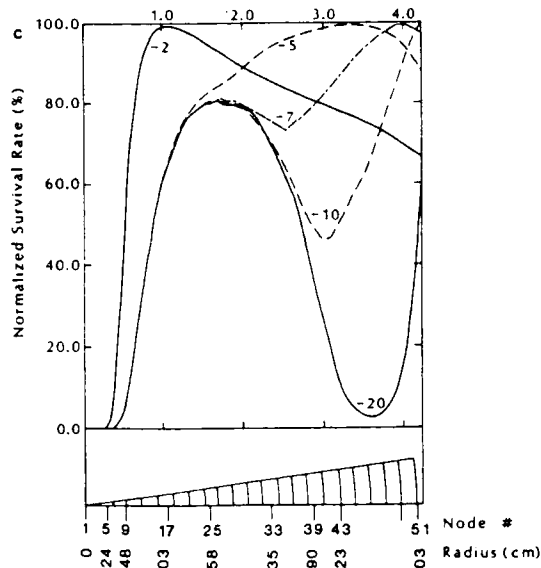


FIG. 72. Spatial distribution in survival rates for a cylindrical specimen cooled at constant surface rates of -2 , -5 , -7 , -10 , and -20 $^{\circ}\text{C}/\text{min}$ to a minimum temperature of -120 $^{\circ}\text{C}$. Interpretation of the cooling rate distribution is presented in terms of each of the three survival signatures defined in Fig. 71. (a) Data modified from freeze/thaw experiments with bone marrow cells. (b) Normal distribution with a standard deviation of 1 $^{\circ}\text{C}/\text{min}$. (c) Normal distribution with a standard deviation of 4 $^{\circ}\text{C}/\text{min}$. (Redrawn from Hayes *et al.* [94, Fig. 9, p. 80], with permission.)

the dependence of the rate process(es) for freeze/thaw damage upon the thermal history of the specimen. The coupling of the biological response to the transient temperature distribution affected during a cryopreservation procedure is an all important factor in determining the degree of success to be achieved. Further, the kinetic phenomena that constitute the survival signature are governed by local temperature. These may vary widely among different cell types, and these dictate the criteria for possible optimization of the thermal protocol design for freezing of specific target cells. Finally, it should be noted from comparison of the various survival plots that application of the cooling rate that is optimum for survival of individual cells at the surface does not necessarily produce the best overall recovery of cells when integrated over the entire volume of a macroscopic dimensioned container.

The above studies have been extended recently to address the kinetics of cell injury during a cryosurgical procedure (Hayes *et al.* [92]). The basic finite element model described above has been applied to simulate the

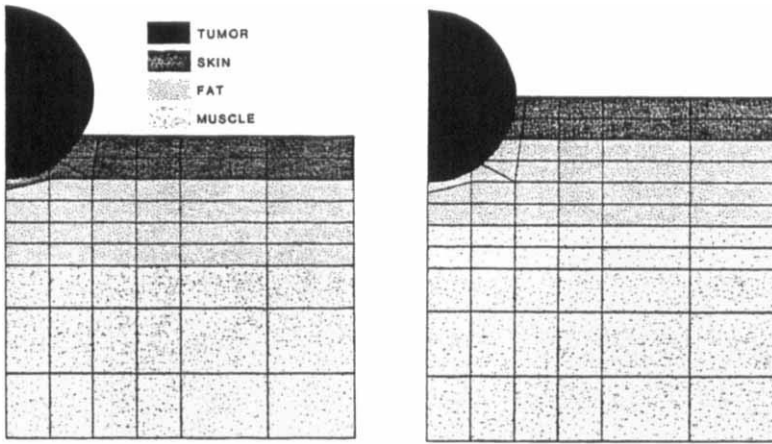
transient temperature history affected in normal tissue and in a superficial tumor during a prescribed cryosurgical procedure produced by application of a LN₂ refrigerated cryoprobe to the tumor-tissue surface. Upon calculation of the transient temperature and cooling rate fields affected and matching with an appropriate survival signature the model produced a contour map of damage within the tissue and tumor for each protocol studied.

The survival signature for the HeLa S3 cell (McGrath *et al.* [143]) was used as the model sensitivity of tissue to cooling velocity during the freeze/thaw stress of cryosurgery. Adoption of this survival signature was justified since the cell line is derived from a human cancer tissue, and the analysis parameters of this investigation were directed to simulation of cryosurgical procedures for tumors. The survival signature was interpreted for cryosurgery in terms of damage rather than survival since the objective of the procedure is to destroy tissue within a designated region.

An axisymmetric three-dimensional physical system was defined for the analysis consisting of adjacent layers of skin, fat, and muscle with an embedded tumor, as shown in Fig. 73. The spherical tumor was represented as a homogeneous mass of HeLa S3 cells having a nominal radius of 0.5 cm. Cases were studied with the center of the tumor 2 radii below the skin surface as well as at the surface and 0.5 radii above the skin surface. The cryosurgical procedure was simulated by application of a LN₂ refrigerated cryoprobe to the tumor-tissue surface. Values of the cooling rates at all positions in the tissue and tumor were calculated as a function of position based on the criterion of exposure of at least 10 s to a local minimum temperature of -5°C or lower. The cooling rate was determined as the time average of the cooling rates produced between the initial phase change temperature of -0.53°C and whichever is higher of -30°C or the minimum temperature reached. The distribution of computed local cooling rates was then applied to the survival signature for HeLa S3 cells to obtain an atlas of injury within the tumor. The normal tissue was modeled as having a survival signature similar to that of a representative mammalian cell line, as shown in Fig. 71, but neither of the signatures was normalized for the present analysis to predict a maximum survival of 100% or to rescale the cooling rate axis. The HeLa S3 cell data had an optimal survival rate of 26.7% for cooling at $-16.7^{\circ}\text{C}/\text{min}$, and the damage increased for either more rapid or slower cooling as dictated by the signature. Similarly, the bone marrow data showed an optimum survival rate of 65% for cooling at $-1.8^{\circ}\text{C}/\text{min}$. The survival signatures are plotted in Fig. 74. Two parameters were evaluated for each relative position of the tumour: probe size and holding period. The probe size varied from 0.5 to 1.5 radii, and the holding period at the minimum temperature ranged from 30 to 300 s.

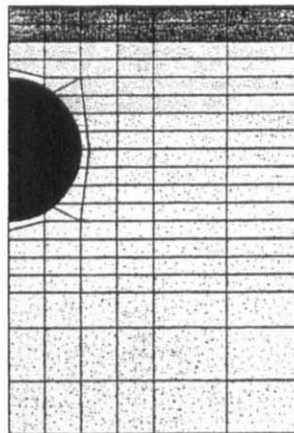
Subsequently the probe was warmed from -196 to 50 °C in a period of 30 s and held at 50 °C for 180 s. The physical dimensions and thermal properties assumed for the model are presented in Table IX.

The results of one series of simulations are shown in Fig. 75. In this case the most superficially positioned tumor was examined for application of probes having 0.5 and 1.5 tumor radii and a surface geometry to match



Case Study 1: Center of tumor 0.5 radii above skin surface.

Case Study 2: Center of tumor is aligned with skin surface.



Case Study 3: Center of tumor is 2 radii below skin surface.

FIG. 73. Geometry assumed for developing a model for cryosurgery of a superficial tumor. (Redrawn from Hayes *et al.* [92, Fig. 1], with permission.)

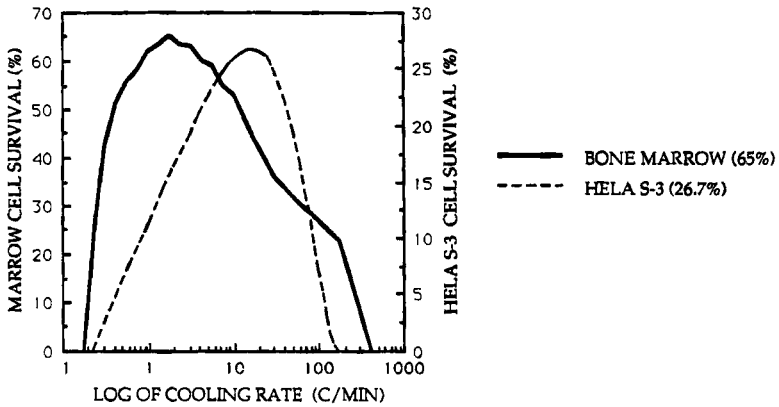


FIG. 74. Survival signatures used to simulate normal and tumor tissues in the cryosurgery simulation model. (Redrawn from Hayes *et al.* [92, Fig. 2], with permission.)

the tumor surface. The probes were assumed to be held in contact for 60 or 300 s, and the map of injury inflicted to the tumor and surrounding tissue was calculated from the thermal histories and survival signatures. Examination of the injury contours indicates that the size of the probe relative to the tumor surface is a much more important factor in producing and controlling damage than is the duration of contact for the range of operating states evaluated. Further simulations with exposure times as long as 1500 s confirmed this behavior.

Interpretation of the results predicted by this model are rather pessimistic regarding the efficacy of cryosurgery from the perspective of achieving full tumor destruction by the standard mechanisms of freezing injury as applied to individual cells. In the best case reviewed only 75% of the tumor was completely killed. However, we know from practice that cryosurgery

TABLE IX
PHYSICAL DIMENSIONS AND THERMAL PROPERTIES (UNFROZEN/FROZEN)
ASSUMED FOR A MODEL OF THE CRYOSURGERY OF A SUPERFICIAL SKIN TUMOR^a

Material	ρC_p (J/cm ³ K)	k (W/cmK)	Thickness (cm)
Tumor	3.793/1.470	0.0055/0.0079	1.0 (diameter)
Skin	2.644/1.470	0.0036/0.0079	0.25
Fat	2.275/1.810	0.0020/0.0025	0.50
Muscle	2.295/1.570	0.0042/0.0108	1.0-2.25

^aFrom Hayes *et al.* [92, Table 1], with permission.

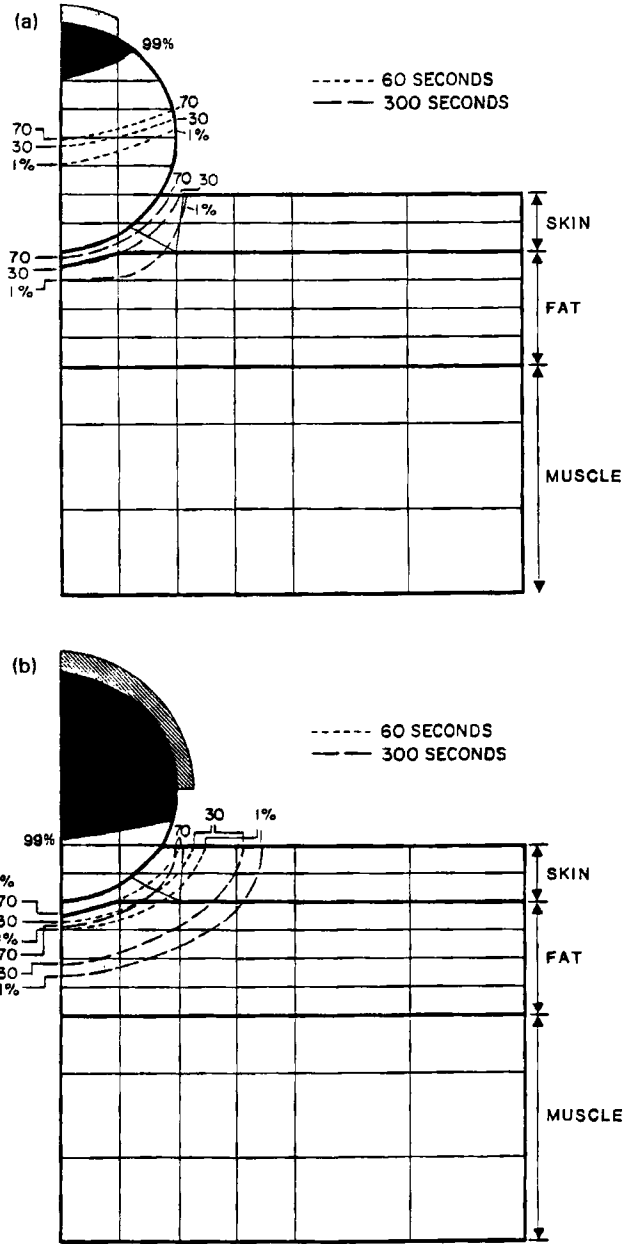


FIG. 75. Survival atlas for freezing of a superficial tumor with probes of (a) 0.5 and (b) 1.5 tumor radii and exposure times of 60 and 300 s. The black area indicates a damage of 99% or more. (Redrawn from Hayes *et al.* [92, Figs. 4 and 5], with permission.)

is successful, and therefore the numerical model must be examined to evaluate why it has failed to predict this performance. One important factor is that tissue damage during cryosurgery is not totally determined by thermal histories and cell freezing. Recently, Onik and Rubinsky [153] and Rubinsky and Pegg [186] have suggested that when tissue freezes, the phase interface propagates preferentially in the general direction of the temperature gradients, but is constrained to follow the blood vessels where there is no barrier for the growth of the ice-water interface. After thawing, structural damage to the vascular system would result in ischemic necrosis of the tissue served by the damaged blood vessels. Therefore, physiologically, tumor destruction does not appear to occur by thermal history effects alone, indicating that the kinetic model for injury assumed in the analysis of Hayes *et al.* [92] is incomplete. The model does predict full penetration of the ice front through the tumor for selected protocols, which would be consistent with eventual total necrosis according to the above criterion. It is likely that direct cell injury and vascular damage contribute to the efficacy of cryosurgery. Thus, there remain further clear challenges to building effective and accurate models for the thermally driven kinetic phenomena that govern the cryosurgical process.

B. THERMAL STRESSES DURING FREEZING AND VITRIFICATION

The frozen preservation of whole organs has been limited by many factors (Pegg and Jacobsen [162]); included among these are the multifaceted difficulties of adding and removing cryoprotective agents (Pegg *et al.* [164]), control of the local thermal histories within a system of macroscopic geometry, differential sensitivity of the individual cells types that constitute a heterogeneous organ to the stress of a cryopreservation protocol, cellular density and extracellular architecture within the organ (Pegg [160]), mechanical stresses owing to differential swelling within the organ, and the possibility of creating thermal stresses within a system of finite size during rapid thermal transients. The latter phenomenon will be discussed in this section.

Rubinsky *et al.* [183] have proposed a model for the formation of thermal stresses during the freezing of an organ. The model was derived to first describe the transient temperature field during solidification of a liquid in a simple symmetric spherical geometry; the solution for the thermal field was then used as the forcing function in the thermal stress equations. As a result it was possible to predict the distribution of radial and azimuthal stresses in the sphere as a function of the imposed thermal protocol and the constitutive properties of the tissue under consideration. Knowledge of the

stress distribution could be used to predict conditions for which the organ could be subjected to mechanical injury or, conversely, to optimize the thermal protocol to minimize the development of the stresses.

Formulation of the equations to solve for the transient temperature field was as already described in Eqs. (3.1) through (3.8) with the exception that a one-dimensional spherical coordinate system was applied rather than one-dimensional rectangular coordinates. The geometry of the system for the combined thermal and mechanical analysis is shown in Fig. 76. Since the liquid phase will not support the formation of mechanical stresses, the focus of this analysis was on the solidified portion of the system. Accordingly, the temperature distribution in the solid phase obeys the expression

$$\frac{\partial \tau_S}{\partial t} = \alpha_S \nabla^2 \tau_S = \alpha_S \left(\frac{\partial^2 \tau_S}{\partial r^2} + \frac{2}{r} \frac{\partial \tau_S}{\partial r} \right), \quad r_F \leq r \leq r_o \quad (5.3)$$

where it was assumed that the liquid phase starts initially at the phase change temperature, which was used as the reference value for τ :

$$\tau(r, 0) = \tau_F = 0, \quad 0 \leq r \leq r_o \quad (5.4)$$

The boundary conditions were stated at the advancing phase boundary and at the outer solidified surface of the sphere as

$$\tau(r_F, t) = \tau_F = 0, \quad r = r_F \quad (5.5)$$

$$\tau(r_o, t) = \tau_F - Bt, \quad r = r_o \quad (5.6)$$

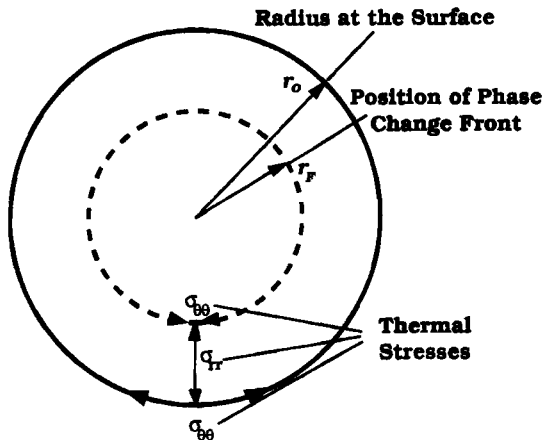


FIG. 76. Geometry of thermal stresses during the freezing of a sphere. (Redrawn from Rubinsky *et al.* [183, Fig. 1, p. 67], with permission.)

where B is the constant cooling rate applied at the surface. At the phase interface the energy balance is given by

$$k_S \frac{\partial \tau_S}{\partial r} = \rho \Lambda \frac{dr_F}{dt}, \quad r = r_F, t > 0 \quad (5.7)$$

Note that since the system is initially at the phase change temperature, the liquid will remain isothermal and therefore support no heat flux until the phase interface is encountered.

Rubinsky *et al.* [183] restated the thermal problem in terms of dimensionless variables and parameters as follows:

$$\begin{aligned} \theta &= \frac{T - T_F}{T_F - T_e} = -\frac{\tau}{\tau_e}, & \text{Fo} &= \frac{\alpha t}{r_o^2} & (5.8) \\ R &= \frac{r}{r_o}, & s(\text{Fz}) &= \frac{r_F}{r_o} \\ \text{Fz} &= \text{Ste} \cdot \text{Fo}, & \text{Ste} &= \frac{c\tau_e}{\Lambda} \\ Y &= \frac{Br_o^2}{\alpha\tau_e}, & Z &= \frac{Y}{\text{Ste}} \end{aligned}$$

where all parameter values are computed based on the solid phase properties. In this application T_e represents the minimum temperature that is reached at the boundary during the cooling process.

With these definitions the problem formulation may be presented completely in terms of nondimensional parameters:

$$\text{Ste} \frac{\partial \theta}{\partial \text{Fo}} = \left(\frac{\partial^2 \theta}{\partial R^2} + \frac{2}{r} \frac{\partial \theta}{\partial R} \right), \quad s \leq R \leq 1 \quad (5.9)$$

$$\theta(R, 0) = \theta_F = 0, \quad 0 \leq R \leq 1 \quad (5.10)$$

$$\theta(s, \text{Fo}) = \theta_F = 0, \quad R = s \quad (5.11)$$

$$\theta(1, \text{Fo}) = -Z \cdot \text{Fo}, \quad R = 1 \quad (5.12)$$

$$\frac{\partial \theta}{\partial R} = \rho \Lambda \frac{ds}{d\text{Fo}}, \quad R = s, \text{Fo} > 0 \quad (5.13)$$

$$s(0) = 1 \quad (5.14)$$

The solution for the transient temperature field and location of the solidification front was obtained with a perturbation method (Rubinsky

and Cravalho [180] resulting in a temperature of

$$\theta(R, Fo) = -Z Fo \frac{R - s}{(1 - s)R}, \quad 0.2 \leq s \leq R \leq 1 \quad (5.15)$$

and an interface position of

$$\frac{Fo^2}{2} = -Y Ste \left(\frac{1}{6} + \frac{s^3}{3} - \frac{s^2}{2} \right), \quad 0.2 \leq s \leq 1 \quad (5.16)$$

These solutions are valid for the freezing process to the point where approximately 90% of the sphere is solidified. They were obtained independently and subsequently applied to determine the expressions for the thermal azimuthal and radial stresses in the frozen region.

An underlying assumption for the stress analysis is that frozen tissue, i.e., ice, behaves as a perfectly elastic medium. Also, as an aqueous solution undergoes solidification it is well known that a minimum value of the density occurs in the liquid phase at 4 °C, below which there is a monotonic increase in density, which can give rise to the creation of large stresses in a solid shell surrounding an inner core of freezing liquid. This phenomenon is very important, but was omitted from the analysis of Rubinsky *et al.* [183].

For a spherically symmetric system the strains produced by thermal stresses are given by

$$\frac{d}{dr} \left[\frac{1}{r^2} \frac{d(r^2 \delta)}{dr} \right] = \beta \left[\frac{1 + \nu}{1 - \nu} \right] \frac{dT}{dr} \quad (5.17)$$

with boundary conditions for the radial stresses at the solid-liquid interface and the outer surface of the sphere:

$$\sigma_{rr} = 0, \quad r = r_F \quad \text{and} \quad r = r_o \quad (5.18)$$

The solution to this equation is given in Boley and Weiner [18]:

$$\delta = \beta \left[\frac{1 + \nu}{1 - \nu} \right] \frac{1}{r^2} \int_{r_o}^r Tr^2 dr + c_1 r + \frac{c_2}{r^2} \quad (5.19)$$

where c_1 and c_2 are constants of integration which are determined from the boundary conditions. The strain-displacement relations for the radial and azimuthal directions are given by (Boley and Weiner [18])

$$\sigma_{rr} = \lambda \left[\frac{d\delta}{dr} + \frac{2\delta}{r} \right] + 2\mu \frac{d\delta}{dr} - (3\lambda - 2\mu)\beta T \quad (5.20)$$

$$\sigma_{\theta\theta} = \lambda \left[\frac{d\delta}{dr} + \frac{2\delta}{r} \right] + \frac{2\mu\delta}{r} - (3\lambda + 2\mu)\beta T \quad (5.21)$$

where the Lamé elastic constants λ and μ are defined in terms of the Young's modulus E and Poisson's ratio ν as (Boley and Weiner [18])

$$\lambda = \frac{\nu E}{(1 + \nu)(1 - 2\nu)} \quad (5.22)$$

$$\mu = \frac{E}{2(1 + \nu)} \quad (5.23)$$

The radial and azimuthal thermal stresses were then written as

$$\sigma_{rr} = \frac{2\mu\beta}{r_o^3 - r_F^3} \left[\frac{3\lambda + 2\mu}{\lambda + 2\mu} \right] \left[\frac{s^3}{r^3} \int_r^{r_o} Tr^2 dr + \frac{r_o^3}{r^3} \int_{r_F}^r Tr^2 dr - \int_{r_F}^{r_o} Tr^2 dr \right] \quad (5.24)$$

$$\begin{aligned} \sigma_{\theta\theta} = & \frac{4\mu\beta}{r_F - r_o} \left[\frac{3\lambda + 2\mu}{\lambda + 2\mu} \right] \\ & \cdot \left[\frac{s^3}{r^2} \int_0^{r_o} Tr^2 dr + \frac{r_o^3}{r^3} \int_{r_F}^r Tr^2 dr + 2 \int_{r_F}^{r_o} Tr^2 dr - (r_o^3 - r_F^3)T \right] \end{aligned} \quad (5.25)$$

Dimensionless expressions for the radial and azimuthal stresses were defined as follows:

$$\sigma_{rr} = \frac{\sigma_{rr}(1 - \nu)\alpha}{E\beta Br_o^2} \quad (5.26)$$

$$\sigma_{\theta\theta} = \frac{\sigma_{\theta\theta}(1 - \nu)\alpha}{E\beta Br_o^2} \quad (5.27)$$

These expressions lead to a dimensionless statement of the stress equations:

$$\begin{aligned} \sigma_{rr} = & \frac{\sqrt{2Z[(1/6) + s^3 - (s^2/2)]}}{(1 - s^3)(1 - s)} \cdot \left\{ \frac{s^3}{R^3} \left[\frac{(1 - R^3)}{3} - \frac{s(1 - R^2)}{2} \right] \right. \\ & \left. + \frac{1}{R^2} \left[\frac{(R^3 - s^3)}{3} - \frac{s(R^2 - s^2)}{2} \right] - \left[\frac{1}{3} - \frac{s}{2} + \frac{s^3}{6} \right] \right\} \end{aligned} \quad (5.28)$$

$$\begin{aligned} \sigma_{\theta\theta} = & \frac{\sqrt{2Z[(1/6) + s^3 - (s^2/2)]}}{(1 - s^3)(1 - s)} \cdot \left\{ \frac{s^3}{R^3} \left[\frac{(1 - R^3)}{3} - \frac{s(1 - R^2)}{2} \right] \right. \\ & \left. + \frac{1}{R^2} \left[\frac{(R^3 - s^3)}{3} - \frac{s(R^2 - s^2)}{2} \right] + 2 \left[\frac{1 - s^3}{3} - \frac{s(1 - s^2)}{2} \right] \right. \\ & \left. - \frac{(1 - s^3)(R - s)}{R} \right\} \end{aligned} \quad (5.29)$$

Rubinsky *et al.* [183] plotted the thermal stresses for different stages during the freezing of a sphere. Figure 77 presents the azimuthal stress distribution as a function of radial position for states in which the phase front has grown to radii of 0.9, 0.6, and 0.3. The general pattern of stresses is consistent for each state; at the interface the stresses are compressive, and they decrease monotonically with distance into the frozen region, becoming tensile at an intermediate position and reaching a maximum magnitude at the surface. As the freezing process progresses the magnitude of both the compressive and tensile stresses increases. A similar pattern in time would be observed by following the stress history for a singular position in the sphere. Upon initially solidifying there will immediately be a large compressive stress, which then will relax progressively, eventually becoming tensile. Although there is no directly supporting experimental evidence, Rubinsky *et al.* [183] speculate that such a transient loading could lead to damage in an organ during cryopreservation. This phenomenon would result in crack formation at the surface.

The various curves in Fig. 77 are plotted for constant values of the parameter Z , which is proportional to the product of the surface area of the

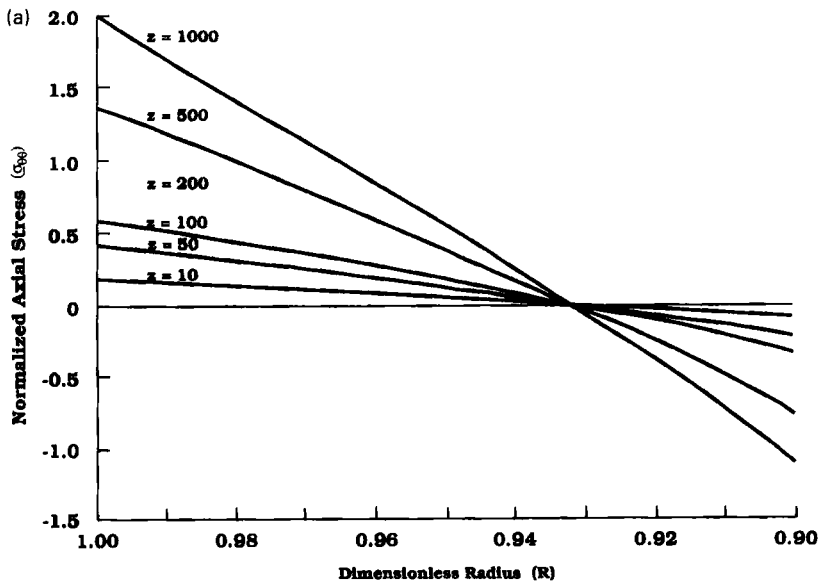
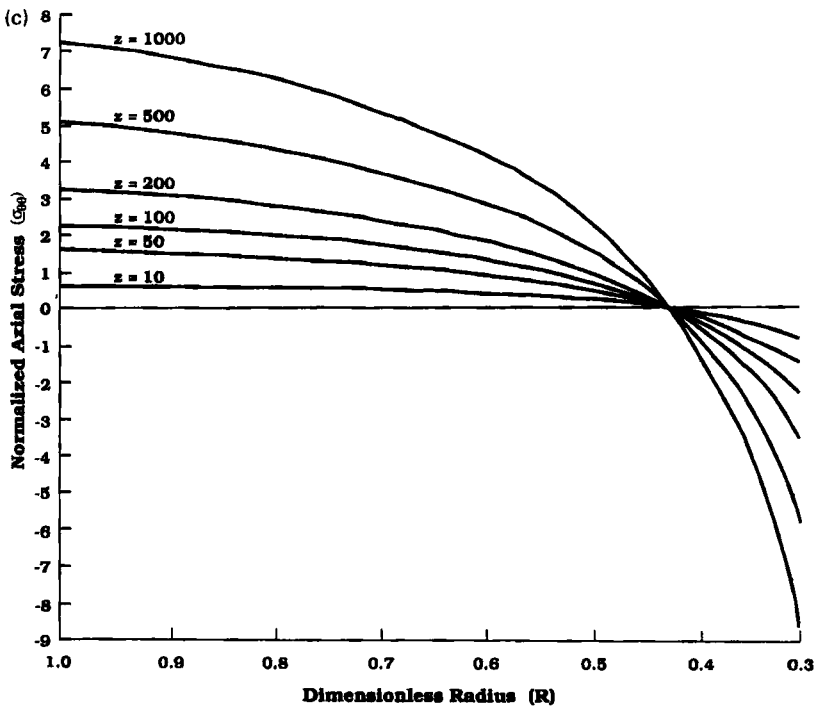
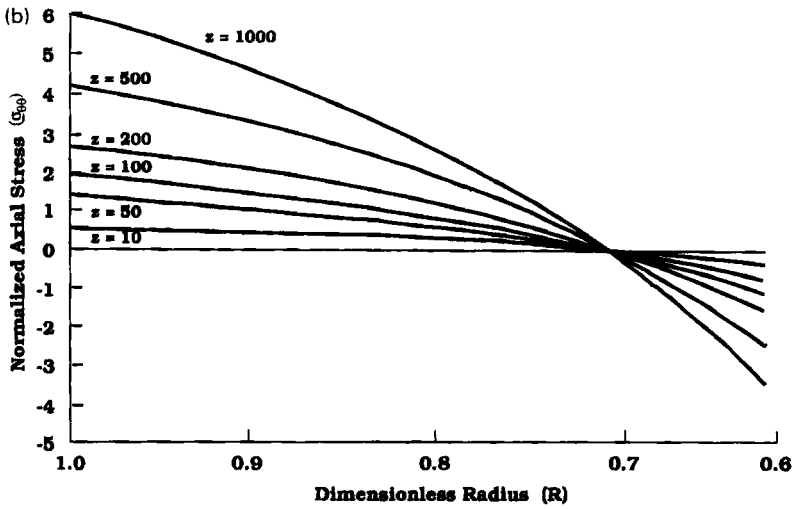


FIG. 77. Dimensionless azimuthal stress patterns within a sphere during freezing for three different stages of phase interface growth. The dimensionless radial interface positions are given respectively by (a) $s = 0.9$; (b) $s = 0.6$; (c) $s = 0.3$. (Redrawn from Rubinsky *et al.* [183, Figs. 3-5, pp. 70, 71], with permission.) (Fig. 77—continued over)

Figure 77—continued



sphere, r_o^2 , and the surface cooling rate B . Thus, the thermal stresses in organs of different size will be identical if the cooling rate is adjusted sufficiently so that Br_o^2 remains constant. The magnitude of azimuthal thermal stresses clearly increases with large values of Z . A complementary set of plots in Fig. 78 shows the development of azimuthal thermal stresses at specific locations as a function of time during the freezing of a sphere. Two cases were analyzed: $Z = 3$, corresponding to the freezing of a sphere of 5 mm radius with a surface cooling rate of $1^\circ\text{C}/\text{min}$, and $Z = 60$, for a 1-mm radius with the identical cooling protocol. The curves show that the same cooling rate applied at the boundary of the different size spheres produces a factor of 10 difference in thermal stresses. An obvious conclusion is that if thermal stresses are an important consideration during the freezing of an organ, it is necessary to apply slower cooling rates for larger dimensioned systems.

Radial stress patterns for the phase front at a radius of 0.6 are shown in Fig. 79. The stresses are continually compressive at all positions, and they increase in magnitude with the sphere size and cooling rate applied. Owing

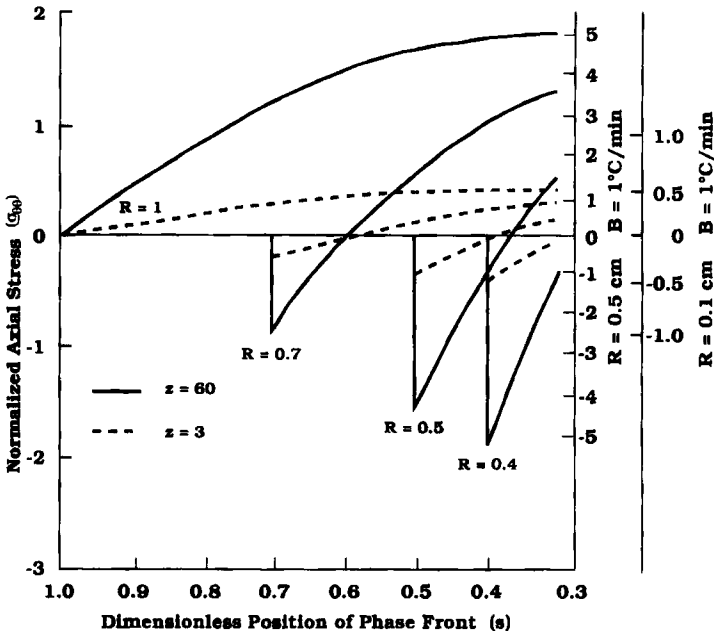


FIG. 78. Development of dimensionless azimuthal stress patterns with time at discrete locations within a freezing sphere. (Redrawn from Rubinsky *et al.* [183, Fig. 6, p. 72], with permission.)

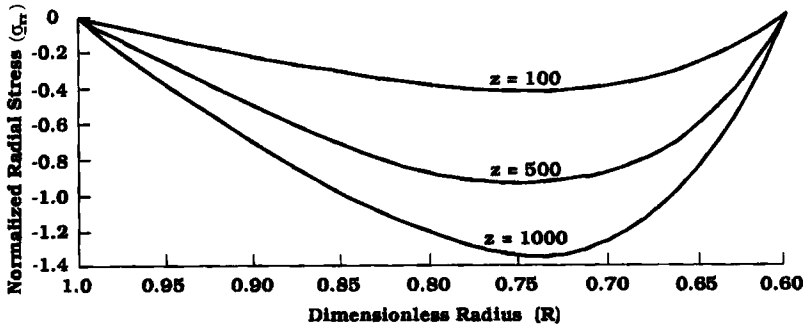


FIG. 79. Radial stress distribution when the freezing front reaches the dimensionless radius $R = 0.6$. (Redrawn from Rubinsky *et al.* [183, Fig. 7, p. 72], with permission.)

to the boundary conditions set forth in Eq. (5.18), the radial stress is zero at both the interface and outer surface of the sphere. Further, the magnitude of the radial stresses is smaller than the azimuthal stresses at all positions. In general the radial and azimuthal stresses may act in concert to define the net mechanical loading on tissue during a solidification protocol.

It is possible that thermal stresses may also form in biological systems that do not undergo a phase transformation during cooling. Over the past decade vitrification has been demonstrated to have potential as a method of long term cryopreservation of living cells and organs for transplantation (Mazur [140]). The major advantage of vitrification for cryopreservation is that as the specimen is cooled to deep subzero temperatures there is no phase change with the attendant rapid concentration of solutes nor the formation of ice crystals either interior or exterior to the cells. Thus, two of the primary sources of cryoinjury are eliminated. Nonetheless, there still remains the potential for cryoinjury during vitrification, due in part to mechanisms unique to the process. One major problem arises during the vitrification of systems having macroscopic dimensions; the tissue may be subject to mechanical fracturing resulting from the buildup of thermal stresses. Owing to the relatively poor thermal conductivity of biological tissues it is easy to create large temperature gradients during the cooling process, which, when coupled with the brittle nature of aqueous glasses, can cause cracking.

Fahy has conducted a series of experiments to identify and describe the process of thermal fracture in aqueous glasses during cooling (Fahy *et al.* [70]). His results indicate that the incidence of thermal fracture is related to the dimensions and thermal history of the system, which are in accord with standard theory (Boley and Weiner [18]; Johns [109]). Although the

equations describing the development of thermal stresses are well known and may be written directly from existing theory as above, solving the problem for the vitrification of tissues is problematic due to the paucity of constitutive property data for these systems in the temperature range of interest.

VI. Thermally Controlled Kinetics at High Temperatures

Exposure to elevated temperatures results in the irreversible destruction of living tissue. The rate at which this process occurs is related directly to the temperature, and it has been frequently and effectively described in terms of a chemical reaction expressed as an Arrhenius function, for which the accrual of damage occurs as an exponential proportional to the absolute temperature. Pioneering studies by Henriques [99] for the modeling of burn injury incorporated this type of function in its most simple format, as given by

$$\text{rate of thermal injury} = \text{scaling constant} * \exp\left(-\frac{\text{activation energy}}{\text{absolute temperature}}\right) \quad (6.1)$$

The scaling constant and activation energy are both dependent upon and unique to the particular chemical process of interest. Since the temperature varies as a function of position within a specimen, the associated pattern of tissue injury also can be calculated. The local rate of injury defined by Eq. (6.1) may be integrated over the duration of a thermal insult scenario to determine the total injury inflicted onto a given tissue. Thus, hyperthermic destruction of biomaterials can be considered to be an explicit consequence of thermally governed rate processes distributed as a function of the temperature history throughout the system, and these processes may be modeled effectively and with justification based on this assumption.

For many years this simple approach to defining and implementing an injury function was applied to a wide spectrum of high temperature processes in living tissues with an acceptable degree of success. In nearly all cases, a single set of scaling factor and activation energy values, as initially determined by Henriques [99] for skin burns at low temperatures, was applied for all thermal damage processes. In recent times it has become necessary to devise more specialized types of mathematical functions and values for the empirical constants to describe the range of thermal injury processes encountered. More sophisticated and sensitive instrumentation has enabled the accurate measurement of both the physiological and physical parameters that cause and define thermal damage. In addition,

devices are now in use, such as high power lasers, that can produce a heat flux of very high energy density which will create a thermal lesion via chemical processes quite different from those that govern the type of burns most frequently encountered heretofore and that are characterized by much slower rate kinetics. Thus, there now exist a number of models for describing the occurrence of tissue owing to hyperthermic insult.

A. RATE OF THERMAL INJURY

Injury to living cells and tissues owing to exposure to elevated temperatures is commonly denoted by the symbol Ω . In the broadest sense, the total accrued injury occurs as a function of the time and temperature that comprise the insult scenario. A concept developed early in the investigation of burns was that injury was realized in proportion to the total amount of energy delivered to the affected tissue. The critical thermal load was defined as the cumulative energy does to produce a given degree of damage, and it could be administered in any thermal protocol for which the time integral of the thermal flux was equal to a specific value. According to this theory, equal doses of energy should produce equal injuries. Eventually, experimental evidence was not in agreement with the CTL theory, and Stoll presented data that conclusively discounted that the severity of a burn injury occurred in proportion with the total amount of energy deposited (Stoll [195]). This argument was particularly convincing for low rates of heating which could be prolonged over periods of days to produce large values of the CTL with no discernable injury.

As noted previously, rigorous analysis of the burn process has indicated that the rate of injury to tissue is dependent on the local magnitude of temperature, which presumably governs the chemical reactions for the irreversible destruction of biomolecules. In this vein, Henriques presented data and postulated a model of the burn injury process for which the extent of damage is a function of the thermal history, with an exponential weighting factor to the highest temperatures achieved (Henriques [99]). The damage function was based on *a priori* knowledge of the transient temperature distribution in the system of interest. This problem was solved by Moritz and Henriques [148], as described in Eqs. (4.3)–(4.5). Thus, for a one-dimensional Cartesian coordinate system

$$\frac{\partial \Omega(x, t)}{\partial t} = \xi \exp - \left[\frac{\Delta E}{\mathfrak{R}T(x, t)} \right] \quad (4.4)$$

and

$$\Omega(x) = \xi \int_0^t \exp - \left[\frac{\Delta E}{\mathfrak{R}T(x, t)} \right] \quad (4.5)$$

This model has been adopted by many subsequent investigators to describe burn injury to the skin. The distinguishing factor among the various models is the unique combinations of the ζ and ΔE parameters which have been identified by matching Eq. (4.5) to experimental data obtained for burn trials over limited domains of exposure temperatures and times. A comparison of the behavior of several different skin burn models is presented in the following section.

The kinetic processes associated with other sources of hyperthermic injury have been the subject of more recent investigations. For example, tissue destruction during laser irradiation has been the subject of ongoing study. Preibe and Welch [166] adapted the Henriques model, Eq. (4.5), to calculate damage resulting from exposure to a laser having a Gaussian intensity distribution radially from the midpoint. Thus, the transient temperature field was taken as a function of both the radial and the axial coordinates, which is typical of laser irradiation protocols. The differences between short and long irradiation protocols were evaluated. Short protocols were defined by the conditions under which the diffusion term in Eq. (4.42) could be neglected so that the transient local temperature was dependent only upon direct absorption from the incident laser beam. Thus,

$$\frac{\partial T(r, z, t)}{\partial t} = \frac{Q(r, z, t)}{\rho c} \quad (6.2)$$

If the source strength is constant over time, then the temperature achieved within the tissue is linearly dependent on the exposure duration:

$$T(r, z) = \frac{Q(r, z)}{\rho c} t \quad (6.3)$$

An alternate interpretation of Eq. (6.3) is that maximum temperature rise per unit energy input is not a function of exposure time. At longer irradiation exposures diffusion of energy away from the site of absorption has a significant effect on the thermal history, and the local temperature rise will be diminished.

The injury process described by Eq. (4.5) depends on the thermal history in its entirety, including the rise and fall times flanking the period at the peak temperature. Depending on the nature of the temperature protocol imposed, it may be possible to make simplifying assumptions to reduce the mathematical complexity of thermal history function which must be integrated to solve Eq. (4.5). Preibe and Welch [166] used different assumptions for short and long irradiation episodes. At short times damage was assumed to be a function of only the peak temperature reached by direct absorption at a point and the subsequent decay transient, for which the

thermal history was dominated by the slower diffusion process. Conversely, at long exposure times the thermal response was approximated by a step function for the duration of irradiation, and the decay process was neglected. For the latter case the net local injury is given by the simple expression

$$\Omega(r, z) = t_p \xi \exp - \left[\frac{\Delta E}{\Re T(r, z)} \right] \quad (6.4)$$

If an injury threshold of $\Omega = 1$ is assumed, then Eq. (6.4) may be solved for the irradiation conditions under which a minimum level of damage is anticipated. Preibe and Welch used the damage model constants of Henriques, $\xi = 3.1 \times 10^{98} \text{ s}^{-1}$ and $\Delta E = 6.27 \times 10^8 \text{ J/kmole}$, to make these calculations. Thus, for a long term exposure of t_p , it should be expected that the threshold level of injury will be realized or exceeded for all locations that satisfy the relationship:

$$T(r, z) = \frac{7.5 \times 10^4}{226.75 + \ln t_p} \quad (6.5)$$

Preibe and Welch used this model coupled with experimental injury data from the literature to define the conditions under which a threshold value of Ω should be anticipated. The temperature field was determined as a function of temperature and time for irradiation of the pigment epithelium of the retina by an argon laser with a 25- μm spot size and a Gaussian radial distribution. The combinations of maximum tissue temperature reached at the $1/e^2$ radial boundary of the image and at a depth of 1.2 μm at which absorption is maximum and of the corresponding time issued in an injury value of $\Omega = 1.0$. Thus, the image boundary was taken to define the demarcation between the normal and the damaged tissue. The Henriques constants as presented previously were applied in Eq. (4.5) to calculate the temperature/time combinations. Figure 80 shows the results of these computations. Consistent with the assumptions of the model, there are two domains of process kinetics; for exposure times less than about 10^{-4} s the peak temperature in the tissue is independent of the duration of irradiation. This behavior is explained by the dominance of the total thermal history by the cool down process subsequent to the cessation of irradiation. Cooling of the target tissue occurs by diffusion of heat, and the effective time constant is orders of magnitude longer than the short irradiation exposures, issuing in a majority of the tissue damage occurring after the radiation source is no longer active. For longer irradiation scenerios the peak temperature diminishes as the time increases logarithmically. This behavior is quite typical of that encountered in a broad spectrum of burn events.

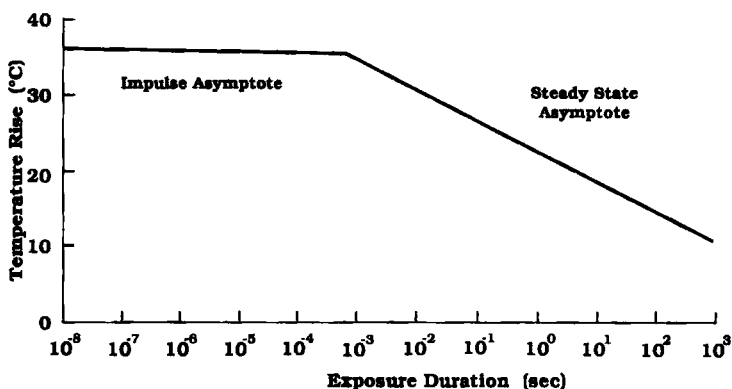


FIG. 80. Calculated combinations of peak temperature and time of exposure to produce a threshold injury of $\Omega = 1.0$ at the edge of a 25- μm argon laser beam directed onto the pigment epithelium of the retina. The values were determined for the axial plane of highest temperature increase. (Redrawn from Preibe and Welch [166, Fig. 4, p. 51], with permission.)

The unique aspect of the asymptotic relationship between peak temperature and exposure time was exploited by Preibe and Welch to explore a further number of cases. Equation (6.3) was solved to obtain an expression for the radial and axial variations in the transient temperature for irradiation with a Gaussian beam into a single layered medium exhibiting simple Beer's law absorption properties. The expression for the temperature distribution following a constant power irradiation for a period t_p is given by

$$T(r, z, t) = \frac{H \exp(-r^2/2\sigma^2)\eta e^{-\eta z}}{\rho c} t_p \quad (6.6)$$

Experimental experience has demonstrated that a minimum lesion must be created to be able to detect the presence of tissue damage. The lesion parameters should include an alteration in the light scattering properties of the tissue over an area of threshold size to render the injury perceptible to ophthalmoscopic observation. Preibe and Welch have shown by their experimental measurements that for image radii below 100 μ the above criteria define a uniformly applicable damage radius of about 15 μm , and at the larger images the damage area necessary for identification grows proportionately. Thus, they used Eq. (6.6) to determine the conditions requisite to produce a constant damage radius for varying irradiation image sizes. If T_d is the peak temperature at the threshold damage radius at the conclusion of an irradiation period t_p and r_d is the uniform minimum observable radius of damage, then the power density at the center of the

laser beam can be determined explicitly as

$$H = \frac{\rho c T(r_d, z, t_p)}{\exp(-r_d^2/2\sigma^2)\eta e^{-\eta z} t_p} \quad (6.7)$$

Figure 81 presents plots of the irradiation power density that must be delivered at the retina to produce damage radii of various constant magnitudes as a function of the image size, as calculated via Eq. (6.7). Note that both the power and the image size axes are logarithmic. As the image size decreases to less than $100 \mu\text{m}$, the required power level increases dramatically. A limited number of experimental data points from other investigators are also plotted with the calculations indicating a qualitative agreement with the model.

Birngruber [16] has taken a more mechanistic approach to analysis of the kinetics governing rate processes leading to thermal lesions. His analysis starts with assumptions that the injury process can be described in terms of a unimolecular reaction and that the kinetics of an Arrhenius process are valid. Thus, the rate of thermal denaturation and inactivation of proteins and enzymes is dependent directly on the temperature of the tissue. Based

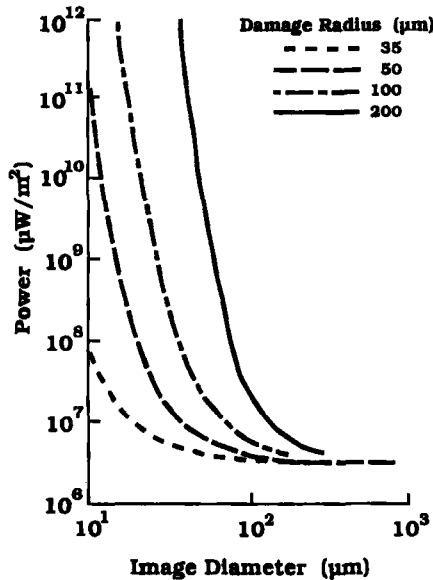


FIG. 81. Predicted power density delivered at the retina to produce a threshold injury of $\Omega = 1.0$ at the indicated radii as a function of the laser image size. The irradiation period is fixed at 30 ns for all protocols. (Redrawn from Preibe and Welch [166, Fig. 6, p. 53], with permission.)

on the methods of Glasstone *et al.* [79], Birngruber demonstrated that a statistical model for the reaction rate could be applied to arrive at a statement of the damage function in which the rate of injury is described by the product of exponential terms containing respectively the differential in entropy between the initial and activated states and the differential in enthalpy divided by absolute temperature for the two states, and a preexponential term that is linearly dependent on the temperature. When this expression was fit to experimental data for laser induced damage to tissue, over the range of states of interest the temperature effect in the preexponential term became negligible and it was combined with the exponential entropy term. The result was an injury model in the format of Henriques's, Eq. (4.5), in which the constants were given by $\zeta = 10^{44} \text{ s}^{-1}$, and $\Delta E/R = 3.5 \times 10^4 \text{ K}$. However, Birngruber performed no calculations to illustrate the performance of this model.

Over the past decade the use of lasers in medical applications has grown at a very rapid pace, and the extreme operating states have been extended continuously. As a consequence, new mechanisms of tissue injury are being encountered associated with very short high power exposures that may produce temperatures well in excess of the thresholds for boiling and carbonization. An additional challenge is detecting and measuring the damage caused by irradiation in these processes. Pearce and collaborators have investigated these phenomena experimentally during the past several years and have accomplished initial stages of development of models to describe the kinetics of thermal injury for high power pulsed laser irradiation.

Pearce [159] has categorized laser irradiation of tissues into three domains according to the temperature levels reached. In a sequence of increasing temperatures, lasers will produce a spectrum of qualitative responses in tissue typified by necrosis, coagulation, desiccation, water vaporization, ablation, and carbonization. In general the higher the operating temperature the faster the rate at which injury is manifested, and the mechanisms of damage vary greatly.

At low temperatures the damage process follows a first order Arrhenius rate process model, as defined in Eq. (4.5). In addition to tissue necrosis and denaturation of collagen, it has been noted that the loss of birefringence in muscle can also be used as an indicator of thermal damage. In particular, this latter phenomenon has proved to be quite useful in quantifying the extent of injury issuing from a graded thermal insult (Thompsen *et al.* [206]). Polarized light microscopy of stained histologic sections is used to reveal changes in the naturally occurring birefringence when muscle is heated to 42°C *in vitro*, thereby providing a sensitive measure of the extent of thermal damage for a range of states over which other morphological

indicators are difficult to detect. Further, thermally coagulated collagens exhibit a gradual birefringence color shift when exposed to temperatures between 50 and 97 °C, providing a quantitative damage indicator in a range of states which is of great concern in hyperthermic induced injury. As would be anticipated, the alterations in birefringence were not a true function of temperature, and extensive experiments by Thomsen *et al.* provided data for which the strongest mathematical correlation was achieved for the Arrhenius class of functions.

Han and Pearce [87] have used data originating from this experimental method of damage assay to determine the kinetic coefficients for an Arrhenius burn model. A series of trials was executed on heart muscle heated to temperatures from 60 to 80 °C for 120 to 1600 s. Normal tissue postburn showed full birefringence and completely damaged tissue had none; the region corresponding to $\Omega = 1.0$ was defined by the physical center of the zone in which the gradient in birefringence was observed. The transient temperature field in the tissue during the heating process was simulated with a finite difference model. The solution to the problem was applied in the damage model, Eq. (4.5), and the coefficients were adjusted to provide a maximal fit with the injury data. The resulting values obtained for heart muscle were $\xi = 3.5 \times 10^{22} \text{ s}^{-1}$, and $\Delta E = 1.64 \times 10^5 \text{ J/mole}$. These values were compared with those of Henriques for skin and with another of Pearce's students for aorta (for which the damage criterion was separation in collagen-elastin apposition). The results are shown in Fig. 82.

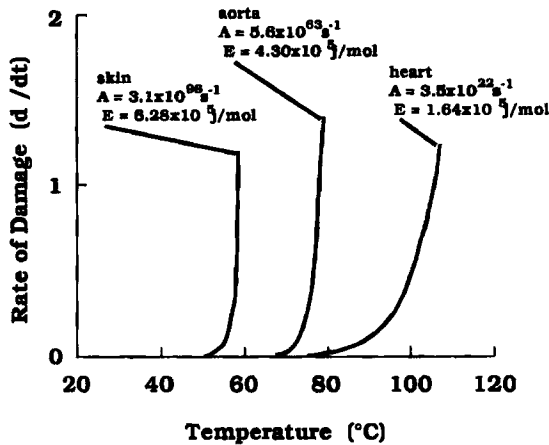


FIG. 82. Comparison between the rates of thermal injury in skin, aorta, and heart muscle as predicted by the standard Arrhenius injury model, Eq. (4.5), with the indicated coefficients. The values for skin are from Henriques [99]. (Redrawn from Han and Pearce [90, Fig. 6], with permission.)

The different model coefficients yield highly unique patterns of injury. The temperatures above which the rate of damage accelerates most noticeably are about 60 °C for skin, 80 °C for aorta, and 100 °C for heart. Although these differentials are dramatic, it must be realized that injury criteria for the experiments from which the constants were determined may also reflect considerably different patterns of sensitivity to thermally induced physiological change.

Pearce [159] has summarized other events that may bear on tissue injury caused by laser irradiation. At higher temperatures the injury processes are governed by a set of phenomena associated with the behavior of water trapped within the tissue and by combustion reactions. The vaporization of water occurs at rates comparable with those of other damage processes for temperatures above 90 °C, and very rapid rates of phase change can give rise to acoustic waves and mechanical stresses in the tissue. Below 100 °C the liquid to vapor phase change is surface diffusion limited, whereas above 100 °C rate kinetics play an increasing role associated with nucleation. It is possible to deposit energy into tissue at a rate higher than water is able to evaporate, resulting in states far from equilibrium. Sudden phase changes may occur with very high associated pressures capable of rupturing and tearing the tissue mechanical structure. The result is encountered frequently at high irradiation fluxes and has been termed the popcorn effect due to the popping and cracking sounds that are generated.

It is also possible to produce temperatures in tissue higher than the critical value, thereby eliminating phase change phenomena. In this range of states the energy deposited from the laser goes into direct alteration of the molecular structure, breaking down the complex macromolecules and eventually leaving a charred residue. The mechanisms of these processes are not as well understood as for injury at more commonly encountered burn temperatures. Consequently, kinetic models for these processes are only in an early state of development, if at all, and they represent an arena in which engineering analysis may issue in important pioneering contributions.

In addition to skin burns and laser irradiation, there are other biomedical applications in which thermally driven kinetic processes play a significant role. Hyperthermic treatment of cancer is a rapidly emerging field, and it has been discussed as a separate topic. At a more fundamental level, the kinetics of thermal injury to individual cells has been investigated by many researchers. Moussa *et al.* [150] measured the time to onset of thermal injury in HeLa cells heated on a special controlled temperature microscope stage (Diller and Cravalho [57]). The cells were observed continuously on the microscope during the heating process, and the criterion for injury was the appearance of irreversible morphological changes in the cells, such as the formation of blebs. Thereby it was possible to quantify the extent of

damage for a reasonably large population of cells, all of which were subjected to an identical thermal insult. The standard Arrhenius injury model (Eq. (4.5)) was fit to the data to determine values for the empirical coefficients as $\xi = 9.09 \times 10^{36} \text{ s}^{-1}$ and $\Delta E = 249 \text{ J/mole}$.

Further trials were also conducted on this system for evaluation of the hemolysis of human erythrocytes (Moussa *et al.* [151]). Twenty to thirty erythrocytes were held in the field of view while the temperature of the stage was raised at $900 \text{ }^\circ\text{C/min}$ to a value between 44 and $60 \text{ }^\circ\text{C}$, where it was held constant until injury was observed. The temperature rise was less than 3 s in all cases, and the damage process varied between 6 and 150 min , so that the protocol could be treated as an isothermal process for purposes of modeling. Damage to the cells was manifested as a series of two discrete events; the first was a morphological transition from biconcave discoid to a sphere, which was reversible, followed by an irreversible expulsion of hemoglobin to form a ghost. Multiple trials were conducted at each temperature so that it was possible to obtain a statistical description of the damage kinetics. These data were analyzed with two models that the authors formulated.

A kinetic model was presented in which a population of initially healthy erythrocytes was assumed to be first altered reversibly by a process acting at a given rate, j_1 , and then irreversibly damaged at a second and different rate, j_2 . The reactions were assumed to be first order, such that the rate of change from a given state, u , was proportional to the first power of the fraction of the population in that state, U_u . Thus, populations were identified with each of three possible states; U_1 initial, U_2 reversibly altered, and U_3 irreversibly damaged, where

$$\sum_{u=1}^3 U_u = 1 \quad (6.8)$$

The conservation equations for the cells in each of the three states lead directly to the standard set of first order equations

$$\frac{dU_1}{dt} = -j_1 U_1 \quad (6.9)$$

$$\frac{dU_2}{dt} = -j_2 U_2 + j_1 U_1 \quad (6.10)$$

$$\frac{dU_3}{dt} = +j_2 U_2 \quad (6.11)$$

Initial conditions for the process are given as $U_1 = 1$, and $U_2 = U_3 = 0$. After an elapsed time t of exposure to elevated temperatures, the fraction

of undamaged cells remaining is determined from the solution of these equations as

$$U_1 + U_2 = \frac{j_2}{j_2 - j_1} \exp(-j_1 t) - \frac{j_1}{j_2 - j_2 - j_1} \exp(-j_2 t) \quad (6.12)$$

The values for the reaction rate coefficients, j_1 and j_2 , were determined by fitting the model to experimental data measured on the controlled temperature microscope, and the results are plotted together as a function of temperature in Fig. 83. The coefficients for both processes display a linear dependency on the inverse absolute temperature and can be described by the Arrhenius function

$$j_u = \xi_u \exp - \left[\frac{\Delta E_u}{\mathfrak{R}T} \right] \quad (6.13)$$

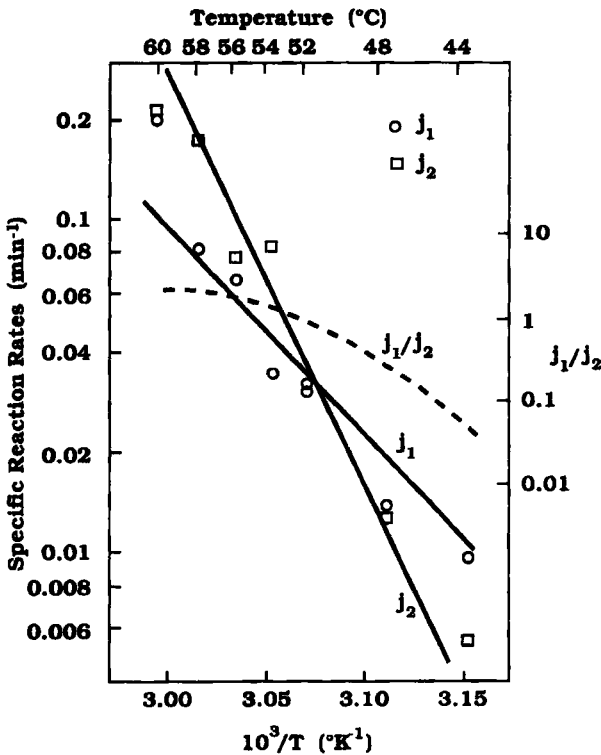


FIG. 83. Temperature dependency of the reaction rate coefficients for the kinetic model of two step thermal damage. (Redrawn from Moussa *et al.* [151, Fig. 3, p. 215], with permission.)

Values for the Arrhenius parameters describing these coefficients were determined as

$$\begin{aligned}\xi_1 &= 4.1 \times 10^{38} \text{ min}^{-1} \\ \Delta E_1 &= 2.5 \times 10^5 \text{ J/mole} \\ \xi_2 &= 1.7 \times 10^{19} \text{ min}^{-1} \\ \Delta E_2 &= 1.3 \times 10^5 \text{ J/mole}\end{aligned}$$

Because the two processes have different activation energies, the ratio of the reaction rate coefficients changes as a function of temperature. For the erythrocyte hemolysis data the two processes are balanced in the region of 52 °C, and at higher temperatures j_1 becomes progressively smaller, indicating that the overall kinetics of the damage process are dominated by the initial reversible morphological alteration. Thus, once the reversible change occurs, it is anticipated that the final irreversible damage should follow very quickly.

Figure 84 shows the history of each of the three possible states of cells during the hemolysis process at a specified temperature. The population of the reversibly deformed intermediate state rises quickly to a maximum value and then diminishes monotonically as the number of cells in the original state is reduced. The experimental observations of Moussa *et al.* [151] are in qualitative agreement with this behavior, although they did not obtain this quantitative information from their results.

Alternatively, Moussa *et al.* [151] also presented a statistical model by which the data could be correlated. It was assumed that a susceptibility to thermal damage, s , could be assigned to each cell as a function of its present state (age, prior damage, etc.). The value of s was assumed to be linearly proportion to the reciprocal of the time to death during exposure to an elevated temperature, T . For a normal distribution of s among a population of cells, the number n having a given susceptibility is given by the standard distribution equation:

$$n(s) = \frac{N}{d\sqrt{2\pi}} \exp\left[-\frac{(s-m)^2}{2d^2}\right] \quad (6.14)$$

where m and d are the mean (50%) and standard deviation of the susceptibility and N is the total number of cells that constitute the population:

$$N = \sum n(s)$$

The cumulative fraction of cells with susceptibility threshold of s or larger is given by the standard integral of the normal distribution

$$F(s) = \frac{1}{N} \int_0^s n(s) ds \quad (6.15)$$

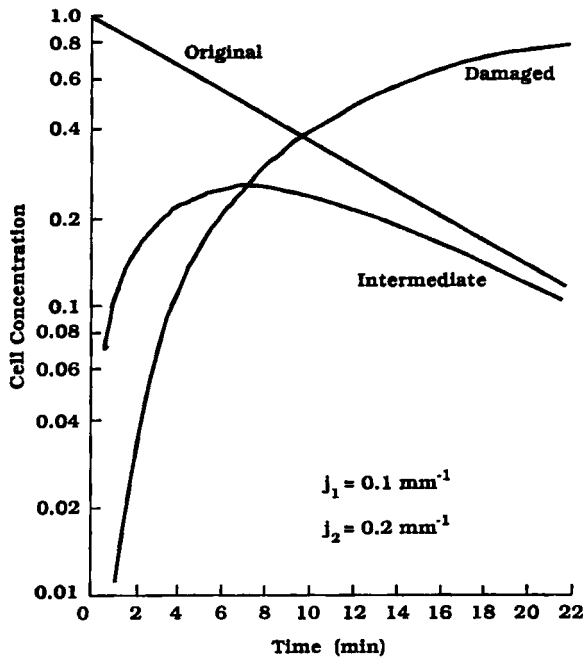


Fig. 84. Transient variation in the distribution of cells among the initial, deformed, and damaged states during exposure to an elevated temperature as predicted by the two stage kinetic injury model. (Redrawn from Moussa *et al.* [151, Fig. 6, p. 216], with permission.)

The temperature dependence of the m and d functions is shown in Fig. 85 as determined from the mean and standard deviations of the experimental hemolysis data. Over the range for which trials were conducted the data indicate that the parameters for the statistical model for injury vary directly with the magnitude of the insult temperature. The difference in criterion for defining the empirical coefficients of the statistical model issue in this difference from adherence to the Arrhenius equation that characterizes other analyses of thermal injury. This model provides no mechanistic interpretation of the injury process as is inherent in the Arrhenius damage models. Nonetheless, the correlation with the experimental data is good, and as Moussa *et al.* noted, it is considerably more accurate than their mechanistically based kinetic model.

The basic Arrhenius format for description and analysis of thermal injury processes has been applied further in many application areas other than those discussed above. For example, Henle [98] has demonstrated the utility of Eq. (4.5) to model the damage to cells and tissues under protocols typical of hyperthermia therapy of cancer. These protocols are effected at much

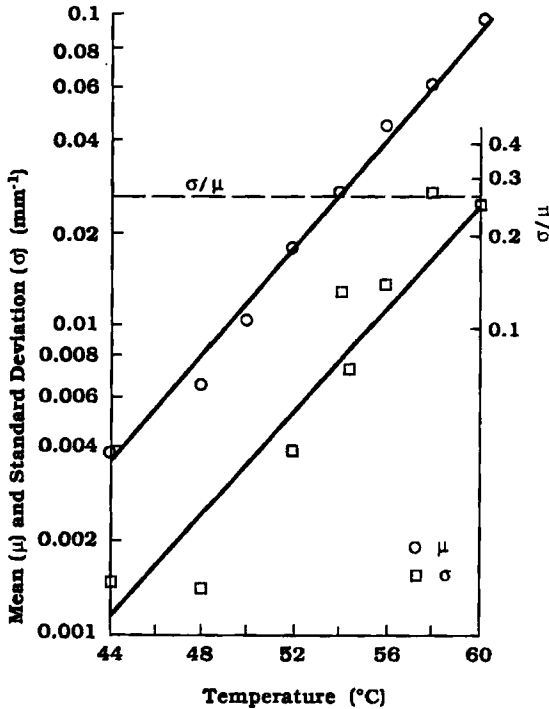


FIG. 85. Temperature dependency of the mean m and standard deviation d of the susceptibility of human erythrocytes to thermally induced hemolysis. (Redrawn from Moussa *et al.* [151, Fig. 5, p. 216], with permission.)

lower temperatures and longer times of exposure than encountered in burns and laser irradiations. In many cases, the thermal state is quite close to the threshold conditions for producing measurable thermally induced damage. It is interesting that the coefficients for the Arrhenius function determined for hyperthermic threshold injury to cells have been extrapolated to describe the creation of a skin burn owing to low level prolonged thermal insult by a common electric heating pad (Diller [56]).

In addition to the above models, most of which correspond in format quite closely with the original work of Henriques more than 40 years ago, Xu *et al.* [229] have recently postulated a new form for the injury function. Their model is based on the assumption that the denaturation of enzymes is quite different from common chemical reactions. In particular, the binding of substrate to enzymes acts to stabilize the enzyme and thereby hinder its participation in the deactivation reaction. As a consequence, only the free enzyme is able to participate in deactivation in contrast with the first order reaction conditions assumed for the standard Arrhenius model in which the

rate of deactivation occurs in direct proportion to the total enzyme concentration. Accordingly, Xu *et al.* have developed a model incorporating two exponential functions and in which temperature is treated as a dimensionless quantity referenced to the normal physiological state, which is taken as the initial conditions for the injury process. This injury model is expressed as

$$\frac{d\Omega(x)}{dt} = \frac{\xi \exp\left[\frac{\Delta E}{\mathfrak{R}T_i(1 - \vartheta^{-1})}\right]}{1 + \mathfrak{A} \exp\left[\frac{\Delta E_{es}}{\mathfrak{R}T_i(1 - \vartheta^{-1})}\right]} \tag{6.16}$$

where ΔE_{es} is the difference in the energies of formation and decomposition of the enzyme/substrate complex. By assuming what they considered to be reasonable values for the five constants (T_i , ξ , \mathfrak{A} , ΔE , and ΔE_{es}) in Eq. (6.16), Xu *et al.* were able to plot the behavior of the damage rate parameter as a function of temperature in comparison with the Henriques model, as shown in Fig. 86. The anticipated break point in the damage

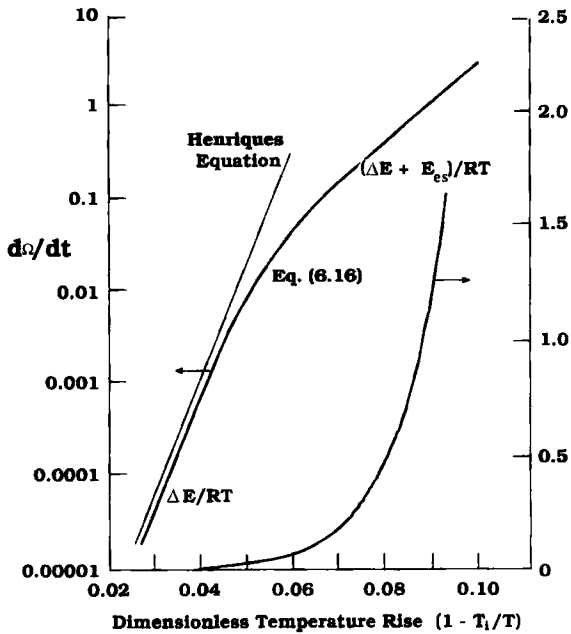


FIG. 86. Comparison of the rate of thermal damage predicted by the Henriques and Xu models as a function of dimensionless temperature. (Redrawn from Xu *et al.* [229, Fig. 1], with permission.)

function is observed at an intermediate range of temperatures for the Xu model. Similar behavior has been achieved by other investigators by designating discontinuous values of the Henriques model constants in order to achieve a better match with burn data over a broader range of temperatures. These modified models will be discussed in the following section. Xu's model is yet to be compared with experimental data to evaluate its ability to describe physiological behavior, but it does present a formulation of the injury process that has a more rigorous mechanistic basis than has been available previously.

B. COMPARISON OF THERMAL INJURY MODELS

The availability of computer simulation models provides a powerful companion to experimental trials for the study of some aspects of thermal burn injury processes in animals and human models. In addition, by using the computer for simulation it is possible to evaluate a large number of alternative burn protocols in a short time. A primary and often overriding consideration in the implementation and evaluation of computer simulations concerns their accuracy and validity in the absence of corroborating experimental data for trials conducted on living subjects. Over the past 40 years a number of different thermal damage models have been hypothesized and tested to varying degrees of rigor and generality. Each of these models was obtained by correlation with a set of burn data defined by a limited set of insult conditions. Confidence in the model results will be greatest for simulations that fall within the range of parameters upon which the model was derived. However, it is often of interest to extrapolate the model to predictions in regimes in which it is difficult to acquire experimental data. Since nearly all damage models are based on extremely nonlinear functions, the accuracy of the results of such extrapolations may be highly questionable, and verification is also a challenging task.

Recent dramatic increases in the capacity and speed of computational machinery and the availability of powerful and versatile numerical modeling techniques have made it relatively easy to model a given burn scenario and to implement burn injury models in order to estimate the overall response in the tissue. Although it is a simple matter to generate numbers on a computer, the crucial question remains as to how the results of a simulation correlate to the real problems encountered in the treatment of clinical burn wounds. Blake *et al.* [17] have performed a comparative analysis of several of the available models for predicting the severity of burns to the skin for defined environmental thermal insults in an attempt to provide some useful information to help answer this question.

The transient temperature distribution in blood perfused skin may be described quantitatively in terms of the bioheat transfer equation as first applied by Pennes [165]:

$$\rho c \frac{\partial T}{\partial t} = \nabla \cdot k \nabla T + \omega_b c_b \rho_b (T - T_a) + Q \quad (6.17)$$

where Q is the metabolic heat generation rate. The term on the left of Eq. (6.17) represents the local rate of energy storage in tissue, whereas the three terms on the right describe in order the conduction of heat in the tissue due to an internal temperature gradient, the convective exchange of heat between the tissue and blood perfused through the microvasculature, and the distributed internal energy generation associated with metabolism.

Blake *et al.* [17] have adapted the finite element method (Diller and Hayes [58]) to solve Eq. (6.17) with initial and boundary conditions appropriate to specific burn scenarios. The temperature solution was then in turn applied to a damage integral equation, such as that initially proposed for this purpose by Henriques and Moritz [100], to determine a map of how the injury develops progressively in the skin during and after a burn exposure. Damage models were based on the assumption that the local injury process obeys an Arrhenius-type function (Benson [11]) so that the rate of injury was dependent on the absolute temperature. For a two-dimensional transient temperature function, as was modeled by Henriques and Moritz, the instantaneous rate of injury induced is given by

$$\frac{\partial \Omega(x, y, t)}{\partial t} = \xi \exp\left(-\frac{\Delta E}{\Re T(x, y, t)}\right) \quad (6.18)$$

where Ω is the damage function, ΔE is an apparent activation energy for the injury process reaction, \Re is the universal gas constant, and ξ is the frequency factor in the damage integral. Ω is a measure of the extent of injury incurred, and is in general a monotonic, nonlinear function. Its value is associated with empirical observations of the degree of thermal damage experienced for controlled experimental trials. The rate of damage described by Eq. (6.18) may be integrated over the elapsed time from the beginning of exposure to elevated temperatures in order to determine the total accrued injury at any site within the tissue. The Henriques injury model then becomes

$$\Omega(x, y, t) = \xi \int_0^t \exp\left(-\frac{\Delta E}{\Re T(x, y, t)}\right) dt \quad (6.19)$$

There exist a number of different combinations of values for the frequency factor ξ and apparent activation energy ΔE that may be applied in Eq. (6.19) for estimation of the extent of thermal injury, each of which

corresponds to a different model of the burn process. Although all of the models will operate with the identical time/temperature data base, each may predict a unique and distinct degree of injury as a function of the values of these empirical coefficients.

Blake *et al.* [17] compared five different burn models as presented by Henriques [99], Fugitt [76], Weaver and Stoll [213], Takata [202], and Wu [228]. All of the models were developed by empirically fitting an equation in the same format as Eqs. (6.18) and (6.19) to experimental data, with some method of adjusting the values of ζ and ΔE to obtain an optimal match over the range of states for which the data were available. The values for ζ and ΔE for each of the five models are listed in Table X. In each of the models, excepting the earliest one of Henriques, the coefficients are temperature dependent in order to obtain a better match with the source data across a broad spectrum of burn scenarios.

The difference in the sets of coefficients are a consequence of variations in the experimental data bases applied to define the models and individual emphases of the investigators in analyzing the burn process. A comparison of the various models as they relate to scald injuries has been performed by Palla [155]. Briefly, Henriques, who was the first to apply the bioheat equation to burn injury prediction, used data from a study of the relationship between exposure times to flowing hot water and the onset of a threshold level of injury. His model did not include any consideration of the continuation of injury during the cool down period after removal of the heat source. Henriques obtained a good match of the model to his

TABLE X
ACTIVATION ENERGY ΔE AND FREQUENCY FACTOR ζ VALUES DEFINED
FOR FIVE THERMAL INJURY MODELS

Model	Temperature range (°C)	Activation energy ΔE (J/kmole)	Scaling factor ζ (1/s)
Henriques	All T	6.27×10^8	3.1×10^{98}
Fugitt	$T \leq 55$	6.27×10^8	3.1×10^{98}
	$T > 55$	2.96×10^8	5.0×10^{45}
Stoll	$T \leq 50$	7.82×10^8	2.185×10^{124}
	$T > 50$	3.27×10^8	1.823×10^{51}
Takata	$T \leq 50$	4.18×10^8	4.322×10^{64}
	$T > 50$	6.69×10^8	9.389×10^{104}
Wu	$T \leq 53$	6.27×10^8	3.1×10^{98}
	$T > 53$	6.27×10^8 $-5.10 \times 10^5 (T - 53)$	3.1×10^{98}

experimental results for long burn times, but there was a significantly greater discrepancy for shorter burns such as those typically experienced during scalding. Fugitt attempted to improve the simulation capability for shorter duration burns by introducing a two stage temperature activation model, but his results were not significantly better. Stoll and Takata determined parameters that best fit their own data and injury criteria. Wu most recently adopted an averaging technique for determining an apparent activation energy, ΔE , which is dependent upon tissue temperature. It is important to realize that all five of these models are based to some degree on their specific experimental protocols. However, in all cases, ξ and ΔE were fit to the data so that values of $\Omega = 0.53$, $\Omega = 1.0$, and $\Omega = 10^4$ corresponded to first-, second-, and third-degree burn injuries, respectively.

A simplified limiting case was also considered in which the temperature is assumed to be constant throughout the injury process. The damage function then becomes

$$\frac{d\Omega}{dt} = \xi \exp\left(-\frac{\Delta E}{\mathfrak{R}T}\right) \tag{6.20}$$

which can be integrated to obtain an expression for the injury after a time t as

$$\Omega = \xi \exp\left(-\frac{\Delta E}{\mathfrak{R}T}\right)t \tag{6.21}$$

Table XI gives the rate of thermal damage for a constant temperature exposure. Damage values are very low for small elevations in tissue temperature and they increase very rapidly for temperatures above the range of 50–60 °C. The models agree qualitatively for low levels of damage. The Henriques and Takata models correspond reasonably well over all temperatures evaluated; however, these data show a pronounced variation among the damage models for high temperatures. Table XII presents

TABLE XI
RATE OF THERMAL DAMAGE CALCULATED BY THE FIVE INDICATED BURN MODELS,
EQ. (6.20), FOR TISSUE HELD AT A CONSTANT TEMPERATURE

Model	Exposure temperature (°C)						
	40	50	60	70	80	90	100
Henriques	2.67×10^{-6}	4.50×10^{-3}	4.75×10^0	3.38×10^3	1.60×10^6	5.77×10^9	1.47×10^{11}
Fugitt	2.67×10^{-6}	4.50×10^{-3}	3.40×10^{-1}	7.53×10^0	1.40×10^2	2.22×10^3	3.00×10^4
Stoll	4.03×10^{-6}	4.18×10^{-2}	1.79×10^0	5.51×10^1	1.39×10^3	2.95×10^4	5.30×10^5
Takata	1.82×10^{-5}	2.60×10^{-3}	4.34×10^0	4.78×10^3	3.50×10^6	1.80×10^9	6.70×10^{11}
Wu	2.67×10^{-6}	4.50×10^{-3}	1.71×10^{-1}	6.90×10^4	1.76×10^8	2.89×10^{11}	3.20×10^{14}

TABLE XII
EXPOSURE TIME (IN SECONDS) REQUIRED TO REACH THRESHOLD 1ST-, 2ND-, AND 3RD-DEGREE BURNS FOR THE FIVE INDICATED BURN MODELS IN TISSUE HELD AT THE INDICATED CONSTANT TEMPERATURES

Model	Burn severity	Exposure temperature (°C)		
		40	60	80
Henriques	1st	1.98×10^5	1.11×10^0	3.30×10^{-7}
	2nd	3.75×10^6	2.10×10^0	6.25×10^{-6}
	3rd	3.75×10^9	2.10×10^3	6.25×10^{-3}
Fugitt	1st	1.98×10^5	1.53×10^{-7}	3.80×10^{-3}
	2nd	3.75×10^6	2.95×10^{-6}	7.14×10^{-2}
	3rd	3.75×10^9	2.95×10^{-3}	7.14×10^1
Stoll	1st	1.31×10^5	2.95×10^{-1}	4.00×10^{-4}
	2nd	2.48×10^6	5.57×10^0	7.20×10^{-3}
	3rd	2.48×10^9	5.57×10^3	7.20×10^0
Takata	1st	2.90×10^4	1.22×10^{-1}	1.50×10^{-7}
	2nd	5.50×10^5	2.30×10^0	2.86×10^{-6}
	3rd	5.50×10^8	2.30×10^3	2.86×10^{-3}
Wu	1st	1.98×10^5	7.31×10^{-2}	7.12×10^{-9}
	2nd	3.75×10^6	1.38×10^0	1.34×10^{-7}
	3rd	3.75×10^9	1.38×10^3	1.34×10^{-4}

the time required to reach first-, second-, and third-degree wounds for a constant temperature exposure according to each of the five models. Once again, significant discrepancies among the models are evident. At low burn temperatures, damage occurs at a relatively slow rate so that these differences are not significant. However, at higher thermal exposures the models predict quite different results.

If the tissue temperature is a linear function of time so that

$$T = t_0 t \quad (6.22)$$

where t_0 is a constant, then the rate of thermal damage accrual is

$$\frac{d\Omega}{dt} = \xi * \exp\left(-\frac{\Delta E}{\Re t_0 t}\right) \quad (6.23)$$

$$\Omega = \frac{\xi \Re t_0}{\Delta E} * \exp\left(-\frac{\Delta E}{\Re t_0 t}\right) * t^2 \quad (6.24)$$

Values for the rate of damage were determined by direct solution of Eq. (6.23) for each of the five models to be studied and are plotted in Fig. 87. Since the value of $\partial\Omega/\partial t$ is a function of both t_0 and time, the

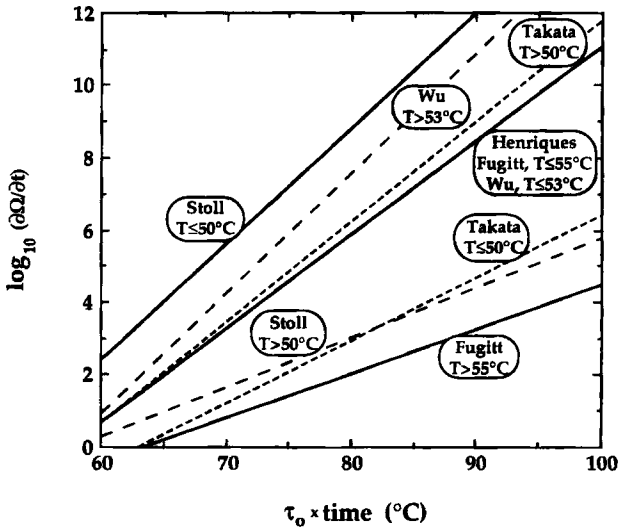


FIG. 87. Analytical solutions for the damage rate function at increasing time of exposure as obtained from Eq. (6.23) for each of the thermal injury models studied. (From Blake *et al.* [17, Fig. 1], with permission.)

horizontal axis represents the product $t_0 \cdot \text{time}$. Four of the five models use two sets of values for parameters, depending upon temperature. Figure 87 includes separate graphs for each of these cases. This result again illustrates that all five models predict very little thermal damage for low temperature elevations or for very short time durations. This function is easily integrated to give the total accumulated injury at any specified location when the linear thermal history is assumed. In the following section the model is applied to thermal insult protocols that more closely correspond to the type of temperature histories experienced in common burn injuries.

A finite element model was used to simulate standard thermal insult protocols in a simulated skin tissue. The computed transient temperature field was applied in the damage equation for each of the five burn models to predict the extent and distribution of thermal injury in the skin. Insult scenarios consisted of direct contact to the skin with a heated circular disc 1 cm in diameter, maintained at a defined constant temperature for a specified period of time. The skin was represented as a three layer structure as illustrated in Fig. 88.

A disc having a constant surface temperature set between 60 and 100 °C was applied to the skin for times varying between 0.2 and 20 s. Simplifying assumptions used in developing the mathematical model include (1) cylindrical symmetry, (2) homogeneous and isotropic properties within

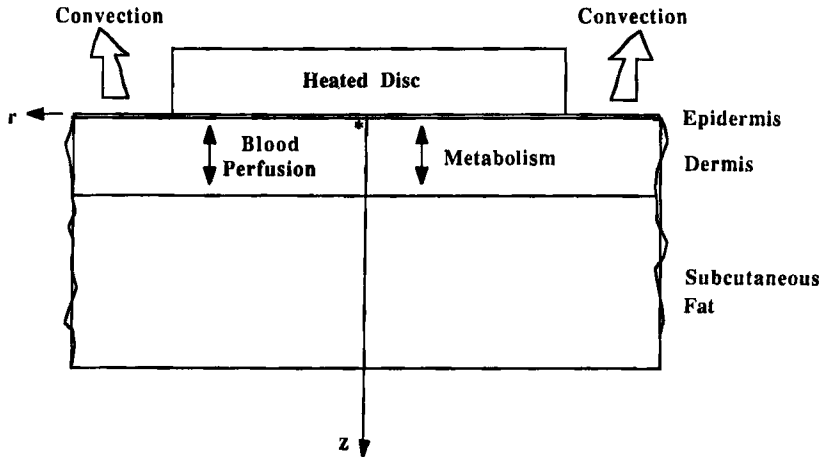


FIG. 88. Multilayered skin model used for burn simulations. A reference location for evaluating the progression of thermal injury is indicated by an asterisk (*) at the interface between the dermis and epidermis along the system centerline. (From Blake *et al.* [17, Fig. 2], with permission.)

the individual epidermal, dermal, and subcutaneous strata, (3) blood perfusion only in the dermis (experimental evidence indicates that the perfusion of blood in the affected tissue may exert a significant influence on the thermal history produced), (4) continuity of energy flux and temperature at all tissue interfaces, and (5) negligible metabolic contributions to the overall energy balance. By applying the above assumptions and accounting for cylindrical geometry, Eq. (6.17) becomes

$$\rho c \frac{\partial T}{\partial t} = \frac{1}{r} \frac{\partial}{\partial r} \left(k \frac{\partial T}{\partial r} \right) + \frac{\partial}{\partial z} k \frac{\partial T}{\partial z} + \omega_b r_b c_b (T - T_a) \quad (6.25)$$

A finite element solution to Eq. (6.25) was obtained after identification of a specific tissue morphology and appropriate initial and boundary conditions. In each of the skin layers, all tissue properties were assumed to remain constant with respect to time, temperature, and position. The temperature and the heat flux were constrained to be continuous at all material interfaces. In the initial state the skin was assumed to have a uniform temperature, T_i , of 34 °C. A step change in temperature was then applied over a 1-cm diameter circular area on the epidermal surface, and maintained constant for a specified period of time. The mathematical conditions describe a burn insult in which the skin is contacted by the heated circular disc. It was assumed that the epidermal surface was in perfect contact with the disc throughout the period of contact. The area of

elevated surface temperature was aligned symmetrically with the cylindrical coordinate system of the model. Surface areas peripheral to the disc were assumed to experience convective heat transfer with ambient air at 27 °C during the burn process. After completion of the insult period, the disc was removed and the entire skin surface was cooled by convection to the air. Zero heat flow conditions at remote boundaries in both the axial (z) and the radial (r) coordinates were implemented. The radial temperature gradient along the centerline of the system ($r = 0$) was held at zero to satisfy conditions of geometric and thermal symmetry. Values of the tissue properties and convective heat transfer parameters that were applied to calculate the transient temperature field in the skin during and subsequent to the period of the insult process are listed in Table XIII.

The boundary value problem defined by Eq. (6.25) and the initial and boundary conditions described above were solved by using a two-dimensional transient finite element program. A grid of rectangular and triangular elements, shown in Fig. 89, was developed which corresponds to the morphology of the composite skin layers and in the approximate pattern anticipated for the two-dimensional temperature distribution during the heating phase of the burn. The grid consisted of 100 linear elements and 116 nodes.

TABLE XIII

PARAMETER VALUES APPLIED FOR BURN INJURY MODEL COMPARISON COMPUTATIONS

Symbol	Parameter	Value
c	Specific heat of skin	4.0×10^3 (J/kg•s)
c_b	Specific heat of blood	3.3×10^3 (J/kg•s)
h	Convection coefficient with air	8.4 (W/m ² •K)
k	Thermal conductivity of skin	
	Epidermis	2.1×10^{-1} (W/m•K)
	Dermis	3.7×10^{-1} (W/m•K)
	Subcutaneous fat	1.6×10^{-1} (W/m•K)
Q	Metabolic heat generation	0
T_a	Temperature of arterial blood	37 (°C)
ρ	Density of skin	1.04×10^3 (kg/m ³)
ρ_b	Density of blood	1.10×10^3 (kg/m ³)
ω_b	Blood perfusion rate	
	Epidermis	0
	Dermis	2.4×10^{-2} (ml blood/ml tissue•s)
	Subcutaneous fat	0

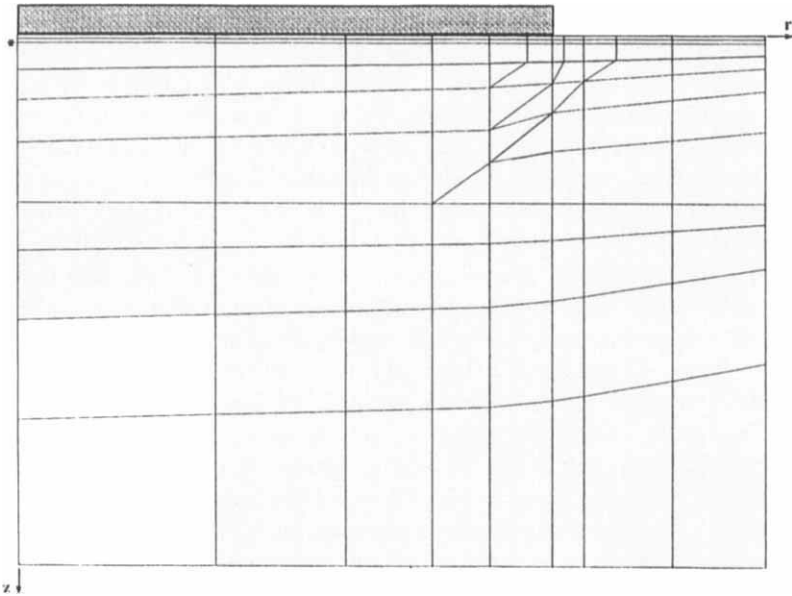


FIG. 89. Finite element grid network to match the geometry of the composite skin model of Fig. 88 and the anticipated contour and concentration of temperature isotherms that develop during surface heating. An asterisk (*) denotes the reference location identified in the previous figure. (From Blake *et al.* [17, Fig. 3], with permission.)

The finite element program produced transient temperature values at nodal points, which were available in both tabular and graphical formats. An example of the temperature contours generated within the skin by an 70°C contact burn after an elapsed time of 5 s is shown in Fig. 90. For any given simulation protocol similar contours were calculated and plotted at time increments for the entire heating and cooling periods. The thermal data were then used to predict the instantaneous rate of injury occurring locally at each of the nodal positions. The local rate of injury was determined at each node for each time interval during the computational process by evaluating Eq. (6.19) for a given injury model. Total injury was accumulated over the entire period of both heating and cooling.

Figure 91 presents a set of injury contours (i.e., values for Ω as a function of position) for the thermal conditions described in Fig. 90, in which damage was determined according to the criteria of Henriques [99]. Values of Ω describe the severity of burn injury on an exponential scale that has been widely adopted from the pioneering work of Henriques, and which provides a basis for quantifying the physiological manifestation of the injury. Although this criterion has been developed progressively on the

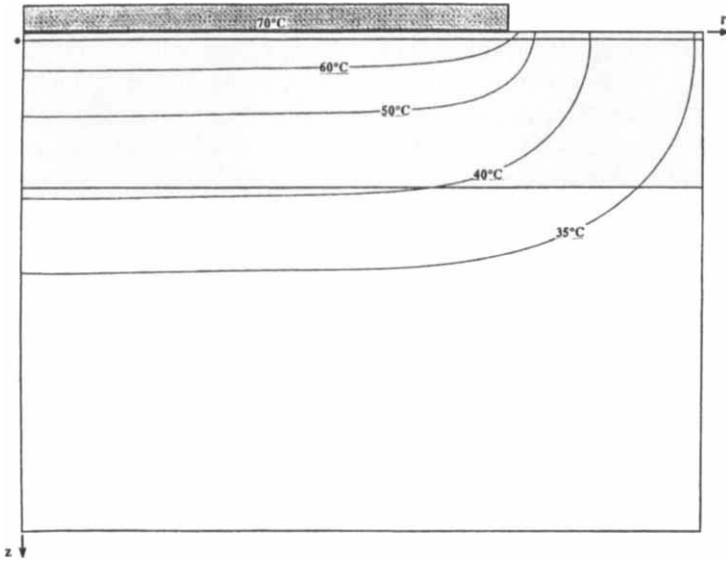


FIG. 90. Temperature contours within the skin after 5 s of exposure to a 70 °C contact heat source on the epidermis. (From Blake *et al.* [17, Fig. 4], with permission.)

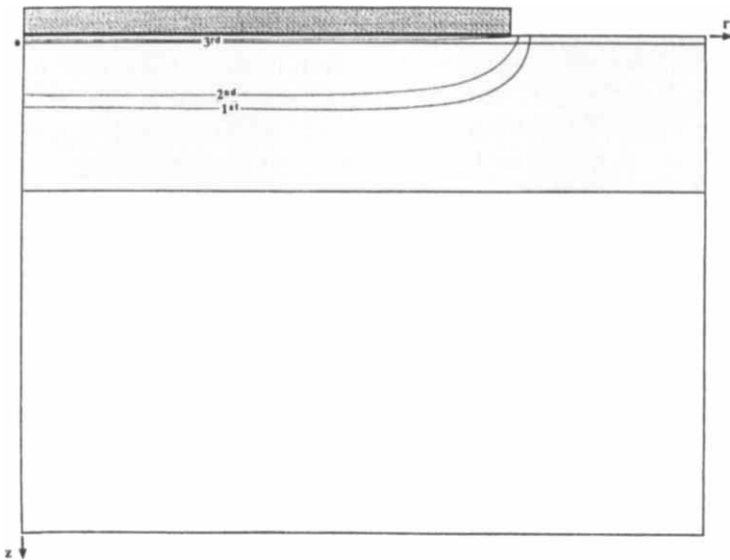


FIG. 91. Injury contours at threshold damage levels within the skin at 5 s after the initiation of exposure to a 70 °C heat source, as calculated by the Henriques model. (From Blake *et al.* [17, Fig. 5], with permission.)

clinical and macroscopic experimental scale, studies of the microscopic scale physiological response have confirmed its validity, at least over the range of mild burns that characterize many experimental protocols. The injury contours can be seen to correspond quite closely to those for temperature, as should be expected from Eq. (6.19) due to the strong dependence of Ω on T .

The injury models were all compared for a range of common burn protocols consisting of combinations of exposure times from 0.2 to 20.0 s and burn temperatures from 60 to 100 °C. These protocols produced a wide spectrum of burn conditions and injury severities which afford a broad basis to compare the injury models, and which provide an extensive map of thermal damage as a function of burn insult history. The first set of comparisons was run for insult temperatures at 10° increments between 60 and 100 °C with a fixed time duration of 1.0 s. The total cumulative injury was determined with each of the five models at a location at the interface between the epidermis and the dermis directly under the center of the burn area. This position in the tissue is indicated in Figs. 88 and 89. These data are plotted in Fig. 92, and display several distinct features that illustrate comparative aspects of the models. All of the models predict an increase in the extent of damage with higher burn temperatures, as they should based on Eq. (6.19). However, the magnitude of this increase with temperature varies dramatically among the models, and the disparity is the largest for the most severe burns. The ratios of predicted injury among the various models also are not constant as the burn protocol changes. As an illustration, for a 60 °C burn Wu and Fugitt predict nearly identical injuries, whereas at 100 °C the damage parameter Ω for Wu exceeds that for Fugitt by a factor of approximately 10 million. At 60 °C Stoll predicts the greatest

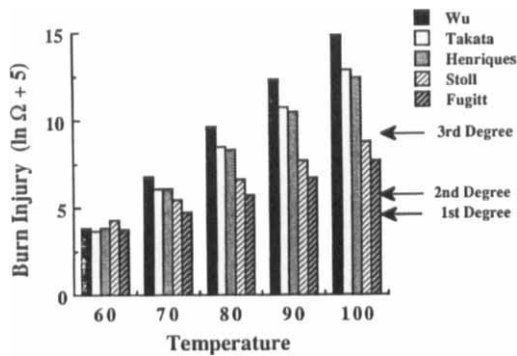


FIG. 92. Total cumulative injury calculated by the five models for 1-s burns at the indicated temperatures. (From Blake *et al.* [17, Fig. 6], with permission.)

injury, but an increase in temperature to only 70 °C results in the higher injury for the Wu, Takata, and Henriques models. Thus, as defined in Eq. (6.21), the damage functions are not linear, and it should therefore not be expected that extrapolation of the models across broad temperature ranges would be straightforward and consequently comparisons among the models will not be linear.

An additional aspect illustrated in Fig. 91 is that the agreement of the models is by far the best at 60 °C, and the discrepancies enlarge progressively as the temperature increases. It may be anticipated that such behavior should be observed since the models are all based on correlations with experimental data weighted to lower temperatures, and their consistency should be best in the regime over which they are fitted. Consequently, in evaluating a burn caused by an insult at 70 °C for 1.0 s, Fugitt’s model predicts a first-degree burn, Stoll’s model predicts a burn intermediate between first- and second-degree, Takata’s and Henriques’s models both predict exactly a second-degree burn, and Wu’s model predicts a burn that is between second and third degree. In general, the predicted degree of injury is exponential with respect to surface temperature, but the sensitivity of the rate of injury with respect to temperature is unique for each model. Therefore as the burn temperature increases, the models have an increasing propensity to deviate one from another.

Figure 93 illustrates for a 5-s burn at 80 °C how total injury severity varies at incremental locations in the skin. Once again, it is apparent that

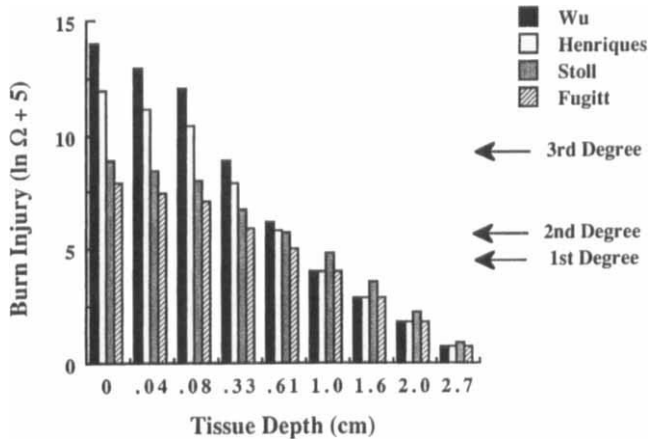


FIG. 93. Total cumulative injury at various depths into the tissue after completion of a burn at 80 °C for 5 s and postburn cooling to the initial temperature. Injury was computed for the same temperature history for four different damage models. (From Blake *et al.* [17, Fig. 7], with permission.)

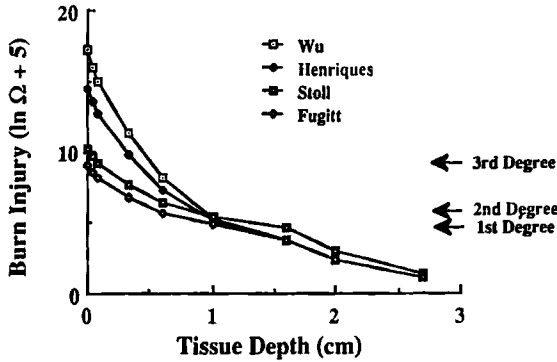


FIG. 94. Total cumulative injury computed for four different damage models at incremental depths into the tissue after completion of a burn at 90°C for 5 s and subsequent postburn cooling back to the initial temperature. The data are viewed from the perspective of a linear depth scale to illustrate the extent of penetration of thermal damage into the tissue. (From Blake *et al.* [17, Fig. 8], with permission.)

deeper in the tissue where only moderate intensity burns are predicted, the agreement among the models is best. When the data for a 90°C burn are viewed from the perspective of a linear depth coordinate in Fig. 94, the relative spatial distribution of injury is illustrated more clearly. Thus, the differentiation among the models is protocol dependent, i.e., intermodel variations do not occur according to a simple linear scaling factor. A manifestation of this effect can be seen by comparing the Henriques and Stoll results in Fig. 93; Henriques predicts a higher degree of injury near the surface where there is more penetration of the boundary perturbations, whereas Stoll predicts a greater injury at deeper locations. With Henriques's model injury accrues more rapidly at elevated temperatures, whereas Stoll's model is less sensitive to temperature variations. Thus, the gradient in injury severity with position into the tissue is smaller for Stoll's model than for that of Henriques, and Stoll has a more uniform injury field than does Henriques.

Interpretation of these differences should take into account the unique features of the individual models. This difference in modeling prediction makes sense when viewed in light of the fact that the different models have been developed to fit different experimental protocols. Henriques's model was derived to fit experimental data for burns caused by running hot water and did not take into account the possibility of continued damage during the period of surface cool down. Consequently, temperature elevation is weighted more strongly than time of exposure in predicting damage. Stoll's data were correlated for surface contact and irradiation-wounds and included the entire progression of thermal injury. Therefore,

her model places more emphasis on time of exposure in comparison to magnitude of temperature elevation. The variations in Figs. 93 and 94 are supported by these differences in model emphasis. The primary location of continuing damage during surface cooling will be deep into the tissue, since kinetic processes occurring near the surface will respond to alterations in the environment more quickly.

Figure 95 presents the injury predictions of the Henriques model over the entire range of time and temperature combinations that were simulated. These data provide a general guideline for determining the degree of injury that can be expected for thermal insults effected by a broad spectrum of protocols. Because the burn functions are linear on a semilogarithmic scale, by interpolating between Figs. 92 and 95 it is possible to estimate the extent of injury that will be predicted by any of the models for burn times between 0.2 and 20 s and temperatures between 60 and 100 °C. Although the simple interpolation of numerical results is straightforward, a spirit of caution must be exercised in interpretation of the results since it is easy to extrapolate the injury model predictions beyond the domain of independent experimental verification. The valid regime of burn protocols must always be realized when using the models as a tool for prediction of thermal injury. In general, confidence in the models will decrease with very severe levels of damage, such as for $\Omega \geq 10^4$.

Figure 96 illustrates the variation of maximum temperature with time at the epidermal-dermal interface for various burn temperatures. These data are obtained from the finite element solution of Eq. (6.25), and are independent of any assumptions relating to specific injury models. The

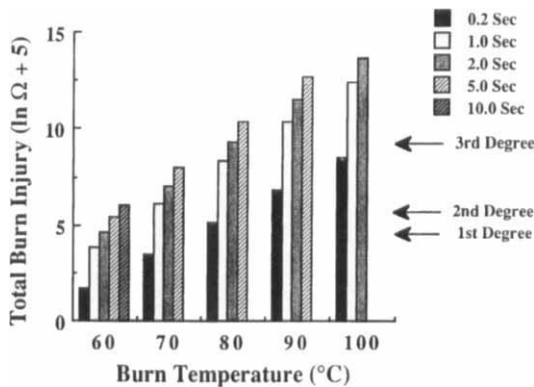


FIG. 95. Total injury accrued at the interface between the epidermis and dermis along the system centerline for combinations of burn time and temperature over the range of parameters evaluated. (From Blake *et al.* [19, Fig. 9], with permission.)

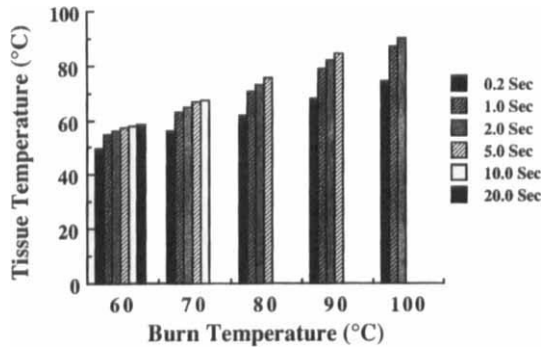


FIG. 96. Maximum temperature reached at the interface between the epidermis and dermis along the system centerline for discrete exposure times to specified surface temperatures. (From Blake *et al.* [17, Fig. 10], with permission.)

maximum temperature achieved is linearly related to surface temperature for each of the burn durations illustrated. However, the temperature field is dependent on the thermal properties of the skin used for modeling, and these values in turn will effect the injury predictions. Palla [155] showed that for extreme combinations of the thermal properties, the fluid temperature requisite to cause a first-degree scald injury during a 1-s exposure could vary as much as 10 °C. It is important that accurate thermal properties be used when modeling a complex process such as the burn injury. Measurement of the thermal transport properties of living tissue is a challenging task, and is particularly difficult when examining how the properties may be changed with temperature.

Powerful numerical computing techniques such as the finite element method afford the capability for performing versatile and extensive modeling studies of burn injury. Simulations are based on obtaining a solution of the transient temperature field in tissue when subjected to a specified thermal insult either at the boundary or as a distributed internal source. Although the latter category of processes has not been addressed traditionally in the context of studies of burns to the skin, there exists an extensive literature dealing with models of thermal injury due to electrical current dissipation (Pearce [158]), laser irradiation (Birngruber [16]; Welch [216]), ultrasound (Lele [124]), and electromagnetic energy deposition (Jain [106]; Heynick [101]), as indicated by these selected references and as pointed out in previous sections. There has also been considerable effort directed towards identifying accurate values for tissue thermal properties (Bowman *et al.* [24]; Chato [35]), but this has been a difficult task, especially when it is necessary to measure how the properties may vary as a function of temperature (Valvano *et al.* [208]).

The study of Blake *et al.* [17] indicates that the various available burn injury models may yield widely disparate results under given conditions of simulation. Apparent activation energy and frequency factor values have been selected in the different models to provide good correlation with the experimental data in regions of specific burn times and temperatures and for particular burn criteria. Outside of these limits, the models may begin to differ among each other and from experimental data which causes significant discrepancies for a given burn injury protocol. Simulation results must be viewed with a realization of the dangers of model extrapolation, and it is necessary that the many factors that may influence numerical values obtained by a model be taken into consideration when evaluating the results. It is also important to realize that when dealing with living tissue, any numerical model can only provide an approximation to real life conditions. Although mathematical models can be very useful in investigating qualitative behavior, they cannot incorporate with full accuracy the heterogeneous physiology of living tissue.

Summary

The modeling of high and low temperature heat transfer processes in biological tissues presents unique challenges in the formulation and solution of the governing equations. Frequently the geometry is highly irregular, materials are heterogeneous and nonisotropic, transport properties vary nonlinearly as a function of state, property data are scarce, the variation in behavior among physiologically similar systems is very large, and processes of interest may involve multimode energy transfers distributed in space and time. One of the major hurdles in the development of effective models for bioheat transfer processes has been the necessity to realize and define the degree of specificity with which many of the systems of interest must be addressed. In many cases physiological structure and function are highly tuned to the accomplishment of specific tasks, and generalized models that do not account properly for these factors are likely to not provide an acceptably accurate description of the process of interest.

The field of bioheat transfer modeling has been developing at an accelerating pace over the past decade. A greater appreciation for the details of important problems, coupled with more sophisticated techniques for performing tissue property measurements and more accessible and powerful computing facilities, has led to the availability of models which simulate bioheat transfer processes with a higher level of accuracy and understanding than ever before.

This review has outlined the paths that have been followed in arriving at the present state-of-the-art in several important areas of bioheat transfer modeling. The breadth and depth of the coverage are far from comprehensive, but it is hoped that these materials will stimulate and assist many other workers in the pursuit of solutions to the numerous challenges in the interesting field of bioheat transfer.

Nomenclature

SYMBOL

<i>A</i>	ratio of solid/liquid phase thermal diffusivities, α_S/α_L	<i>g</i>	depth of thermal penetration for a flash burn (m)
\mathfrak{A}	reaction rate constant, Eq. (6.16)	<i>H</i>	center magnitude of spectral irradiance (W/m^2)
<i>a</i>	irradiation attenuation factor, Eq. (4.107)	<i>h</i>	convection heat transfer coefficient ($W/m^2 \cdot K$)
<i>B</i>	cooling rate (K/min)	HF	dimensionless heat flux during freezing, Eq. (3.37)
<i>b</i>	radial distribution function of irradiation, Eq. (4.102)	<i>i</i>	current density (A/m^2)
Bi	Biot number, $h \cdot L/k$, $h \cdot r_o/k$	<i>J</i>	molecular flux ($mole/m^2 \cdot s$)
<i>C</i>	concentration ($mole/m^3$)	<i>j</i>	reaction rate constant for thermal injury processes ($1/s$)
<i>C</i>	heat capacity matrix for finite element formulation ($J/m^3 \cdot K$)	<i>K</i>	spatial gradient in temperature (K/m)
<i>c</i>	specific heat ($J/kg \cdot K$)	<i>K</i>	thermal conductivity matrix for finite element formulation ($W/m^3 \cdot K$)
ρ	apparent specific heat, Eq. (3.20) ($J/kg \cdot K$)	<i>k</i>	thermal conductivity ($W/m \cdot K$)
CR	dimensionless cooling rate, $CR = \partial\Theta/\partial Fo$	<i>L</i>	length dimension of a system (m)
CRR	dimensionless cooling rate ratio, Fig. 3	<i>l</i>	position along Cartesian coordinate (m)
<i>d</i>	depth (m)	<i>m</i>	mean susceptibility of a cell population to thermal injury ($1/s$)
<i>d</i>	standard deviation for a population of cells to thermal injury ($1/s$)	<i>N</i>	function defined in inverse Wissler transform, Eq. (4.69)
<i>E</i>	electric field strength (V/m)	<i>N</i>	total number of cells in a population
ΔE	energy of activation ($J/mole$)	Nu	Nusselt number
<i>F</i>	position of an equivalent freezing front, Eq. (3.35) (m)	<i>n</i>	number of cells having susceptibility <i>s</i> to thermal injury
<i>F</i>	fraction of cells with a threshold susceptibility <i>s</i> to injury	<i>P</i>	permeability of membrane (m/s)
<i>f</i>	frequency (Hz)	<i>p</i>	function defined in Wissler transform, Eq. (4.66)
Fo	Fourier number, $\alpha \cdot t/L^2$, $\alpha \cdot t/r_o^2$	Q	point heat source at phase interface, Eq. (3.32) (W/m^2)
Fo*	cooling parameter for containers, Eq. (3.42a) ($K \cdot mm^2/s$)	<i>Q</i>	heat generation rate (W/m^3)
Fz	dimensionless freezing parameter, Eq. (5.8)	<i>q</i>	heat flux (W/m^2)
<i>G</i>	dimensionless heat flux function, Eq. (4.15)		
<i>g</i>	acceleration of gravity (m/s^2)		

R	dimensionless position in cylindrical and spherical coordinates, r/r_o	t	time constant for laser irradiation (s)
\mathfrak{R}	universal gas constant, Eq. (4.4) (J/gmole \cdot K)	U	fraction of a cell population in a particular stage of injury
r, ϕ, z	cylindrical coordinates (m)	u	dimensionless thermal diffusion time, Eq. (4.23)
r, ϕ, θ	spherical coordinates (m)	V	velocity (m/s)
Ra	Rayleigh number, Eq. (3.41)	v	dimensionless irradiation image profile
S	ratio of solid and liquid phase properties, Eq. (3.14)	W	transmission of irradiation through tissue
s	dimensionless phase front position	w	weight (kg)
s	susceptibility of a cell to thermal injury (1/s)	X	dimensional position in Cartesian coordinates, x/L
Ste	Stefan number, $c\tau/\Lambda$	x, y, z	rectangular coordinates (m)
T	temperature (K)	Y	dimensionless parameter for freezing analysis, Eq. (5.8)
ΔT_{sat}	temperature difference between boiling surface and saturation state of liquid nitrogen, Eq. (3.41) (K)	Z	dimensionless parameter for freezing analysis, Eq. (5.8)
t	time (s)		

GREEK LETTERS

α	thermal diffusivity (m ² /s)	λ	wavelength (m)
β	volumetric coefficient of expansion (1/K)	λ	Lamé constant of elasticity, Eq. (5.22) (N/m ²)
β_n	roots of transcendental, Eqs. (2.7), (2.14), (2.18), (3.12)	μ	Lamé constant of elasticity, Eq. (5.23) (N/m ²)
γ	time constant for therm diffusion to a depth l , $l/2\sqrt{\alpha}$ (s ^{1/2})	μ	viscosity (N s/m ²)
δ	displacement (m)	ν	Poisson's ratio
ϵ	anisotropy constant for light scattering in tissue, Eq. (4.134)	Ξ	cooling rate representation parameter
ζ	scaling constant for temperature distribution (K/m)	ζ	frequency scaling parameter in rate process models (1/s)
η	absorption coefficient (1/m)	Π	nodal stretching ratios for finite difference grids
Θ	dimensionless temperature differential, $T - T_e/T_i - T_e$	ρ	density (kg/m ³)
θ	dimensionless temperature differential, $T - T_F/T_F - T_e$	ρc	equivalent specific heat capacity, Eq. (3.34) (J/m ³ K)
I	penetrating radiation flux (W/m ²)	ς	dimensionless diffusion time, Eq. (4.17)
ϑ	nonpenetrating radiation flux (W/m ²)	σ	$1/e^2$ radius of a Gaussian irradiation pattern (m)
K	reflection coefficient, Eq. (4.30) (1/m)	σ	electrical conductivity (Ω^{-1} /m)
κ	attenuation coefficient, Eq. (4.110) (1/m)	σ_{rr}	radial stress component (N/m ²)
$\underline{\kappa}$	equivalent thermal conductivity, (Eq. (3.33) (W/m K)	$\underline{\sigma}_{rr}$	normalized radial stress component, Eq. (5.26)
Λ	latent heat of fusion or vaporization (J/m ³)	$\sigma_{\theta\theta}$	azimuthal stress component (N/m ²)
		$\underline{\sigma}_{\theta\theta}$	normalized azimuthal stress component, Eq. (5.27)
		τ	temperature differential, $T - T_i$ (K)

Φ	dimensionless position in a diffusing medium, $x/2(\alpha t)^{1/2}$	χ	scattering coefficient (1/m)
Φ	normalized fluence rate for light	Ψ	constants in series solutions (2.5), (2.12), (2.16)
ϕ	fluence rate for light (W/m^2)	Ω	thermal injury damage function, Eq. (4.5)
ϑ	dimensionless temperature rise, T/T_i	ω	perfusion rate of blood through the microvasculature (1/s)
φ	dimensionless time during a burn, t/t_b		

SUBSCRIPTS

a	arterial blood state	m, n	grid indices
b	reference burn state	max	maximum
c	cold	min	minimum
cl	clothing	o	outermost boundary of system
d	threshold conditions for thermal damage to tissue	p	pulse period during irradiation
e	environment	q	chemical species
F	phase front	r	cylindrical coordinate system
g	reference state	S	solid phase
gl	glass transition state	s	spherical coordinate system
h	hot	ss	steady state
i	initial	T	temperature
i, j, k	coordinate indices	t	time
L	liquid phase	u	state of thermal injury to a cell population
l	laser beam	V	vapor phase
m	melting conditions	x	Cartesian coordinate system

SUPERSSCRIPTS

p time increment index (in finite difference models)

Acknowledgments

This work was supported by grants from the National Science Foundation, No. CBT-8713600, the Texas Advanced Technology Program, No. 003660-009, the Texas Advanced Research Program, No. 003658-129, U.S. Air Force Office of Sponsored Research Grant No. L800069, and a John E. Fogarty Senior International Fellowship from the National Institutes of Health, No. 1FO6 TW01412-01 at the MRC Medical Cryobiology Group, University of Cambridge Department of Surgery, U.K. Ms. Hannah Dieball has provided considerable support in assembling figures from various reference sources in the literature.

References

1. S. J. Aggarwal, S. J. Shah, K. R. Diller, and C. R. Baxter, Fluorescence digital microscopy of interstitial macromolecular diffusion in burn injury. *Comput. Bio. Med.* **19**, 245-261 (1989).
2. R. G. Allen and G. D. Polhamus, Ocular thermal injury from intense light. In "Laser Applications in Medicine and Biology" (M. L. Wolbarsht, ed.), Vol. 4, pp. 247-278. Plenum Press, New York, 1989.
3. American Institute of Physics, Temperature in biology & Temperature and its regulation in man. In "Temperature: Its Measurement and Control in Science and Industry," pp. 409-584. Reinhold, New York, 1941.
4. R. R. Anderson and J. A. Parrish, Microvasculature can be selectively damaged using dye lasers: A basic theory and experimental evidence in human skin. *Lasers Surg. Med.* **1**, 263-276 (1981).
5. G. Arturson, Pathophysiology of acute plasma loss in burns. *Bibl. Haematologica* **23**, 1130-1135 (1965).
6. X. Bai and D. E. Pegg, Thermal property measurement on biological materials at subzero temperatures. *Trans. ASME, J. Biomech. Eng.* **113**, 423-429 (1991).
7. W. B. Bald, "Quantitative Cryofixation." Adam Hilger, Bristol 1987.
8. C. R. Baxter, Present concepts in the management of major electrical injury. *Surg. Clin. North Am.* **50**, 1401-1406 (1970).
9. J. J. Beaman and H. M. Paynter, "Modeling of Physical Systems." Harper & Row, New York, 1992, in press.
10. J. Beckmann, Ch. Körber, G. Rau, A. Hubel, and E. G. Cravalho, Redefining cooling rate in terms of the front velocity and thermal gradient: First evidence of relevance in freezing injury of lymphocytes. *Cryobiology* **27**, 279-287 (1990).
11. S. W. Benson, "The Foundations of Chemical Kinetics." Robert E. Krieger, Malabar, Florida, 1982.
12. T. Bergquist, B. Kleman and B. Tangroth, Laser irradiance levels for retinal lesions. *Acta Ophthalmol.* **43**, 331-349 (1965).
13. M. W. Berns, Laser surgery. *Scientific American* **264-6**, 84-90 (1991).
14. H. Bingham, Electrical burns. *Clinics. Plast. Surg.* **13**, 75-85. (1986).
15. R. C. Birkebak, Heat transfer in biological systems. *Intl. Rev. Gen. Exper. Zool.* **2**, 269-344 (1966).
16. R. Birngruber, Thermal modeling in biological tissues. In "Lasers in Biology and Medicine" (F. Hillenkamp, R. Pratesi, and C. A. Sacchi, eds.), pp. 77-97. Plenum Press, New York, 1980.
17. G. K. Blake, K. R. Diller, and L. J. Hayes, Analysis of several models for simulating skin burns. *J. Burn Care Rehab.* **12**, 177-189 (1991).
18. B. A. Boley and J. H. Weiner, "Theory of Thermal Stresses," Wiley, New York, 1960.
19. A. Bollinger, U. K. Franzeck, and K. Jäger, Quantitative capillaroscopy in man using fluorescence video-microscopy. *Prog. Appl. Microcirc.* **3**, 97-118 (1983).
20. C. Bonacina, G. Comini, A. Fasano, and X. Prinicero, On the estimation of thermo-physical properties in nonlinear heat-conduction problems. *Intl. J. Heat Mass Trans.* **17**, 861-867 (1976).
21. J. L. Boulnois, Photophysical processes in recent medical laser developments: A review. *Lasers Med. Sci.* **1**, 47-67 (1986).
22. P. Boutron, More accurate determination of the quantity of ice crystallized in low cooling rates in the glycerol and 1,2-propanediol aqueous solutions: Comparison with equilibrium. *Cryobiology* **21**, 183-191 (1984).

23. P. Boutron, Comparison with the theory of the kinetics and extent of ice crystallization and of the glass-forming tendency in aqueous cryoprotective solutions. *Cryobiology* **23**, 88-102 (1986).
24. H. F. Bowman, E. G. Cravalho, and M. Woods, Theory, measurement and application of thermal properties of biomaterials. *Ann. Rev. Biophys. Bioengr.* **4**, 43-80 (1975).
25. P. I. Branemark, U. Breine, and M. Joshi, Microvascular pathophysiology of burned tissue. *Ann. N.Y. Acad. Sci.* **150**, 474-494 (1968).
26. K. Büttner, "Physikalische Bioklimatologie." Akadem. Verlagsgesellschaft, Leipzig, 1938.
27. K. Büttner, Effects of extreme heat on man. *JAMA* **144**, 732-738 (1950).
28. K. Büttner, Effects of extreme heat and cold on human skin. I. Analysis of temperature changes caused by different kinds of heat application. *J. Appl. Physiol.* **3**, 691-702 (1951).
29. K. Büttner, Effects of extreme heat and cold on human skin. II. Surface temperature, pain and heat conductivity in experiments with radiant heat. *J. Appl. Physiol.* **3**, 703-713 (1951).
30. K. Büttner, Numerical analysis and pilot experiments of penetrating flash radiation effects. *J. Appl. Physiol.* **5**, 207-220 (1952).
31. C. P. Cain and A. J. Welsh, Measured and predicted laser induced temperature rise in the rabbit retina. *Invest. Ophthalmol.* **13**, 60-70 (1974).
32. H. S. Carslaw, "Introduction to the Mathematical Theory of the Conduction of Heat in Solids." Macmillan, New York, 1921.
33. H. S. Carslaw and J. C. Jaeger, "Conduction of Heat in Solids," 2nd Ed. Clarendon Press, Oxford, 1959.
34. B. Chalmers, "Principles of Solidification." Wiley, New York, 1964.
35. J. C. Chato, Heat transfer in bioengineering. In "Advanced Heat Transfer" (B. T. Chao, ed.), pp. 395-414. Univ. of Illinois Press, Urbana, 1969.
36. J. C. Chato, Heat transfer in blood vessels. *Trans. ASME, J. Biomech. Eng.* **102**, 110-118 (1980).
37. J. C. Chato, Fundamentals of bioheat transfer. In "Clinical Thermology: Thermal Dosimetry and Treatment Planning" (M. Gautherie, ed.), pp. 1-65. Springer-Verlag, Berlin, 1990.
38. M. M. Chen, The tissue energy balance equation. In "Heat Transfer in Medicine and Biology: Analysis and Applications" (A. Shitzer and R. C. Eberhart, eds.), Vol. 1, pp. 153-164. Plenum Press, New York, 1985.
39. H. Chmiel, N. Stroh, and E. Walitza, Verfahrenstechnische Aspekte der Gefrierkonservierung von Blutbestandteilen. *Biomed. Tech.* **25**, 52-57 (1980).
40. W.-F. Choeng and A. J. Welch, A model for optical and thermal analysis of laser balloon angioplasty. *IEEE Trans. Biomed. Eng.* **BME-36**, 1233-1243 (1989).
41. S. W. Churchill and L. B. Evans, Coefficients for calculation of freezing in a semi-infinite region. *Trans. ASME, J. Heat Trans.* **93**, 234-236 (1971).
42. I. Çilesiz and K. R. Diller, A modified time constants model by network thermodynamics: Temperature distribution in laser irradiated tissue. *Lasers Surg. Med.* (1992), submitted.
43. A. M. Clarke, W. J. Geeraets, and W. T. Ham, Jr., An equilibrium thermal model for retinal injury from optical sources. *Appl. Opt.* **8**, 1051-1054 (1969).
44. F. H. Cocks, W. H. Hildebrandt, and M. L. Shepard, Comparison of the low temperature crystallization of glasses in the ternary systems H_2O -NaCl-dimethyl sulfoxide and H_2O -NaCl-glycerol. *J. Appl. Phys.* **46**, 3444-3448 (1975).
45. R. Cogger, B. Rubinsky, and D. E. Pegg, Dependence of probability of vitrification on time and volume. *Cryo-Letters* **11**, 359-372 (1990).
46. O. Cope and F. D. Moore, A study of capillary permeability in experimental burns shock, using radioactive dyes in blood and lymph. *Am. J. Path.* **23**, 915-934 (1944).
47. R. X. Cotran and G. Manjo, A light and electron microscopic analysis of vascular injury. *Ann. N.Y. Acad. Sci.* **116**, 750-764 (1964).

48. J. Crank, "Free and Moving Boundary Problems." Oxford Univ. Press, Oxford, 1984.
49. K. R. Diller, Analysis of skin burns. In "Heat transfer in Medicine and Biology: Analysis and Applications" A. Shitzer and R. C. Eberhart, eds.), Vol. 2, pp. 85-134. Plenum Press, New York, 1985.
50. K. R. Diller, The influence of controlled ice nucleation on regulating the thermal history during freezing. *Cryobiology* **22**, 268-281 (1985).
51. K. R. Diller, A note on optimal techniques of rapid cooling for low temperature preparation of electron microscopy specimens. *Cryo-Letters* **11**, 75-88 (1990).
52. K. R. Diller, Coefficients for solution of the analytical freezing equation in the range of states for rapid solidification of biological systems. *Proc. Institut. Mech. Eng. J. Eng. Med.* **204**, 199-202 (1991).
53. K. R. Diller, A simple procedure for determining the spatial distribution of cooling rates within a specimen during cryopreservation I. Analysis. *Proc. Institut. Mech. Eng. J. Med.* **204**, 179-187 (1991).
54. K. R. Diller, A simple procedure for determining the spatial distribution of cooling rates within a specimen during cryopreservation. II. Graphical solutions. *Proc. Institut. Mech. Eng. J. Eng. Med.* **204**, 188-197 (1991).
55. K. R. Diller, Analysis of thermal gradients and thermal stresses during cooling of large biological systems for vitrification. Unpublished ms. (1992).
56. K. R. Diller, Analysis of burns by long term exposure to a heating pad. *J. Burn Care Rehabil.* **12**, 214-217 (1991).
57. K. R. Diller and E. G. Cravalho, A cryomicroscope for the study of freezing and thawing process in biological cells. *Cryobiology* **7**, 191-199 (1970).
58. K. R. Diller and L. J. Hayes, A finite element model of burn injury in blood perfused skin. *Trans. ASME, J. Biomech. Eng.* **105**, 300-307 (1983).
59. K. R. Diller and L. J. Hayes, Control of rate processes during phase change. *Proc. U.K. Natl. Conf. Heat Trans.*, pp. 327-338. IME, London, 1988.
60. K. R. Diller and L. J. Hayes, Analysis of tissue injury by burning: Comparison of *in situ* and skin flap models. *Intl. J. Heat Mass Trans.* (1992), in press.
61. K. R. Diller, L. J. Hayes, and C. R. Baxter, A mathematical model for the thermal efficacy of cooling therapy for burns. *J. Burn Care Rehab.* **4**, 81-89 (1983).
62. K. R. Diller, L. J. Hayes, and M. E. Crawford, Variation in thermal history during freezing with the pattern of latent heat evolution. *AIChE Symp. Ser.* **81**, 234-239 (1985).
63. B. K. Dussan and R. K. Weiner, "Study of burn hazard in human tissue and its implication on consumer product design." ASME 72- WA/HT-39, 1971.
64. K. Eurenus and J. Rotherberg, Platelet aggregation after thermal injury. *J. Lab. Clin. Med.* **83**, 344-363 (1974).
65. B. Fagrell, Microcirculation of the skin. In "The Physiology and Pharmacology of the Microcirculation" (N. A. Mortillaro, ed.), Vol. 2, pp. 133-180. Academic Press, Orlando, 1984.
66. G. M. Fahy, Analysis of "solution effects" injury: Equations for calculating phase diagram information for the ternary systems NaCl-dimethylsulfoxide-water and NaCl-glycerol-water. *Biophys. J.* **32**, 837-850 (1980).
67. G. M. Fahy, Biological effects of vitrification and devitrification. In "The Biophysics of Organ Cryopreservation" (D. E. Pegg and A. M. Karrow, Jr., eds.), pp. 265-297. Plenum Press, New York, 1987.
68. G. M. Fahy, Vitrification. In "Low Temperature Biotechnology: Emerging Applications and Engineering Contributions" (J. J. McGrath and K. R. Diller, eds.), pp. 113-146. ASME, New York, 1988.

69. G. M. Fahy, D. R. McFarlane, C. A. Angell, and H. T. Meryman, Vitrification as an approach to cryopreservation. *Cryobiology* **21**, 407-426 (1984).
70. G. M. Fahy, J. Saur, and R. J. Williams, Physical problems with the vitrification of large biological systems. *Cryobiology* **27**, 492-510 (1990).
71. R. H. Fallon and C. A. Moyer, Rates of insensible perspiration through normal, burned, tape-stripped, and epidermally denuded living human skin. *Ann. Surg.* **158**, 276-290 (1963).
72. M. C. Flemings, "Solidification Processing." McGraw-Hill, New York, 1974.
73. N. H. Fletcher, "The Chemical Physics of Ice." Cambridge Univ. Press, Cambridge, 1970.
74. F. Franks, The properties of aqueous solutions at subzero temperatures. In "Water A Comprehensive Treatise" (F. Franks, ed.), Vol. 7, pp. 215-338. Plenum Press, New York, 1982.
75. F. Franks, Storage in the undercooled state. In "Low Temperature Biotechnology: Emerging Applications and Engineering Contributions" (J. J. McGrath and K. R. Diller, eds.), pp. 107-112. ASME, New York, 1988.
76. C. E. Fugitt, "A Rate Process of Thermal Injury." Armed Forces Special Weapons Project, AFSWP-606 (1955).
77. L. A. Geddes, and L. E. Baker, The specific resistance of biological material: A compendium of data for the biomedical engineer and physiologist. *Med. Biol. Eng.* **5**, 271-293 (1967).
78. J. Gittus, "Creep Viscoelasticity and Creep Fracture in Solids." Halsted-Wiley, New York, 1975.
79. S. Glasstone, K. Laidler, and H. Eyring, "The Theory of Rate Processes. McGraw-Hill, New York, 1941.
80. S. S. Gorelik, "Recrystallization in Metals and Alloys." MIR Publishers, Moscow, 1981.
81. J. Gosse, "Technical Guide to Thermal Processes." Cambridge Univ. Press, Cambridge, 1986.
82. D. M. Green and K. R. Diller, Measurement of burn induced leakage of macromolecules in living tissue. *Trans. ASME, J. Biomech. Eng.* **100**, 153-158 (1978).
83. H. Gröber, S. Erk, and U. Grigull, "Fundamentals of Heat Transfer." McGraw-Hill, New York, 1961.
84. A. W. Ham and K. H. Cormack, "Histology," Eighth Ed. J. B. Lippincott, Philadelphia, 1979.
85. W. T. Ham, H. Wiesinger, F. G. Schmidt, R. C. Williams, R. S. Ruffin, M. C. Schaffer, and D. Guerry, III, Flashburns in the rabbit retina. *Am. J. Ophthalmol.* **46**, 700-723 (1958).
86. W. T. Ham, R. C. Williams, H. A. Mueller, R. S. Ruffin, F. H. Schmidt, A. M. Clarke, and W. J. Geeraets, Effects of laser radiation on the mammalian eye. *Ann. N. Y. Acad. Sci.* **28**, 517-526 (1966).
87. A. J. Han and J. A. Pearce, Kinetic model for thermal damage in the myocardium. In "Advances in Measuring Temperatures in Biomedicine; Thermal Tomography Techniques and Bioheat Transfer Models" (R. B. Roemer, J. W. Valvano, L. J. Hayes, and G. T. Anderson, eds.), pp. 59-66. ASME, New York, 1990.
88. J. W. Hand, Biophysics and technology of electromagnetic hyperthermia. In "Methods of External Hyperthermic Heating" (M. Gautherie, ed.), pp. 1-60. Springer-Verlag, Berlin, 1990.
89. U. Hartmann, B. Nunner, Ch. Körber, and G. Rau, Where should the cooling rate be determined in an extended freezing sample?, *Cryobiology* **28**, 115-130 (1991).
90. L. J. Hayes and K. R. Diller, Implementation of phase change in numerical models of heat transfer. In "Proceedings ASME, Second International Offshore Mechanics and Arctic

- Engineering Symposium" (J. S. Chung and V. J. Lunardini, eds.), pp. 642-648. ASME, New York, 1983; and *Trans. ASME, J. Energy Resourc. Tech.* **105**, 431-435 (1983).
91. L. J. Hayes and K. R. Diller, Computational methods for analysis of freezing bulk systems. In "Low Temperature Biotechnology: Emerging Applications and Engineering Contributions" (J. J. McGrath and K. R. Diller, eds.), pp. 253-272. ASME, New York, 1988.
 92. L. J. Hayes and K. R. Diller, and C. G. Ambrose, Analysis of thermal damage during cryosurgery. Unpublished ms. (1992).
 93. L. J. Hayes and K. R. Diller, and H. J. Chang, A robust numerical model of latent heat release during phase change. In "Numerical Methods in Heat Transfer" (J. L. S. Chen and K. Vafai, eds.), pp. 63-69. ASME, New York, 1986.
 94. L. J. Hayes and K. R. Diller, H. J. Chang and H. S. Lee, Prediction of local cooling rates and cell survival during the freezing of cylindrical specimens. *Cryobiology* **25**, 67-82 (1988).
 95. L. J. Hayes and K. R. Diller, and M. E. Crawford, "The Influence of Local Temperature History During Freezing of Impure Solutions on the Kinetics of Thermally Coupled Processes." ASME Heat Transfer Paper, 85-WA/HT-82, 1985.
 96. L. J. Hayes and K. R. Diller, H. S. Lee, and C. R. Baxter, On the definition of an average cooling rate during cell freezing. *Cryo-Letters* **5**, 97-110 (1984).
 97. M. P. Heisler, Temperature charts for induction and constant temperature heating. *Trans. Am. Soc. Mech. Eng.* **69**, 227-236 (1947).
 98. K. J. Henle, Arrhenius analysis of thermal responses. In "Hyperthermia in Cancer Therapy" (F. K. Storm, ed.), pp. 47-53. G. K. Hall Medical Publishers, Boston, 1983.
 99. F. C. Henriques, Studies of thermal injury. V. The predictability and the significance of thermally induced rate processes leading to irreversible epidermal injury. *Arch. Pathol.* **43**, 489-502 (1947).
 100. F. C. Henriques and A. R. Moritz, Studies of thermal injury. I. The conduction of heat to and through skin and the temperatures attained therein. A theoretical and experimental investigation. *Am. J. Pathol.* **23**, 531-549 (1947).
 101. L. N. Heynick, "Critique of the Literature on Bioeffects on Radiofrequency Radiation: A Comprehensive Review Pertinent to Air Force Operations." USAFSAM-TR 87-3 (1987).
 102. W. H. Hildebrandt, F. H. Cocks, and M. L. Shepard, The primary ice phase field in the H₂O-NaCl-dimethyl sulfoxide ternary system. *J. Mater. Sci.* **13**, 1099-1104 (1978).
 103. P. B. Hobbs, "Ice Physics." Clarendon Press, Oxford, 1974.
 104. J. D. Hunt, K. A. Jackson, and H. Brown, Temperature gradient microscope stage suitable for freezing materials with melting points between -100 and +200C. *Rev. Sci. Instrum.* **37**, 805 (1966).
 105. K. Hynynen, Biophysics and technology of ultrasound hyperthermia. In "Methods of External Hyperthermic Heating" (M. Gautherie, ed.), pp. 61-116. Springer-Verlag, Berlin, 1990.
 106. R. K. Jain, Analysis of heat transfer and temperature distributions in tissues during local and whole-body hyperthermia. In "Heat Transfer in Medicine and Biology: Analysis and Applications" (A. Shitzer and R. C. Eberhart eds.), Vol. 2, pp. 3-54. Plenum Press, New York, 1985.
 107. O. P. Jakobsson and G. Arturson, The effect of prompt local cooling on oedema formation in scalded rat paws. *Burns* **12**, 8-15 (1983).
 108. K. M. Jay, R. N. Barlett, R. Danet, and P. A. Allyn, Burn epidemiology: A basis for burn prevention. *J. Trauma* **17**, 943-947 (1977).
 109. D. J. Johns, "Thermal Stress Analysis." Pergamon Press, Oxford, 1965.

110. C. L. Johnson, E. J. O'Shaughnessy, and G. Ostergren, "Burn Management." Raven Press, New York, 1981.
111. M. Jochem and C. Körber, Extended phase diagrams for the ternary solutions H₂O-NaCl-glycerol and H₂O-NaCl-hydroxyethylstarch (HES) determined by DSC. *Cryobiology* **24**, 513-536 (1987).
112. D. R. H. Jones, Improved techniques for the quantitative optical microscopy for solid-liquid systems in a temperature gradient. *Rev. Sci. Instrum.* **41**, 1509-1511 (1970).
113. D. C. Karnopp, D. L. Margolis, and R. C. Rosenberg, "System Dynamics: A Unified Approach," Second Ed. Wiley-Interscience, New York, 1990.
114. C. A. Knight, A. L. DeVries, and L. D. Oolman, Fish antifreeze protein and the freezing and recrystallization of ice. *Nature (London)* **308**, 295-296 (1984).
115. C. A. Knight and J. G. Duman, Inhibition of recrystallization of ice by insect thermal hysteresis proteins: A possible cryoprotective role. *Cryobiology* **23**, 256-262 (1986).
116. C. Körber, Phenomena at the advancing ice-liquid interface: Solutes, particles and biological cells. *Quart. Rev. Biophys.* **21**, 229-298 (1988).
117. C. Körber and M. W. Scheiwe, Observation on the non-planar freezing of aqueous salt solutions. *J. Crystal Growth* **61**, 307-316 (1983).
118. S. Kourosh, K. R. Diller, and M. E. Crawford, Microscopic study of coupled heat and mass transport during unidirectional solidification of binary solutions. II. Mass transfer analysis. *Intl. J. Heat Mass Trans.* **33**, 39-53 (1990).
119. T. J. Krizek, M. C. Robson, and R. C. Wray, Jr., Care of the burned patient. In "The Management of Trauma" (W. F. Ballinger, R.B. Rutherford, and G. D. Zuidema, eds.), 2nd Ed., pp. 650-718. W. B. Saunders, Philadelphia, 1973.
120. P. Kubelka, New contributions to the optics of intensity light scattering materials. *J. Opt. Soc. Amer.* **38**, 448-457 (1948).
121. P. Kubelka, New contributions to the optics of intensity light scattering materials: II. Nonhomogeneous Layers. *J. Opt. Soc. Amer.* **44**, 330-335 (1954).
122. R. C. Lee and M. S. Kolodney, Electrical injury mechanisms: Dynamics of the thermal response. *Plast. Reconstr. Surg.* **80**, 663-671 (1987).
123. R. C. Lee and M. S. Kolodney, Electrical injury mechanisms: Electrical breakdown of cell membranes. *Plast. Reconstr. Surg.* **80**, 672-679 (1987).
124. P. P. Lele, Physical aspects and clinical studies with ultrasonic hyperthermia. In "Hyperthermia in Cancer Therapy" (F. K. Storm, ed.), 333-367, 1983.
125. R. L. Levin, Water permeability of yeast cells at subzero temperatures. *J. Memb. Biol.* **46**, 91-124 (1979).
126. R. L. Levin, Osmotic behavior of cells during freezing and thawing. In "Low Temperature Biotechnology: Emerging Applications and Engineering Contributions" (J. J. McGrath and K. R. Diller, eds.), pp. 177-188. ASME, New York, 1988.
127. S. Licht, "Therapeutic Heat and Cold," Second Ed. Waverly Press, Baltimore, 1965.
128. S. H. Lin, Analytical solutions for transient thermal behavior in biological systems. *Bull. Math. Biophys.* **34**, 413-418 (1972).
129. B. J. Luyet, An analysis of the notions of cooling and of freezing velocity. *Biodynamica* **7**, 293-335 (1957).
130. B. J. Luyet, An attempt at a systematic analysis of the notion of freezing rates and at an evaluation of the main contributory factors. *Cryobiology* **2**, 198-205 (1966).
131. D. R. MacFarlane, Aqueous solutions: Crystallization, vitrification and liquefaction. In "The Biophysics of Organ Cryopreservation" (D. E. Pegg and A. M. Karrow, Jr., eds.), pp. 143-146. Plenum Press, New York, 1987.
132. D. R. MacFarlane and M. Forsyth, Devitrification and recrystallization of glass forming aqueous solutions. In "The Biophysics of Organ Cryopreservation" (D. E. Pegg and A. M. Karrow, Jr., eds.), pp. 237-263. Plenum Press, New York, 1987.

133. M. A. Mainster, T. J. White, and R. G. Allen, Spectral dependence of retinal damage produced by intense light sources. *J. Opt. Soc. Am.* **60**, 848-855 (1970).
134. M. A. Mainster, T. J. White, J. H. Tips, and P. W. Wilson, Retinal-temperature increases produced by intense light sources. *J. Opt. Soc. Am.* **60**, 264-270 (1970).
135. M. A. Mainster, T. J. White, J. H. Tips, and P. W. Wilson, Transient thermal behavior in biological systems. *Bull. Math. Biophys.* **32**, 303-314 (1970).
136. P. Mazur, Cryobiology, The freezing of biological systems. *Science* **168**, 939-949 (1970).
137. P. Mazur, The role of intracellular freezing in the death of cells cooled at supraoptimal rates. *Cryobiology* **14**, 251-272 (1977).
138. P. Mazur, Slow freezing injury in mammalian cells. In "The Freezing of Mammalian Embryos," pp. 19-42. Excerpta Medica, Amsterdam, 1979.
139. P. Mazur, Freezing of living cells: Mechanisms and implications. *Am. J. Physiol.* **247**, C125-C142 (1984).
140. P. Mazur, Equilibrium, quasi-equilibrium and nonequilibrium freezing of mammalian embryos. *Cell Biophys.* **17**, 53-92 (1990).
141. P. Mazur, S. P. Leibo, J. Farrant, E. H. Y. Chu, M. G. Hanna, and L. H. Smith, Interactions of cooling rate, warming rate and protective additive on the survival of frozen mammalian cells. In "The Frozen Cell" (G. E. W. Wolstenholme and M. O'Connor, eds.), pp. 69-84. Churchill, London, 1970.
142. J. J. McGrath, Membrane transport properties. In "Low Temperature Biotechnology: Emerging Applications and Engineering Contributions" (J. J. McGrath and K. R. Diller, eds.), pp. 273-331. ASME, New York, 1988.
143. J. J. McGrath, E. G. Cravalho, and C. E. Huggins, An experimental comparison of intracellular ice formation and freeze-thaw survival of HeLa S-3 cells. *Cryobiology* **12**, 540-550 (1975).
144. W. R. McMantus, K. Eurenus, and B. Pruitt, Disseminated intravascular coagulation in burned patients. *J. Trauma* **13**, 416-422 (1973).
145. H. T. Meryman, The interpretation of freezing rates in biological materials. *Cryobiology* **2**, 165-170 (1966).
146. D. C. Mikulecky, Network thermodynamics: A simulation and modeling method based on the extension of thermodynamic thinking into the realm of highly organized systems. *Math. Biosci.* **71**, 1-23 (1984).
147. J. A. Moncrief, Burns. *N. Engl. J. Med.* **288**, 444-454 (1973).
148. A. R. Moritz and F. C. Henriques, Studies of thermal injury. II. The relative importance of time and surface temperature in the causation of cutaneous burns. *Am. J. Pathol.* **23**, 695-720 (1947).
149. M. Motamedi, S. Rastegar, G. LeCarpentier, and A. J. Welch, Light and temperature distribution in laser irradiated tissue: The influence of anisotropic scattering and refractive index. *Appl. Opt.* **28**, 2230-2237 (1989).
150. N. A. Moussa, J. J. McGrath, E. G. Cravalho, and P. J. Asimacopoulos, Kinetics of thermal injury in cells. *Trans. ASME, J. Biomech. Eng.* **99**, 155-159 (1977).
151. N. A. Moussa, E. N. Tell, and E. G. Cravalho, Time progression of hemolysis of erythrocyte populations exposed to supraphysiological temperatures. *Trans. ASME, J. Biomech. Eng.* **101**, 213-217 (1979).
152. R. Olsen, L. J. Hayes, E. H. Wissler, H. Nikaidoh, and R. C. Eberhart, Influence of hypothermia and circulatory arrest on cerebral temperature distributions. *Trans. ASME, J. Biomech. Eng.* **107**, 354-360 (1985).
153. G. Onik and B. Rubinsky, Cryosurgery: New developments in understanding and technique. In "Low Temperature Biotechnology: Emerging Applications and Engineering Contributions" (J. J. McGrath and K. R. Diller, eds.), pp. 57-80. New York, 1988.

154. G. F. Oster, A. S. Perleson, and A. Katchalsky, Network thermodynamic modelling of biophysical systems. *Quart. Rev. Biophys.* **6**, 1-134 (1973).
155. R. L. Palla, Jr., A heat transfer analysis of scald injury. *Nat. Bureau Stds. Int. Rpt.* 81-2320 (1981).
156. K. D. Paulsen, Calculation of power deposition patterns in hyperthermia. In "Clinical Thermology: Thermal Dosimetry and Treatment Planning" (M. Gautherie, ed.), pp. 57-118. Springer-Verlag, Berlin, 1990.
157. H. M. Paynter, "Analysis and Design of Engineering Systems." MIT Press, Cambridge, 1961.
158. J. A. Pearce, "Electrosurgery." Chapman and Hall, London, 1986.
159. J. A. Pearce, "Thermodynamic principles of laser-tissue interaction." *Proc. IEEE BMES* **12**, 1108-1110 (1990).
160. D. E. Pegg, The nature of cryobiological problems. In "Low Temperature Biotechnology" (J. J. McGrath and K. R. Diller, eds.), pp. 3-21. ASME, New York, 1988.
161. D. E. Pegg and F. G. Arnaud, Equations for obtaining melting points in the quaternary system propane-1,2-diol/glycerol/sodium chloride/water. *Cryo-Letters* **9**, 404-417 (1988).
162. D. E. Pegg and I. A. Jacobsen, Current status of cryopreservation of whole organs with particular reference to the kidney. In "Renal Preservation," pp. 301-322. Williams and Wilkins, Baltimore, 1983.
163. D. E. Pegg and A. M. Karrow, "The Biophysics of Organ Cryopreservation." Plenum Press, New York, 1988.
164. D. E. Pegg, B. Rubinsky, M. P. Diaper, and C. Y. Lee, Analysis of the introduction and removal of glycerol in rabbit kidneys, using a Krogh cylinder model. *Cryobiology* **23**, 150-160 (1986).
165. H. H. Pennes, Analysis of tissue and arterial blood temperatures in the resting human forearm. *J. Appl Physiol.* **1**, 93-122 (1948).
166. L. A. Preibe and A. J. Welch, Asymptotic rate process calculations of thermal injury to the retina following laser irradiation. *Trans. ASME, J. Biomech. Eng.* **100**, 49-54 (1978).
167. L. A. Preibe and A. J. Welch, A dimensionless model for the calculation of temperature increase in biologic tissues exposed to nonionizing radiation. *IEEE Trans. Biomed. Eng.* **BME-26**, 244-250 (1979).
168. L. A. Preibe, A. J. Welch, E. H. Wissler, and K. R. Diller, Significance of blood flow in calculations of temperature in laser irradiated tissue. In "1979 Advances in Bio-Engineering" (M. K. Wells, ed.), pp. 165-168. ASME, New York, 1979.
169. B. A. Pruitt, Jr. and A. D. Mason, Jr., High tension electrical injury. *Lancet* **3**, 124-137 (1970).
170. A. P. Rinfret, Thermal history. *Cryobiology* **2**, 171-180 (1966).
171. A. W. Robards and U. B. Sleytr, "Low Temperature Methods in Biological Electron Microscopy." Elsevier, Amsterdam, 1985.
172. M. C. Robson, Discussion of Lee and Kolodney. *Plast. Reconstr. Surg.* **5**, 680-681 (1987).
173. R. B. Roemer, Thermal dosimetry. In "Clinical Thermology: Thermal Dosimetry and Treatment Planning" (M. Gautherie, ed.), pp. 119-214. Springer-Verlag, Berlin, 1990.
174. R. B. Roemer, Heat transfer processes in hyperthermia. In "Progress in Hyperthermia" (D. B. Leeper, ed.), Vol. 1, 1992. In press.
175. D. C. Ross and K. R. Diller, An experimental investigation of burn injury in living tissue. *Trans. ASME, J. Heat Trans.* **98**, 292-296 (1976).
176. D. C. Ross and K. R. Diller, The therapeutic effects of postburn cooling. *Trans. ASME, J. Biomech. Eng.* **100**, 149-152 (1978).

177. A. Roulier, Calculation of temperature increase in the eye produced by intense light. *Bull. Math. Biophys.* **32**, 403-427 (1970).
178. B. Rubinsky, The equations for modelling heat and mass transfer during freezing of biological tissue. In "Low Temperature Biotechnology: Emerging Applications and Engineering Contributions" (J. J. McGrath and K. R. Diller, eds.), pp. 189-202. ASME, New York, 1988.
179. B. Rubinsky, A. Amir, and A. L. Devries, Cryopreservation of oocytes using directional cooling and antifreeze glycoproteins. *Cryo-Letters* **12**, 93-106 (1991).
180. B. Rubinsky and E. G. Cravalho, The determination of the thermal history in a one dimensional freezing system by a perturbation method. *Trans. ASME, J. Heat Transfer* **101**, 326-330 (1979).
181. B. Rubinsky and E. G. Cravalho, A finite-element method for the solution of one-dimensional phase change problems. *Intl. J. Heat Mass Trans.* **24**, 1587-1589 (1981).
182. B. Rubinsky and E. G. Cravalho, An analysis method to evaluate cooling rates during cryopreservation. *Cryobiology* **21**, 303-320 (1984).
183. B. Rubinsky, E. G. Cravalho, and B. Mikic, Thermal stresses in frozen organs. *Cryobiology* **17**, 66-73 (1980).
184. B. Rubinsky and M. Ikeda, A cryomicroscope using directional solidification for the controlled freezing of biological material. *Cryobiology* **22**, 55-68 (1985).
185. B. Rubinsky, C. Y. Lee, J. Bastaky, and T. L. Hayes, The mechanism of freezing in biological tissue: The liver. *Cryo-Letters* **8**, 370-381 (1987).
186. B. Rubinsky and D. E. Pegg, A mathematical model for the freezing process in biological tissue. *Proc. Royal Soc. London* **B234**, 343-358 (1989).
187. B. Rubinsky and A. Shitzer, Analysis of a Stefan-like problem in a biological tissue around a cryosurgical probe. *Trans. ASME, J. Heat Trans.* **98**, 514-519 (1976).
188. T. J. Ryan, Dermal vasculature. In "Methods in Skin Research" (D. Skerrow and C. J. Skerrow, eds.), pp. 559-586. Chichester, 1985.
189. R. E. Salisbury and B. A. Pruitt, "Burns of the Upper Extremity." W. B. Saunders, Philadelphia, 1975.
190. P. J. Schneider, "Conduction Heat Transfer." Addison-Wesley, Reading, Massachusetts, 1955.
191. M. L. Shepard, C. S. Goldston, and F. H. Cocks, The H₂O-NaCl-glycerol phase diagram and its application in cryobiology. *Cryobiology* **13**, 9-23 (1976).
192. A. Shitzer, Studies of bioheat transfer in mammals. In "Topics in Transport Phenomena" (C. C. Gutfinger, ed.) pp. 211-341. Halstead Press, New York, 1975.
193. A. Shitzer and R. C. Eberhart, "Heat Transfer in Medicine and Biology: Analysis and Applications," Vols. 1 & 2. Plenum Press, New York, 1985.
194. I. N. Snedon, "Fourier Transforms." McGraw-Hill, New York, 1951.
195. A. M. Stoll, A computer solution for determination of thermal tissue damage integrals from experimental data. *Inst. Radio Eng. Trans. Med. Elect.* **7**, 355-358 (1960).
196. A. M. Stoll, Heat transfer in biotechnology. In "Advances in Heat Transfer (J. P. Hartnett and T. J. Irvine, eds.), Vol. 4, pp. 65-141. Academic Press, New York, 1969.
197. A. M. Stoll and M. A. Chianta, Burn production and prevention in convective and radiant heat transfer. *Aerospace Med.* **39**, 1097-1100 (1968).
198. A. M. Stoll and M. A. Chianta, A method and rating system for evaluation of thermal protection. *Aerospace Med.* **40**, 1232-1238 (1969).
199. A. M. Stoll and M. A. Chianta, Heat transfer through fabrics as related to thermal injury. *Ann. N.Y. Acad. Sci.* **33**, 649-670 (1971).

200. A. M. Stoll and L. C. Green, Relationship between pain and tissue damage due to thermal radiation. *J. Appl. Physiol.* **14**, 373-382 (1959).
201. F. K. Storm, "Hyperthermia in Cancer Therapy." G. K. Hall Medical Publishers, Boston, 1983.
202. A. N. Takata, Development of criterion for skin burns. *Aerospace Med.* **45**, 634-637 (1974).
203. A. N. Takata, L. Zaneveld, and W. Richter, Laser-induced thermal damage of skin. SAM-TR-77-38, USAF School of Aerospace Medicine.
204. M. J. Taylor, Physico-chemical principles in low temperature biology. In *The Effects of Low Temperatures on Biological Systems*" (B. W. W. Grout and J. J. Morris, eds.), pp. 3-71. Edward Arnold, London, 1987.
205. K. F. Thompson and K. R. Diller, Use of computer image analysis to quantify contraction of wound size in experimental burns. *J. Burn Care Rehab.* **2**, 307-321 (1981).
206. S. Thomsen, J. A. Pearce, and W.-F. Cheong, Changes in birefringence as markers of thermal damage in tissues. *IEEE Trans. Biomed. Eng.* **36**, 1174-1179 (1989).
207. J. W. Valvano, Low temperature tissue thermal properties. In "Low Temperature Biotechnology Emerging Applications and Engineering Contributions" (J. J. McGrath and K. R. Diller, eds.), pp. 331-345. ASME, New York, 1988.
208. J. W. Valvano, J. R. Cochran, and K. R. Diller, Thermal conductivity and diffusivity of biomaterials measured with self-heated thermistors. *Intl. J. Thermophys.* **6**, 301-311 (1985).
209. M. J. C. van Gemert, R. Verdaasdonk, E. G. Stassen, G. Schets, G. H. M. Gijsbers, and J. J. Bonnier, Optical properties of human blood vessel wall plaque. *Lasers Surg. Med.* **5**, 235-237 (1984).
210. M. J. C. van Gemert and A. J. Welch, Time constants in thermal laser medicine. *Lasers Surg. Med.* **9**, 405-421 (1989).
211. G. Vigier and R. Vassoille, Ice nucleation and crystallization in water-glycerol mixtures. *Cryobiology* **24**, 345-354 (1987).
212. J. J. Vos, A theory of retinal burns. *Bull. Math. Biol.* **24**, 115-128 (1962).
213. J. A. Weaver and A. M. Stoll, Mathematical model of skin exposed to thermal radiation. National Air Defence Command Memo Report 6708, 1967.
214. J. A. Weaver and A. M. Stoll, Mathematical model of skin exposed to thermal radiation. *Aerospace Med.* **40**, 24-30 (1969).
215. A. J. Welch, The thermal response of laser irradiated tissue. *IEEE Trans. Quant. Electr.* **QE-20**, 1471-1481 (1984).
216. A. J. Welch, Laser irradiation of tissue. In "Heat Transfer in Medicine and Biology. Analysis and Applications" (A. Shitzer and R. C. Eberhart, eds.), Vol. 2, pp. 135-184. Plenum Press, New York, 1985.
217. A. J. Welch, J. A. Pearce, K. R. Diller, G. Yoon, and W. F. Cheong, Heat generation in laser irradiated tissue. *Trans. ASME, J. Biomech. Eng.* **111**, 62-68 (1989).
218. A. J. Welch and G. D. Polhamus, Measurement and prediction of thermal injury in the retina of the rhesus monkey. *IEEE Trans. Biomed. Eng.* **BME-31**, 633-644 (1984).
219. A. J. Welch, J. W. Valvano, J. A. Pearce, L. J. Hayes, and M. Motamedi, Effect of laser irradiation on tissue during laser angioplasty. *Lasers Surg. Med.* **5**, 251-264 (1985).
220. A. J. Welch, M. J. C. van Gemert, and A. B. Bradley, Optical and thermal events in laser angioplasty. In "Primer on Laser Angioplasty" (R. Ginsburg and J. C. White, eds.), pp. 89-119. Futura Publ., Mount Kisco, New York, 1989.
221. A. J. Welch, E. H. Wissler, and L. A. Priebe, Significance of blood flow in calculations of temperature in laser irradiated tissue. *IEEE Trans. Biomed. Eng.* **BME-27**, 164-166 (1980).

222. T. J. White, M. F. Mainster, J. H. Tips, and P. W. Wilson, Chorioretinal thermal behavior. *Bull. Math. Biophys.* **32**, 315-322 (1970).
223. E. H. Wissler, An analysis of chorioretinal thermal response to intense light exposure. *IEEE Trans. Biomed. Eng.* **ENG-23**, 207-215 (1976).
224. K. Wollhöver, M. W. Scheiwe, U. Hartmann, and C. Körber, On morphological stability of planar boundaries during unidirectional transient solidification of binary aqueous solutions. *Intl. J. Heat Mass Trans.* **28**, 897-902 (1985).
225. R. T. Woodburne and W. E. Burkel, "Essentials of Human Anatomy," Eighth Ed. Oxford Univ. Press, Oxford, 1988.
226. J. L. Wray, Model for prediction of retinal burns. Technical Staff Study, DASA 1281, Headquarters Defence Atomic Support Agency, Washington, D.C., 1962.
227. Y. C. Wu, Material properties criteria for thermal safety. *J. Mater.* **7**, 572-579 (1972).
228. Y. C. Wu, A modified criterion for predicting thermal injury. *Nat. Bureau. Stds. Rpt.* (1980).
229. Y. Xu, R. Qian, and Z. Yang, Analysis of thermal injury process. *Trans. ASME, J. Biomech. Eng.* (1992), in press.
230. J. Yoo and B. Rubinsky, Numerical computation using finite elements for the moving interface in heat transfer problems with phase transformation. *Numer. Heat Trans.* **6**, 209-222 (1983).
231. B. W. Zweifach, "Functional Behavior of the Microcirculation." Charles C. Thomas, Springfield, Illinois, 1961.